

**Magnetic Optical Bearing (MOB) Design
for Mirror Wavelength Scans in a
Spaceborne Interferometer**

by

Lawrence Scott Schwartz

S.B. Massachusetts Institute of Technology
(1994)

Submitted to the Department of
Mechanical Engineering
in Partial Fulfillment of the Requirements for the
Degree of

Master of Science in Mechanical Engineering

at the

Massachusetts Institute of Technology

May 1995

© 1995 Massachusetts Institute of Technology

The author hereby grants to MIT permission to reproduce and to
distribute publicly paper and electronic copies of this thesis document
in whole or part.

Signature of Author _____
Department of Mechanical Engineering
May 15, 1995

Certified by _____
Professor David L. Trümper
Faculty Thesis Supervisor

Certified by _____
Jamie W. Burnside
Company Thesis Supervisor

Accepted by _____
Ain A. Sonin
Chairman, Department Committee on Graduate Students

MASSACHUSETTS INSTITUTE
OF TECHNOLOGY

AUG 31 1995

1

ARCHIVES

LIBRARIES

Magnetic Optical Bearing (MOB) Design for Mirror Wavelength Scans in a Spaceborne Interferometer

by

Lawrence Scott Schwartz

Submitted to the Department of Mechanical Engineering at the
Massachusetts Institute of Technology on May 10th, 1995 in partial fulfillment of
the requirements for the degree of Master of Science in Mechanical Engineering

Abstract

The conception of a novel hybrid magnetic bearing is presented, analyzed, and proved with a prototype. The Magnetic Optical Bearing (MOB) is a magnetic actuator that is capable of controlling two degrees of freedom, a short transverse one and a long scanning one, by means of hybrid electromagnetics on the former and electrostatics on the latter. The permanent magnets in the circuit perform dual roles in this unique design, serving both axes of motion. The bearing is designed with a satellite-based scanning mirror interferometer in mind, which would use three of these actuators in a triangular fashion to yield six degrees-of-freedom overall.

The prototype is a scaled up version of a satellite point design. It utilizes digital control to stabilize and control the inherently unstable transverse direction as well as to control the stable voice coil. Tests are presented which demonstrate suspension and step response in the transverse suspension. In addition, some of the effects of the two axes coupling are presented, as well as initial tests in the scan direction.

From the tests, sub-micron stability is demonstrated in the transverse suspension with step responses as fast as twenty milliseconds. Correlation between the theoretical modeling equations, simulations, and experimentation proves to be very close for this direction. The initial scan direction tests demonstrate system capability. A two degree-of-freedom fixture is designed that allows for the two proscribed motions; one short, and the other perpendicular and long. The prototype is also suitable for analog control.

Faculty Thesis Supervisor: Dr. David Trumper

Title: Professor of mechanical Engineering

Company Thesis Supervisor: Jamie Burnside

Title: Staff Engineer

Acknowledgments

First and foremost I would like to thank my two advisors on the project, Professor David Trumper of the Mechanical Engineering Department at MIT, and Jamie Burnside, a staff member of the Control Systems Engineering Group at MIT Lincoln Laboratory. Professor Trumper patiently taught me everything I needed to know about magnetic bearings, and was a constant source of inspiration and ingenuity in the project. Jamie Burnside was the man who first introduced me to the project, and was always there to listen to every design scheme as it was hatched.

If anything was to be learned from putting this project together, it was how any engineering project requires a lot of input, assistance, and cooperation. At Lincoln Laboratory, I learned in the crash course of one year what it takes to take a project from conception to production, and there are many people I am thankful to. First I would like to thank the two leaders of Group 76, Control Systems Engineering; Carl Much, the Group Leader, and Ed Corbett, the assistant Group Leader. Carl willingly took me into the controls group from the optical systems group when I saw the project I wanted to do. He provided me with a desk and a lab, and a general nod of encouragement, as he's done for many other graduate students before me. Ed entrusted me with the laser position transducer, and went to bat for me when critical parts were being held up in the shop. His career counseling on the side was also very useful.

My right hand man at the lab, who was always extremely resourceful and literally catered to all my construction whims was Doug Whitcomb. Without him, the design would have never successfully left the paper stage. John Orthmann, most definitely the lab's finest and most caring machinist, is someone I also owe a great deal to. In the darkest hour of the project, when it looked like the prototype was beyond repair (and graduation way out of reach), he offered his hand, and just as importantly, his moral support. Bob Corby was to the project's electronics what Doug was to the mechanical aspect. He took my vague ideas of what I wanted to see in my electronics and made reliable and intelligently designed electronics boxes. I learned everything I ever wanted to know about adhesives from Pete Anderson and Susan Dacier, of group 72, who were both constantly supplying me with all sorts of epoxies and other types of

assistance. Lucio Cociani, of group 84, also taught this Macintosh user everything he knows about PCs and helped me build one, literally, from the motherboard up.

Besides those I have mentioned, just about everybody in Group 76 deserves thanks for their input and responsiveness at some point in the project. Pete Smith's experience in mechanical control system implementation is impressive, and showed me how to use the really neat controls related equipment. My office mate Paul Murray put up with me for a year and lent me some of his personal equipment, and his constant good humor was well appreciated. Group secretary Ardeth Grant was quick to answer all my questions and help me out in various time crunches. The technicians, many of whom contributed parts and equipment in one form or another, were also some of the best people to come to for electronics systems implementation, as well as discussions about nearly anything under the sun. Mark Williams, at Trumper's lab, must also be thanked for some of his initial direction and help in conceptualization, including figure 3.14.

Outside of the lab, I must thank the friends who were always there to listen to new ideas, and put up with constant amounts of complaining. Willy Ziminsky was there from the start, hearing the initial ideas of the first summer, checking my drawings, and carefully listening to the problems I encountered all around. My roommate Sumul Shah must be thanked, not only for helping to conceive the title (once you have a good acronym, you're halfway there!), but also for listening to the daily trials and tribulations of the thesis. John Kerwin, my other roommate, also listened to his fair share of whining with good patience. Both John and Sumul were also helpful in reading over parts of the draft.

Of course, I owe my mother and father a great deal of thanks. Without them, as they say, this wouldn't have been possible. They always encouraged all of my academic endeavors and instilled the value of working hard. I would also like to thank my Uncle David, who has always been a great supporter of education in the Schwartz family, and a role model to us all as well.

This work was performed at the MIT Lincoln Laboratory.

Table of Contents

| | |
|---|-----------|
| Abstract | 2 |
| Acknowledgments | 3 |
| 1 Introduction | 10 |
| 1.1 Introduction To Areas of Research | 11 |
| 1.2 Motivation and Objectives | 13 |
| 1.3 Overview of Thesis..... | 15 |
| 2 Literature Review | 17 |
| 2.1 Prior Art in Interferometric Scanning Mirrors..... | 18 |
| 2.2 Prior Art in Magnetic Actuator and Bearing Design | 21 |
| 2.2.1 ADEOS design..... | 21 |
| 2.2.2 Ball Aerospace's voice coils..... | 23 |
| 2.2.3 Studer's patented flywheels and bearings | 25 |
| 2.2.4 SVGL stage design..... | 27 |
| 3 Theory | 29 |
| 3.1 Basic Terms, Definitions and Assumptions | 29 |
| 3.2 Fundamentals Associated with Prior Art..... | 32 |
| 3.2.1 ADEOS MAMS: One approach to scan mirror dynamics..... | 32 |
| 3.2.2 Ball Aerospace: A creative voice coil..... | 34 |
| 3.2.3 Studer's rotor: A well designed hybrid magnetic circuit | 36 |
| 3.3 MOB Free Body Dynamics Formulation..... | 42 |
| 3.3.1 Kinematics overview..... | 43 |
| 3.3.2 Actuator Jacobian..... | 45 |
| 3.3.3 Mass properties | 49 |
| 3.3.4 Lagrange's equations of motion | 52 |
| 3.3.5 Sensor placement | 54 |
| 3.4 The MOB Hybrid Magnetic Circuit..... | 55 |
| 3.4.1 MOB permanent magnetic effects..... | 57 |
| 3.4.2 MOB electromagnetic coil effects..... | 61 |
| 3.4.3 MOB resultant electromagnetic and electrodynamic forces ... | 63 |
| 3.5 Actuator Linearization Techniques..... | 66 |
| 3.6 Design Implementation..... | 69 |
| 3.6.1 Design method | 69 |
| 3.6.2 Design point..... | 76 |
| 3.7 Two Degree-of-Freedom Test Fixture Design Study..... | 82 |
| 4 Hardware | 86 |
| 4.1 System Overview | 86 |
| 4.1.1 Digital control system | 87 |
| 4.1.2 Table layout | 89 |
| 4.2 Actuator and Platen | 93 |
| 4.2.1 Stationary actuators..... | 94 |
| 4.2.2 Moving platen..... | 99 |
| 4.3 Air Bearing | 102 |
| 4.3.1 Specifications | 102 |
| 4.3.2 Pendulum design and attachment | 104 |
| 4.4 Laser Position Transducer | 105 |
| 4.5 Capacitive Probe and Board | 108 |
| 4.6 Control System Electronics and Software | 110 |
| 4.6.1 A/D and D/A boards..... | 110 |

| | |
|--|------------|
| 4.6.2 Computer environment and affiliated software..... | 112 |
| 4.7 Amplifier Design..... | 114 |
| 5 Control System..... | 120 |
| 5.1 Objectives..... | 120 |
| 5.2 Control System Development | 121 |
| 5.2.1 System parameters..... | 121 |
| 5.2.2 Continuous electromagnetic model and control | 124 |
| 5.3 Simulink Model of Electromagnetic Control..... | 131 |
| 6 Results and Conclusions | 136 |
| 6.1 Tested Transverse Step Responses..... | 136 |
| 6.1.1 Straight proportional and lead control..... | 137 |
| 6.1.2 PI and lead control..... | 141 |
| 6.2 Scanning Direction Tests..... | 144 |
| 6.2.1 Centering force in the scanning direction..... | 144 |
| 6.2.2 Open loop control of voice coils | 146 |
| 6.2.3 Scan direction step responses | 147 |
| 6.3 Comparison of Actual Results to Simulations..... | 150 |
| 6.3.1 Straight proportional and lead control..... | 151 |
| 6.3.2 PI and lead control..... | 154 |
| 6.3 Conclusions and Suggestions for Further Work..... | 156 |
| 7 Alternate Designs | 158 |
| 7.1 Bridged Center and Tapered Flux Area | 159 |
| 7.2 Shim Designs..... | 161 |
| 7.2.1 Silicon iron shims | 161 |
| 7.2.2 Saturated iron shims..... | 161 |
| 7.2.3 Permanent magnet shims | 163 |
| 8 Bibliography..... | 164 |
| Appendix A: Control Code..... | 166 |
| Appendix B: Drawings | 184 |

List of Figures

| | | |
|------|--|-----|
| 2.1 | Porch swing design..... | 20 |
| 2.2 | ADEOS MAMS scanning mirror design..... | 22 |
| 2.3 | Ball Aerospace pointing mirror design..... | 24 |
| 2.4 | Studer flywheel design..... | 26 |
| 2.5 | SVGL stage design..... | 28 |
| 3.1 | MAMS free-body dynamics..... | 33 |
| 3.2 | Ball magnetic actuator arrangement..... | 35 |
| 3.3 | Studer's hybrid; an overall schematic..... | 36 |
| 3.4 | Studer's hybrid; flux paths created by permanent magnet alone..... | 37 |
| 3.5 | Studer's hybrid; resulting B-field from coil..... | 40 |
| 3.6 | MOB triangular kinematics overview..... | 43 |
| 3.7 | MOB coordinate frames and dimensions for Jacobian..... | 46 |
| 3.8 | MOB actuator motion clarified..... | 56 |
| 3.9 | MOB overall design..... | 57 |
| 3.10 | MOB permanent magnet effects..... | 58 |
| 3.11 | MOB B-fields from EM coils with voice coils removed..... | 61 |
| 3.12 | MOB combined magnet and electromagnetic coil effects..... | 64 |
| 3.13 | MOB geometric design point..... | 80 |
| 3.14 | MOB actuator conceptual 3D drawing..... | 82 |
| 3.15 | Two degree-of-freedom suspension method..... | 85 |
| 4.1 | Digital control system..... | 88 |
| 4.2 | Electronic Vibration Isolation (EVIS) table layout (top view)..... | 90 |
| 4.3 | Picture of overall layout..... | 91 |
| 4.4 | Top view picture of overall layout..... | 92 |
| 4.5 | Overview schematic of actuator, platen, and probe..... | 94 |
| 4.6 | Picture of actuator, platen, and probe..... | 95 |
| 4.7 | Actuator housing component drawing..... | 96 |
| 4.8 | Platen assembly..... | 99 |
| 4.9 | Picture of center platen..... | 100 |
| 4.10 | Pendulum attachment..... | 105 |
| 4.11 | General amplifier control loop block diagram..... | 115 |
| 4.12 | Electromagnetic coil amplifier control loop..... | 117 |

| | | |
|------|---|-----|
| 4.13 | Electrodynamic coil amplifier control loop..... | 117 |
| 5.1 | EM general block diagram..... | 124 |
| 5.2 | Bode of lead compensated electromagnetic coils. | 127 |
| 5.3 | Displacement step of lead compensated EM coils. | 127 |
| 5.4 | Current step of lead compensated EM coils. | 128 |
| 5.5 | Bode of lead and PI compensated electromagnetic coils..... | 129 |
| 5.6 | Closed loop Bode PI and lead compensated EM coils..... | 130 |
| 5.7 | Electromagnetic proportional plus lead Simulink model..... | 133 |
| 5.8 | Electromagnetic PI plus lead Simulink model..... | 134 |
| 6.1 | Injection of Bias into P controlled system (displacement)..... | 138 |
| 6.2 | Injection of Bias into P controlled system (current)..... | 138 |
| 6.3 | Positive step response of P controlled system (displacement)..... | 139 |
| 6.4 | Negative step response of P controlled system (displacement)..... | 140 |
| 6.5 | Positive step response of P controlled system (current)..... | 140 |
| 6.6 | Positive step response of PI controlled system (displacement)..... | 142 |
| 6.7 | Negative step response of PI controlled system (displacement)..... | 142 |
| 6.8 | Positive step response of PI controlled system (current)..... | 143 |
| 6.9 | Transverse readings of scanning oscillation..... | 145 |
| 6.10 | Open loop scanning oscillation. | 146 |
| 6.11 | Transverse readings of open loop scan..... | 147 |
| 6.12 | Scan direction small step responses for 3 mil and 6 mil steps. | 148 |
| 6.13 | Transverse response to a 3 mil scan step. | 149 |
| 6.14 | Transverse response to a 6 mil scan step. | 150 |
| 6.15 | P control of 10 micrometer step (actual displacement)..... | 151 |
| 6.16 | P control of 10 micrometer step (simulated displacement). | 152 |
| 6.17 | P control of 10 micrometer step (actual current)..... | 153 |
| 6.18 | P control of 10 micrometer step (simulated current). | 153 |
| 6.19 | PI control of 10 micrometer step (actual displacement)..... | 154 |
| 6.20 | PI control of 10 micrometer step (simulated displacement). | 155 |
| 6.21 | PI control of 10 micrometer step (actual current)..... | 155 |
| 6.22 | PI control of 10 micrometer step (simulated current). | 156 |
| 7.1 | Bridged center with tapered flux area. | 160 |
| 7.2 | Silicon iron shims. | 162 |
| 7.3 | Saturated iron shims. | 162 |
| 7.4 | Permanent magnetic shims. | 163 |

List of Tables

| | | |
|-----|--|-----|
| 3.1 | ADEOS MAMS actuator to global degree-of-freedom correlation..... | 33 |
| 3.2 | MOB actuator global to local degree-of-freedom correlation..... | 44 |
| 3.3 | Design parameters: inputs and outputs..... | 73 |
| 3.4 | Satellite requirements. | 77 |
| 3.5 | Permanent magnet properties. | 79 |
| 3.6 | Design point table. | 81 |
| 3.7 | Bearing type comparison. | 83 |
| 5.1 | General control parameters..... | 123 |
| 5.2 | Electromagnetic lead compensator and system parameters..... | 126 |
| 5.3 | Electromagnetic PI compensator parameters. | 129 |

Chapter 1

Introduction

NASA maintains a fleet of satellites entirely devoted to weather observation. The Geosynchronous Operational Environmental Satellites (GOES) are particularly useful as observation stations for severe weather development as well as observing anomalies in the atmosphere, such as the greenhouse effect. An important part of these weather stations are the various instruments employed for detecting traces of different elements in the atmosphere. Fourier Transform Infrared (FTIR) interferometers are used in these systems to assist in atmospheric element detection. FTIRs are common to many space-based applications, having been used on the Shuttle, Mariner, and Voyager spacecraft just to name a few. An integral part of any infrared interferometric device is the scanning mirror used to observe different wavelengths of light entering into the system. Traditionally, these scanning mirrors rely on some sort of mechanical bearing configuration to allow for their required single axis of motion. Occasionally, an alternative method is employed such as air bearings. However, in satellite design, these methods can be unreliable or extremely difficult to implement. Clearly there must be a better way than the all mechanical design.

Magnetic bearings have been successfully employed in many precision control applications. In terms of scanning mirror design, Japan is using magnetic bearing technology in their latest and most advanced weather satellites. The time has truly come to place this useful technology into spaceborne FTIR development. This thesis proposes a novel and efficient approach to a bearing configuration specifically designed with these spaceborne scanning mirrors in mind. Whereas the Japanese design is bulky, heavy, and requires four separate pairs of actuators and a linear motor, the

design herein is much more efficient and relies on three, two degree-of-freedom, magnetic hybrid actuators to control a scanning mirror. The unique magnetic circuitry is developed and proved in the hardware implementation of one of these hybrid function actuators.

1.1 Introduction To Areas of Research

In the design of this system, two areas of research provide the focus for the effort. The first, in a general sense, is that of general spaceborne FTIR design, focusing on the scanning mirror design to meet optical and satellite conditions. The second, in a more technical sense, is magnetic bearing technology, which is at the heart of the Magnetic Optical Bearing (MOB) design. The former field helps one to understand the broad ideas and design point requirements. The latter field provides the vehicle in which one can implement a design.

The first successful interferometer was developed by Michelson in order to observe hypothesized aether drift in the atmosphere. Since then, interferometers have evolved quite a bit, and are useful today in determining everything from the makeup of our atmosphere to the composition of distant stars. An interferometer takes in light from a source, which in many cases contains the emission spectrum of some element, and operates on that beam to determine its frequency spectrum. The beam is first collimated and focused. Next, it goes into a beam splitter, breaking the beam into two separate paths. One path is then reflected back onto a detector. The other path is reflected off of a moving mirror and then proceeds to the detector. At the detector the two paths recombine, and depending on their respective OPDs (optical path differences), they either combine constructively or destructively. At what intervals they combine constructively as the mirror scans is a function of the frequency composition of the light. Hence if the light is made up of many wavelengths, an understanding of what

frequencies of the spectra are prominent can be inferred. In an FTIR, an interferogram can be made, which is the curve of output intensity from an interferometer versus OPD. Classical Fourier transform techniques may then be applied to discern the sinusoidal components of the incoming light. All of this technology is applicable to the infrared spectrum.

At the heart of the FTIR interferometer is the scanning mirror. Indeed "the success of rapid scanning interferometry depends principally on the engineering of the interferometer and the drive system." [Johnston 1991] The bearing and drive requirements on the scanning mirror are challenging. The scanning mirror must keep a constant angle of orientation with respect to the optical axis. There are several common methods of maintaining this angle. Cube corner retro-reflectors inherently compensate a scanning drive system that is incapable of preventing tilt motion of the scanning mirror. So called "cat's eye" interferometers also decrease system sensitivity to such undesirable disturbances. The first method however requires additional reflection surfaces, and the second method is rather expensive. Other, more mechanical adaptations include the "porch-swing" design (a parallelogram method) which insures a nearly constant angle with respect to the optical axis and which usually employs flexure pivots. It is a popular design that will be discussed extensively next chapter in the context of the MIT Lincoln Laboratory system. This is the design used in the Nimbus, Voyager, and Mariner spacecraft. It is a dependable design, but inherently suffers because of it's mechanical nature. Another alternative final design, is the "rocking wishbone" configuration [Johnston 1991]. This design is a combination of a pendulum and a corner cube. However, the design here too suffers from typical mechanical drawbacks, as well as its tendency to amplify errors. Finally, the occasional use of air bearings for theses scanning mirrors can be found. Combined with a linear motor, an air bearing seems like an ideal solution. However, in practice, they have been often inadequate. They have a lower load-supporting capability, need a variety of extraneous

support equipment, and either have a lower stiffness, or exhibit instability at a higher one. To quote an early pioneer in his research "while the mechanical performance of the system has been adequate, the use of an air bearing in a large, lightly built interferometer, incorporating liberal use of long and thin members of light alloys, has nevertheless been a mistake." [Johnston 1991] Besides, a space application such as a satellite can hardly afford an air system. Magnetic bearings are another way to provide non-contact bearing capability, and are useful in environments such as space where an air bearing cannot venture.

In order to develop a unique suspension system, one which is tailored for the motion requirements of scanning mirror, a new and creative magnetic circuit design is required. Two fields of electromagnetic theory will be introduced in the third chapter. The first deals with the types of suspension forces normally associated with magnetic bearing technology. The second focuses on the types of driving forces associated with voice coils and speakers. These two designs can be packaged in a complementary fashion so that a single actuator harnesses both of these capabilities. This design will be extensively examined. The design evolves from some work done on other hybrid designs, particularly those found in several patents filed by one researcher [Studer 1977] who has done an extensive amount of work on magnetic flywheels. The voice coil part of the design evolved from work that Ball Aerospace was developing for their pointing mirror systems. The unique design herein is a combination of sorts between two designs, extracting the best of both designs, and paring down the respective permanent magnets required in the two systems.

1.2 Motivation and Objectives

A variety of reasons exist for exploring a new magnetic bearing alternative to a scanning mirror. As mentioned above, there are many general ways in which a

magnetic bearing is better suited to a spaceborne optical environment. Because there are no mechanical attachments across the bearing parts involved in the system, there is no wear. Satellites have lifetime requirements of five years or more. Instead of extensive life cycle testing, which is required for satellite components, magnetic bearings eliminate this worry. In many of the mechanical designs, a single point failure can destroy the entire optical array. Another advantage of no contact is the absence of friction. Since it is difficult to radiate heat in a space environment, this is also another critical concern. More important than general satellite requirements are the stringent optical ones. Heat introduced into the array could cause misalignment. Often the mechanical bearing system, particularly those of the flexure variety, must be kept thermally separated from the rest of the optical array. A final advantage of the non-contact system is that no lubricants, either fluidic or gaseous are required. Since satellites are unserviceable, this becomes an important consideration.

Besides the mechanical advantages offered by non-contact nature of these bearings, one other design asset is worthy of mentioning, and that is the complete, six degree-of-freedom active control found on the scanning mirror. More often than not, the scanning axis is the only actively actuated degree of freedom. If alignment errors arise from the mirror (or anywhere else in the system for that matter), they often need correction from a commandable pointing mirror. In the MOB configuration, with all degrees-of-freedom controlled, small corrections in the other axes can be obtained without the use of these other mirrors. Final related advances are in disturbance rejection of unwanted vibrations and increased bandwidth with the lack of structural resonances. The MOB controllable system goes one step beyond the Japanese design in this regard, since their design only passively stabilizes the roll axis.

Beyond the scope of academic curiosity, there is a real world desire to see the development of this technology. NASA plans their satellite development many years in advance. For their weather satellite program, they have dictated many new

improvements that they would like to see in the next generation of GOES and other similar satellites. In their list of top five advances in technology for this area, they listed magnetic bearings as a potential for new development.

Finally, there is a hardware motive in this thesis. The actuator designs are quite novel. Rather than relying purely on hand calculations and computer simulations (which are often inadequate in three-dimensional magnetic circuit design) for this project development, a decision was made to try to implement a prototype actuator for the design. As previously mentioned, the MOB configuration consists of three two degree-of-freedom actuators. In order to limit the scope of this project, the design and development of only one of these actuators was researched and implemented to prove the magnetic circuit design as viable.

Given the variety of motivations that initiated this project development, the objectives for the research are straightforward. The first objective is to design on paper a full six degree-of-freedom magnetically suspended scanning mirror. The second is to design, build, and test a prototype actuator for such a scanning mirror: a concept verification of sorts. Finally, the last main objective is to examine the issues involved with satellite implementation of such a design. By these objectives, the feasibility of a new magnet scanning mirror will be proven herein.

1.3 Overview of Thesis

This thesis covers the MOB conception, development, application and experiments. A comprehensive literature overview begins the thesis, explaining relevant ideas and technologies both in the field of electromagnetics and in interferometers. The theory section, chapter 3, after introducing some of the basic concepts and terms, then proceeds to give a more detailed and mathematically comprehensive analysis of many of the key concepts introduced in the literature review, as a "warm-up" to the MOB

analysis. The free body dynamics for the proposed full satellite MOB system are then explored, and then the specifics of the individual MOB actuators are introduced, ending with specific numbers for the experiment.

The subsequent chapter discusses the hardware implementation of the system, including the details of the facility that was created to test the machine, the manufacturing of the specialty parts, and the computer which controls the affiliated electronics. Chapter 5 then discusses the control system and the logic behind its design. Chapter 6, results and conclusions, gives an account of relevant experimental results and their implications. Finally, an exploration of alternate designs is discussed in chapter 7.

Chapter 2

Literature Review

As previously discussed, the technology associated with this project overlaps two general fields. Besides examining elements technically similar to the MOB design in each field, it is of particular interest to sort through pieces of technology that fall in both the realms of interferometric design as well as magnetic bearing design. Both technologies have their respective origins at the beginning of this century. Michelson was pursuing his aether investigations in the 1880, and one of the earliest patents related to magnetic bearings is the work of Herman Anschutz-Kaempfe in 1923 [Anschutz-Kaempfe 1926]. Much progress has been made in the intermittent years. This review will focus on relevant work within the past twenty years.

Interferometric scanning mirror design takes many forms. One form which is used quite often is the so-called porch swing. The porch swing design chosen for discussion here is the latest in technology that's being developed at the MIT Lincoln Laboratory. This design is chosen because it is typical of mechanical solutions for the control of scanning mirror motions. Another reason for this choice is that I am quite familiar with the details of this design since I have had the opportunity to see the prototype in operation at Lincoln Laboratory. As for magnetic bearing and actuator technology, four specific design will be examined in depth. The first is that of the Japanese ADEOS MAMS system. Although the magnetic bearing technology employed is traditional, it is the only other current example of a magnetically suspended spaceborne interferometric scanning mirror design of which I am aware. The design thus can serve as a basis of comparison for the proposed MOB system, particularly when examining its free body dynamics. The next type of magnetic actuation to be discussed will be that of the voice

coil design employed in a Ball Aerospace pointing mirror. A pointing mirror has some different operating requirements than a scanning mirror, but since both are used as part of optical systems packages and have tight tolerances on their respective control, a discussion of this other optical design family members is warranted. Beyond the optical comparison though, at the center of Ball Aerospace's design, is their unique voice coil, which was one of the seeds of the MOB actuator design.

The last two examples are not in the optical realm, and are more centered on similar magnetic circuits. Philip Studer has been involved with magnetic bearing technology for twenty years. In that period of time, he has published a number of patents. Of particular interest in examining are his magnetically suspended flywheels, which employ a number of variations on interesting hybrid magnetic circuit designs. Studer's paper on "a practical magnetic bearing" [Studer 1977] is an inspiration that drove the design of the MOB electromagnetic circuit. A final magnetic circuit design example, which has similarity to the single MOB actuator, allows for two degree-of-freedom magnetic actuation, is the design being developed for x-y lithography stages at SVGL. Although this design is similar in that it uses a permanent magnet to provide bias for electrodynamic coils, it is not a hybrid configuration like the MOB system in that there is no electromagnetic coil system. This distinction will be made clear through further descriptions. The permanent magnet does however provide a force bias for the air bearing, which supports the moving stage.

2.1 Prior Art in Interferometric Scanning Mirrors

Having done the research for the MOB project at the MIT Lincoln Laboratory, the author has had the advantage of seeing the laboratory's current work in satellite interferometric design first hand. Lincoln is heading up two projects for NASA for their weather observing satellites. The first platform, the Polar Operational Environmental

Satellite, already has a working porch swing prototype designed for it. For the second platform, the aforementioned GOES system, Lincoln is designing an entirely new interferometer as a plug-in improvement over the current NASA design. This package includes a scanning mirror. Since this was a design still being worked out at the onset of the MOB development, MOB adapted its requirements, from the optical specifications to the hostile environment conditions, as a reference point to design around and to test concept feasibility.

The porch swing is shown in figure 2.1 below. The design is purely mechanical, with the general shape of a parallelogram. In this particular adaptation, the porch swing can be thought of as upside down, with the "swing," or mirror assembly, at the top. The swing is suspended by means of a series of flexure pivots. A torque motor is then situated at the bottom of the swing, and serves to drive it. The rotations of the torque motor are transferred through the arm of the swing, resulting in purely linear motion of the bottom platform. As the swing rotates, the overall profile goes from the shape of a rectangle to that of a trapezoid. In doing so, in the ideal case (pure pivots), the mirror, whose orientation is perpendicular to the optical axis, swings back in forth remaining parallel to its original orientation. While the mirror may experience some off-axis vertical motion in this process, it is spared any changes in its angular orientation. This specification is a requirement on optical scanning mirrors. In reality, it should be noted, that a small change in angular orientation does tend to occur since flexure pivots are being employed, and these pivots will exhibit error motions as a function of their rotation

Because of its simple mechanical structure, and it's proven effectiveness at Lincoln Laboratory and previously at many other places, the porch swing is an often-used design. However, it does suffer its limitations. Since it will be in a space-based platform, any such scanning mirror design cannot be routinely serviced on demand. Because it is purely mechanical, it's flexure pivots must be designed carefully with a

huge life cycle in mind. Typically satellites must have a lifetime of at least five years. Considering that this particular infrared scanning example scans at a rate on the order of 1 Hz, the design must be able to survive at least 100 million cycles in its lifetime, putting an enormous strain on the design. In many regards, the porch swing's simplicity of design is also its short-fall. The swing motion allows for only one controlled degree-of-freedom of actuator motion. Any unplanned for misalignments in the interferometer must be compensated for by a separate commandable mirror. With the added complexity of the MOB design, which yields full six degree-of-freedom control, comes the advantage of not only accurate scanning motion control, but also the capability for small corrections in alignment about any angular axes. Of particular interest in this regard is the ability to control mirror tip and tilt.

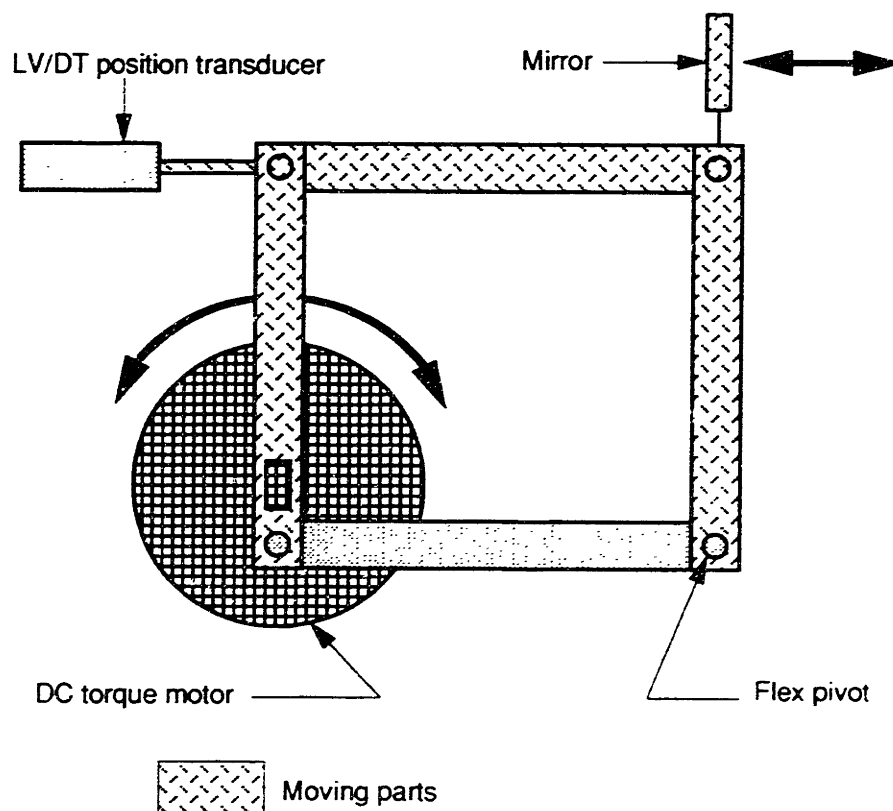


Figure 2.1: Porch swing design.

2.2 Prior Art in Magnetic Actuator and Bearing Design

Magnetic actuator and bearing design cover a wide range of technologies. Basic magnetic suspension is seen in applications ranging from lithography stages to flywheels. Voice coil designs, most commonly seen in speakers, can also be found in complex devices such as pointing mirrors. The examples below present the most relevant and similar approaches existing in the context of the MOB design. A complete analysis of the details of these designs will be presented in the next chapter.

2.2.1 ADEOS design

The ADEOS interferometric scanning mirror design is a good example of how well-understood magnetic bearing technology can be applied to spaceborne interferometry. The Interferometric Monitor for Greenhouse gasses (IMG) is going to be used specifically for the investigation of the global greenhouse effect, examining greenhouse gasses, air pollution, and gaseous exchange between the troposphere and lower stratosphere [Akiba et al 1992], [Shimoda et al 1991]. The particular scanning mirror required for this FTIR system is a lot larger than what was required for the NASA GOES system. Particularly, its scanning requirements are an order of magnitude larger than GOES, since it must travel 5 cm. This makes for a much larger system, with weight limitations a lot higher too, at 10 kilograms. The resulting design developed at Toshiba is shown below in figure 2.2.

The prototype concept is quite simple. Four pairs of suspension type magnetic actuators are used by the system which allow for the control of tip/tilt motion as well as x-y translation of the mirror. A final, elongated voice coil type linear motor is used for the actual scanning control. The magnetic bearings actively restrain four of the free body degree-of-freedoms, and the linear motor controls one. This leaves the sixth

degree of freedom, the roll of the mirror, generally not of primary concern, to be passively stabilized by the shape of the magnetic bearing field. A full free-body dynamics examination, to serve as a basis of comparison for the MOB design, will be discussed in the next chapter.

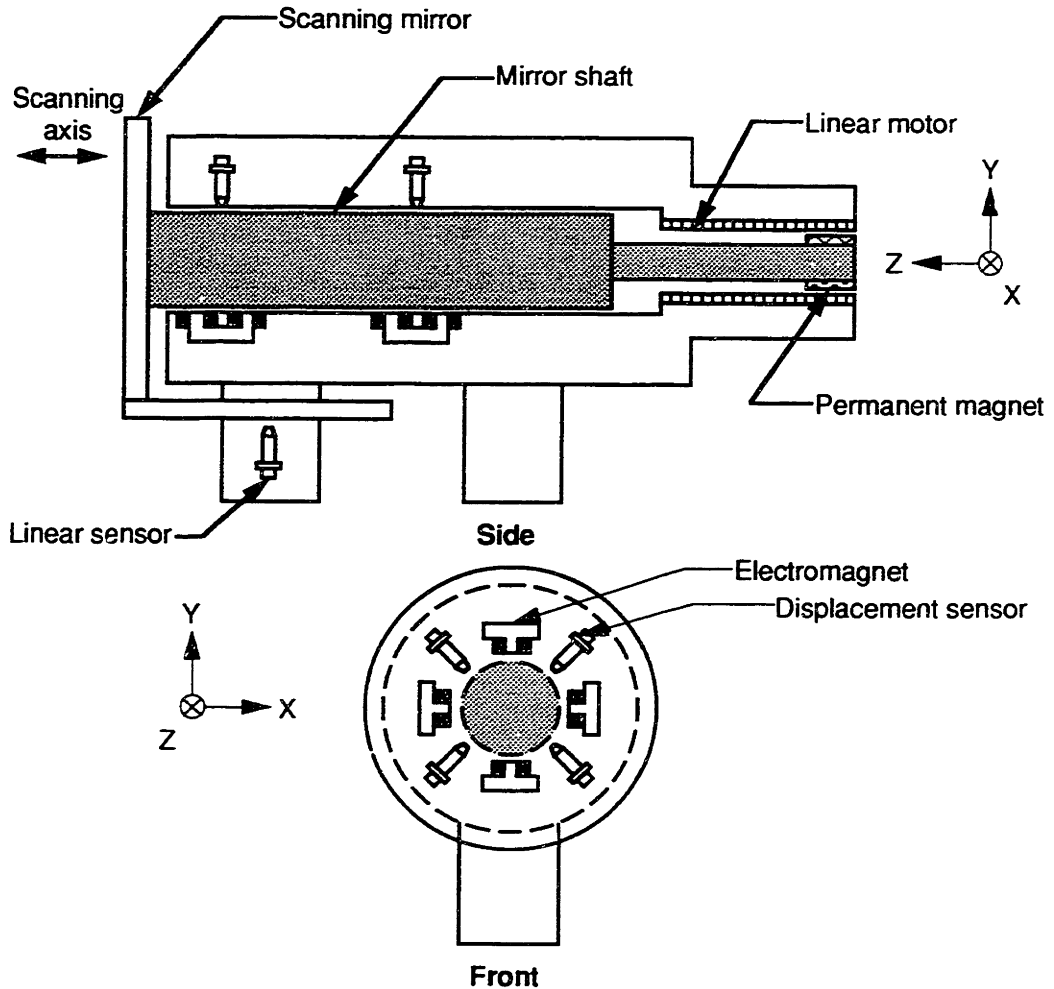


Figure 2.2: ADEOS MAMS scanning mirror design.

The ADEOS MAMS prototype is reported to have successfully met its projected goals. However, with a mass of 2.7 Kilograms and a power requirement of 18 Watts, the design warrants the examination into ways to cut down these large size and power requirements. The GOES interferometer, for example, utilizes a passive radiator to rid

itself of the heat generated by the interferometer, namely in the scanning mirror mechanism. This radiator allows for at most about 0.5 Watts of dissipation, which is much lower than any bearing based on the MAMS design can yield. Furthermore, NASA, in the short term, is looking for a plug-in replacement interferometer, since they do not plan to make any major design changes to the overall GOES satellite for several years to come. Because of this, the plug-in space available for the interferometer is very constrained, leaving tight spatial requirements on any type of scanning mirror system. Whereas in future designs for NASA, allocation could be made for a larger size scanning mirror, presently size is a very real limitation. Again, a design like the MAMS would be inadequate here. These limitations prompted a study by Lincoln Laboratory into the possibilities of entirely new magnetic configurations for an interferometric scanning mirror design, spearheaded by Professor David Trumper of MIT.

2.2.2 Ball Aerospace's voice coils

The hybrid magnetic technology employed by the MOB actuator not only employs standard suspension type magnetic pairs, but also uses the hybrid's permanent magnet for generating a magnetic field that can be used in conjunction with a voice coil. Ball Aerospace has developed a particularly interesting voice coil design for their Fine Steering Mirror (FSM) system. FSMs are utilized in pointing systems on both the ground and in space. Their applications range from laser communication to Earth observation instruments like the ADEOS and GOES, to astronomy experiments [Medbery et al 1991]. Like the MAMS and MOB systems, Ball's steering mirror system is designed using magnet actuators to avoid the problems associated with flexures, which are commonly used in steering mirrors as well as scanning mirrors. Their system is shown below in figure 2.3.

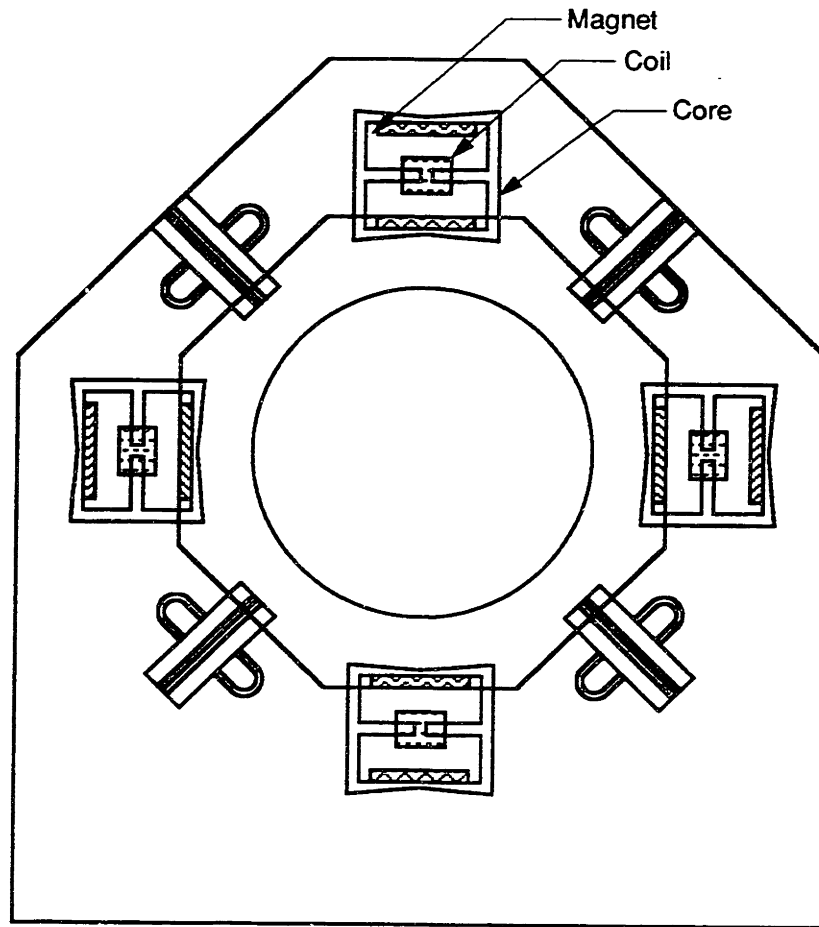


Figure 2.3: Ball Aerospace pointing mirror design.

The design uses four sets of voice coil pairs. A key distinction must be made between the actuator pairs used by the ADEOS system and those used here. Whereas the ADEOS suspension actuator pairs control the motion along the line that intersects the centers of the pair, in the ball design, since voice coils are employed, the motion controlled by opposing voice coils pairs is the motion *transverse* to the centers of each pair. This presents an entirely new set of actuator dynamics, which is a little bit less straightforward than simple, all suspension control. What is seen from the diagram, is that the first two set of opposing actuators, whose cross sections are shown, control the in plane x-y translations as well a the rotation around the z axis, (which comes out of the page). The other two sets of actuators, each having out of plane motion control as

their respective actuation directions, can handle the other free-body motions. Specifically, small z-direction scanning motions are allowed for as well as mirror tip and tilt. The configuration is therefore an excellent one when small rotations and displacements are required, with approximately equal travel in the three translational degrees of freedom.

Looking specifically at the actuators employed, they are of the Lorentz-Force type. The uniqueness of the actuator design lies in its vertical symmetry, particularly in the return flux path for the permanent magnets. From the diagram, the basics of the actuator are shown, with an inner voice coil, permanent magnet array, and the core for the flux return. The specifics of the voice coil operation are discussed in detail in the next chapter.

2.2.3 Studer's patented flywheels and bearings

A particularly interesting application of a hybrid magnetic circuit design can be found in the flywheel designs of Studer. Philip Studer has a number of patents and papers in this field. They include "A Practical Magnetic Bearing" [1977], "Magnetic Bearing System" [1977], and "Radial and Torsionally Controlled Magnetic Bearing" [1987]. The first and last design are most relevant here; the latter of which is a more complex implementation of the first. As the title of the first patent implies, effective means to implement hybrid technology are explored in his design. Like the MOB design, samarium cobalt is used as the permanent magnet for the hybrid. Unlike the MOB design, use of the permanent magnet is restricted to hybrid suspension, and passive stabilization is relied on for axial disturbances. The general design implementation is shown below.

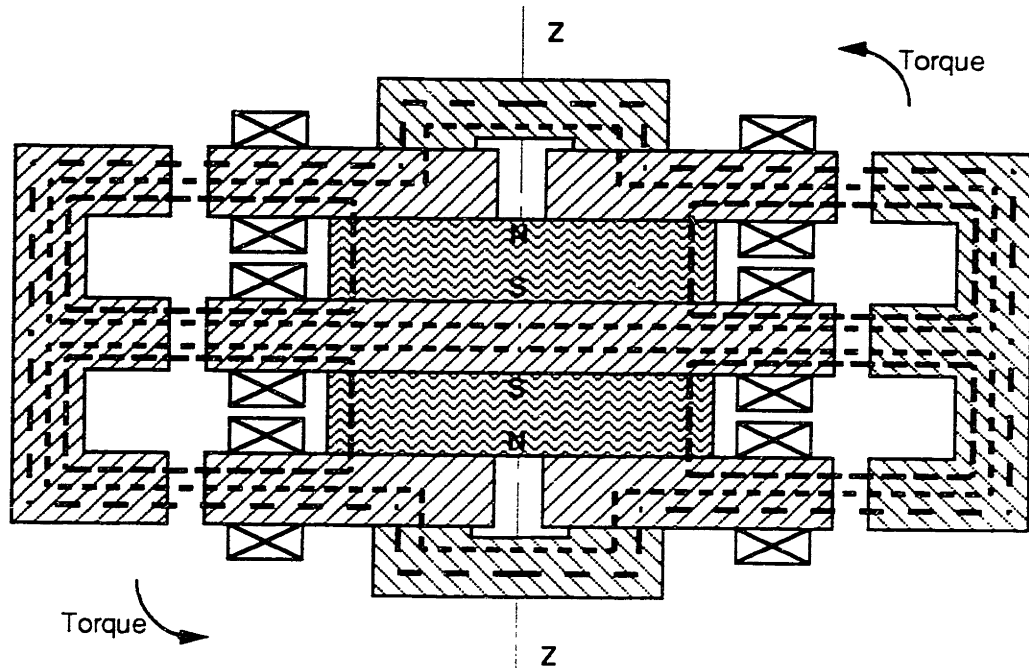


Figure 2.4: Studer flywheel design.

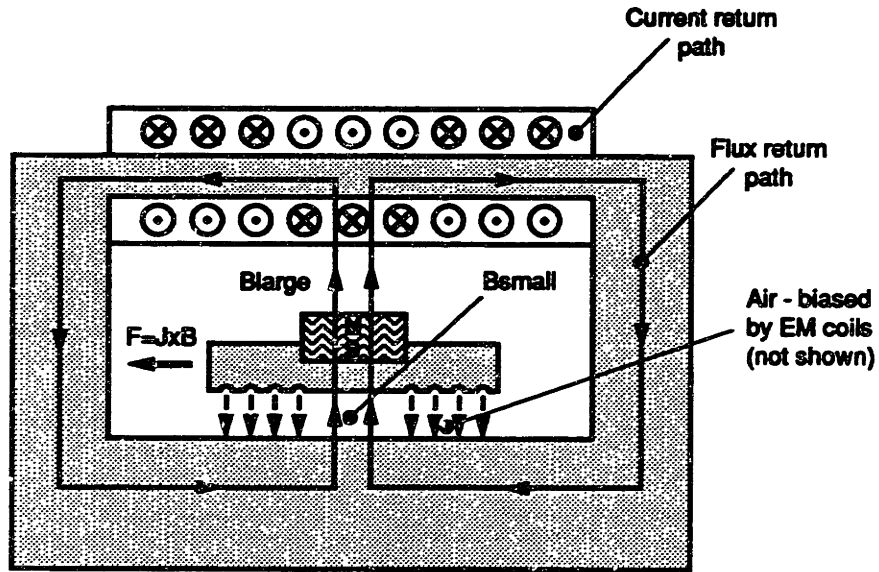
Whereas the other designs explored so far are specifically tailored to optical systems, Studer's work has very different operating requirements. What is interesting to note in his designs however, are the permanent magnetic circuits, the simplest of which will be rederived next chapter. Whereas the Ball voice coils are seen in one part of the MOB magnetic circuit, Studer's flywheel hybrid design is very close to what is seen in another part. The big advantage of hybrid suspension magnets is their inherent ability to linearize the force's dependence on the current. In most magnetic suspensions, force increases as the current squared. The trick is now to go one step beyond the hybrid design and utilize the permanent magnet for larger distance Lorentz-Force actuation.

2.2.4 SVGL stage design

The final piece of magnetic actuator technology worthy of discussion is that of SVGL design for a lithography stage [Buckley et al 1989]. Actuator development for lithography stages is an important rising application for magnetic bearings, much research of which is being done presently at MIT under the direction of Professor David Trumper. In some aspects, the SVGL design looks very similar to the MOB suspension system. Electromagnetic forces bias air bearings which control three degrees of freedom, and electrodynamic forces control the other three. As an interesting side note, mentioned at the beginning of the chapter, the test fixture for the MOB actuator employs an air bearing, to allow for just two degrees of freedom of control. Similarly, the SVGL stage employs an air bearing as part of their system, although in a "hockey-puck" configuration as shown in figure 2.5.

From this simplified figure, the use of a permanent magnet and voice coils can be seen. The flux paths, which extend from the top of the magnet, through open space, to the core material at the center of the voice coils, back around through the sides, and returning through a smaller gap, have a multiplicity of effects. First, and most importantly, they set up a field which, by means of the Lorentz Force, interacts with the coils to make the permanent magnet assembly move either left or right in this one degree-of-freedom adaptation. SVGL then also maintains a necessary bias force from the forced air through the holes at the bottom of this moving platen. This bias force can be adjusted to counteract both gravity and the attractive force created by the resulting B-field at this small gap. Comparisons back to this design will be presented in the next chapter. Note that the voice coils here are fairly inefficient, as the return path of the coils is not used to create any forces. The MOB actuator, in its own way, uses its full complement of voice coils more effectively, as will be demonstrated next chapter. This is an important consideration because required power of operation is directly related to

the size of the voice coils. The flux in the SVGL magnetic circuit is not used to bias an active magnetic bearing, and thus the MOB design is clearly distinguishable and novel vis-a-vis the SVGL design.



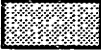


-  Highly permeable iron core
-  Permanent magnet
-  Wound coil

Figure 2.5: SVGL stage design.

Chapter 3

Theory

The MOB scanning mirror concept has evolved from a variety of ideas and technologies, many of which were introduced last chapter. In order to understand the details of the MOB design, a good understanding technically of the prior art is essential, particularly to those less familiar with magnetic bearing applications for optical design work. This first subject of this chapter is therefore a thorough evaluation of the most relevant issues that arise from the previously mentioned designs. Next, the MOB system is introduced with an analysis which discusses the free-body dynamics of the full scanning mirror design. This issue is raised first, so that an overall picture of the MOB design may be presented first. Preceding this analysis comes a discussion of the specific electromagnetic circuit theory and analysis of the actuators, which are at the core of the MOB design. Following the fully developed equations, linearization techniques are presented to help make the control of the system more realizable. Finally, the chapter closes with the design issues faced in making the prototype actuator, with a section devoted to the details of the satellite design and specific design choices, and another on techniques explored to fixture a single actuator for subsequent testing.

3.1 Basic Terms, Definitions and Assumptions

Before reintroducing the various designs, perhaps it is worth clearly defining a few terms and equations used throughout this thesis. The first few terms are associated with the motion of a scanning mirror. The analogy is best thought of when comparing the

scanning mirror to an aircraft. In this case, instead of having a cabin at the fore section of a plane, we have a mirror which must be controlled. The z-axis can be thought of as the primary travel axes for the aircraft, and is also the primary axis of travel for the scanning mirror. The roll direction is defined as rotation about this axis. Perpendicular to the travel axes, the plane can rise or descend, and move side to side. This defines the x-y plane, as it does for the scanning mirror. Similarly a plane can yaw and pitch, which are rotations about the y- and x- axes respectfully. A scanning mirror can tip and tilt. When the free-body dynamics for the MOB system are developed, since the body will only be making small angular changes in orientation overall, the respective kinematics can be derived based on linearized results for small angles. This will be discussed further in a later section.

A few terms and equations commonly arise in connection with the specifics of actuator design. Prior to mentioning the key equations, a quick definition of some of the terms is in order. There is the magnetization density denoted by \mathbf{M} , the magnetic field strength denoted by \mathbf{H} , and the magnetic flux density denoted by \mathbf{B} . Now for the essential electromagnetic equations. These are all based on Maxwell's equations for quasi-static magnetic field systems [Haus and Melcher 1989]. The equations of interest can be written as

$$\oint_C \mathbf{H} \cdot d\mathbf{l} = \int_S \mathbf{J}_f \cdot n d\mathbf{a} \quad (3.1)$$

$$\oint_S \mathbf{B} \cdot n d\mathbf{a} = 0 \quad (3.2)$$

$$\mathbf{B} = \mu_0(\mathbf{H} + \mathbf{M}). \quad (3.3)$$

For the subsequent equations that will be employed herein, the above equations can be somewhat simplified. Some assumptions can be made, particularly on the first equation. For wound magnetic wire, with parameters i for current and N for number of turns, the first equation can be written the following way, where the right half of the equation is the current enclosed

$$\oint_C \mathbf{H} \cdot d\mathbf{l} = Ni. \quad (3.4)$$

An even simpler form of the equation arises when the closed loop path encircles no current carrying wires; the right hand term goes to zero. For all of the electromagnetic development herein, the analysis is done in two dimensions. This implies that the closed loop path is one dimensional, and that the surfaces enclosed are two-dimensional. Other frequent assumptions include letting the permeability of the magnetically permeable E-cores approach infinity, and the permeability of free space, μ_0 , be the same for air as for the permanent magnet. For permanent magnets operating under no external magnetic field, the field is based entirely on the inherent magnetization.

Electromagnetic and electrodynamic forces are terms that will be frequently utilized throughout the thesis, particularly in the final stages of the theoretical actuator development sections, both for Studer's design as well as the MOB. In the context of this thesis, these are best defined in terms of their fundamental equations. The first, electromagnetic, refers to the magnetic forces that arise on the face of a permeable body which has magnetic flux passing through it. If two permeable bodies have flux passing through them, with an air gap and magnetic field in between them, then the force at the area A where the bodies face each other is given by

$$F_{em} = \frac{B^2 A}{2\mu_0}, \quad (3.5)$$

under the assumption that the field B is uniform throughout the gap, and that B is perpendicular to the pole faces. For a more general treatment, see [Melcher 1982]. The other type of force that is often used herein is that of the electrodynamic type. These are simply Lorentz-Forces, which arise when a current travels perpendicular to a magnetic field. This force is given by

$$F_{ed} = J \times B. \quad (3.6)$$

The former variety is seen most commonly in small suspension gaps, and the latter is seen mostly in so called voice coil actuators.

3.2 Fundamentals Associated with Prior Art

Much of the MOB theory is an extension of the fundamentals presented in this section. While the entire theory may be derive from first principles, approaching the MOB theory through these specific and closely related examples is the most educational. Unlike the literature review section which introduced these examples and where they came from, this section focuses on the specifics, so the detailed elements may be compared and contrasted with the MOB design.

3.2.1 ADEOS MAMS: One approach to scanning mirror dynamics

The problem in designing for the dynamics and control of a fully suspended scanning mirror is straightforward at first glance. The requirement is for a system that can move the mirror through a specified scan length, while suspending it in its five other degrees of freedom. From this broad requirement, a number a configurations can be imagined. As an example, the ADEOS MAMS design is shown in figure 3.1.

The diagram focuses on just the actuator layout for the required dynamics. The correlation between actuator and overall controlled motion is stated in the table below. Electromagnetic actuator pairs handle most of the dynamics, including the x-y translation, pitch about the x-axis, and yaw about the y-axis. The linear motor, acting on the suspended body, controls the larger scanning motion in the z-axis. Finally, the

roll dynamics are passively stabilized by the variable reluctance of the electromagnetic bearings. Using a rectangular body configuration is a common approach in an electromagnetically suspended body. Full precision magnetic suspension work on rectangular bodies is well documented in other designs outside the optical field [Trumper 1990].

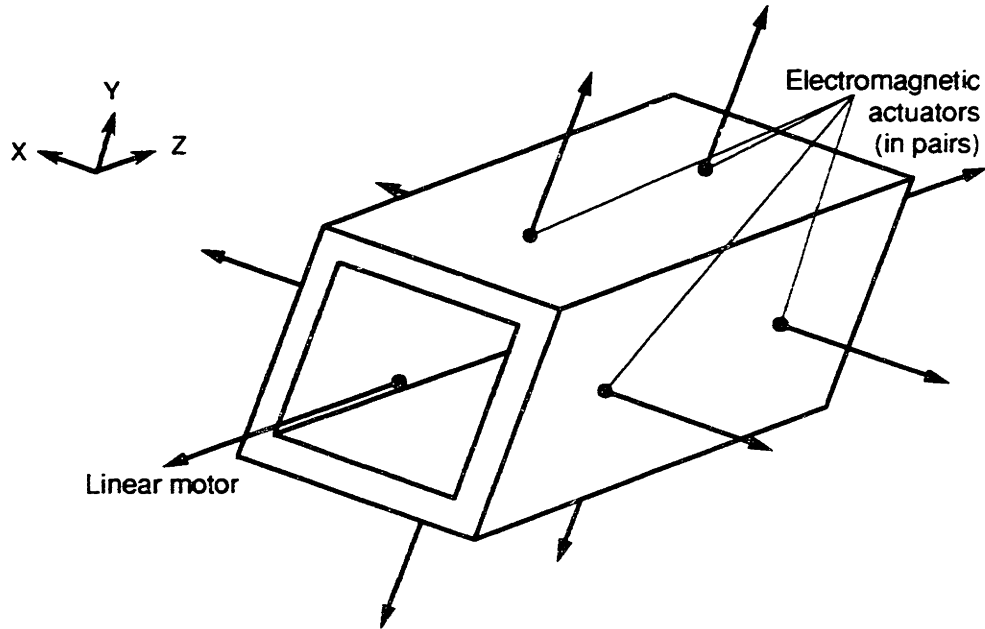


Figure 3.1: MAMS free-body dynamics.

Table 3.1: ADEOS MAMS actuator to global degree-of-freedom correlation.

| Control type | Degrees controlled |
|-----------------|---|
| Electromagnetic | X & Y translation, pitch (about X), yaw (about Y) |
| Linear motor | Z translation |
| Passive | Roll (about Z) |

3.2.2 Ball Aerospace: A creative voice coil

Voice coils come in many shapes and forms. The design requirements on these devices are relatively straight forward as well. A constant and even magnetic field is required for a set of coils to transverse. Most of the details of the design fall in creating return magnetic flux paths for the permanent magnet flux to follow a well-defined closed loop path. Ball Aerospace's FSM design utilizes a design package which works quite well for a pure voice coil. However, this design uses the field only for generating electrodynamic forces, as opposed to the MOB design, which uses the permanent magnets to bias the electromagnetic bearings as well. The configuration of the Ball Aerospace actuators is shown below in figure 3.2, in an enlarged view of what was previewed in figure 2.3.

The permanent magnets' flux follows the path pointed out in the diagram. First, it transverses the large gap, and then it travels in the iron core, made from a highly permeable substance, through which it returns to the other side of the magnet. This behavior is symmetrical around the center, so the activity can be though of as occurring in each of the four quadrants. This sets up an approximately uniform field across the gap. Around the center of the return cores, a wound coil can be inserted. As current flows in the coils, electrodynamic Lorentz-type forces arise. In the top half, current goes into the page, and in the given configuration this yields a force that pushes the coil to the right. Similarly, on the bottom half, the current goes into the page, and then crosses with the magnetic field (a mirror image of the top field); this combination also yields a force to the right.

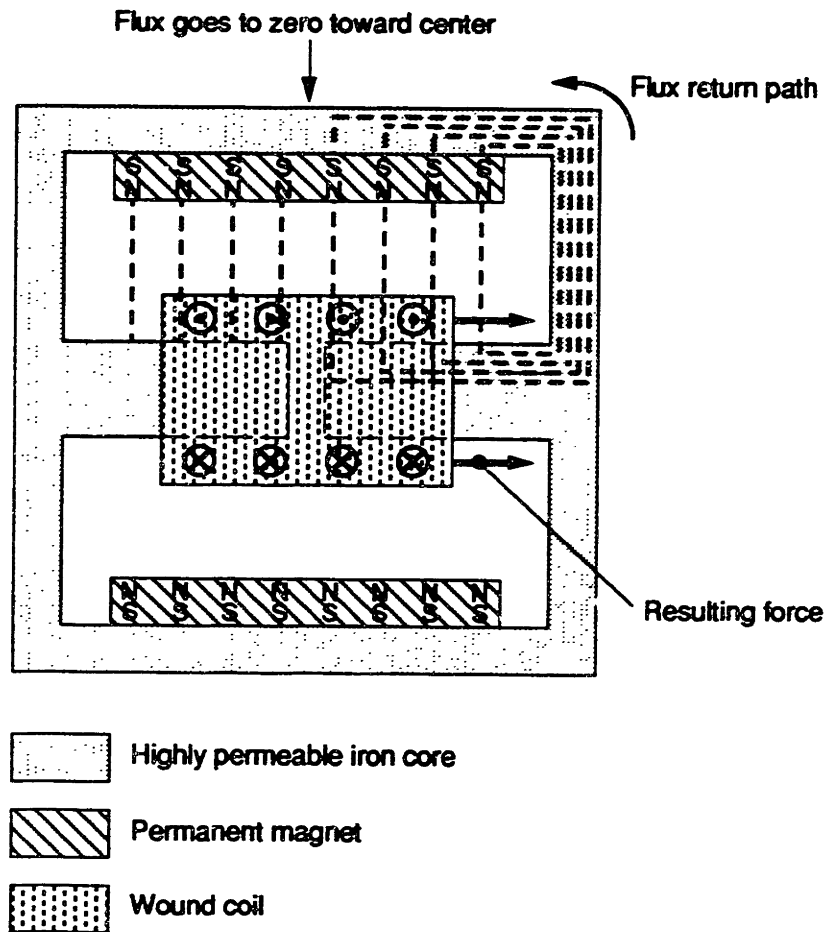


Figure 3.2: Ball magnetic actuator arrangement.

One of the considerations of this design is keeping the possible saturation of the permeable core in check. For example, the way that the flux concentrates at the top and bottom of the actuator is worth noting. As can be seen from the diagram, looking at the flux paths back into the magnets from the e-cores, the amount of flux returning becomes less and less, and approaches zero at the center. By maintaining the flux at different critical points, optimum permeable material cross sections can be determined for the most compact and lightweight design. While not as evident in the Ball Aerospace design, these dramatic changes in area can be seen in some of Left Handed Design's actuators, an off-shoot company of Ball Aerospace. These voice coils can be made exceedingly small. The Ball actuator is no larger than a dime.

3.2.3 Studer's rotor: A well designed hybrid magnetic circuit

Magnetic suspension is also used in a variety of motors, where the rotor is either partially or completely suspended from the stator. Although a lot of Studer's most complex developments can be seen in his various approaches to flywheels, it is more helpful to examine his most simple and fundamental design, that of his "Practical Magnetic Bearing" [Studer 1977]. Since the application is quite a bit different than the previously discussed designs for optical applications, the focus will be on just the magnetic circuit theory of this system and how it influences the MOB. A simplified of this magnetic circuit is shown in figure 3.13. Note in the drawing that the gaps are highly exaggerated for clarity.

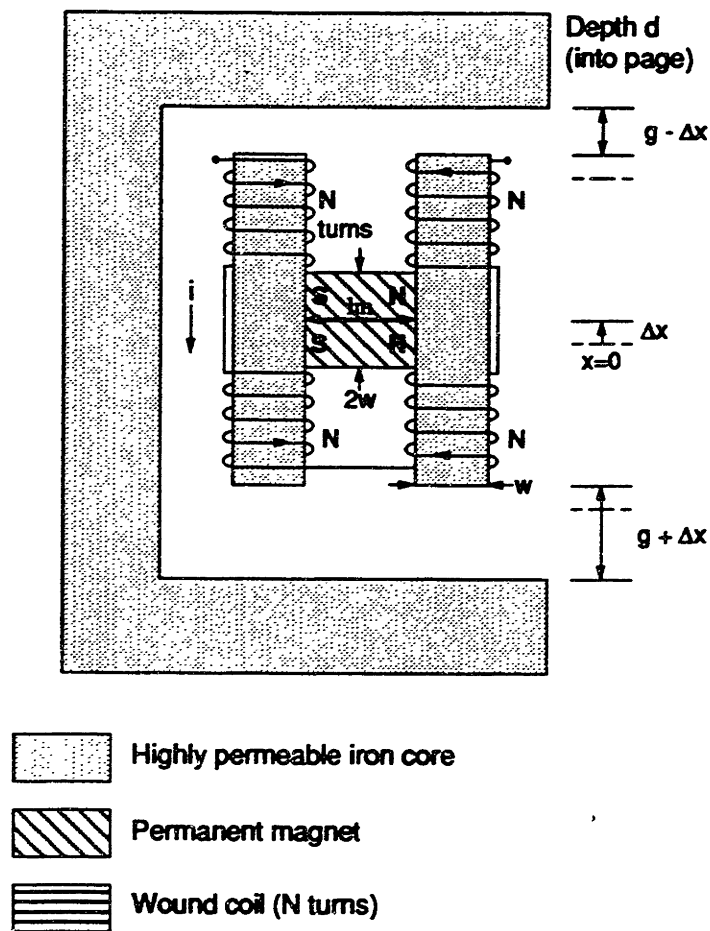


Figure 3.3: Studer's hybrid; an overall schematic.

As with the Ball Aerospace design, two different types of materials are employed. We have sections of highly permeable cores, and one permanent magnet. Control is exerted in the x direction in this case, over the small gaps between the center iron piece and the outer iron C-core. Using the principle of superposition for the magnetic (\mathcal{E}) fields that will be generated, it is best to break up the analysis into two separate halves. The first half consists of examining the B-fields created across the small gaps by the permanent magnet. The second half consists of examining the B-fields created across the small gaps by the coils. At the last stage of analysis, the resulting B-fields across these small gaps can be summed and used to calculate the resulting electromagnetic forces on the center body. Hence, the analysis will start with just the permanent magnet, as shown in figure 3.4.

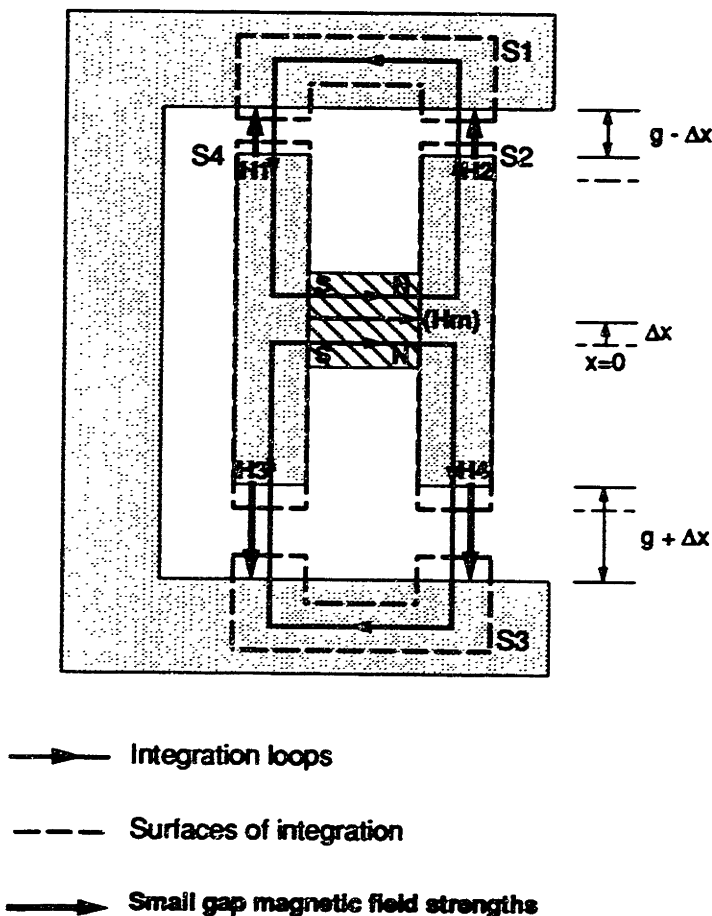


Figure 3.4: Studer's hybrid; flux paths created by permanent magnet alone.

First the integral of the magnetic field strength around the inner closed loops will be examined. As aforementioned the permeability of the iron for now will be assumed to be infinite, which means that the magnetic field in these sections of the contour is zero. Hence, the only H field seen is across the gaps themselves. From the first and second loops respectively, by examining the integrals of the magnetic field strength, the following is derived,

$$H_m l_m + H_2(g - \Delta x) - H_1(g - \Delta x) = 0 \quad (3.7)$$

$$H_m l_m + H_4(g + \Delta x) - H_3(g + \Delta x) = 0. \quad (3.8)$$

Looking now at the surfaces s_1 and s_2 , the surface integral of the magnetic flux density can be taken. The only flux going in and out of the volume is at the small gap interfaces. This reduces the equation to

$$B_1(wd) + B_2(wd) = 0. \quad (3.9)$$

Around surface s_3 , a similar development is given by

$$B_3(wd) + B_4(wd) = 0. \quad (3.10)$$

Now, on s_2 , the integral of the flux density around the surface yields

$$-2B_m(wd) + B_2(wd) + B_4(wd) = 0. \quad (3.11)$$

Similarly, on surface s_4 we have

$$-2B_m(wd) + B_1(wd) + B_3(wd) = 0. \quad (3.12)$$

The fundamental equations to arrive at the magnetic fields B_1 , B_2 , B_3 and B_4 , based on just the permanent magnet, have now been presented. By combining equations 3.7 to 3.12, and utilizing the relationship between flux density, field strength, and MMF (equation 3.3), the results yield

$$B_1 = -\mu_0 M_0 \left(\frac{(g + \Delta x) l_m}{2(g - \Delta x)(g + \Delta x) + l_m g} \right) = -B_2 \quad (3.13)$$

$$B_3 = -\mu_0 M_0 \left(\frac{(g - \Delta x) l_m}{2(g - \Delta x)(g + \Delta x) + l_m g} \right) = -B_4. \quad (3.14)$$

When centered, these results yield

$$B_1 = B_3 = \frac{-\mu_0 M_0 l_m}{2g + l_m} = -B_2 = -B_4. \quad (3.15)$$

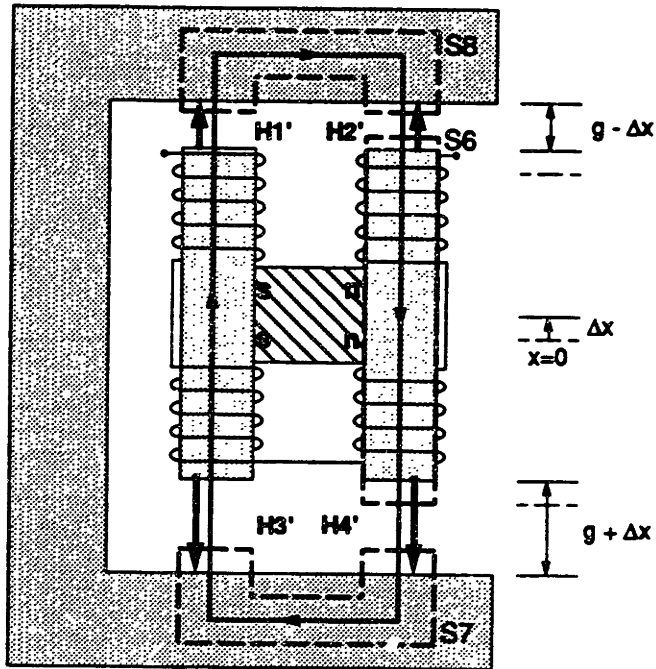
This is an interesting result, that is compatible with some simple reasoning. As the permanent magnet length gets much larger than the gap length, the resulting magnetic flux densities across the gaps approach what they would be based on the permanent magnet magnetization M_0 alone. With the converse result, when the gap becomes quite large, the resulting flux density begins to diminish as $1/g$.

The other set of magnetic flux densities that arise in the gaps comes from the addition of the electromagnetic coils. Because of superposition, under the assumption of magnetic linearity, the effects of the magnet can be put aside temporarily and the resulting B-fields due to the coils alone can be found. The configuration of surfaces used for this analysis is shown in figure 3.5.

The analysis of this circuit construct starts with examining the integral of the magnetic field strength around the closed loop which passes through the C-core and all the way through the two permeable strips, yielding

$$H'_1(g - \Delta x) - H'_2(g - \Delta x) + H'_4(g + \Delta x) - H'_3(g + \Delta x) = 4Ni. \quad (3.16)$$

The prime in this case is used to distinguish magnetic field strengths and flux densities based on the coils, versus the ones previously developed based on the magnet. Now, by following a series of closed surfaces and taking the respective integrals of the magnetic flux densities about each one, the following equations can be derived.



- ▶ Integration loops
- - - Surfaces of integration
- ▶ Small gap magnetic field strengths

Figure 3.5: Studer's hybrid; resulting B-field from coil.

On s_7

$$B_3'(wd) + B_4'(wd) = 0, \quad (3.17)$$

on s_6

$$B_2'(wd) + B_4'(wd) = 0, \quad (3.18)$$

on s_8

$$B_2'(wd) + B_4'(wd) = 0. \quad (3.19)$$

Reducing these equations with equation 3.3, and then combining them all yields the following result

$$B'_1 = B'_4 = \frac{\mu_0 Ni}{g} = -B'_2 = -B'_3. \quad (3.20)$$

Note that there are four coils of N turns each, thus this result has g in the denominator, even though the field crosses four gaps.

Some interesting distinctions can be inferred when comparing these results to the B-fields arising from the permanent magnets. Here, as would be expected, there is no dependence of this magnetic field on the offset position. Also, the symmetry is different. Whereas before (in the centered case, to simplify the comparison) $B_1 = B_3$ and $B_2 = B_4$, in the case of the coils, $B'_1 = B'_4$ and $B'_2 = B'_3$.

The juxtaposition of B-field symmetry has an interesting effect on the resulting forces. The total force on the suspended body (neglecting any gravity effects) is found from

$$\sum_1^4 F_n = F_{up} - F_{down} = F_1 + F_2 - F_3 - F_4. \quad (3.21)$$

Using the definition of the electromagnetic force based on the B-field from the introduction to the chapter, forces at each gap can be found from

$$F_n = \frac{AB_{n_{tot}}^2}{2\mu_0}, \quad (3.22)$$

where each B_{tot} is

$$B_{n_{tot}} = B_n + B'_n. \quad (3.23)$$

Combining all the equations that have been derived so far for this hybrid design yields the total force on the center piece, as a function of offset and current given by

$$F_{tot} = 4\mu_0 wdM_0 l_m \left[\frac{M_0 g l_m \Delta x}{[2(g - \Delta x)(g + \Delta x) + l_m g]^2} - \frac{Ni}{2(g - \Delta x)(g + \Delta x) + l_m g} \right]. \quad (3.24)$$

To better understand the full implications of this formula, it is instrumental to examine the result when the suspended body is centered. In this case

$$F_{centered} = -4\mu_0 wd \left(\frac{M_0 l_m}{2g + l_m} \right) \left(\frac{Ni}{g} \right) + \left[\frac{M_0 l_m}{g(2g + l_m)^2} \right] \Delta x. \quad (3.25)$$

This simplified result demonstrates the advantages of having a hybrid design. The force is linearly dependent on the applied current. This result simplifies the control of these actuators, particularly if implemented in the form of an analog circuit. Also, the dependence of the force on the strength of the permanent magnet should be noted. In essence, the first term in parenthesis is an effect of the permanent magnet. The second term that is in parenthesis is derived from the coil. When the fields are squared and added to yield the forces, all the squared terms drop out, leaving only the above stated multiplicative, linear portions.

3.3 MOB Free Body Dynamics Formulation

The best way to obtain an overall picture of how the fully suspended MOB system works is to understand the kinematics and dynamics of the proposed scanning mirror. Initially, by seeing the actuator layout, an understanding of which actuators control which overall degrees of freedom can be understood. In a detailed analysis of the kinematics for this specific system, an understanding of some of the parameters that drive the system design can be gained. The section therefore starts with an overall picture, moves onto the kinematics details such as the Jacobian, works through the dynamics with the Lagrangian, and ends on a brief discussion of possible sensor placement positions.

3.3.1 Kinematics overview

The overall motion and control requirements for the MOB system were the initial driving forces behind the design. The ADEOS MAMS found one way to use electromagnets and electrodynamics to suspend and control a scanning mirror. The MOB design can be thought of as a new overall approach. The decisions on where to place the assorted actuators very much determine the type of actuators required as well as their specific design requirements. To start with the analysis, an overall picture of actuator placement is shown in the figure below.

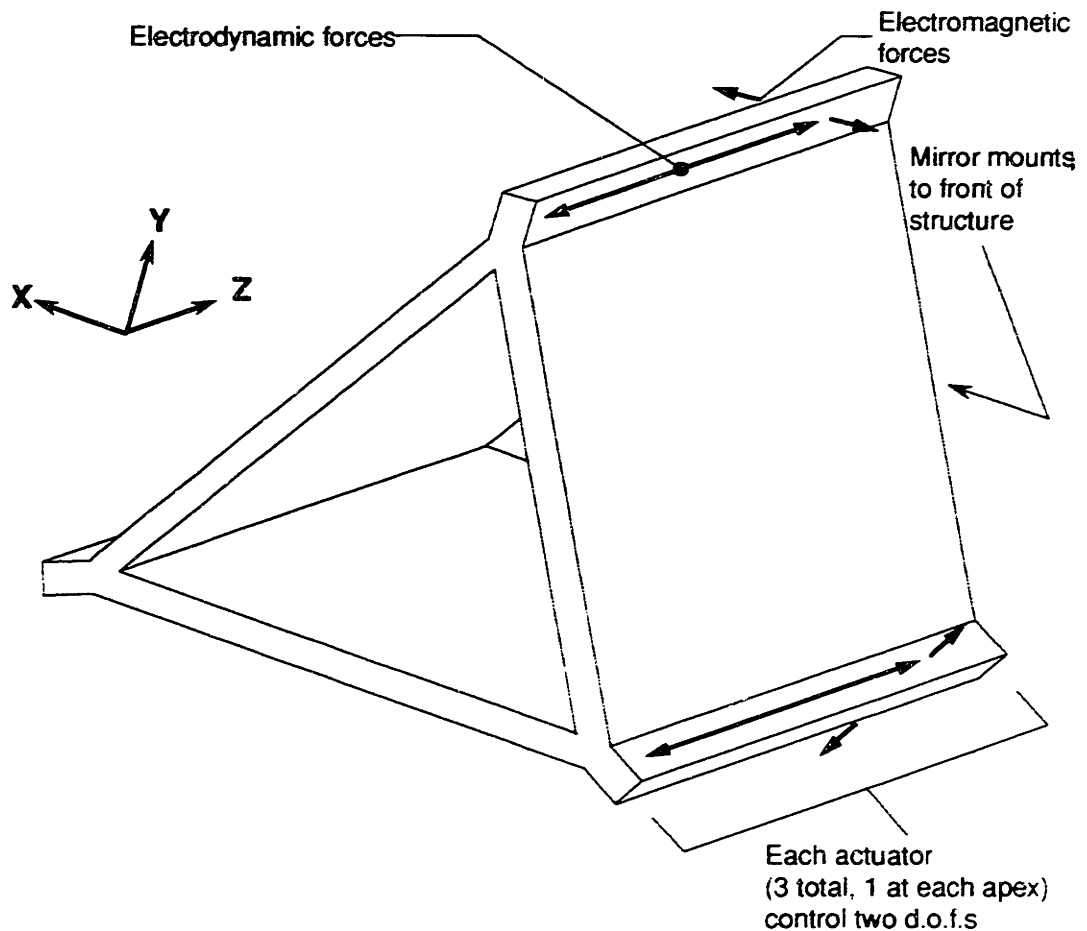


Figure 3.6: MOB triangular kinematics overview.

The actuators are arranged in a triangular fashion, at each apex of the triangle. Each actuator can control two degrees of freedom, as indicated by the arrows. One degree-of-freedom, along the scanning direction, is controlled by means of electrodynamic forces. The other degree-of-freedom per actuator is in a direction tangential to the center of the triangle, and is controlled by means of an electromagnetic force. The specifics of how the actuators each control these different degrees of freedom will be fully examined in the next section. For now, the focus is on how these local degrees of freedom influence the overall control of the body.

Table 3.2: MOB actuator global to local degree-of-freedom correlation.

| Control type | Degrees controlled |
|---------------------|--|
| Electromagnetic | X & Y translation Roll (about Z) |
| Electrodynamic | Z translation (scan) Pitch (about x) Yaw (about y) |

A basic understanding of just how they do so can be inferred from this picture. The electrodynamic forces are all parallel to the direction of the scanning motion. The first global degree of freedom that they control with this type of motion is the scanning motion; the major motion of the body. The second and third controlled degrees-of-freedom are the tip and tilt of the mirror. Note that these are only meant to be controlled over a very small range. The electromagnetic forces handle the other degrees-of-freedom. First, they can be employed to "roll" or "spin" the body. This feature can be contrasted with the MAMS design, where only passive stabilization is used to inhibit any roll motion. The final two degrees of freedom, motion of the body in the x-y plane,

can be handled by these electromagnetic forces as well. Again, these are only small translations, on the order of tens or hundreds of micrometers.

3.3.2 Actuator Jacobian

Development of the MOB system Jacobian matrix is essential to developing a detailed understanding of how the kinematics and dynamics of the design work. The Jacobian can be used to relate local actuator displacements and static forces to global body motion and force. In the next section, the Jacobian will be useful for determining the Lagrangian dynamics of the body. It is much easier to start by finding the inverse Jacobian, which in essence is just the displacement of the free body in terms of the three actuators. This can then be inverted to yield the Jacobian. For the kinematics formulation, the angular changes in orientation are assumed to be small. This greatly simplifies their derivation. The assumptions are valid as far as that they match the motions that the MOB system would go through. The dynamics in a full, nonlinear form, would be quite unwieldy, and make the design of controllers much more difficult, and are not particularly useful here. The diagram and respective coordinate systems is shown in figure 3.7.

The global coordinates are based on the geometric center of the mirror support body, and are denoted by the x-y-z frame (removed from the inside of the body for clarity). The individual actuator single-axis motions are denoted a_1 through a_6 (a_3 and a_6 are hidden from view). Note that a_1 through a_3 all head parallel to each other towards the front of the structure, whereas the positive directions for a_4 , a_5 , and a_6 all head in a counter-clockwise fashion. The analysis will start by writing the actuator displacements in terms of the free-body displacements. The resulting six equations are, based on just the geometry of the system,

$$a_1 = z + \left(\frac{l}{\sqrt{3}}\right)\theta_x \quad (3.26)$$

$$a_2 = z - \left(\frac{l}{2\sqrt{3}}\right)\theta_x + \left(\frac{l}{2}\right)\theta_y \quad (3.27)$$

$$a_3 = z - \left(\frac{l}{2\sqrt{3}}\right)\theta_x - \left(\frac{l}{2}\right)\theta_y \quad (3.28)$$

$$a_4 = x - \left(\frac{l}{\sqrt{3}}\right)\theta_z \quad (3.29)$$

$$a_5 = -\left(\frac{1}{2}\right)x + \left(\frac{\sqrt{3}}{2}\right)y - \left(\frac{l}{\sqrt{3}}\right)\theta_z \quad (3.30)$$

$$a_6 = -\left(\frac{1}{2}\right)x - \left(\frac{\sqrt{3}}{2}\right)y - \left(\frac{l}{\sqrt{3}}\right)\theta_z \quad (3.31)$$

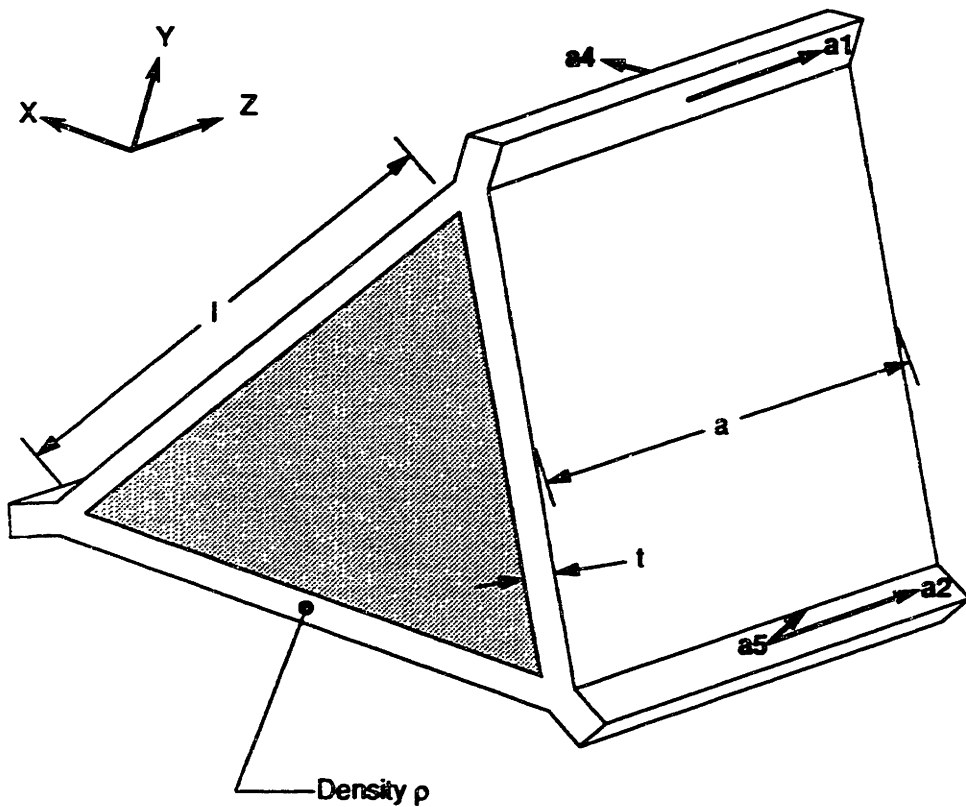


Figure 3.7: MOB coordinate frames and dimensions for Jacobian.

The Jacobian is given by the following,

$$\mathbf{n} = \mathbf{J}\mathbf{a}. \quad (3.32)$$

Where the Jacobian itself is a matrix, \mathbf{n} is the vector position of the global displacements and \mathbf{a} is the vector of the local actuator displacements. The equations listed above are in the form of

$$\mathbf{a} = \mathbf{J}^{-1}\mathbf{n}. \quad (3.33)$$

Written out, the inverse Jacobian is just a compilation of the above equations

$$\mathbf{J}^{-1} = \begin{bmatrix} 0 & 0 & 1 & \frac{l}{\sqrt{3}} & 0 & 0 \\ 0 & 0 & 1 & -\frac{l}{2\sqrt{3}} & \frac{l}{2} & 0 \\ 0 & 0 & 1 & -\frac{l}{2\sqrt{3}} & -\frac{l}{2} & 0 \\ 1 & 0 & 0 & 0 & 0 & -\frac{l}{\sqrt{3}} \\ -\frac{1}{2} & \frac{\sqrt{3}}{2} & 0 & 0 & 0 & -\frac{l}{\sqrt{3}} \\ -\frac{1}{2} & -\frac{\sqrt{3}}{2} & 0 & 0 & 0 & -\frac{l}{\sqrt{3}} \end{bmatrix}. \quad (3.34)$$

This can be inverted to yield the Jacobian,

$$\mathbf{J} = \begin{bmatrix} 0 & 0 & 0 & \frac{2}{3} & -\frac{1}{3} & -\frac{1}{3} \\ 0 & 0 & 0 & 0 & \frac{1}{\sqrt{3}} & -\frac{1}{\sqrt{3}} \\ \frac{1}{3} & \frac{1}{3} & \frac{1}{3} & 0 & 0 & 0 \\ \frac{2}{\sqrt{3}l} & -\frac{1}{\sqrt{3}l} & -\frac{1}{\sqrt{3}l} & 0 & 0 & 0 \\ 0 & \frac{1}{l} & -\frac{1}{l} & 0 & 0 & 0 \\ 0 & 0 & 0 & -\frac{1}{\sqrt{3}l} & -\frac{1}{\sqrt{3}l} & -\frac{1}{\sqrt{3}l} \end{bmatrix}. \quad (3.35)$$

With the Jacobian derived, the static forces seen on the body can be determined [Asada 1986] in terms of the actuator local forces. All that is required is a transpose of the Jacobian:

$$\mathbf{F}_a = \mathbf{J}'\mathbf{F}_n \quad (3.36)$$

It is instrumental to examine this transpose,

$$\mathbf{J}' = \begin{bmatrix} 0 & 0 & \frac{1}{3} & \frac{2}{\sqrt{3}l} & 0 & 0 \\ 0 & 0 & \frac{1}{3} & -\frac{1}{\sqrt{3}l} & \frac{1}{l} & 0 \\ 0 & 0 & \frac{1}{3} & -\frac{1}{\sqrt{3}l} & -\frac{1}{l} & 0 \\ \frac{2}{3} & 0 & 0 & 0 & 0 & -\frac{1}{\sqrt{3}l} \\ -\frac{1}{3} & \frac{1}{\sqrt{3}} & 0 & 0 & 0 & -\frac{1}{\sqrt{3}l} \\ -\frac{1}{3} & -\frac{1}{\sqrt{3}} & 0 & 0 & 0 & -\frac{1}{\sqrt{3}l} \end{bmatrix} \quad (3.37)$$

Besides an understanding of what forces are required of each actuator, another key result can be pulled out of this analysis. When examining the determinant of this matrix, it can be shown to be,

$$\text{Det}(\mathbf{J}') = -\frac{4}{3^{\frac{3}{2}}l^3} \quad (3.38)$$

This determinant is clearly non zero. Hence, for any type of force required on the free-body, a corresponding force can be produced by the actuators. The null space of the matrix is empty. Of course, this is based solely on geometric constraints. There are very real limits on the actuator output, as will be seen in later sections.

3.3.3 Mass properties

On the road to determining the full equations of motion for this body, the mass properties of the structure must be determined. In order to simplify the mass properties matrix which will be developed, some assumptions will be made. First of all, three plates will be assumed to determine the shape of the triangular structure. The additional mirror attachment will be ignored for now, since the mirror size does not necessarily scale directly with the structure. The details of the ends, where the triangular structure has the actuator tabs coming off, will also be ignored for now. Assume that each wall has a thickness t small enough so that edge effects when the slats combine can be ignored. Also, the notation is as follows; anything with a subscript 'plate' is a general result for all the plates, 'base' refers to the bottom plate (as shown in the figure), and 'side' refers to the two z axis inclined plates .

The analysis will start by looking at each moment of inertia independently, and then adding all the components together to form a matrix. Before proceeding though, the mass of a single wall and therefore the whole structure can be estimated. Looking at one wall, since it is simply a rectangle,

$$m_{plate} = alt\rho . \quad (3.39)$$

The most straightforward moment of inertia to analyze will be the roll moment, about the z axis. First, the moment through the center of each rectangle, parallel to the z axis, is simply given by,

$$I_{roll(plate)} = \frac{ml^2}{12} . \quad (3.40)$$

Using the parallel axis theorem and transferring this to the center, the roll moment for one plate around the center can be determined. Multiplying this by three yields the full roll moment,

$$I_{roll(total)} = \frac{ml^2}{2}. \quad (3.41)$$

The yaw moment, based on the y axis, can now be determined. This figure will be calculated first by looking at the yaw moment generated by the bottom plate (perpendicular to its center and the easiest one to calculate). Then the effects of the two side plates will be added in later. For the bottom plate, the moment calculated about and perpendicular to its center is,

$$I_{yaw(base)} = \frac{m(a^2 + l^2)}{12}. \quad (3.42)$$

Now, the effects of the two tilted side plates can be added. For one of the plates, if it were aligned with the y axis, its moment of inertia would be given by equation 3.40, replacing l with a . However, these side plates are rotated 30° from that axis, plus removed from it by a distance. When rotated, the new orientation is a blend of the basic orientation behind the aforementioned equation 3.40 (with an axis through it's center, parallel to the yaw axis), plus that of the orientation seen in equation 3.42 (with an axis perpendicular to the center, as if the plate were laid out flat and parallel to the bottom one). Let's call these orientations '1' and '2' respectively. Note that '2' is actually an associated pitching inertia of the plate. Based on just the angular change, the new resulting moments of inertia for these side plates becomes the following,

$$I_{yaw(101)} = I_1 \cos^2 30^\circ + I_2 \sin^2 30^\circ. \quad (3.43)$$

Similarly, from doing this transformation, two other moments arise. First, there is a pitch moment, which will be discussed later on. Secondly, there is a coupled moment, between the pitch and the yaw, which is,

$$I_{p/y} = \frac{I_2 - I_1}{2} \sin 60^\circ. \quad (3.44)$$

Let's rewrite the yaw moment. When substituting in for the above two results, and using the parallel axis theorem on the pure yaw, the following moments are obtained,

$$I_{yaw(tot)} = \frac{m(l^2 + a^2)}{4} \quad (3.45)$$

$$I_{p/y(tot)} = \frac{\sqrt{3}ml^2}{4}. \quad (3.46)$$

The remaining mass property to obtain now is the pitching moment. Starting again with the bottom plate, the formula through the bottom's own center, parallel to the pitch axis, is given by a variation of equation 3.40 with a substituted for l . This needs to be translated through the parallel axis to yield,

$$I_{pitch(base)} = \frac{m(a^2 + l^2)}{12}. \quad (3.47)$$

This result is strikingly similar to equation 3.42. Now, for the effects of the tilted side plates. This result is just the complementary form of what was done with rotating the side plates for equation 3.43, and it yields,

$$I_{pitch(sides)} = I_2 \cos^2 30^\circ + I_1 \sin^2 30^\circ. \quad (3.48)$$

Summing up all the pitch moments yields a total now of,

$$I_{pitch(tot)} = \frac{m(a^2 + l^2)}{4}. \quad (3.49)$$

This is the exact same result as was derived for the yaw motions.

These results can be conveniently compiled into a matrix form, which contains the body's inertias and masses. The matrix will be very useful in the next section, in determining the dynamics formulation. It will be defined as [Asada 1986],

$$\mathbf{H} = \begin{bmatrix} m & 0 & 0 & 0 & 0 & 0 \\ 0 & m & 0 & 0 & 0 & 0 \\ 0 & 0 & m & 0 & 0 & 0 \\ 0 & 0 & 0 & I_{pitch} & I_{p/y} & I_{p/r} \\ 0 & 0 & 0 & I_{y/p} & I_{yaw} & I_{y/r} \\ 0 & 0 & 0 & I_{r/p} & I_{r/y} & I_{roll} \end{bmatrix}. \quad (3.50)$$

The property matrix is a combination of equations 3.39, 3.42, 3.46, 3.47, and 3.49.

Notice that some of the coupled inertia terms are zero,

$$H = \left(\frac{m}{4}\right) \begin{bmatrix} 12 & 0 & 0 & 0 & 0 & 0 \\ 0 & 12 & 0 & 0 & 0 & 0 \\ 0 & 0 & 12 & 0 & 0 & 0 \\ 0 & 0 & 0 & l^2 + a^2 & \sqrt{3}l^2 & 0 \\ 0 & 0 & 0 & \sqrt{3}l^2 & l^2 + a^2 & 0 \\ 0 & 0 & 0 & 0 & 0 & 2l^2 \end{bmatrix}. \quad (3.51)$$

With the mass property matrix in hand, some of the dynamic properties can be explored.

3.3.4 Lagrange's equations of motion

All the ingredients are now here to set up the equations of motion for this free-body. The Lagrangian can be derived in the following way [Asada 1986]. First, the Lagrangian function is stated as,

$$L(q_i, \dot{q}_i) = T - U. \quad (3.52)$$

The T describes the kinetic energy, and the U describes the potential energy, which in this case is zero. The q 's are the generalized displacements, representing linear and angular translations. Using the Lagrangian, the equations of motion of the dynamic system are given by,

$$\frac{d}{dt} \frac{\partial L}{\partial \dot{q}_i} - \frac{\partial L}{\partial q_i} = Q_i. \quad (3.53)$$

Here the Q is the generalized force corresponding to the generalized displacements. The kinetic energy is given by,

$$T_i = \frac{1}{2} m_i \mathbf{v}_{c_i}^T \mathbf{v}_{c_i} + \frac{1}{2} \boldsymbol{\omega}_i^T \mathbf{I}_i \boldsymbol{\omega}_i. \quad (3.54)$$

Working through the specifics [Asada 1986], and because this is a free body with independent angular motion, the resulting dynamics equation reduces to,

$$\mathbf{H} \ddot{\mathbf{q}}_n = \mathbf{Q}_n. \quad (3.55)$$

The matrix \mathbf{H} was derived in the last section, and \mathbf{q} and \mathbf{Q} are vectors representing displacements and forces on the overall body. Through some manipulation, these results can be transferred to the frame of the local actuators, by means of the following transformation,

$$\mathbf{Q}_a = (\mathbf{J}^{-1})^T \mathbf{Q}_n. \quad (3.56)$$

This yields for the system here equation 3.57 which follows.

These results can now be hooked up to the actuator inputs, relating input variables such as current to the overall behavior of the body. Once this is done, a full blown multivariable control system may be developed for the MOB.

$$\begin{bmatrix} F_{a1} \\ F_{a2} \\ F_{a3} \\ F_{a4} \\ F_{a5} \\ F_{a6} \end{bmatrix} = \left(\frac{m}{4} \right) \begin{bmatrix} 0 & 0 & 4 & \frac{2(a^2 + l^2)}{\sqrt{3}l} & 2l & 0 \\ 0 & 0 & 4 & \frac{-a^2 + 2l^2}{\sqrt{3}l} & \frac{a^2}{l} & 0 \\ 0 & 0 & 4 & -\left(\frac{a^2 + 4l^2}{\sqrt{3}l} \right) & -\left(\frac{a^2}{l} \right) - 2l & 0 \\ 8 & 0 & 0 & 0 & 0 & -\frac{2l}{\sqrt{3}} \\ -4 & 4\sqrt{3} & 0 & 0 & 0 & -\frac{2l}{\sqrt{3}} \\ -4 & -4\sqrt{3} & 0 & 0 & 0 & -\frac{2l}{\sqrt{3}} \end{bmatrix} \begin{bmatrix} \ddot{x} \\ \ddot{y} \\ \ddot{z} \\ \ddot{\theta}_x \\ \ddot{\theta}_y \\ \ddot{\theta}_z \end{bmatrix}. \quad (3.57)$$

3.3.5 Sensor placement

Just as a variety of options exist for actuator placement, so do as many exist for sensor placement. The criteria is of course that the sensor array must be able to pick up the static displacements of the body, as well as all of its dynamic modes. The transverse, electromagnetic actuator induced motion could easily be detected by means of small displacement probes nearly collocated to the actuators themselves. Hence, half of the actuator Jacobian seen would be nearly identical to a sensor Jacobian. This is what was employed in the prototype, where a capacitive probe is used for the short distances involved.

The longer, electrodynamic induced displacements and affiliated rotations would require a little extra work and calculation to extract. One way to do this would be to use an interferometric laser position transducer, where three distinct beams would be bounced off the face in a triangular fashion. Just like the electrodynamic portions of the actuator yield the tip, tilt, and scan of the actuator based on a similar triangular fashion, the position detected by these laser transducers would mimic this actuator control and map it to a similar looking scan Jacobian. Again, this method that is suggested is just

what was employed in the prototype actuator sensing system, limited though to the scan direction.

3.4 The MOB Hybrid Magnetic Circuit

The arrangement of actuators as described in the last section is one of the novel ideas for the scanning mirror design. What will be presented in this chapter is the other leg of the MOB which allows the entire concept to stand; that of the new magnetic circuit design proposed to make the system a reality. Following through with the following analysis is somewhat similar to the Studer hybrid design outlined earlier. The MOB design though is more complex, and often a little more difficult to visualize, since two degrees of freedom are being driven via one magnetic circuit. Also, unlike Studer's design, the MOB makes use of the permanent magnet for biasing electrodynamic as well as electromagnetic forces. A "black-box" simplified drawing of the MOB actuator, indicating what components are moving and which ones are not, is introduced in figure 3.8. The long arrows denote electrodynamic force and motions, and the shorter ones the hybrid electromagnetic ones. Figure 3.9 then indicates the geometric parameters and the physical composition of the actuator.

The critical dimensions from for figure 3.9 are as follows. g defines the nominal size of the small gap, t describes the thickness of the outer leg of the E-core (note the middle leg is twice this), d is the side E-core depth into the page, h is the height of the large voice coil gap, and n is the area of the through face of the permanent magnet normalized by $d t$. Also shown is the voice coil volume V as well as the cross sectional area A of the electromagnetic coils.

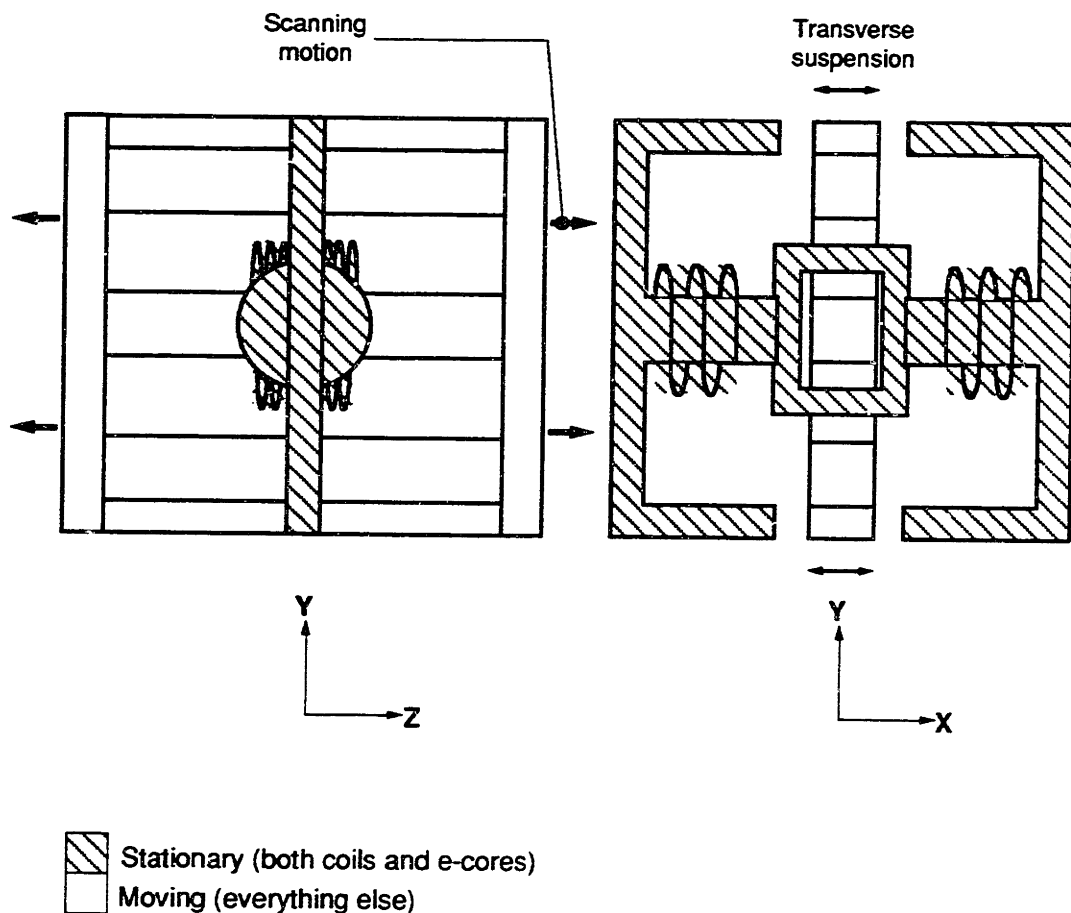


Figure 3.8: MOB actuator motion clarified.

Similar to the Studer design, several different types of materials are utilized in the makeup of the MOB system, and are shaded as such. As before, a highly permeable core is used. In this design though, a laminated iron core is specified, to maximize the allowable flux buildup in the cores as well as to reduce the effects of eddy currents, which limit the frequency response. Next is the permanent magnet, key to both parts of the circuit. Wire coils are used in two capacities, one for the electromagnetic flux generation, the other serving as a voice coil. In this drawing, only the outline of a support structure is used, since a lot of pieces must come together and be held in place.

The resulting displacements and forces will be gradually developed. Keep in mind though for now that electromagnetics will be used to exert control in and out of the page (as viewed from the left side drawings), while electrodynamics will be used to exert control left to right as seen on the page (again, as viewed from the left drawings).

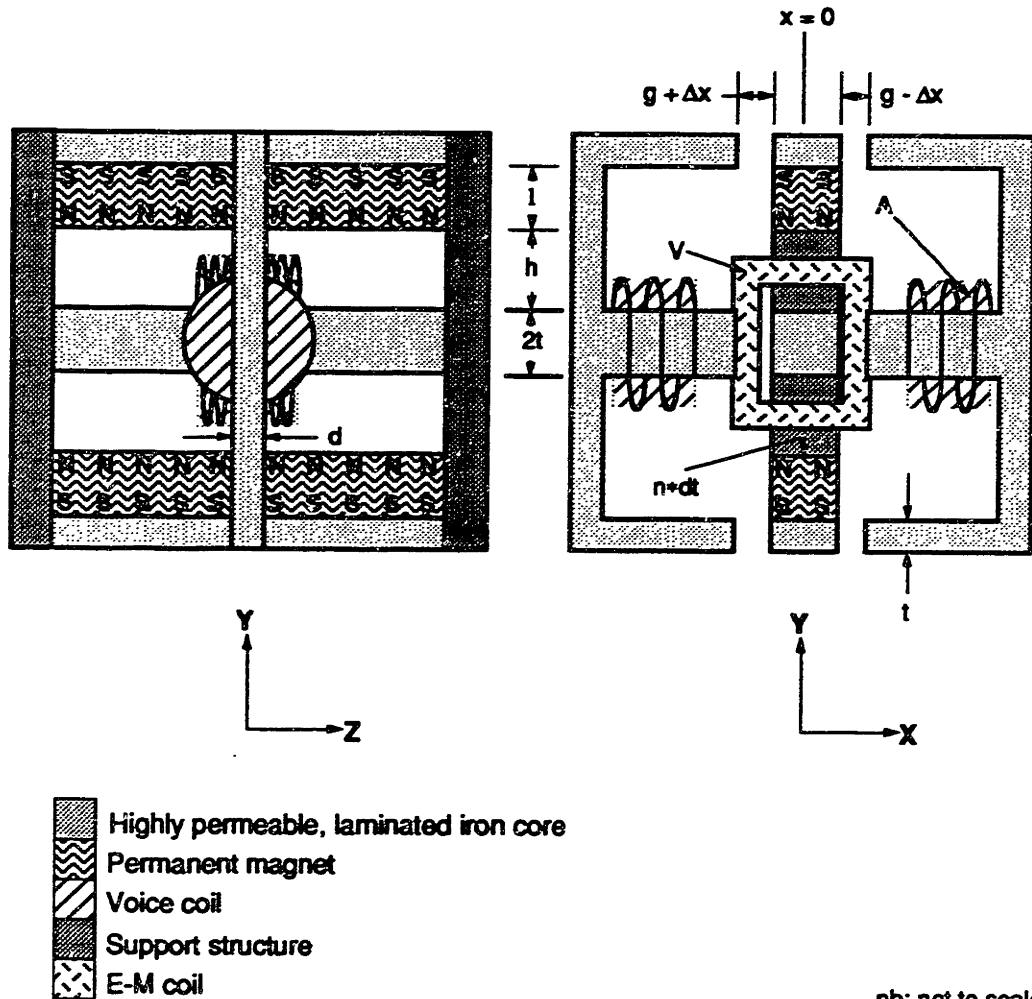
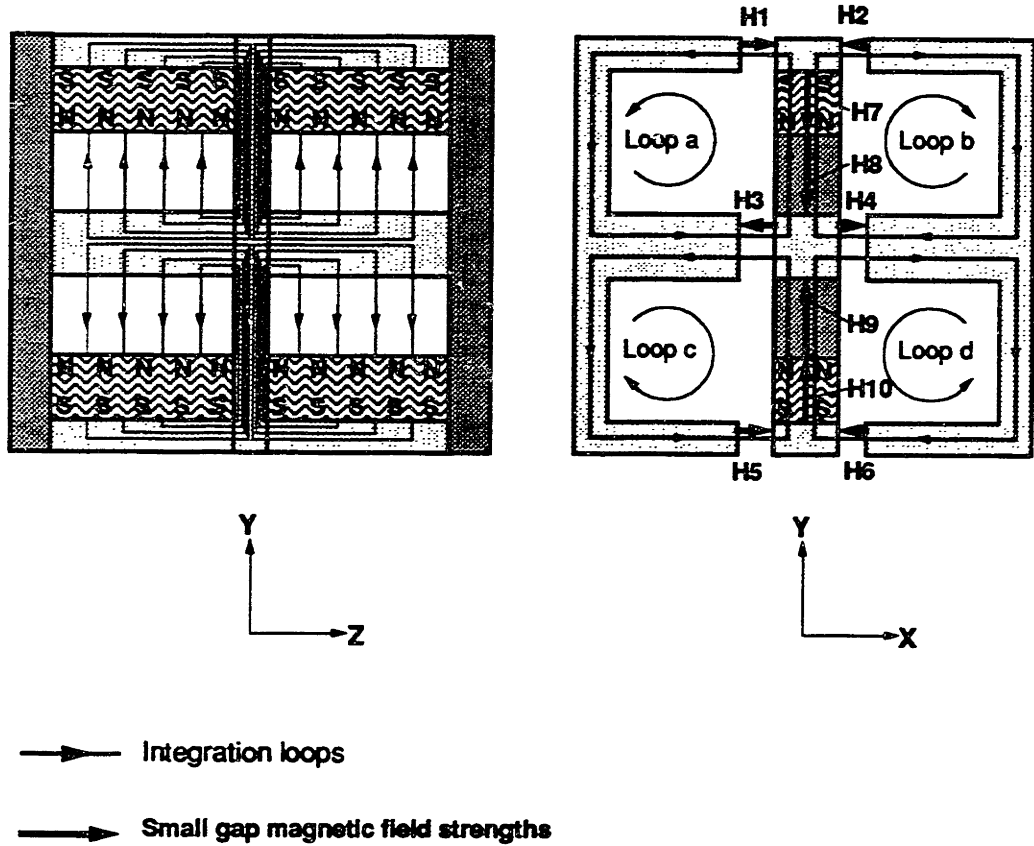


Figure 3.9: MOB overall design.

3.4.1 MOB permanent magnetic effects

The MOB analysis starts by re-presenting the MOB circuit, showing only the voice coils, as described in the figure below.



nb: not to scale

Figure 3.10: MOB permanent magnet effects.

First the integrals of the magnetic field strengths around the four inner loops are examined (recall equation 3.4). For the first level of two-dimensional analysis presented herein on the MOB, the same assumptions as stated for the Studer analysis apply, including near infinite permeability of the iron. By examining closed loops 'a' through 'd' the following equations are derived,

$$-H_8h - H_7l - H_1(g + \Delta x) - H_3(g + \Delta x) = 0 \quad (\text{loop a}) \quad (3.58)$$

$$-H_8h - H_7l - H_2(g - \Delta x) - H_4(g - \Delta x) = 0 \quad (\text{loop b}) \quad (3.59)$$

$$-H_9h - H_{10}l - H_3(g + \Delta x) - H_5(g + \Delta x) = 0 \quad (\text{loop c}) \quad (3.60)$$

$$-H_9h - H_{10}l - H_4(g - \Delta x) - H_6(g - \Delta x) = 0. \quad (\text{loop d}) \quad (3.61)$$

Since there are ten variables to be solved for (each numbered B or H can be thought of as one variable since they can be written in terms of each other by equation 3.3), an additional six equations are required. These can be acquired by examining the surface integral of the magnetic flux density (equation 3.2) around a variety of selected surfaces. To avoid too much mayhem on the accompanying figure, these surfaces will just be briefly described in the text. First there are the surfaces which encapsulate each side E-core, resulting in two equations,

$$\int d(B_6 + B_2 - 2B_4) = 0 \quad (3.62)$$

$$\int d(B_1 + B_5 - 2B_3) = 0. \quad (3.63)$$

Four more equations are desired. Referring back to equation 3.3 which holds in the magnet, looking at the flux in and out of the top and bottom iron core bars yields,

$$H_1 + H_2 - nH_7 = nM_0 \quad (3.64)$$

$$H_5 + H_6 - nH_{10} = nM_0. \quad (3.65)$$

The parameter n that arises here is worthy of some special attention. This parameter is the ratio of the permanent magnet facial area divided by the cross sectional area of the returning flux path. It may best be thought of as a weighting factor, which in a sense determines the relative strength of the impacting strength of the permanent magnet. Its full effects will be discussed later, after the complete analysis. Proceeding, two more remaining equations are needed, which are found from the flux leaving the permanent magnets into the large gaps,

$$H_7 - H_8 = -M_0 \quad (3.66)$$

$$H_{10} - H_9 = -M_0. \quad (3.67)$$

Finally, ten equations (3.58 to 3.67) have been derived for the total of ten variables desired. The large number of variables and equations is best solved in matrix form.

Carrying out this analysis yields the following results (in terms of magnetic flux density),

$$B_1 = B_3 = B_5 = \frac{\mu_0 M_0 n l (g - \Delta x)}{2(g(h+l+ng) - n\Delta x^2)} \quad (3.68)$$

$$B_2 = B_4 = B_6 = \frac{\mu_0 M_0 n l (g + \Delta x)}{2(g(h+l+ng) - n\Delta x^2)} \quad (3.69)$$

$$B_7 = B_{10} = \frac{\mu_0 M_0 (-g(h+ng) + n\Delta x^2)}{g(h+l+ng) - n\Delta x^2} \quad (3.70)$$

$$B_8 = B_9 = \frac{\mu_0 M_0 l g}{g(h+l+ng) - n\Delta x^2}. \quad (3.71)$$

The results when centered are instrumental to a better understanding of some of the key design choices. They are presented for reference below,

$$B_1 = B_2 = \dots = B_6 = \frac{\mu_0 M_0 n l}{2(h+l+ng)} \quad (3.72)$$

$$B_7 = B_{10} = -\frac{\mu_0 M_0 (h+ng)}{h+l+ng} \quad (3.73)$$

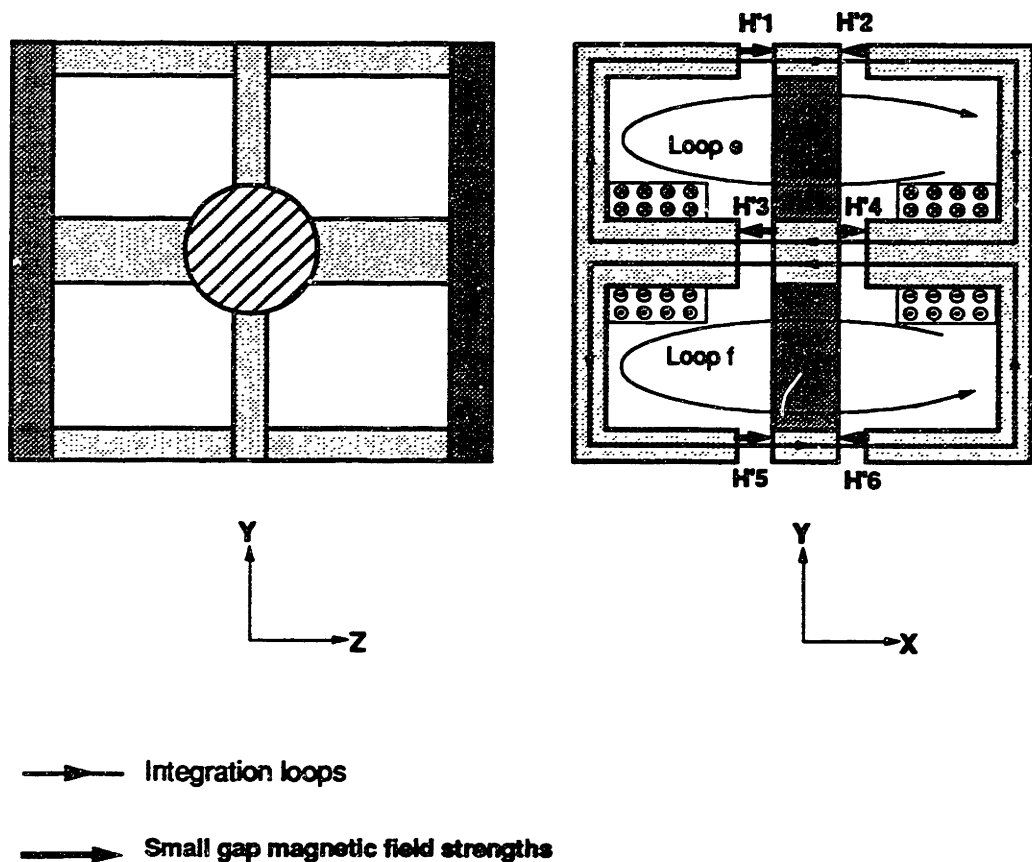
$$B_8 = B_9 = \frac{\mu_0 M_0 l}{h+l+ng}. \quad (3.74)$$

Some simple observations about these resulting centered magnetic fields can be stated at this point. First of all, consider, for a given configuration, that the denominator is fixed. That happens to the resulting magnetic fields as other key dimensions take up more or less of this fraction can be discussed. For the small gaps (B_1 to B_6), the magnetic flux density increases as the permanent magnet length in the z-axis gets longer (and hence n gets larger. For the large gaps (B_8 and B_9), the flux density also increases at a rate proportional to the permanent magnet length, differing only by a factor of $n/2$ smaller. In the following sections on design choices, this is an important relationship that places one overriding limit on the basic MOB design, making it hard to apply the concept to a longer Scan mirror such as the ADEOS MAMS. As a final observation,

note in the figure the approximately uniform field set up in the large gaps. These fields provided the bias for the electrodynamic (voice coil) portion of the MOB actuator.

3.4.2 MOB electromagnetic coil effects

The other set of magnetic flux densities that arise in the gaps comes from the addition of the electromagnetic coils. Once again, applying superposition, the effects of the permanent magnets are set aside for the present, and the resulting B-fields due to the electromagnetic coils alone can be solved. The configuration for this portion of the analysis is shown in the figure below.



nb: not to scale

Figure 3.11: MOB B-fields from EM coils with voice coils removed.

The analysis of this portion of the circuit starts with examining the integrals of the magnetic field strengths around the closed loops which encompass the top and bottom loops (e and f), yielding the following two equations,

$$H'_3(g + \Delta x) - H'_4(g - \Delta x) - H'_2(g - \Delta x) + H'_1(g + \Delta x) = JA \quad (3.75)$$

$$H'_3(g + \Delta x) - H'_4(g - \Delta x) - H'_6(g - \Delta x) + H'_5(g + \Delta x) = JA. \quad (3.76)$$

The J term refers to the current density of each coil, and the A term refers to the cross sectional area of the coils. As with the Studer analysis, the prime here is used to denote magnetic field strengths and flux densities driven solely by the coils. Four more equations are needed to extract all the desired variables. A set of surfaces, similar to those chosen in the last section for the analysis of the permanent magnet effect, can be used to examine the integrals of the magnetic flux densities entering and exiting. From the surfaces enclosing the two side E-cores,

$$td(B'_6 + B'_2 - 2B'_4) = 0 \quad (3.77)$$

$$td(B'_1 + B'_5 - 2B'_3) = 0. \quad (3.78)$$

Now, examining the surface enclosing the bottom and top pieces of iron core yields the last two equations,

$$dt(B'_1 + B'_2) = 0 \quad (3.79)$$

$$dt(B'_5 + B'_6) = 0. \quad (3.80)$$

The system of six equations and six unknowns can now be solved by means of linear algebra. The resulting fields that are set up are therefore (again, switching from H to B),

$$B'_1 = B'_3 = B'_5 = \frac{\mu_0 JA}{4g} \quad (3.81)$$

$$B'_2 = B'_4 = B'_6 = -\frac{\mu_0 JA}{4g}. \quad (3.82)$$

From these results, the conclusions are somewhat similar to what was seen with Studer's example. This second set of magnetic fields does not depend on the offset position Δx .

3.4.3 MOB resultant electromagnetic and electrodynamic forces

Now that all of the respective fields have been derived, the forces on the centerpiece can be calculated. Once again, the Studer development is closely followed. This subsection will start with deriving the electromagnetic force, F_{EM} . The total forces on the suspended body, left to right across the small gaps, is given by,

$$\sum_1^6 F_{nEM} = F_{right} - F_{left} = F_2 + F_4 + F_6 - F_1 - F_3 - F_5. \quad (3.83)$$

How these forces are derived is made clear in figure 3.12 . Only one quadrant is shown for clarity, though the analysis is done with all the loops over all the gaps.

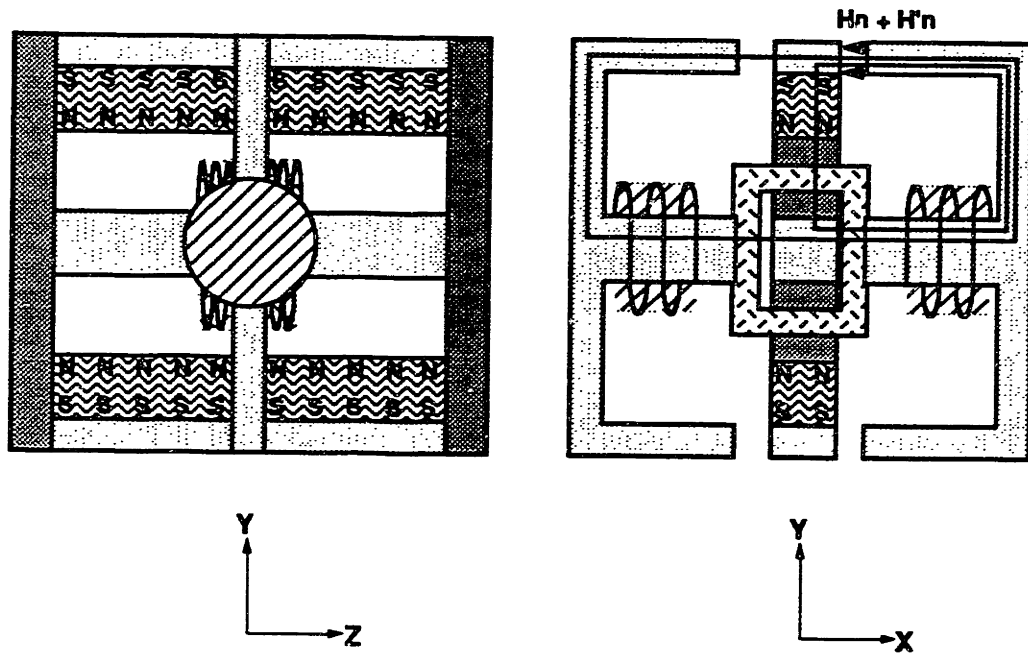
The B-fields can be summed at the small gaps and used to find resultant electromagnetic forces. This is done through equations 3.22 and 3.23. The second equation yields the following,

$$B_{odd(tot)} = B_{1(tot)} = B_{3(tot)} = B_{5(tot)} = \frac{\mu_0}{2} \left[\frac{M_0 n (g - \Delta x) l}{g(h+l+ng) - n\Delta x^2} + \frac{JA}{2g} \right] \quad (3.84)$$

$$B_{even(tot)} = B_{2(tot)} = B_{4(tot)} = B_{6(tot)} = \frac{\mu_0}{2} \left[\frac{M_0 n (g + \Delta x) l}{g(h+l+ng) - n\Delta x^2} - \frac{JA}{2g} \right]. \quad (3.85)$$

Using the first equation (3.22) and the above stated equation 3.83, the total electromagnetic force for this system is given by,

$$F_{EM(tot)} = \frac{2dt}{\mu_0} [B_{even}^2 - B_{odd}^2 - 2|B'| (B_{even} + B_{odd})]. \quad (3.86)$$



→ Small gap magnetic field strengths

nb: not to scale

Figure 3.12: MOB combined magnet and electromagnetic coil effects.

Plugging in for the known values of the B-fields yields the full force equation,

$$F_{EM(tot)} = \mu_0 dt M_0 n l \left[\frac{2 M n g l \Delta x}{[g(h+l+ng) - n \Delta x^2]^2} - \frac{A J}{g(h+l+ng) - n \Delta x^2} \right]. \quad (3.87)$$

When centered this force reduces to the following,

$$F_{EM(center)} = -\mu_0 dt \left(\frac{M_0 n l}{h+l+ng} \right) \left(\frac{A J}{g} \right). \quad (3.88)$$

Not surprisingly, this result is very similar to that of equation 3.25, with a few of the geometric parameters changed. It's advantages are the same as those discussed after the Studer analysis. The biggest noticeable change is the added effect of the large gap h ,

and how the electromagnetic or "hybrid" forces are diminished accordingly by it. This is due to the decrease of the permanent magnet bias field with increasing h .

The resulting electrodynamic, or "voice coil" forces still remain to be solved for. Doing so is far less complex than was just derived above. The formula for this force is given, per unit volume, by equation 3.6. The assumption here is that the flux generated by the voice coil itself is small relative to the bias fluxes, and thus the voice coil does not, for instance, drive the iron into saturation. This assumption is physically reasonable since the voice coil flux does not link the main magnetic circuit through the E-cores.

Adding the appropriate volume of voice coil here yields,

$$F_{ED} = (\mathbf{J} \times \mathbf{B})[V]. \quad (3.89)$$

The B-field across this large gap was derived in the section before last, and is given by equation 3.71. Since the coil current density vector is perpendicular to this field, the electrodynamic force is therefore

$$F_{ED} = \frac{\mu_0 M g l J V}{g(h + l + ng) - n \Delta x^2}. \quad (3.90)$$

And when the body is centered across the small gaps,

$$F_{ED} = \frac{\mu_0 M l J V}{h + l + ng}. \quad (3.91)$$

This result makes sense in terms of the magnet thickness. For a given configuration or geometry (the denominator), the voice coil force diminishes as the magnet's strength M_0 , and length, shrink.

3.5 Actuator Linearization Techniques

The basic operating equations that were derived in the last section simplify very nicely and are easy to comprehend when the actuator is centered. The off-center results become more complex, particularly for the small gap forces. The off-center case is best addressed when the equations of the last section for the forces are linearized. This is a particularly useful step for developing linear control algorithms, which will be described later in this thesis.

The electromagnetic forces, based on offset position and input current, can be re-written in state-space form, as shown in the following equations,

$$\dot{x}_1 = x_2 \quad (3.92)$$

$$\dot{x}_2 = \frac{c_1}{M} \left[\frac{c_2 x_1}{(c_3 - x_1^2)^2} - \frac{c_4 i}{(c_3 - x_1^2)} \right] + \frac{F_d}{M}. \quad (3.93)$$

To arrive at this form, the offset position, Δx is relabeled x_1 , making x_2 the velocity, and its derivative acceleration. In this case, M is the mass of the moving piece, or platen (not the magnetization density of the magnet), and F_d accounts for any additional disturbance force in the transverse direction. The constants c_1 through c_4 are used to help simplify the collection of geometric and material constants and are defined as follows,

$$c_1 = \frac{\mu_0 dt M_0 n l}{m} \quad (3.94)$$

$$c_2 = \frac{2 M_0 g l}{n} \quad (3.95)$$

$$c_3 = \frac{g(h + l + ng)}{n} \quad (3.96)$$

$$c_4 = \frac{N}{n}. \quad (3.97)$$

Equation 3.94 can be linearized with the following transformations,

$$\mathbf{x}_1 = \mathbf{x} + \delta\mathbf{x} \quad (3.98)$$

$$\mathbf{i} = \mathbf{I} + \delta\mathbf{i} \quad (3.99)$$

$$\mathbf{F}_d = \mathbf{F}_d + \delta\mathbf{F}_d. \quad (3.100)$$

Here the bold, non-scripted letters are the operating points, and the delta quantities are the variations from that point. This transforms equations 3.92 and 3.93 by

$$\delta\dot{\mathbf{x}}_1 = \delta\mathbf{x}_2 \quad (3.101)$$

$$\delta\dot{\mathbf{x}}_2 = F_{EM}(\mathbf{x}, \mathbf{i}, \mathbf{F}_d) + \frac{\partial F_{EM}}{\partial \mathbf{x}_1} \delta\mathbf{x}_1 + \frac{\partial F_{EM}}{\partial \mathbf{i}} \delta\mathbf{i} + \frac{\partial F_{EM}}{\partial \mathbf{F}_d} \delta\mathbf{F}_d. \quad (3.102)$$

In the second equation, the constant term (first one) and the partial derivatives are given by,

$$F_{EM}(\mathbf{x}, \mathbf{i}, \mathbf{F}_d) = D_c(\mathbf{x}, \mathbf{i}) = \frac{c_1}{M} \left[\frac{c_2 \mathbf{x}}{(c_3 - \mathbf{x}^2)^2} - \frac{c_4 \mathbf{i}}{c_3 - \mathbf{x}^2} \right] \quad (3.103)$$

$$\frac{\partial F_{EM}}{\partial \mathbf{x}_1} = D_x = \frac{c_1}{M} \left[\frac{c_2}{(c_3 - \mathbf{x}^2)^2} - \frac{4c_2 \mathbf{x}^2}{(c_3 - \mathbf{x}^2)^3} + \frac{2c_4 \mathbf{x} \mathbf{i}}{(c_3 - \mathbf{x}^2)^2} \right] \quad (3.104)$$

$$\frac{\partial F_{EM}}{\partial \mathbf{i}} = -D_i = -\frac{c_1}{M} \left[\frac{c_4}{c_3 - \mathbf{x}^2} \right] \quad (3.105)$$

$$\frac{\partial F_{EM}}{\partial \mathbf{F}_d} = D_{F_d} = \frac{1}{M}. \quad (3.106)$$

These terms must be evaluated at a given operating point. Typically, at this operating point, a zero velocity is desired, which means \mathbf{x}_2 is zero. This then requires that the electromagnetic force F_{EM} is equal to any disturbance force F_d divided by the platen mass, and thus imposes a constraint between all the operating point variables (\mathbf{x} , \mathbf{J} and \mathbf{F}_d). At this equilibrium, the linearized state equations are,

$$\delta\dot{\mathbf{x}}_1 = \delta\mathbf{x}_2 \quad (3.107)$$

$$\delta\dot{\mathbf{x}}_2 = D_c(\mathbf{x}, \mathbf{i}, \mathbf{F}_d) + D_x \delta\mathbf{x}_1 - D_i \delta\mathbf{i} + D_{F_d} \delta\mathbf{F}_d. \quad (3.108)$$

This form has the time derivatives of the states in terms of all the states and inputs. In terms of inputs and outputs, this equation could be compared to a simple mass-and-spring system,

$$\ddot{x} + \left(\frac{k}{m}\right)x = F(\text{inputs}). \quad (3.109)$$

In terms of the MOB electromagnetic actuation capability, equations 3.107 and 3.108 can be re-written as,

$$\delta\ddot{x}_1 - D_x \delta x_1 = -D_i \delta i + D_{F_d} \delta F_d + D_c(\mathbf{x}, \mathbf{i}, \mathbf{F}_d). \quad (3.110)$$

The effect of the offset Δx_1 is dramatically seen in this linearized case. The term in front of the x_1 acts like a negative spring, clearly showing that the system is, by itself, unstable, and will definitely require a stabilizing compensator to be adequately controlled.

It is instructive to take the transfer function from the incremental current to the incremental displacement, ignoring for now any disturbance, and setting the constant term to zero (centered, with no bias current). This yields,

$$\frac{\mathbf{X}(s)}{\mathbf{I}(s)} = \frac{-D_i}{s^2 - D_x}, \quad (3.111)$$

resulting in two poles (one of which is unstable) at the positions,

$$\omega_k = \sqrt{D_x} = \frac{1}{c_3} \sqrt{\frac{c_1 c_2}{m}} = \frac{M_0 l n}{h + l + n g} \sqrt{\frac{2 \mu_0 d t}{m g}}. \quad (3.112)$$

The further out this unstable real pole is from the origin, the more unstable the system will inherently be. What this final equation does is to show which geometric factors influence this unsteady pole the most. The n factor, discussed previously and defined as the ratio of the permanent magnet face to the E-core cross-sectional area, has a large impact on stability, as well as the length of the permanent magnet relative to a given

configuration. This would be expected since both play a major role in the full electromagnetic force equation.

As a brief note, it should be stated that linearization for the electrodynamic forces is trivial. When linearized, the centered result appears as equation 3.91. In reality, for a typical case, when the effect of an offset is plotted, it has a very small effect on the overall electrodynamic forces, as would be expected since the dependence is proportional to Δx^2 . Said another way, this is so because the fixed gaps for the voice coils, h , are much larger than the electromagnetic gaps g .

3.6 Design Implementation

With the operating theory established for the MOB actuator, the question still remains of how to flesh out a real design from all the parameters. Furthermore, the design should be reasonably well suited to actual satellite and optical constraints, which have had little mention at all so far. This section will approach the design in two steps. The first step is to understand all the tradeoffs, in geometric and material properties, that are made in choosing an adequate design. The next step is then to look at the specific requirements on a real platform, such as the GOES, and propose a workable design.

3.6.1 Design method

The large number of geometric and material parameters involved with the design make it difficult to state a "best" design for any given application. Many external constraints must first be placed on the system before a sufficient design can be developed. As with any application, material properties have well defined limits which must be imposed. In this case, particularly for the prototype, severe geometric limits

were in place as well. Particularly, the E-core laminations used only came in a set variety of geometric configurations (they are normally used in transformer designs), which dictated what shapes were available. In an actual production model, these could be special cut, but not without cost increases and extra machining effort.

To fully understand the implications, it is best to redirect attention to the fundamental operating equations. To simplify the analysis, the equations will all be presented again in their centered forms, and the design will be developed to meet specifications in this state. The first two equations recall the magnetic flux densities seen at the small and large gap. Only the "left side" small gap flux density is presented, since the right side merely reflects it by a few minus signs. They are (based on equations 3.84 and 3.74),

$$B_{small} = \frac{\mu_0}{2} \left[\frac{M_0 n l}{h + l + n g} + \frac{J A}{2 g} \right] \quad (3.113)$$

$$B_{large} = \frac{\mu_0 M_0 l}{h + l + n g} \quad (3.114)$$

Even though the centered results are presented, a few comments should be made about offset values for these critical B-fields. First of all, the small gap is nearly linearly dependent on these B-fields, going to about twice it's center value when the platen hits one of the sides. This factor of two is key to remember when designing to avoid saturation of the E-cores, which will be discussed later. As aforementioned, the offset has only a secondary effect on the large gap flux, reducing it by about 10% or less in the design eventually used, as the offset varies between g and $-g$. Second, it should also be noted that current through the electromagnets can increase or decrease the small gap field, but has no significant effect on the large gap. In a brief summary, although these two equations look somewhat alike, the former is very dependent on position and electromagnetic current density while the latter is not.

The forces are also shown again in their centered form. These are equations 3.88 and 3.91,

$$F_{EM} = -\mu_0 dt \left(\frac{M_0 nl}{h+l+ng} \right) \left(\frac{AJ}{g} \right) \quad (3.115)$$

$$F_{ED} = \frac{\mu_0 M I J V}{h+l+ng} \quad (3.116)$$

Some of the same observations about the B-fields may be applied here. Before making generalizations based on the centered equations, a few notes about offset effects are applicable. First of all, the electromagnetic forces are, as the small gap B-fields, highly dependent on offset position. In fact, depending on the specific geometric and material choices, the offset effects could easily end up outweighing any possible current control through the coils, which is for obvious reasons very undesirable. The electrodynamic forces, like the large gap B-fields, only feel a secondary impact of the offset.

Before discussing parameters, a final set of equations should be introduced - that of the dissipative power requirements. Normally, the power is only important in the interest of making an efficient design. However, because of the hoped-for space-based application of the MOB system, this will become a critical issue. On the GOES satellite, for the interferometer package, only passive dissipation is allowed for, which severely limits what can be radiated into space. Dissipative power is defined as follows,

$$P_{dis} = \frac{2J^2V}{\sigma} \quad (3.117)$$

Here, the σ is the electrical conductivity of the coil material (for copper $\sigma = 5.6 \times 10^7$ s/m). The relation is approximate. The factor of two represents a reasonable packing factor for the coils. In the centered case, both the electromagnetic and electrodynamic forces are linearly dependent on the current densities employed. This means that any set of terms that linearly diminishes the forces will increase the power requirements by a squared amount. The power requirements when centered are,

$$P_{EM} = \frac{2}{Ar_{sf}\sigma} \left[\frac{g(h+l+ng)}{\mu_0 diM_0 nl} \right]^2 (F_{EM})^2 \quad (3.118)$$

$$P_{ED} = \frac{2}{V\sigma} \left[\frac{(h+l+ng)}{\mu_0 Ml} \right]^2 (F_{ED})^2. \quad (3.119)$$

In the first equation, the volume for the electromagnetic coils (akin to a cylinder) can be written as a function of their rectangular cross-sectional area, times some implicit radius to give a volume. This gives rise to the r_{sf} term, which depends on the exact rectangular form of the cross-sectional area and how it is wound around the E-core. The effect of each term squared is shown in the equations. Of interest to note is that for a given required force, the power requirements diminish as coil volumes and areas get bigger.

Finally, for completeness of the design method, the stability of the system will also be touched upon again. Recall equation 3.112,

$$\omega_k = \frac{M_0 ln}{h+l+ng} \sqrt{\frac{2\mu_0 dt}{mg}}. \quad (3.120)$$

An array of equations now exist to fully analyze the respective behavior of the MOB system. Through these seven equations (3.113 to 3.116, and 3.118 to 3.120) a matrix can be made up showing how each parameter choice effects these critical outputs. This is presented in table 3.3.

In the table, a '+1' denotes linear dependence, and '-1' an inverse linear dependence. A '2' denotes squared dependence and a '.5' a square root dependence. It should be stressed that these all indicate first order dependence when centered. For example, the g term appears in many denominators and numerators added to h and l . It is considered a lot smaller for the discussions to follow, but in reality, the effect of the gap can be quite large if n is large.

Table 3.3: Design parameters: inputs and outputs.

| | B_{small} Perm | B_{small} Control | B_{large} | FEM | FED | PEM | PED | ω_k |
|--------------------------------|---------------------|------------------------|-------------|-----|-----|-----|-----|------------|
| M | +1 | - | +1 | +1 | +1 | -2 | -2 | +1 |
| $l/(h+l+ng)$ | +1 | - | +1 | +1 | +1 | -2 | -2 | +1 |
| g | - | -1 | - | -1 | - | +2 | - | -.5 |
| dt | - | - | - | +1 | - | -2 | - | +.5 |
| n | +1 | - | - | +1 | - | -2 | - | +1.5 |
| A | - | +1 | - | +1 | - | -1 | - | - |
| V | - | - | - | - | +1 | - | -1 | - |

Before discussing the specific implications of each parameter, a discussion of what is desirable and what is not is in order. Proceeding through the columns, the small gap flux comes first. At first it may seem desirable to keep this flux as large as possible for the simple reason that more flux means greater forces over the small gap. However, what type of flux is generated is of critical importance. Referring back to equation 3.113 and it is obvious that the flux is from two sources. The first, from the permanent magnet, can be thought of as "bad" flux. It must be overcome by the "good" flux; the flux generated by the coils. Around the center, the good flux dominates, but getting way off the center towards the sides and the coils are fighting the tendency for the platen to stick to the side, rather than working against a disturbance force or for a desired acceleration. Thus, a substantial amount of control flux is desired. A second consideration on this flux is saturation limits for the E-cores, at about 1.6 Tesla for silicon steel. Recall that as the platen hits one side, its flux is roughly twice that of its centered position, making saturation a very real concern.

The next column is the large flux, used for the voice coil. Without question, this should be as large as possible to generate the largest forces. However, this increases in nearly the same fashion as the small gap flux. This creates a substantial tradeoff issue. However, this tradeoff can be changed by some of the alternate designs presented in

chapter 7. The electrodynamic forces, a direct result of the B-fields, follows much of the same reasoning as those fields in design. However, the cross sectional area of the side E-cores are now of concern. Likewise, this relationship is noticeable in the large gap and its resultant electrodynamic force, which now also depends on the volume of the voice coils. The power requirements closely follow the force requirements, differing in most cases (except volume and area) by a square factor for the parameters, which was discussed when the power terms were introduced. Finally, the relative stability of the system heads up the last column. Unfortunately, what's good for forces and B-fields isn't necessarily good for stability, which would like to see the unstable pole closer to the origin in the s-plane.

Now that it has been stressed what is desirable and what is not, the discussion is clear to explore what effects each of the critical parameters have on each of the key system characteristics. The first two rows will be discussed together, since they affect the system nearly the same way in all the results except for the stability, where they differ only slightly. The two terms combined really imply the strength of the permanent magnet relative to the rest of the system. The magnetization M_0 is a material characteristic, and the second fraction is a description of how thick the magnet is compared to the overall gap lengths. The more of this combined muscle that is applied, the greater the resulting fields, forces, and inherent instability, coupled with a decrease in the power coefficient. The more the better, except in the small gaps, where greater fluxes require more control flux. A geometric limitation exists across the large gap for the second factor. If the permanent magnet is too thick compared to the large gap, although the large gap fluxes would be fairly large, the remaining room for the voice coil would be limited, requiring a longer coil and tighter tolerances.

The next parameter that arises is that of the small gap length. Generally, the smaller the gap, the better. A larger gap reduces the control flux, as well as, to a lesser extent, the electrodynamic forces, and increases the required power by a squared factor.

Interestingly though, to a first order approximation, a larger gap makes the system more stable. Its diminished effect on the fractional length parameter just discussed is worthy of a quick mention. Although the gap is generally small, when combined with the n factor (to be discussed soon), it can be large enough to diminish slightly everything that the permanent magnet thickness increases. A gap size is also limited by motion control requirements and machining and system tolerances. The following parameter, $d t$, is the cross-sectional area of the E-cores. Quickly stated, it will increase forces seen from the coils and decrease the power coefficient. Not obvious from the above matrix however is its geometric effect. When the e-core is up against the side of the platen, if this area (particularly the length t) is large, it uses up a lot of the permanent magnet length that could be otherwise utilized for travel. In other words, the bigger this area, the more the permanent magnet is lost to "dead space."

The next, and most interesting factor, is the n factor. Recall that this is the ratio of the permanent magnet facial area over the cross sectional area of the E-cores. It is a measure of how the permanent magnet's flux gets concentrated in the E-cores. This factor is generally adverse in nature. A variety of geometric constraints particular to the design, such as required travel, and the cross sectional area $d t$, set a requirement on the minimum size that this can be. Whereas the first two parameters would raise both the large gap flux and the smaller gap flux, this one only raises the small gap permanent magnet flux, which is undesirable. As aforementioned, if it is large enough, it can amplify the effects of the small gap which normally are otherwise not seen in the second fractional parameter. The MOB system can get away with a reasonably sized n , but it does tie the hands of the designer. If the travel requirements increased tenfold, to the size of the MAMS for example, this factor would increase on that order, creating much more flux density than is reasonable to allow to travel through the E-cores and the small gaps. Ways around this fundamental tradeoff are discussed the alternative design derivation (chapter 7) at the end of the thesis.

Finally, the parameters describing electromagnetic area and voice coil volume are mentioned. As would be expected, the larger the coil the larger the forces and flux. However, there exist very real limits on the geometry. In the prototype for example, the allowable window on the E-core where the coils could be placed is for the most part set by the lamination manufacturer. The voice coil must also reasonably fit into a small window space.

All of the key parameters have now been discussed. The biggest conflict in the design is now apparent. What is good for the large gap fluxes and voice coil efficiency, isn't good for the small gaps, which must be controllable and cannot saturate. This was a very considerable design limit on the MOB system. The other overriding MOB limits were geometrical; trying to make everything fit into a tight three-dimensional space. Smaller level tradeoffs had to be made for this process. For example, the pole face rectangular rather than square. The reason for this is to have a thinner dimension t , is so that less permanent magnet is required for the specified travel length. Voice coil placement also dictated how much of the window area could be filled with electromagnetic coils, as the voice coil had to have an anchoring point on the E-cores. As with any design, the final choices made reflect a complex web of tradeoffs.

3.6.2 Design point

With all the equations for MOB established, and an understanding of the various parameters involved, along with their ramifications, an actual prototype can be constructed. In order to flesh out the prototype, first an understanding of the GOES specifications (the MOB design platform) is in order. Once reviewed, geometric as well as material parameters best fitting these requirements will be discussed. Finally, the specific design parameters at the design point for the MOB prototype will be presented.

The interferometer required for the GOES project has a variety of optically specified design points. These are summarized in the table below.

Table 3.4: Satellite requirements.

| | |
|----------------------------|--------------------------------|
| Scan speed | 2.13 cm/sec |
| Turnaround time | 25 msec |
| Acceleration | 1.7 m/s ² (0.2G) |
| Scan extent | 0.5 cm |
| Power dissipation | 0.5 Watts |
| Mass | 1 kg (pref) |
| Velocity error | 0.02 cm/sec |
| Static misalignment | 20 μ rad rms (oscillatory) |
| Jitter | 4 μ rad |
| Temperature | 220 K |
| Launch | Δ type |
| Life Expectancy | 5 years |

There are several requirements here that are of great importance to the prototype design. The most difficult to design around is the power requirement. In the design process, the voice coil could be made to fit within this requirement, particularly since the required acceleration is relatively small. However, the power requirements, at least over a short duration, can be exceedingly high for the electromagnetic coils. While not consuming much power over a small region (about 10 to 20% over the entire transverse travel), if the small gaps should see a large offset, the required aligning forces can be exceedingly large (recall they increase as offset squared). One real way around these large offset requirements, and that was employed in the MOB system, is to use a series of stops which prevent the platen from coming too close to the sides. Scan extent inherently determines the size of the platen and the permanent magnet. This extent is an order of magnitude less than that of the MAMS system. The lifetime requirement

should be expectedly met by use of the magnet bearing. After all, one of the reasons it is chosen as to overcome problems such as friction and wear. However, the complete system including control electronics must meet this specification. The MOB prototype attempts to match the basic motion requirements (extent, acceleration, turnaround, and velocity) with one actuator, versus the three required in a full system. Power and weight are designed while keeping in mind that two other actuators will be present in the full system.

Some of the parameters acquire a secondary importance to other design issues. The very specific jitter requirements, for example, cannot be well tested by the prototype, in part because of measurement device accuracy. The prototype is by no means space qualifiable either. These last two shortcomings could be overcome after the concept is proved. Launch survivability and caging schemes are two issues that must also be considered before any further design can be put to test. While the prototype is not designed with caging in mind, the MOB system could perhaps be caged by keeping the platen stuck to one side during a launch. In the prototype, as aforementioned, this is generally undesirable though.

Keeping the general GOES requirements in mind, coupled with what is desirable in the system as was discussed in the last section, some material choices for the prototype can be made. There are two materials which drive all of the key choice: the E-cores and the magnet. Starting with the E-cores, these pieces have the ideal requirement that they saturate at as high a flux density as possible. A great material for this would be Vanadium Permadrur (CoFe) which has a saturation flux density of 2.2 Tesla. However, this was ruled out for the prototype because of its relative unavailability compared to other materials; it would have taken several months to obtain. Nickel iron (50% NiFe) could be used, which is very readily available, however, this material saturates at around 0.8 T. The final choice was to go with silicon iron (SiFe) which saturates at about 1.6 T. Laminations of these were readily available from a transformer

lamination manufacturer (Magnetic Materials). In an actual design for a satellite, Vanadium Permadrur could surely be obtained for the extra bit of performance it allows. The fact that laminations were used over solid materials, as previously mentioned, is due to their ability to allow a reasonable frequency response. By electrically isolating each shim (the shims in this case are 6 mils each), eddy currents are virtually eliminated, allowing changes in field at the rate of about 400 Hz or so with no significant eddy current effects.

The next material consideration is what to use for the permanent magnets. A strong (high MMF) magnet is desirable, particularly to keep the voice coil efficient. However, too strong of a magnet for the actuator will saturate the E-cores and create possibly uncontrollable flux. A further point of consideration that should be mentioned is temperature requirements. Given the extreme temperature changes typical of space, the material must handle temperature changes well. Rare earth magnets are ideally suited because of their high magnetization density M_0 , linear B-H curves, and high coercive force. The two common types of rare earth magnets are samarium cobalt (SmCo) and Neodymium Iron Boron (NdFeB). A comparison of the two materials, each having several advantages and disadvantages, are shown in the following table.

Table 3.5: Permanent magnet properties.

| | SmCo | NdFeB |
|---------------------|-------------------------|---|
| Energy product | 32 MGOe | 45 MGOe |
| Mechanical strength | More fragile | Less susceptible to chipping and cracking |
| Density | 0.3 lbs/in ³ | 0.267 lbs/in ³ |
| Oxidation | Not a problem | Highly susceptible |
| Temperature effects | Not a problem | Very sensitive Knee in curve 60-140 C |
| Cost | Expensive due to cobalt | Cheaper |
| Remanence | 0.86 T | 1.23 T |

Although the energy product of NdFeB seems to make it highly desirable, as shown earlier, a higher flux here is not necessarily optimal for this design prototype. While it is stronger, weighs a little less, and is a bit cheaper, these effects are outweighed by its tendency to oxidize unless coated (bad for the prototype) and its poor temperature performance (bad for the satellite design). The Samarium cobalt is therefore the magnet of choice here.

The resulting design point for the system is given in the figure below, followed by a chart summarizing its theoretically anticipated operating points. From the sketch, the prototype actuator that is shown is quite large, measuring about 4-1/2" x 3" x 1-1/2". The larger size actuator made construction a little easier to handle. All of the results for this system could be appropriately scaled down by a fraction for use in the complete MOB system.

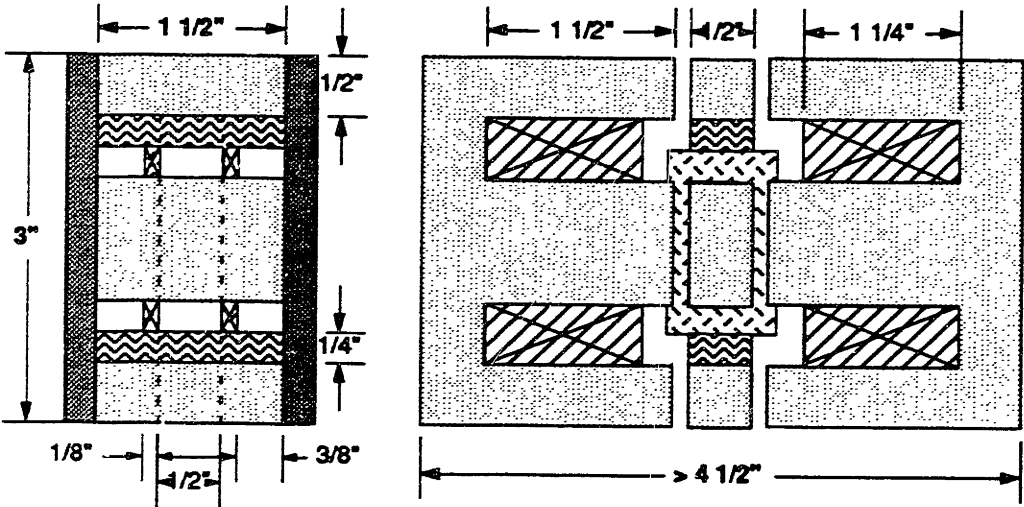


Figure 3.13: MOB geometric design point.

The SiFe fluxes noted in table 3.6 identify operating flux, and flux when the platen is at either side of the restricted gap. Pull-off power describes the actual power that would theoretically be required should the platen extend to one side of the gap, which

doesn't happen in the prototype because of the shims used. The key requirements for the GOES, including that of the stroke and the power, are met, in theory, by this MOB design. Saturation fluxes are carefully avoided (note the maximum at one side is three times that of the center). The force per area for the electromagnets as well as the force per volume for the voice coils is also presented, as a reference for efficiency. The first figure is small as compared to typical electromagnetic actuators, which are normally about five times that amount. The second is rather small for a voice coil (which can be three times as much or higher). This lack of voice coil efficiency again results from some of the required MOB tradeoffs, most notably the limited speed of the control electronics, which yields limited ability to suppress the high frequency unstable pole. The weight shown is for just the moving part (the platen), and is reasonable considering that this is much larger than a production model. Finally, the high pull-off power, which is the power should the platen transversely displace all the way to one side, is why mechanical stops (plastic shims, 78 mils thick) are employed to prevent this scenario, and also reflects the tradeoff between efficient voice coils and overbearing electromagnetic fluxes. Using the prototype setup, an alternate, more efficient design is presented in chapter seven, should a faster control loop be available, such as one that would be analog in nature.

Table 3.6: Design point table.

| | |
|---------------------------------|----------------------|
| Stroke | 0.5 cm |
| Dissipated power | 0.1 W |
| SiFe flux (op & max) | 0.4 T, 1.3 T |
| Large gap flux | 0.34 T |
| EM F/A | 17 N/m ² |
| ED F/V | 0.3 N/m ³ |
| Small gap size | 2 mm |
| Total moving weight | 337 g |
| Pull-off power | 50 W |

Now that the design point has been settled, a full sketch of the actuators can be presented to give a three-dimensional feel of what the actuators look like, and how the coils, cores, and magnets fill the allotted space. This representation can be seen in the conceptual drawings below in figure 3.14.

261777-1

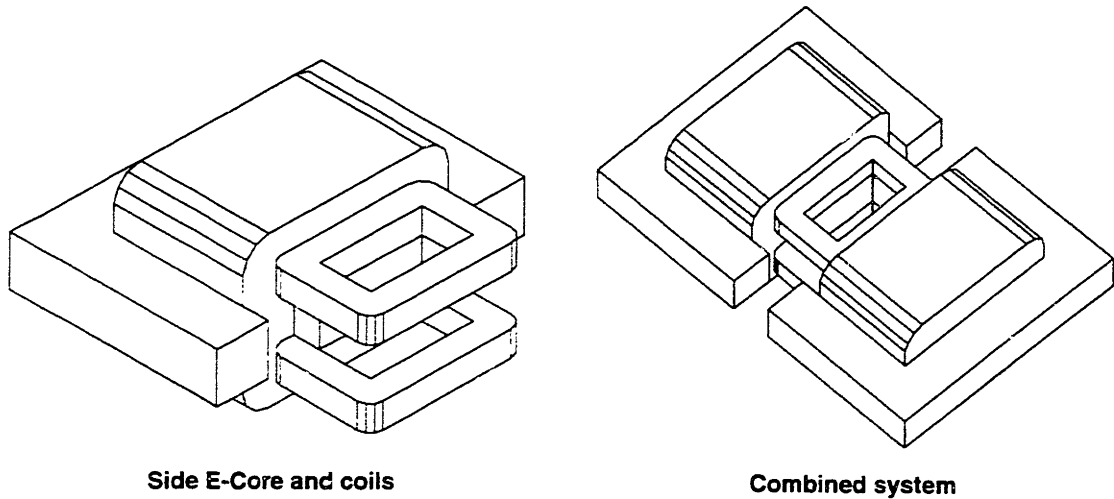


Figure 3.14: MOB actuator conceptual 3D drawing.

3.7 Two Degree-of-Freedom Test Fixture Design Study

For prototyping and proof testing the MOB actuator concept, one of the three anticipated actuators was assembled and tested. This approach allows the testing of the key actuator concepts in the simplest possible experimental framework. In the full MOB system, all 6 degrees of freedom are controlled. With only one actuator however, only two degrees of freedom can be controlled. The question of how to fixture a single actuator is nontrivial. For the full MOB system to actually be built, each actuator would surely have to be tested individually as well, making the fixture design an important consideration. The basic problem is that the single actuator has to be fixtured in such a way that 4 degrees-of-freedom are constrained by the fixture, while 2 specific degrees

are allowed for, i.e., the scanning motion and the smaller transverse motion. In these 2 free degrees-of-freedom, several properties are very desirable; namely low friction, low noise, high repeatability, and reasonable cost.

Before discussing which configurations seem most suitable, it is of interest to take a moment to review the different options for candidate bearing choices. The air bearing information is courtesy of Space Electronics, which manufactures such systems.

Table 3.7: Bearing type comparison.

| | Air Bearings | Ball or Roller Bearings | Flexure |
|---|-------------------------------|--|---|
| Runout | As small as 1 μ inch | > 50 μ inch | NA |
| Small deflection stiffness | 1×10^6 lb/in or more | Preload dependent. Can be < 1×10^3 lb/in | 1×10^6 lb/in or more |
| Wear | None | Depends on unbalance, preload, speed | Depends on # cycles of operation |
| Resistance to dirt | Excellent | Poor | Excellent |
| Stick-slip at very low speeds | No | Yes | No |
| Friction torque | Typically < .01 lb-in | $f(\text{preload, temp})$. Typ. >1 & <50 lb-in | Depends on deflection required. ≈ 25 #-in/in |
| Bearing noise | Unmeasurably small | Significant for critical applications | None |
| Resistance to shock load | Excellent | Poor | Good |
| Max speed | 3×10^5 rpm or more | Typ. 1×10^4 rpm | Depends on size, ω_n |
| Sensitivity to Δt | Operates over a wide range | Sudden Δt can cause seizure | Excellent. Depends on material choice |
| Multi DOF possible | Yes | Yes | No |
| Cost | High (\approx \$1K min.) | Low | Low |

This table is particularly useful here because an air bearing seems like a good candidate from the start, but its higher cost must be justified. Inherently, air bearings meet all of the specific requirements for suspension. The argument will therefore proceed by ruling out other possibilities first, starting with the simple, mechanical roller or ball bearings. This choice would be the cheapest and easiest type of bearing to use. However, problems with stick-slip at low speeds are a very real, particularly since the MOB motions, for both the scanning direction as well as the transverse motion do not proceed continuously in one direction, but are repetitive back and forth, stick slip is a real issue. In even the highest performance mechanical roller or ball bearings, this would also add a nonlinearity to the system, which is very undesirable. Fluid bearings and lubricated bearings are poor choices in general for this project as well. The fluid levels in the bearing may critically change.

The next type of bearing to consider, would be some sort of flexure design. These have been used in other air bearing suspension methods [Olson 1994]. The flexures, by nature of their design, are suitable only here if an extended arm is placed on the flexure to amplify their small angular deflections. Such flexures have the advantage of principally allowing one degree-of-freedom, ideally constraining all of the other ones. They also overcome all of the stick-slip problems associated with the roller or ball bearings. Flexures are also relatively cheap and easy to make. However, they inherently add a torsional spring term to whichever degree of freedom is in suspension. With a good design though, the spring natural frequency can be kept well below the desired range. The biggest limitation of flexures is a limit on travel, typically only a few degrees of rotation. Ball or roller bearings can be manufactured in such fashions to allow two-degrees of freedom for example, which simplifies the design. Flexures do not readily have this feature, without literally stacking them on each another.

Air bearings can be used for either type of motion. Production linear slides are available without custom order. These provide only for the long axes of travel.

Attempting to allow for a transverse motion on a basic slide leads to instability due to growth of the air gap. An x-z air bearing system can also be built to comprise a straightforward solution (an air puck), but this configuration for the MOB actuator would allow out of plane yaw instabilities. Sleeve journal bearings are available which combine linear travel and rotary motion by means of a special sleeve. This design can be modified to meet the requirements of the project, allowing for the long axes of travel, and a smaller extended transverse direction of travel. This final solution is illustrated in figure 3.15 below.

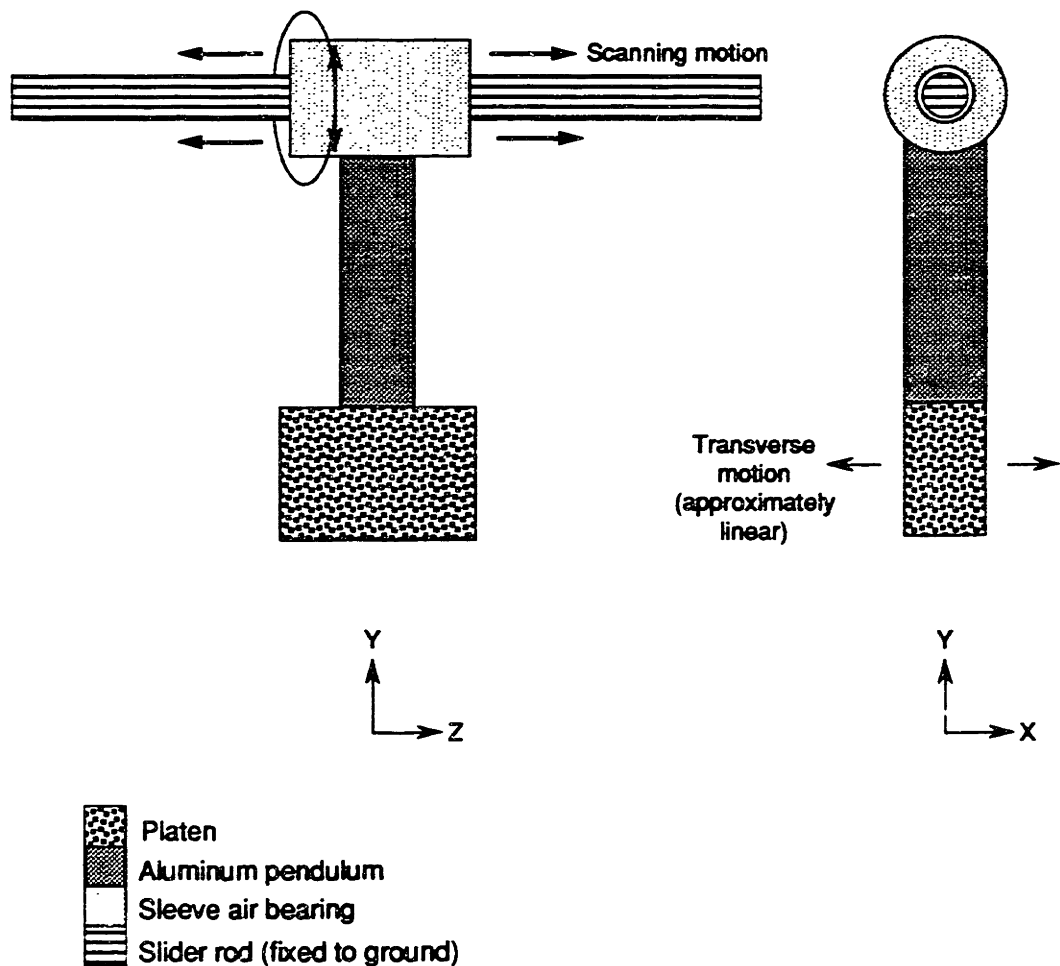


Figure 3.15: Two degree-of-freedom suspension method.

Chapter 4

Hardware

In terms of hardware application, this project required a significant effort in systems integration. The prototype is controlled by a personal computer with several a/d and d/a boards. Commands originating and calculated from the computer must be converted into signals to run the MOB prototype, and read back through appropriate position detection devices. Not only is the physical form of the MOB prototype worthy of discussion; all of the supporting devices used at each stage of the signal processing are also important to mention. This chapter starts by presenting the overall picture of the physical layout and control system. It then moves onto discussing the support structure, fixtures, and manufacturing techniques of the platen and stationary E-cores. Specifics of the air bearing are then discussed. The two measurement devices, the laser position transducer as well as the capacitive probe follow. The chapter ends with a focus on the electronics, including the interface a/d and d/a boards and the power amplifier circuits.

4.1 System Overview

Before getting into the specifics of the design, it is best to step back to obtain an overall picture of the workings of the entire system. This can be done from two vantage points. The first is a conceptualization of the feedback control system, mentioning at each point the piece of hardware required to implement such choices. The second is a look at the overall physical setup to give an idea of where all the pieces go and how

they fit together. After this brief introduction and overview, each component will be discussed in detail in terms of performance and integration.

4.1.1 Digital control system

The control system for a satellite measurement system, given today's standards and requirements for radiation hardness, would most probably be of the analog type. A well-built analog system is very reliable, and all of the required components could be obtained in a space-qualifiable format. For the future generations of spaceborne measurement devices, digital control will most likely become more and more common. Control specific chips, such as digital signal processors (DSPs) can be specially programmed for an ever-increasing number of control specifications. In fact, a DSP was considered as a possibility in the case of the MOB prototype. However, while this may be a very efficient digital device, the required time to properly program and integrate it would have been too long for the time frame of this project. Other system factors also tend to limit full DSP speed in application. To meet versatility and development time constraints, a 486/66 PC coupled with the Microsoft C language was chosen as the basis for the digital control method.

The components of the digital control system are shown below in figure 4.1. As was described in the last chapter, because of the small angles anticipated, the control of the two different degrees of freedom of the prototype can be described independently, allowing for two distinct control loops. These two control loops, for the scanning motion via the voice coils, and for the transverse small gap motion via the electromagnetic coils, will therefore be described independently. Note however, that they share much of the same controller equipment, such as the PC platform, the clock, and the d/a board.

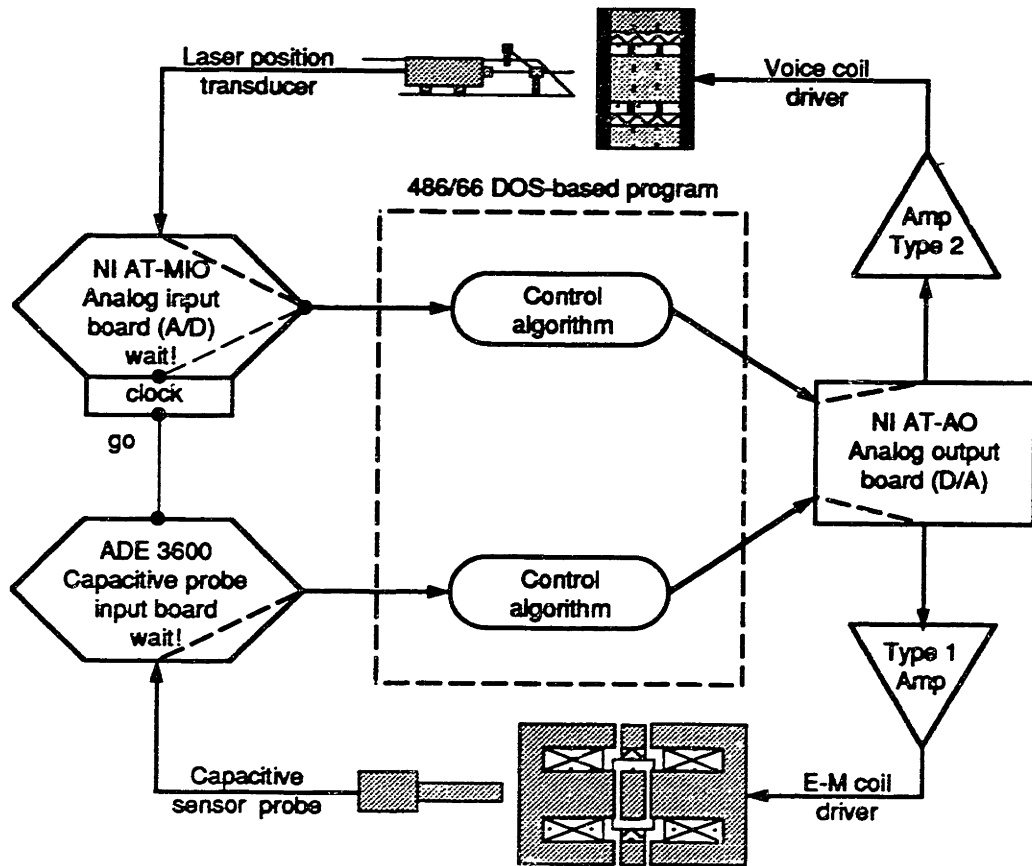


Figure 4.1: Digital control system.

Starting with the scan loop (top of figure), the overall speed and timing is pre-determined by a clock that is housed in the National Instruments AT-MIO-16 a/d board. When the input board gets the clock signal, it allows the next loop of the control program to proceed. The control algorithm acts on these measured signals to generate actuator commands. These commands are then output through another National Instruments board, their AT-AO-6, which is of the d/a variety. The outgoing voltage signal from this, as a small signal level, is fed into an amplifier circuit, where the voltage can be applied to achieve the corresponding required amount of current. At the heart of this amplifier circuit is a 300 W Crown amplifier. The next stage of the system diagram includes the actual voice coils of the MOB system, where the applied current is converted into electrodynamic forces, which in turn drive the platen. The motion of the

platen is tracked by a Hewlett-Packard laser position transducer. This is a very accurate device, with resolution capabilities down to a fraction of the laser's wavelength. By a two stage process, which will be described in detail later, an analog voltage signal proportional to displacement is generated by this device. The analog signal is read by the a/d board, providing the first loop's feedback signal. This completes the first control loop, as the reference signal waits for the clock input to be run through the control software once again.

The second loop proceeds much in the same way as the first, as would be expected. Once the clock gives the initiating signal, the control loop proceeds, yielding a desired output. Again, this is fed into the d/a board. An electronic circuit, using the same Crown amplifier (different channel), is then utilized as well to drive the electromagnets. However, as will be pointed out later, the circuitry around this amplifier differs slightly from that seen in the other loop, primarily because the two types of coils, electrodynamic and electromagnetic, must be compensated for differently due to their differing inductance. The signal from the amplifier drives these electromagnetic coils, which in turn create the aforementioned hybrid forces to position the platen with respect to the small air gap. The transverse platen position is monitored by an ADE capacitive type probe, specifically tailored for very small displacements. The signal from the probe feeds directly into a special ADE board, which, through a series of low level commands, can be transferred into a number proportional to the displacement to be read by control program. This is the block which completes the second loop.

4.1.2 Table layout

Whereas the last sub-section focused primarily on the system from a signals and controls viewpoint, this section will touch on the overall setup in terms of a physical viewpoint. While the physical setup description of the computer and measurement

systems is not necessary, as such components are widely adaptable, a discussion of the setup of the specialty designed components is worth mentioning. The setup is schematically illustrated in figure 4.2, and shown in the pictures, figure 4.3 and 4.4.

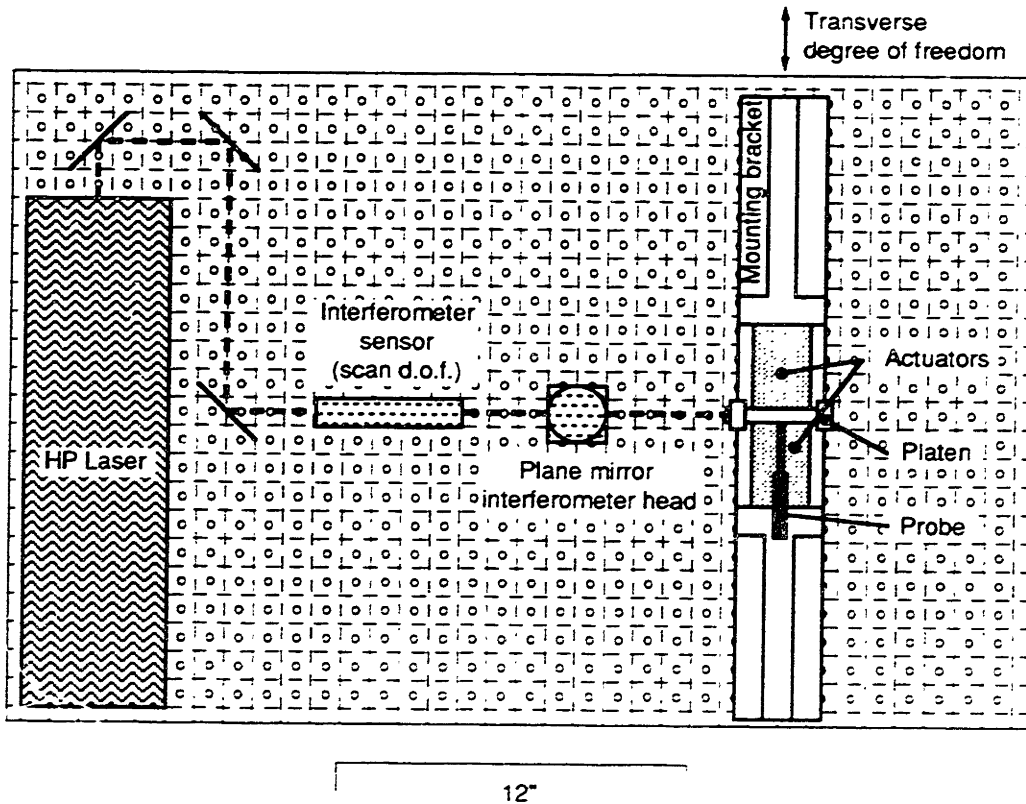


Figure 4.2: Electronic Vibration Isolation (EVIS) table layout (top view).

From the diagram, the overall layout should be clear. First of all, the key elements of the entire setup are bolted to the top of a Newport Instruments Electronic Vibration Isolation (EVIS) table; useful in helping to cut out unwanted background vibrations (although it was disabled for the experiments reported herein). The table contains a layout of 1/4-20 screw holes, serving as an excellent hardware prototyping platform. The actuators, in their respective housings, sandwich the moving platen without contact as it scans over its requisite distance. Each actuator is supported by two steel angle brackets. This means that the bottom of the assembly of actuators and platen clears the

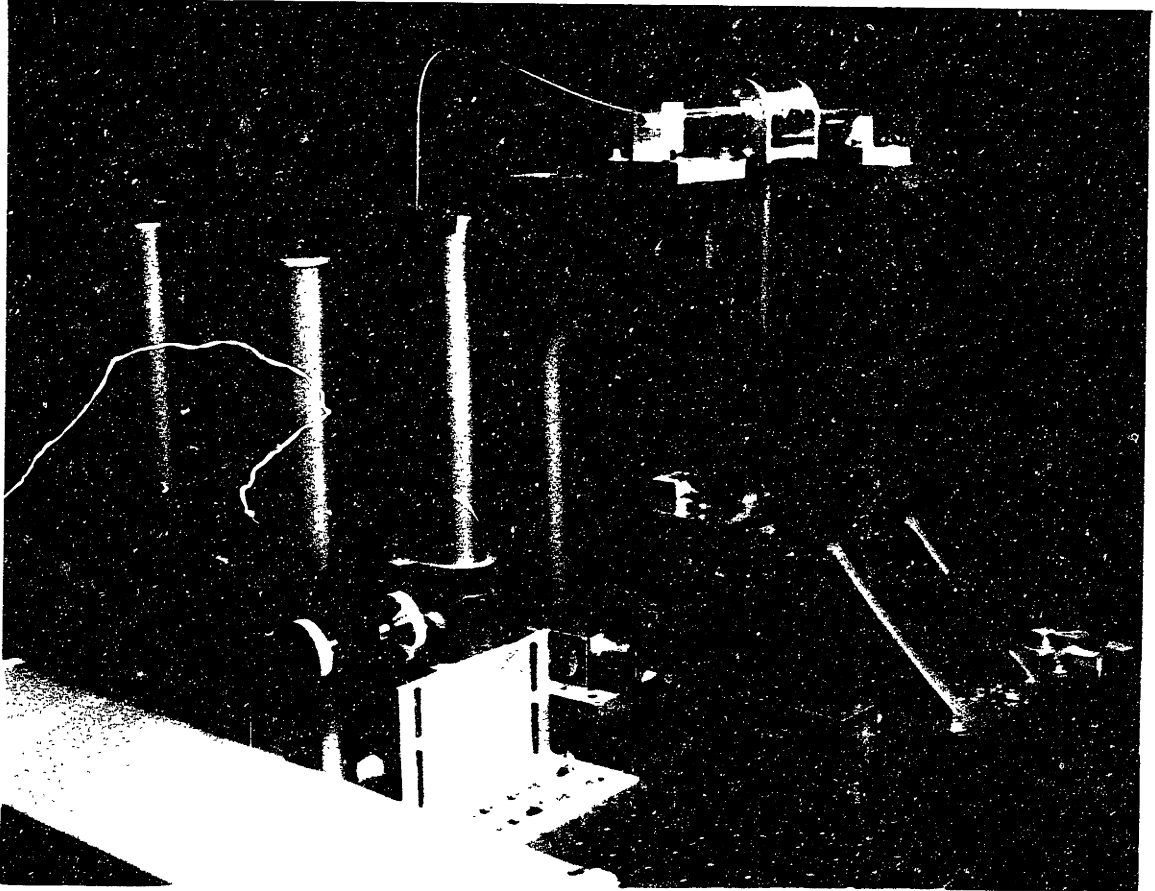


Figure 4.3: Picture of overall layout.

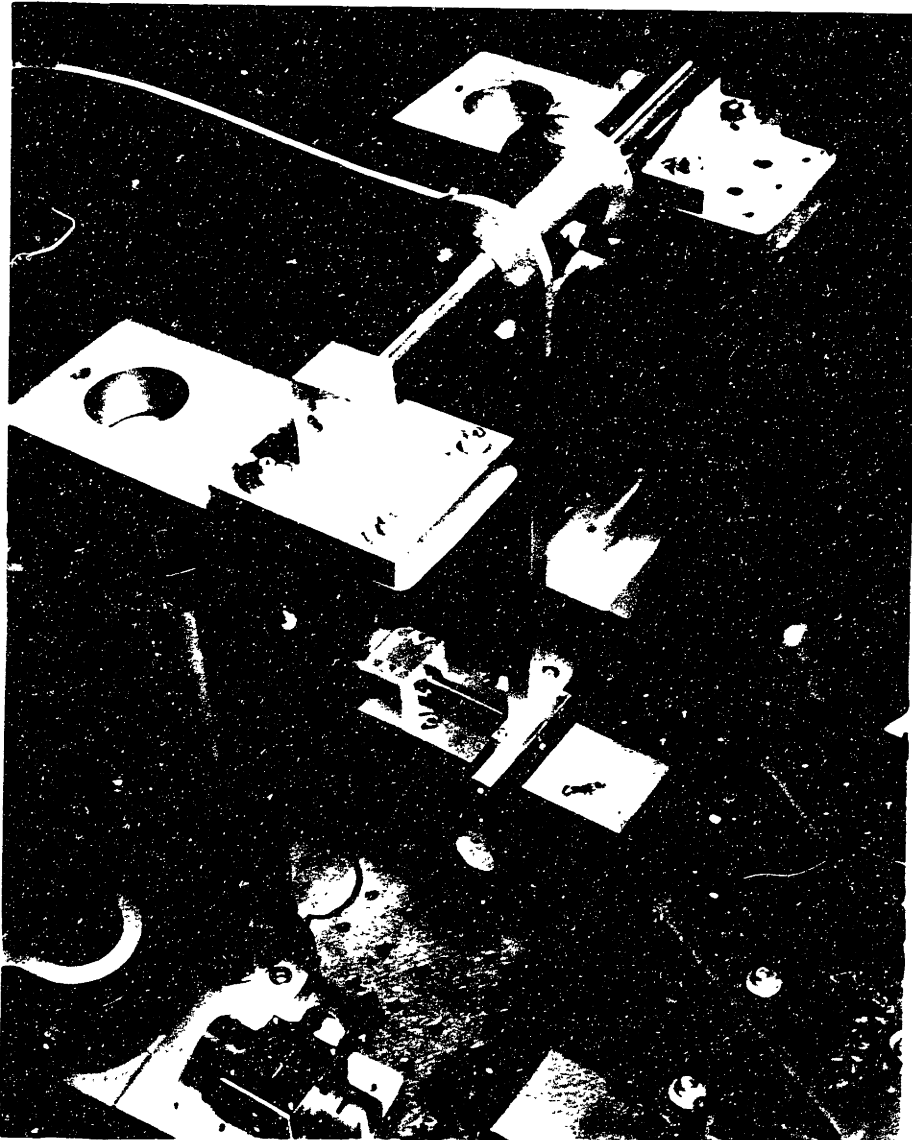


Figure 4.4: Top view picture of overall layout.

table by a about an inch. The sensors of the two measurement devices (but not their supporting electronic hardware) are also on top of the table, protected also from external disturbances. The probe, because of its small operating range, must be mounted extremely close to the actuators, whereas the laser position transducer has a much greater flexibility in its mounting configuration. The laser beam, as is done here, can easily be bent by a series of mirrors and directed over a distance to the scanning platen. The required support equipment, including the air filtration system for the air bearing, the electronics box for the laser position transducer, the amplifier and its electronics box, and the computer system with its various internally mounted measurement boards is located elsewhere in the lab independent of the isolation table.

4.2 Actuator and Platen

The actuator system is a combination of the stationary actuator which contains the E-cores, electromagnetic and voice coils, and the moving platen which contains the permanent magnet and through-flux paths. Overall, for the MOB design, close to thirty individual pieces of aluminum had to be cut for the manufacture of all of the system's pieces. For most of the pieces, once obtained from the machine shop, assembly is relatively easy. This is not the case for the actuator and the platen. Once the skeletons of these pieces are obtained, a large number of manufacturing steps are required. Many laminations have to be glued together and potted into place, coil structures had to be assembled, and magnets had to be inserted. All of is done under tight tolerances for many of the pieces, particularly at the small gap and large gap interfaces. The assembly and associated manufacturing processes are described next. Figures 4.5 and 4.6 shows what the assembled actuator and platen look like without the voice coils.

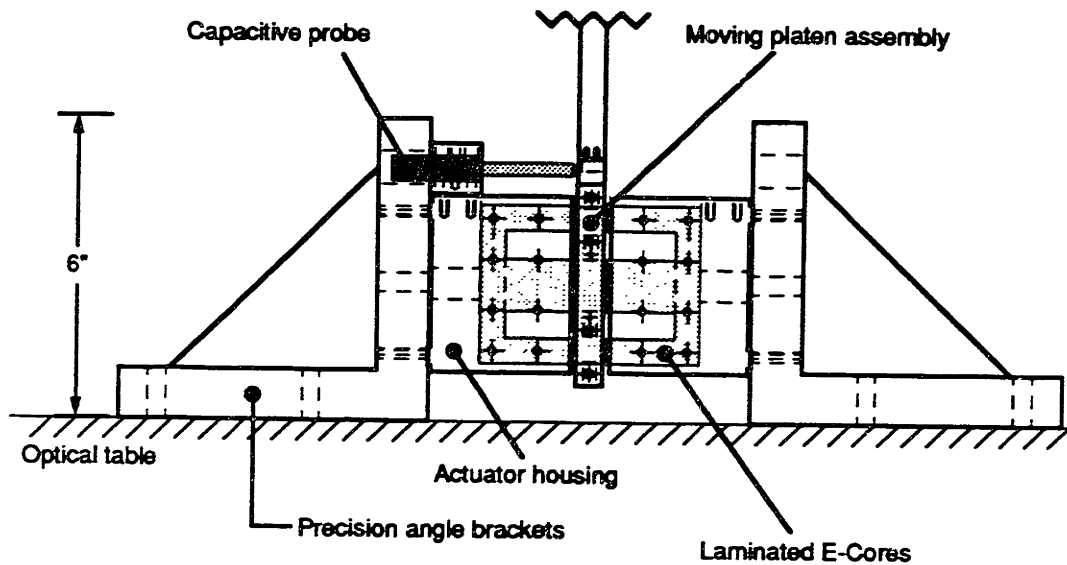


Figure 4.5: Overview schematic of actuator, platen, and probe.

4.2.1 Stationary actuators

The stationary actuators consist of several components. The heart of the actuators are the laminations and coils, all housed in an aluminum shell. The overall assembly plan for these actuators starts with the epoxying of the laminations into the aluminum housing. Once set, the face of the lamination stack is ground and polished flat and parallel to the base of the aluminum structure. The electromagnetic coils, and then later the voice coils, complete the structure.

The basic shape of the laminations used for the actuator are shown in figure 3.13. Each of these laminations are 6 mils thick and must be epoxyed together, and, concurrently, into the aluminum structure, which is shown in figure 4.7. A low viscosity, highly thermally conductive, insulated, slow setting epoxy is chosen for this function. The low viscosity insures that the laminations require minimal amounts of epoxy to hold them together. The thermal properties are required to avoid any heat



Figure 4.6: Picture of actuator, platen, and probe.

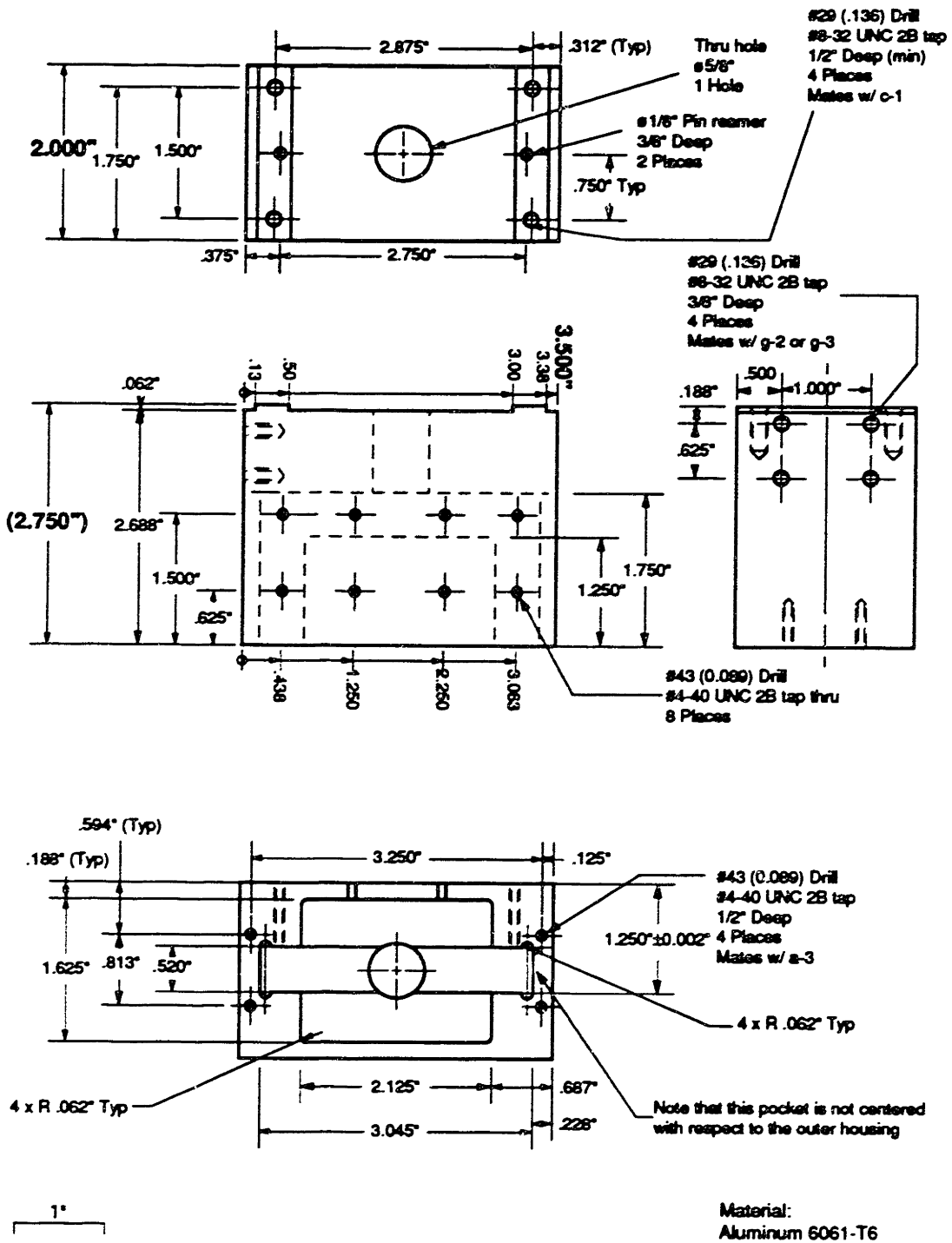


Figure 4.7: Actuator housing component drawing.

buildup in the actuator. The electrically isolating property is desirable for keeping the laminations electrically separate from each other, maximizing the effectiveness of the choice of laminations over solid materials. In preparation for the epoxying of the laminations, the cavity is first thoroughly cleaned with acetone. The housing has been anodized after manufacture to prevent any oxidation layer buildup, which would inhibit the epoxy bonding. On one side of the cavity, (opposite the side of the six set screws), #34 wires are inserted to act as spacers insuring about a 5 mil separation between the first lamination and the cavity side, for a good, solid interfacial bond. The rest of the E-core shaped cavity is painted with epoxy. In the plane perpendicular to the longest dimension of the E-core, plastic shims are used to press the laminations to the opposing cavity wall. The E-core shaped cavity is made slightly longer than the E-cores themselves to allow for variations in E-core dimension tolerances. Laminations are then "battered up" with a thin layer of epoxy and set into place. A total of 81 laminations can be in the assembly of each actuator, for a total thickness of 1.27 cm (1/2"). This accounts for a 5.1 μm (200 μinch) average bondline between layers. Once all laminations are set in place, six set screws are torqued in from the side to hold them together as they set in place. For the center of the E-core, special blocks are utilized (appendix B - part A2) to temporarily span the empty void where the electromagnetic coils eventually go, to insure an even pressure for the setting process. Once dried, the actuator with laminations is surface ground and polished to make the E-core pole faces flat and parallel within 5.1 μm (200 μinch) of the actuator base. Note that the e-core face sticks out of the housing by roughly 1/2 cm (2/10"). This is to allow for enough space to strap the voice coils to the protruding cores.

The coils are the next piece of the actuator puzzle. These are wound from #22 wire. The windings are done on specially made bobbins (appendix B - parts F1-F4). The electromagnetic coils consist of 575 turns, and the voice coils of 15 turns each. The coils are set into a solid fixture not by epoxy, but rather by the unique properties of the

thermally self-bonding wire used. A high current can be sent through the wound coil over a brief duration, heating a special thermo-setting outer coating enough to fixture the coil as a single piece. The wound coils are then ready for insertion into the actuator itself. To insure that the electromagnetic coils do not short out on the E-cores, the E-cores' exposed sides are coated with a thicker, insulating epoxy, and the exiting wires are covered with heat shrunk tubing. Finally, mylar sheets are used around all exposed E-core legs and housing to avoid problems with coil-to-housing shorts. The electromagnetic coils structure is placed over the center of the E-core assembly, and held in place by an insulating potting epoxy. The voice coils tended to be a bit more difficult to assemble. They must be strapped to the protruding E-core by means of a special fixture (appendix B - part A3), which holds the coils down by pressure to the face. The voice coils may then be permanently attached with epoxy.

Moving to the outside perimeter of the actuator housing, several important features should be mentioned. The actuators are designed to allow for modular attachments. They are also identical and thus ideally interchangeable. The modular capability can be seen with the 4 x 8-32 screw holes on one of the small actuator sides. These holes are mates for two entirely different pieces. First, they have the capability to mate with the capacitive probe sensor. Second, they can mate with the stopper device (appendix B - part G3). This eases the complexity involved with replacing or redesigning the actuators, should the need arise. On a final note, the actuators are mounted to precision angle brackets (appendix B - part C1). These steel brackets are flat and perpendicular to better than $12.7 \pm 5.1 \mu\text{m}$ (1/2 mil) over 15.3 cm (6 inches). They are chosen here to insure proper overall actuator alignment over the small gap, particularly with respect to the actuator tip. The interface holes from these angle brackets to the EVIS table are also made larger than required, to allow for minor adjustments over the small gaps, in the gap direction and its transverse. The holes can also compensate for actuator housing tilt.

4.2.2 Moving platen

The assembly of the moving platen (see figure 4.8) is by far the most challenging part of the prototype fabrication. First of all, several materials must interface, including specially cut E-cores, the permanent magnets, and the aluminum support structure. Furthermore, the opposing faces also must be flat and parallel for the small gap interface. The assembled platen picture is shown in the two figures below, which is composite sketch of all the assembled pieces. Several steps are taken in the assembly of this structure, as described next. First, the E-core slats are cut and assembled separately, in a what is referred to as an assembly trough. They are then epoxied into the overall platen frame. Once this is set, the permanent magnets are then placed in the structure. Following assembly, the structure is then surface ground to specification.

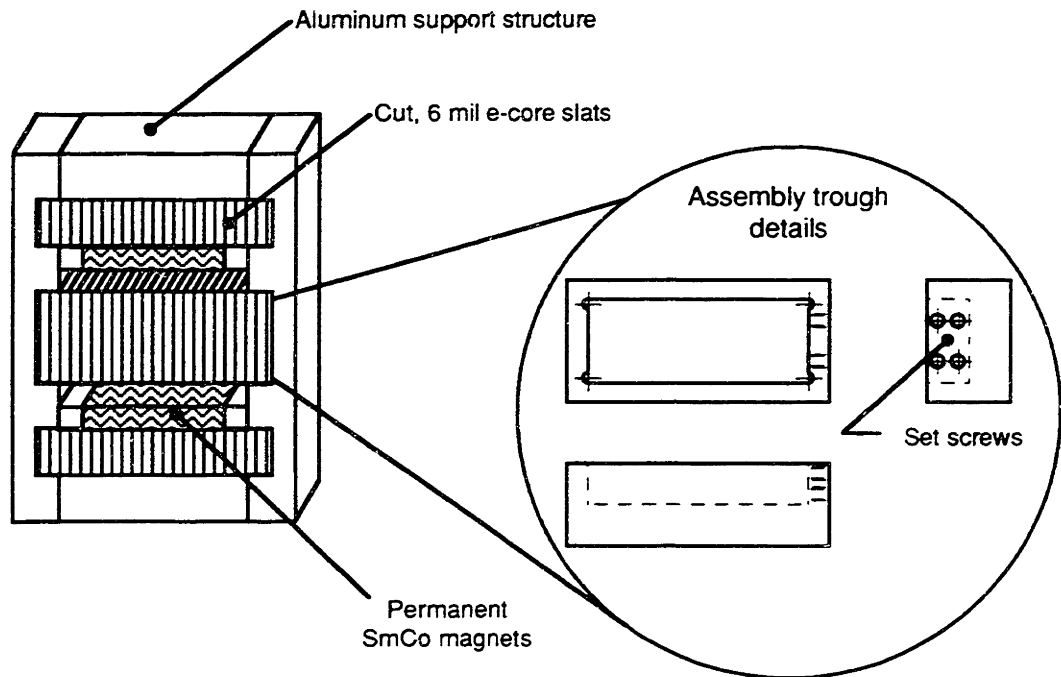


Figure 4.8: Platen assembly.

The first step is the assembly of the E-core slats. These slats are cut down to size from a standard E-core shape. As shown in figure 4.8, assembly troughs are used to

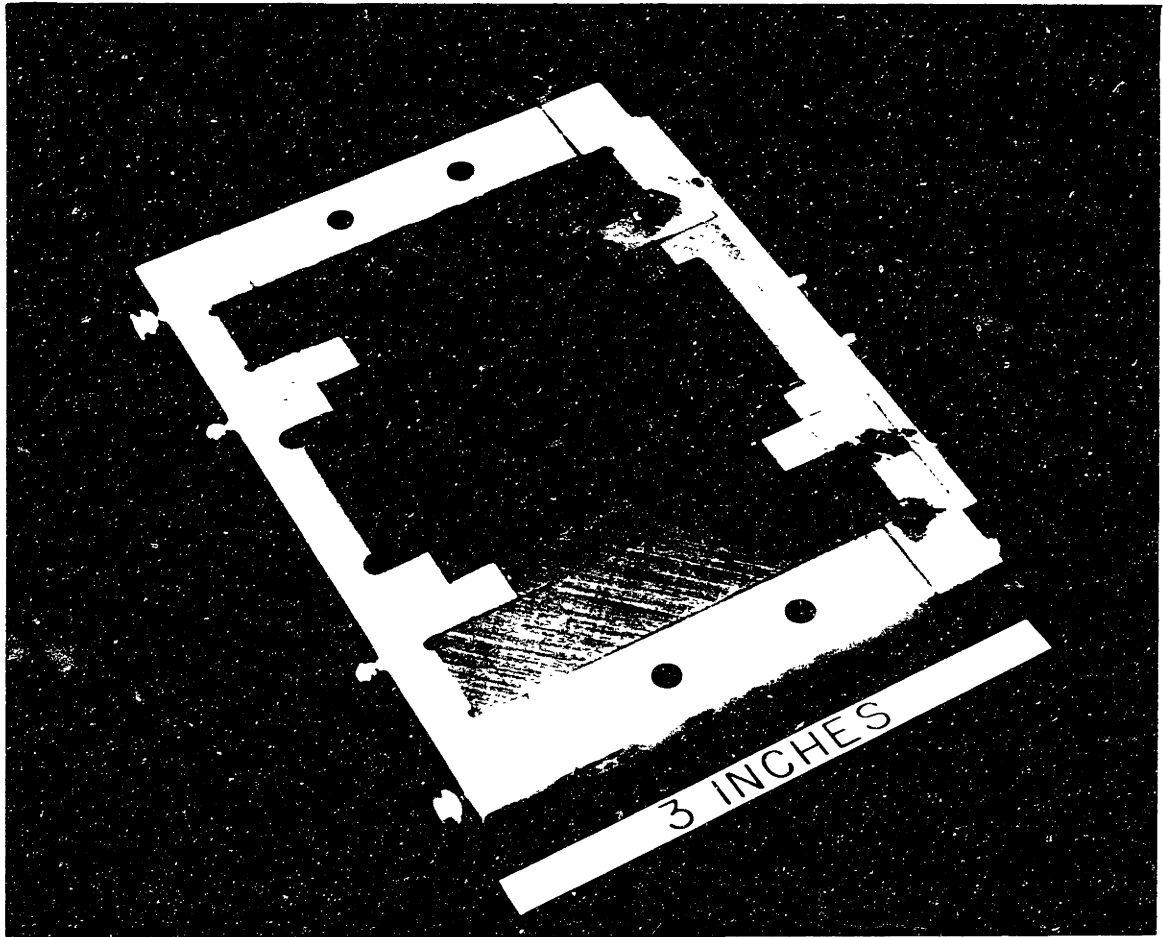


Figure 4.9: Picture of center platen.

assemble the slats (appendix B - parts B7 & B8). Two different trough sizes are required, one for the middle set of slats, which are wide, the other for the end slats; twice as many, but half as wide. These must be stacked parallel to the stationary E-cores to allow for maximum traveling flux capabilities. The trough undergoes extensive surface preparation before the introduction of the E-core slats. It is first sprayed with several coatings, at intervals, of a standard mold-release spray. Once these layers have been allowed to dry, an additional coating of Teflon spray is applied. This extra caution is invoked to insure that the assembled slats properly release from the initial assembly structure. The slats were epoxied together in much the same fashion as was discussed in the last sub-section for the E-cores in the actuator, including the use of moderately sized set screws to press the laminations during epoxy setting. To insure proper release, sprayed shims (5 mil) are used on the bottom, along with a series of jacking screws. The resulting stacks are all vertical and parallel, though an alternate configuration where the slats are horizontal could be envisioned.

Following assembly, the strips are inserted into the frame of the platen and bonded in place by epoxy. For this first platen insertion, the frame is set on a slab, and aluminum blocks (appendix B - part B4) are used (also sprayed with mold release) where the permanent magnets and voice coil gap will eventually go. Shims are placed under the aluminum support structure to insure that the slats stick out by several mils on each side of the platen to allow for surface grinding of the entire assembled structure. Once the slats are set in their final configuration, the permanent magnets, the last part of the platen structure, are added. The resulting structure's opposing faces are then surface ground and polished to the same specifications seen with the E-core side actuators.

The platen frame was designed in such a manner that one side can be readily unscrewed and detached. This ability of the platen to open is essential in order to allow the voice coil to be inserted so as to surround the center piece in the final assembly. After construction, the platen proved to be much more delicate than had been originally

anticipated with the center leg prone to fracture. Instead of having the entire platen side be removable, it was modified so that only an area of the side near the center leg had to be removed to insert the voice coil. This removable hat shaped piece on the right side of figure 4.9 demonstrates this capability. In addition, 10 and 20 mil ground G10 slats were used on the magnets and above and below the center leg respectively to alleviate the fracturing problems associated with the voice coil insertion.

On a final note, the assembly piece that the platen is immediately attached to (appendix B - part D5), which leads to the pendulum structure is specified with a very high-grade machine finish of 32 μ inches (AA rating) on the face which the capacitive probe sees. This is specified to insure the best readings by the probe as the platen moves in the scan direction.

4.3 Air Bearing

The air bearing is one of the most expensive parts of the MOB prototype. Not only is the bearing assembly itself required, but also its supporting pumps and filters. The specifics of the ready-made air bearing also drive the design of the moving parts of the actuator, which must mate with this piece. Because of the overall system impact of this part, its specifications and design implications warrant brief discussion.

4.3.1 Specifications

Once the choice for a round-rod slider air bearing was settled upon (see end of last chapter), the question remained which manufacturer to obtain the bearing from, since the devices are relatively expensive and in many cases, custom built. One of the main secondary concerns on the air bearing is stiffness of the roller in pitch and yaw as it moves along the slider. The first company found that could meet these specifications

was Space Electronics, whose slider had a cylindrical inner diameter, and a rectangular outer shape. Their pitching stiffness was satisfactory for small angular offsets, and the mounting platform was excellent for hanging a pendulum. The other candidate, and the company eventually used, was PI (Professional Instruments). Their housings are completely cylindrical, and allow for complete 360° roll around the slider rod, unlike Space Electronic's design, which was limited to 10°. In general, their product line was more tailored towards round-rod sliders and spindles, whereas Space Electronics could do the job, but it would require custom designing. The PI mounting platform was more difficult to build onto, having only interfaces at either end of the housing, which in turn required extra manufacturing for the platen assembly. However, they did an excellent job in providing a filtration system for the air. Normally, air bearings cannot run off standard lab supplies. They require especially low humidity and particle-free air.

The bearing housing choice has two major, coupled tradeoffs. The first is the radial weight capacity. Generally, the higher, the better. While the prototype has a fixed capacity requirement, a stronger air bearing could serve as an excellent test fixture for future platen testing and design. The other side of the tradeoff is the bearing weight; the more it can support, and generally the heavier it is. This becomes a problem when the weight of the housing approaches that of the bearing itself. In this situation, Professional Instrument's E.P. 750 air bearing was chosen, which has a radial load capacity of 0.17 lbs/psi with a maximum pressure of 200 psi.

The air, as aforementioned, must meet stringent requirements for the system. The air for the bearing must be free of oil and of particles larger than 200 μinches. Furthermore, the air must be maintained at less than 90% relative humidity. Professional Instruments provides a nearly fully assembled dryer filter regulator system (model D4-A) which combines the necessary components from Van-Air filters and regulatory valves. At the heart of the filtration system is a pressure cylinder filled with

deliquescent tablets, which combine with water vapor to form a drainable liquid. The saturated air is therefore reduced to about 80% relative humidity in this situation.

4.3.2 Pendulum design and attachment

The tolerances on the slider-rod and housing are very strict (to 200 μ inches) and must be carefully maintained. This places extra requirements on any fixtures designed for the air bearing housing and rod. Anything that attaches to the rod must not introduce any strain onto the pieces, which could significantly impact overall performance. The design for the housing attachments and rod are therefore briefly reviewed.

The rod, in this case cut to a special length (10 inches versus the standard 6 inches) to allow for ample travel, must be mounted at each end to the EVIS table. The first stage of this mounting process includes the use of specially damped Newport mounting posts, which are used for a wide variety of optical applications. Special fixtures are then used to go from the two posts to the bearing rod. One end of the rod is rigidly screwed into one of the posts (appendix B - part E1) by means of the fixture. To make sure the rod is then properly constrained, without introducing any possible over-constraints, the other end is set to rest on a 'V' shaped block (appendix B - part E2). This allows for any dimensional growth of the rod, e.g., under changing temperature, while providing vertical and horizontal support while not overconstraining any torsional modes.

The housing attachments also face some of the same concerns as the rod. The configuration of the attached pendulum can be seen below in figure 4.7. From the figure, the pendulum is shown attached to a platform, which then connects at two points to the housing. The first housing direct attachment (appendix B - part D1), fully clamps onto structure by means of the pre-sunk holes on the housing fixture. The other housing attachment cannot follow this configuration, as it would overconstrain the

housing by means of the platform that connects the two. Instead, the hole is made slightly larger than the diameter of the housing (appendix B - part D2) to fit around it. It then uses a series of nylon set screws are then used to clamp it onto the other end of the housing. This allows pendulum attachment, but does not over-constrain the two ends.

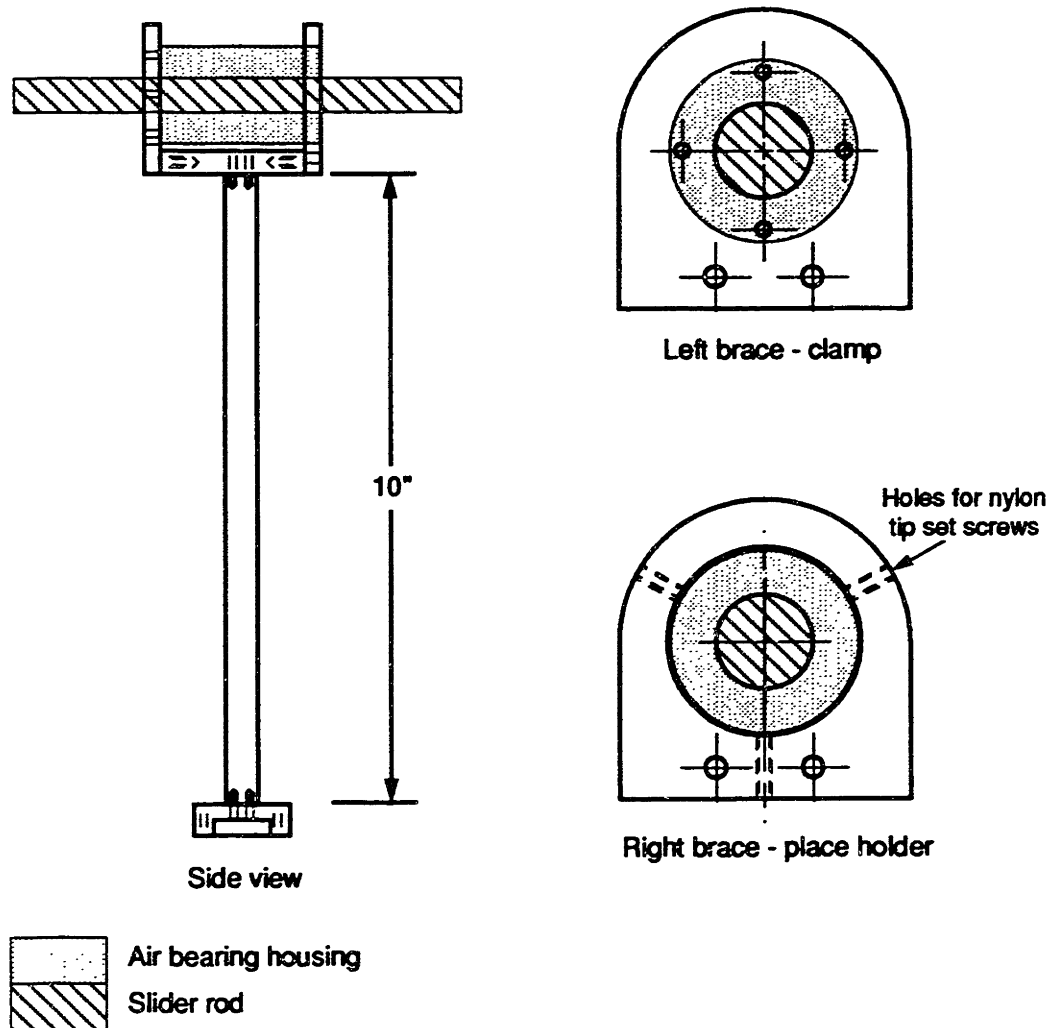


Figure 4.10: Pendulum attachment.

4.4 Laser Position Transducer

The prototype for the MOB system requires accurate control for its two degrees of freedom of motion. As part of such a control system, a set of sensors are required to

detect the displacements. The first sensor required is that for the scanning motion of the actuator. The basic requirements for the scanning motion sensor is that it be able to cover the full scanning range of about 1 cm, and be of the non-contacting variety. It must also allow motion in the transverse degree-of-freedom. Furthermore, as high of a degree accuracy as possible is desirable within a reasonable cost. Ideally, for the requirements of a complete six degree-of-freedom MOB system, optical quality resolution (on the order of a fraction of the smallest detected wavelength) is required. Finally, the scanning measurement system must be able to detect displacement at a rate sufficient to allow accurate 2 Hz actuator scans.

An HP (Hewlett Packard) 5527B Laser Position Transducer is used for this purpose. All of the requirements are met inherently with this system. The choice is simplified in part because Lincoln Laboratory's Control System Group already has one of these devices, which was available for this project. Normally, such a measurement device would have been well beyond the financial means of this project, but turned out here to be a nice luxury to have at the project's disposal. The HP 5527B Laser Position Transducer System is a laser interferometer. It comprises a set of optical and electrical components that use the interference patterns of laser light waves to make very precise displacement measurements. It consists of three basic subsystems: the laser head, the optics, and the electronics. Used together, these subsystems combine to form an advanced Michelson interferometer. The laser head supplies an essentially monochromatic light source, the optics direct the laser beam and generate interference, and the electronics detect the light and dark interference fringes, process the data, and provide an analog output voltage (through some in-house modifications) proportional to the displacement changes detected. The positioning of the various components can be seen in figure 4.1, showing the layout of these components on the EVIS table.

In the HP 5527B system, a Helium-Neon laser (low power), emits a coherent light beam composed of two optical frequencies, f_1 and f_2 , that differ in frequency by about

2 MHz. Part of the beam is used for a reference signal, while most of the rest of the beam exits the laser head and is used in the interferometer array. The interferometer reflects one frequency to the reference cube corners and transmits the other directly to the reflector. The transmitted beams are reflected back to the interferometer where it is recombined with the reference frequency and sent to the receiver. Relative motion between the interferometer and the mirror reflector causes a Doppler shift in the difference frequency measured by the receiver. The Doppler-modulated difference frequency, $f_2 - f_1 \pm \Delta f_1$, is amplified to become the ultimate measurement signal. The electronics then take the reference and measurement signals, process them, and yield the change in position.

Some of the limitations on the system should be noted. First of all, not really a limitation, but more so an important consideration, is that the laser position transducer looks at relative changes in displacement, rather than on an absolute scale. This means that every time the system is up and running, a zero-displacement must be set or defined as a relative point. This is done in the software developed for the control (Appendix A). Another consideration is the measurement precision. The digital word representing the signal is produced in a 32 bit format. For plane mirror optics, the least resolvable bit corresponds to $\lambda/128$. In the helium-neon laser, $\lambda = 632.991372$ nm, so that the maximum range based on full use of the bits is 21.2 meters. Initially, this seems like an ample amount of range for the device. However, the GPIO format for the digital word is used, which is first of all incompatible with the PC used, and secondly, and more importantly, is available at much too slow of a data transfer rate. A card could have been specially purchased to read the information directly to the PC eliminating these concerns, however, the card was on the expensive side. Fortunately, the basic system had been modified by Ed Corbett of Group 76 a number of years earlier to allow for direct, in box D/A conversion of the bits desired. This conversion however is limited to 12 bits, creating a trade-off between range desired and resolution capability.

In order to cover the full range of motion adequately, bits 11 to 22 were accessed instead of starting with the lowest bit 0. This yielded a range of values from 2.07 cm maximum, with 5 μ m resolution (1 in 4096). The accuracy however is reduced slightly later down the line with the A/D input board chosen (to be discussed later). Hence, while control can be tested, optical quality resolution can not be tested with the prototype without the purchase of the interface card for the PC.

4.5 Capacitive Probe and Board

The other type of measurement device is used to detect changes in the small gap. The basic requirements for the small gap sensor is that it be able to cover the full gap range of about $\pm 50 \mu\text{m}$ (2 mils), and be of the non-contacting variety. Furthermore, a high degree of resolution is desired within a reasonable cost. The resolution requirements are not as tight as the scanning motion however. In the full MOB system, recall that the small displacements map to the overall motions of in plane mirror displacement and roll. While it is desirable to keep these to a minimum, changes in these overall MOB system degrees of freedom would result in changes that are less critical to optical quality parameters. The update rate requirements are much higher though over this small gap. Magnetic bearings are typically stabilized at approximately the rate of 100 Hz for crossover, so the digital sampling rate should be at least ten times this figure, i.e., 1000 Hz.

An ADE Technologies Series 2000 Microsense Probe coupled with their 3600 Gaging Board was the measurement device of choice. All of the requirements specified are met with this system. The choice, as with the laser position transducer, was simplified in part because Lincoln Laboratory already had one of these devices, which was available for use in this project. The probe is of the capacitive-type. It is used in conjunction with the board to make dimensional measurements. The system is based on

the principle that capacitance varies with the distance between two conductive plates. The tip of the probe incorporates a sensor plate that is positioned directly above the target surface. The sensor and target surface may be thought of as two plates of a capacitor. The air gap between the two acts as the capacitor dielectric. The driver portion of the electronics supplies proper excitation to the sensor, setting up the electric field between the target and the sensor. The measurement will vary with the capacitance of the tip/target combination, which, in turn, is a direct function of tip-to-target separation. Therefore, when the voltage applied to the sensor is monitored, remote electronics can accurately determine the distance between the tip and the target.

In order to quickly review the concepts involved in the basic capacitive transduction method, the theory will be described assuming that the target is flat, conductive, and grounded to the instrument electronics. Placing a flat plate sensor in close proximity to such a target effectively creates a parallel plate capacitor. The capacitance is then described by the following equation:

$$C = \frac{K \times E_0 \times A}{d}. \quad (4.1)$$

Here the constants are defined as follows: C is the capacitance of the sensor/target combination, K is the relative dielectric constant of the medium between the plates, E_0 is the permittivity of free space, A is the plate area, and d is the distance between the plates. Hence a change in the distance d will be reflected inversely in the capacitance.

The 3600 board serves as an interface to the computer. First, the board serves to excite the probe for the measurement cycle. Second, the board generates displacement data in computer format based on the probe signal generated and read. This numerical representation of the distance can be accessed by a register level program. The coded displacement lends itself to a digital position measurement. The target must be ground flat in order to insure accurate measurements over the small gap. The probe used can be set to a maximum operating range of $\pm 500 \mu\text{m}$ (± 20 mils) and a minimum one of ± 50

μm (± 2 mils). Given this range, the measurement resolution, based on the minimum 12 bit conversion size, is $0.25 \mu\text{m}$ ($10.0 \mu\text{inch}$) for the largest, and 25 nm ($1.0 \mu\text{inch}$) for the smallest (1 in 4096). The sampling/driving rate is about 15 kHz, which is plenty adequate for the above stated specifications.

4.6 Control System Electronics and Software

As was introduced in the first section of this chapter, the computer with its associated boards is at the heart of the digital control system. Because of the computer's central role, several of its associated characteristics and components require examination. The computer itself was built up from a PC 486/66 motherboard. The architecture of the motherboard allowed for several expansion slots, three of which contained boards critical to the control systems. The first was discussed in the last section; the board affiliated with the capacitive probe. The other two slots were occupied by National Instruments A/D and D/A boards. The operating environment for the system was DOS version 5.00, and the control program was primarily written in Microsoft C version 7.

4.6.1 A/D and D/A boards

The National Instruments AT-MIO-16 Multifunction I/O Board for the PC AT was chosen to read the analog signals in from the laser position transducer. Ideally, since the output of the laser position transducer is converted internally by a 12 bit D/A converter, a following A/D converter should have at least one more bit than this in order to pick up the full resolution. To have a 12 bit A/D converter, which was a common format at the time of this study, would insure a bit loss in this awkward, double signal

conversion. Unfortunately, the project was limited by resources, which dictated that an already available 12 bit A/D board be used.

The relevant specifications on the board are as follows. The number of possible input channels is eight. Spread over these 8 channels, a maximum sampling rate of 100,000 cycles/second is available, which is quite ample for the scanning loop. This board was also particularly useful for the timing chip it came with, which was eventually used to clock the loop rate. The timers are 16 bit, and the available clock rates are 1 MHz, 100 kHz, 10 kHz, 1 kHz, and 100 Hz. The anticipated clock rates are, recall, a little higher than 1 kHz, so that the middle sampling range of 1 kHz can be altered slightly in the software to obtain several divisions of 10 kHz in this range.

The National Instruments AT-AO-6/10 Expansion Board for the PC AT/EISA was chosen as the D/A board to output the analog signals from the control program to the two amplifiers. Since the amplifier (described next section) is fully analog, the output resolution is only limited by the capability of the analog output from the board. Given the 12 bit restrictions from both the capacitive probe and A/D board, analog output resolution from this board would be wasted if more than twelve bits were specified. As with much of the other equipment used in the project, the decision was already made for the type of board to use, as this National Instruments board was already available.

The relevant specifications of the board are as follows. Six output channels are available on the board (two of which are actually used). The maximum output rate, based on a settling time to 0.5 LSB (least significant bit), for a 10 V step is 200,000 steps per second. As with the input board, the rate on the output board is also very heavily dependent on the software and computer rate. The noise from the board is 1 mV rms, dc level, up to 1 MHz.

One big advantage to having both the A/D and D/A board produced by the same manufacturer is the compatibility between the driving software. First of all, while both boards are accessible for programming at the register level, National Instruments

provides the NI-DAQ Driver software, which is a company custom product to directly control the boards through higher level languages, such as C, Basic, or Pascal. The NI-DAQ has an extensive library of functions that can be called from these application programming environments. These functions include the routines for analog input and output, counter and timer operation, self-calibration, initialization, and error and board status messaging. These functions are used extensively throughout the control program, which is described in the next sub-section.

4.6.2 Computer environment and affiliated software

At the crux of any digital control loop is the processor employed. The speed of the processor is what ultimately limits the speed of the control system. Only in recent years has the speed of digital processors been brought up to a level where they can be implemented in magnetic bearing control. In Trumper's work on precision suspension techniques [Trumper 1990] the use of digital control in one of his early suspension attempts yielded less than desirable results due to insufficient sampling rates. Because the interactions between boards, computer, environment, and software ultimately determine the maximum operating speed of the control loop, it is difficult to quantify beforehand how fast the loop can be made to go. Only through projects with similar technologies [Olson 1994] could the speed be roughly estimated beforehand. Olson's project, which suspended a bearing in one degree of freedom, which used a PC 486/50 and the same output board and capacitive probe (literally), was able to achieve a loop rate of 4000 Hz. Desiring to keep in this ballpark range, keeping in mind that two loops had to be run instead of just one, a 486/66 was used as the operating environment. As with Olson's project, the computer runs under a DOS environment, which requires less processor power than its more recent counterpart Windows, and uses a C Program to

execute the control code. The eventual measured maximum rate is 3.6 kHz for one loop and 1.42 kHz for two, which matches the empirical estimate very well.

The control program itself, listed in full in appendix A, is what was used to control both of the loops. The heart of the program is the actual control routine, which is described in full in the control systems chapter. Although the control portion is the most critical aspect of the program, it only takes up a small amount of the full coding. The different routines used in setting up the program and looking at the data, are therefore mentioned briefly here. The first part of the program defines a wide range of variables, many of which are specific to the various boards employed. The headers for various functions, such as the NI-DAQ function and graphing functions are also included. The first function, `board_setup()`, is used to initialize the A/D, D/A, and ADE boards and to check their status. The next function, `calibration()`, is used, when necessary, to calibrate the input signals read proportional to the two read displacements. Both displacements are calibrated against actual micrometers. Note that the laser position transducer must also have a zero-position set to use in subsequent readings. From taking measurements at two points for both displacements and checking the computer readings against the micrometers, zero-points can be calibrated as well as numerical factors to transfer actual readings into displacements with real units (mils). These factors may then be stored as variables in the program, used in the actual control and measurement loops. The `user_inputs()` function takes in prompts from the user, for such variables as loop size, clock rates, and controller gains. The `clock_setup()` function uses the basic clocks available on the A/D and breaks them into usable rates, such as the ultimate rate of 200 Hz. The `controller()` function, is the control of the boards, discussed later. The `graphit_em()` and `graphit_ed()` functions will quickly plot the measured data, if desired, to see whether it is useful, or possibly junk. The last few functions are used to save the data, and reinitialize the boards from their last commanded state. A final function, not accessed in the main loop, but repeatedly used in the above functions, is the control

function for the ADE board. Per manufacturer's instructions, it must be coded to access the ADE functions through the register level.

4.7 Amplifier Design

Once the signals have been processed by the computer and its affiliated boards, the output voltages must then be controlled from the low-signal levels to ones that have enough power to run the two sets of coils. Because the electromagnetic and electrodynamic coils have different resistance and inductance, which must be compensated uniquely for each coil, two separate amplifier circuits are employed in the signal output phase of the system. The main component that amplifies the signal in both circuits is the aforementioned 300 W Crown Amplifier. This is a ruggedized DC-coupled stereo amplifier, adapted from Crown's audio amplifier line. A variety of surrounding circuitry is then attached to this amplifier to yield desirable signal transfer characteristics. This system serves as a transductance or "current" amplifier, in that it converts an input voltage into a proportional coil current. The operation of this local feedback loop is described as follows.

The circuit diagrams for these amplifiers are given in figures 4.12 and 4.13. The general loop characteristics can be seen by the simplified amplifier control loop of figure 4.11 below, applicable to either circuit. First, the incoming voltage command from the computer sees a large resistor, yielding a very small feed signal. Before entering the Crown amplifier, the signal is fed into an op-amp, which carries a resistance and capacitance around it. This component is here to compensate for coil effects on the transmission, seen later in the forward path. After the Crown amplifier come the actual coils. After the coils, the signal is split between a current sensor and a feedback path to complete the loop.

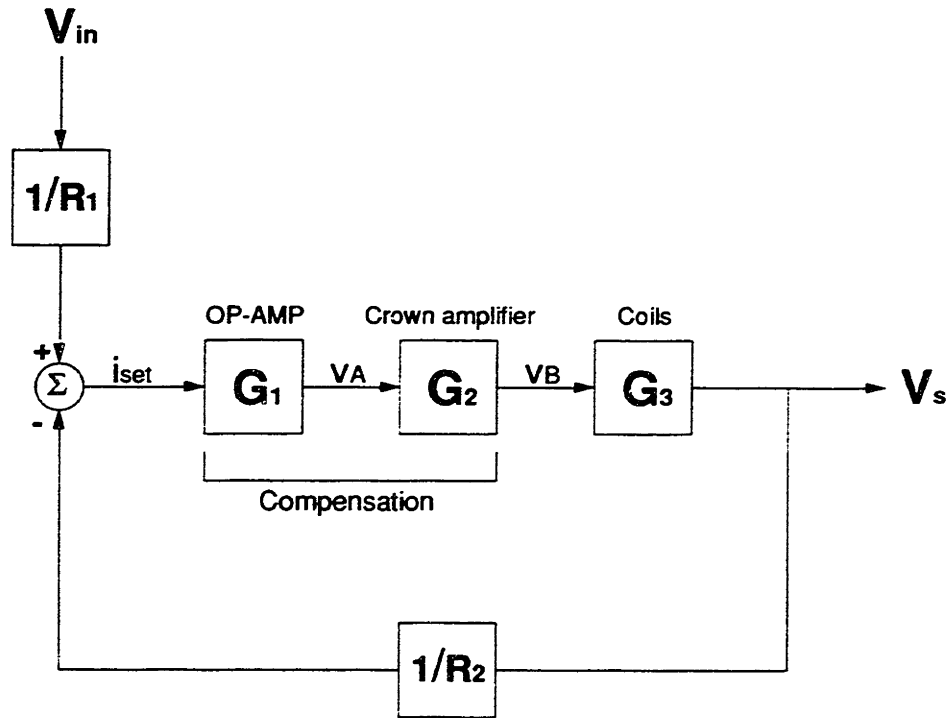


Figure 4.11: General amplifier control loop block diagram.

The actual circuit implementations of the two amplifier loops are given in figures 4.11 and 4.12. Before discussing the hardware details of each design, the mapping and mathematical implications of these components in the control loop needs to be discussed. From the loop block diagram, the following transmission characteristics are as specified. First, G_1 , from the op-amp is given simply by

$$G_1 = \frac{v_A}{i_{set}} = -\left(R_3 + \frac{1}{C_S}\right). \quad (4.2)$$

The next term seen in the forward path is from the amplifier, which is given by

$$G_2 = \frac{v_B}{v_A} = A. \quad (4.3)$$

This value for A was adjusted experimentally to be about 20. The final value in the forward path, seen from the sensor resistor, is based on a voltage divider,

$$G_3 = \frac{v_s}{v_B} = \frac{R_s}{L_c s + R_c + R_s}. \quad (4.4)$$

Based on these three terms, the forward path is therefore given by

$$F.P. = - \left(\frac{AR_s / C}{R_s + R_c} \right) \left(\frac{R_3 C s + 1}{s \left[\left(\frac{L}{R_c + R_s} \right) s + 1 \right]} \right). \quad (4.5)$$

This may at first seem like an unwieldy equation. However, by making the following simple condition,

$$R_3 C = \frac{L_c}{R_c + R_s}. \quad (4.6)$$

Equation 4.5 simplifies to the following expression

$$F.P. = G = \frac{V_s}{i_{set}} = - \frac{AR_s}{(R_s + R_c)CS}. \quad (4.7)$$

The usefulness of this substitution will be explained shortly.

Outside of the forward path lie two resistors. The first, as previously mentioned, is used to take the input voltage and make a usable current for control. In order to match this type of input into the system, the voltage seen at the output must be converted back into a current to complete the control loop, hence a resistor is also found in the feedback path. This yields the block with gain $1/R_2$. Using Black's formula, the overall closed-loop transfer function, from the input v_{ref} to the output current i_c is

$$T.F. = \frac{i_c}{v_{ref}} = - \frac{\frac{A}{R_1(R_s + R_c)C}}{s + \frac{AR_s}{R_2(R_s + R_c)C}}. \quad (4.8)$$

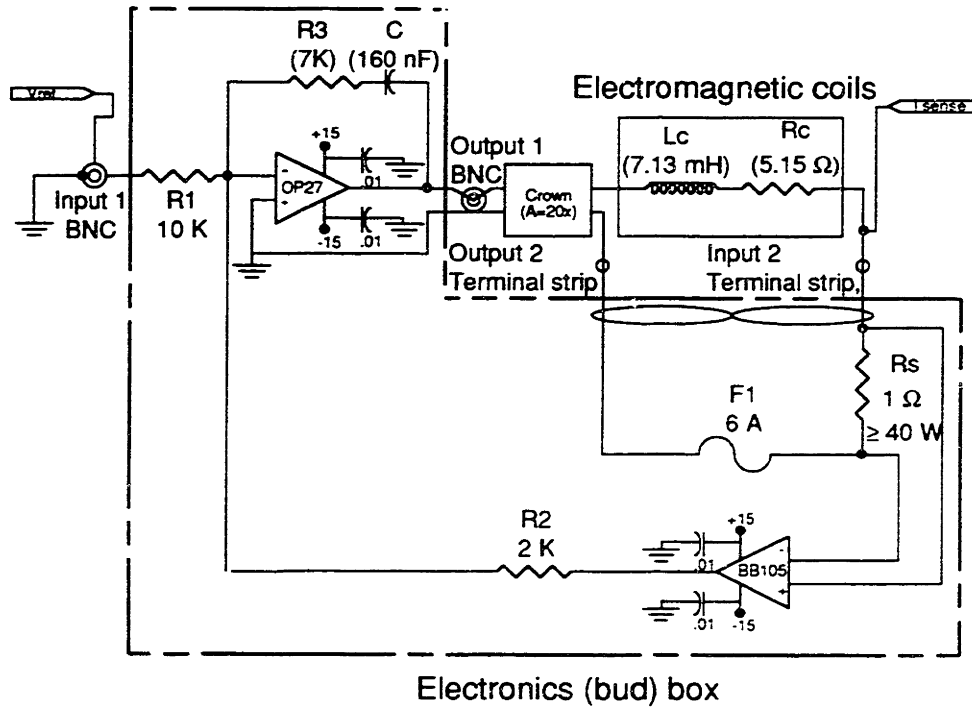


Figure 4.12: Electromagnetic coil amplifier control loop.

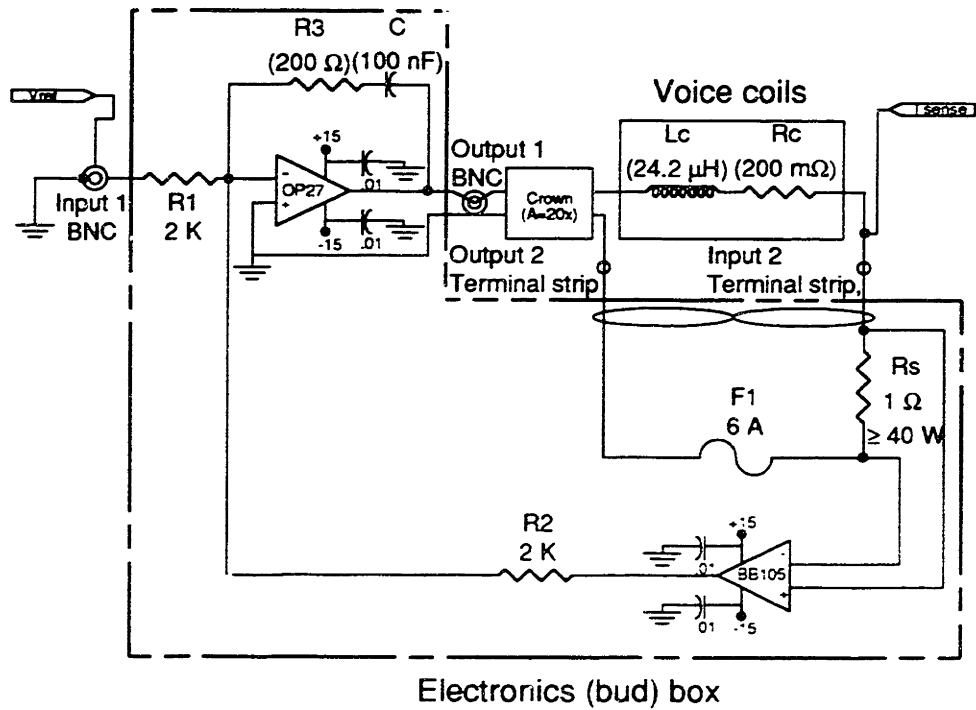


Figure 4.13: Electrodynamic coil amplifier control loop.

In steady-state this reduces to

$$T.F._{ss} = -\frac{R_2}{R_1 R_5} \quad (4.9)$$

The corner frequency is given by

$$\omega_c = \frac{AR_5}{R_2(R_5 + R_c)C} \quad (4.10)$$

By making the substitution of equation 4.6, the closed loop transfer function characteristics can be made nearly independent of the coil parameters. Equation 4.6 sets the feedback path around the op-amp to do this compensation, so that the combination of R_3C is set to equal the time constant of the coil. This substitution still leaves some of the parameters open. A way to reduce the number of choices is to set R_2 at one fifth the value of R_1 . This insures that in steady-state, with an R_5 equal to 1 Ω , that the maximum input voltage of 10 volts will lead to a maximum current of 2 amps as an example.

After specifying the 1/5 criterion, and an R_5 of 1 Ω (so that 1 A is sensed as 1 V), C and R_3 can be solved explicitly by setting a desired crossover frequency of 10,000 Hz. First, from equation 4.10, C is solved for,

$$C = \frac{AR_5}{R_2(R_5 + R_c)\omega_c} \quad (4.11)$$

Secondly, by substituting this result into equation 4.6,

$$R_3 = \frac{L_c R_2 \omega_c}{AR_5} \quad (4.12)$$

The actual implementations of the two loops can be seen in the aforementioned figures 4.11 and 4.12. Again, the loops differ (excluding the coils) only in the choice of R_3C used for coil compensation. Hence, the hardware implementation for the

electromagnetic circuit will be discussed first, and then differences in the second circuit can be briefly addressed. The circuitry is implemented on a wire-wrapped board. The unit is then contained in an aluminum chassis for protection. Besides the basic circuitry, this box also contains the power supply for the op-amps employed. Following the loop from the left hand side, the input from the computer D/A board enters through a BNC cable. An OP27 op-amp is used with the required compensation resistor and capacitor. Note the decoupling capacitors and resistors used between the power source and the op-amp. This is to reject any high-frequency noise from the power supply, and to provide a low-impedance voltage source at the op-amp power input pins. BNC connections then come out of the box to feed the signal into the Crown amplifier. This is then fed to the coil, which is series with the sensor resistor. Note the high power requirement on the sensing resistor, since the current may reach the value of several amps. Additionally, a 6 amp Slo-Blo fuse is in series with the coil, to prevent damage to the actuator in the event of an amplifier failure. The voltage from the R_S is then picked off by means of a BB105 op-amp, rigged in a standard differential amplifier (voltage follower) configuration. By means of the feedback resistor, the current signal is then returned to close the loop. The loop for the electrodynamic coils differs in its R_3C compensation values, and smaller current and hence resistor power and fuse requirements on the returning current to the amp. The disparity in current between the two loops is due to the fact that the electromagnetic coils require large currents should if the platen is displaced far off-center.

Chapter 5

Control System

Control systems are found in a variety of applications in the MOB design. They have already been used in the closed loop amplifier feedback design to insure reasonable cutoff frequencies. More importantly, digital implementations of control loops are used to control the transverse motion of the platen as well its scanning motion. The control of the first of these two motions is particularly challenging, since the system is open-loop unstable in this axis, as was demonstrated in chapter 3. The present chapter starts by stating the control system objective for the two controlled motions, proceeds onto discussing their continuous control schemes, and presents a detailed physical model of the stabilized transverse direction using the simulation language Simulink. The last section explains the final implementation of the model.

5.1 Objectives

An unstable pole is commonly present in hybrid magnetic bearing systems. Many non-hybrid magnetic bearing systems of a similar nature to the one described herein utilize a lead compensator in one form or another to insure stabilization, as presented in [Trumper 1990], [Roberge 1975], [Olson 1994]. It will be shown in the subsequent section how such a lead compensator was applied to the transverse control. Such a controller is also well suited to the scanning motion, but primarily due to lack of time at the end of the project, simple proportional plus integral (PI) control was applied on the actual prototype.

The objectives of the control system may be summarized as follows. First and foremost in importance is achieving robust stabilization. Secondly, zero steady state error is important. If the mirror relies on the bearings to make corrections, then over some time the bearing must meet the exact corrections specified. Third, a fast settling time is desirable. The quicker corrections can be made, the better the system will be able to follow the command signals. Fourth, good disturbance rejection is desirable, to insure a isolation from external jitter. The quantitative design objectives are crossover at 200 Hz for the transverse motion, and 50 Hz for the scanning motion. The former number is based on the location of the unstable pole in the first case, as will be discussed later. The latter is based on desired tracking bandwidth capability. With these basic specifications in mind, the control systems may now be developed.

5.2 Control System Development

Though many of the same principles and parameters can be seen in the electromagnetic versus electrodynamic control system behavior, each one must be developed separately. Because transverse suspension was obtained, as is necessary before scanning travel can be pursued, it will be presented and developed in full. Due to the aforementioned lack of time, scanning motion was only nominally tested and is not fully developed. Before the discussion of both directions begin, a quick recall of the relevant equations and parameters is in order, and is presented in the next subsection.

5.2.1 System parameters

So far, all the relevant system equations have been presented in terms of key system variables. To design a specific control system though, all the relevant numbers (and

equations) must be known. Recall first the control equations. For the electromagnetic coils the centered, linearized equation from equation 3.111 is,

$$\frac{X}{I} = \frac{-D_i}{s^2 - \omega_k^2}. \quad (5.1)$$

Where the gain term and poles are found to be,

$$D_i = \frac{\mu_0 dt N M_0 n l}{mg(h+l+ng)} \quad (5.2)$$

$$\omega_k = \pm \frac{M_0 n l}{(h+l+ng)} \sqrt{\frac{2\mu_0 dt}{mg}}. \quad (5.3)$$

For the voice coils, the equations at the centered point are linear in the state variables. The relevant control equation is based on what was developed in equation 3.91, and is restated here,

$$\frac{Z}{I} = \frac{E_i}{s^2}. \quad (5.4)$$

Where the gain term is found to be,

$$E_i = \frac{2\mu_0 M I N \bar{c}}{m(h+l+ng)}. \quad (5.5)$$

Note that this is what is expected from the control of a free body, based on the uncoupling assumptions, and holds true theoretically for the scanning motion. A new parameter is introduced as equation 5.5 is re-written in terms of number of windings and current. The parameter is \bar{c} , and it is a measure of the transverse length of the top and bottom of the voice coil. This length is important because it represents the length of the voice coil that is exposed to the permanent magnets and is therefore useful to do work via the Lorentz Force.

So far it has been okay to leave the equations expressed in terms of their critical variables. However, to actually implement a real control system, a reasonable

approximation of these parameters is necessary and will now be presented. Some of the numbers here have been seen before, particularly in the last chapter where the specifics of the hardware were presented. Others are presented below for the first time. They reflect as close as possible the actual key predicted parameter values of the system.

Table 5.1: General control parameters.

| Parameter: | Value: |
|-------------------|--|
| \bar{c} | 9.17 cm |
| d | 1.27 cm |
| g | 2 mm |
| h | 6.35 mm |
| l | 6.35 mm |
| m | 0.5 kg |
| M_0 | 6.84×10^5 A/M |
| n | 3 |
| t | 1.27 cm |
| μ_0 | $4\pi \times 10^{-7}$ N/A ² |

The derivation of a mass to use warrants a brief explanation, particularly in terms of the electromagnetic control. The platen, due to the nature of the setup of the prototype, is not really a free mass because it is attached to the pendulum structure. The mass is really an effective mass, based on this body's moment of inertia, and is given by,

$$m = \frac{I_{tot}}{r_{eff}^2}. \quad (5.6)$$

Where I_{tot} is the total pendulum moment of inertia and r_{eff} is the radius from the center of the air bearing to the center of the platen. The design was chosen so that the effects of the pendulum would be minimal, and for the platen to approach the conditions of a free body in its two free d.o.f.s as closely as possible. Because they are near the center of rotation, the added moments of inertia of the pendulum and the air bearing cylindrical

housing are small compared to that of the platen itself. This leaves the effective mass to be about equal to that of the platen by itself.

5.2.2 Continuous electromagnetic model and control

A lead compensator in the feedback path is the first control element added to stabilize the system. PI control is then added on later to fine tune the controller and to insure a zero steady state error and good disturbance rejection. The overall setup of this loop is shown in the block diagram below.

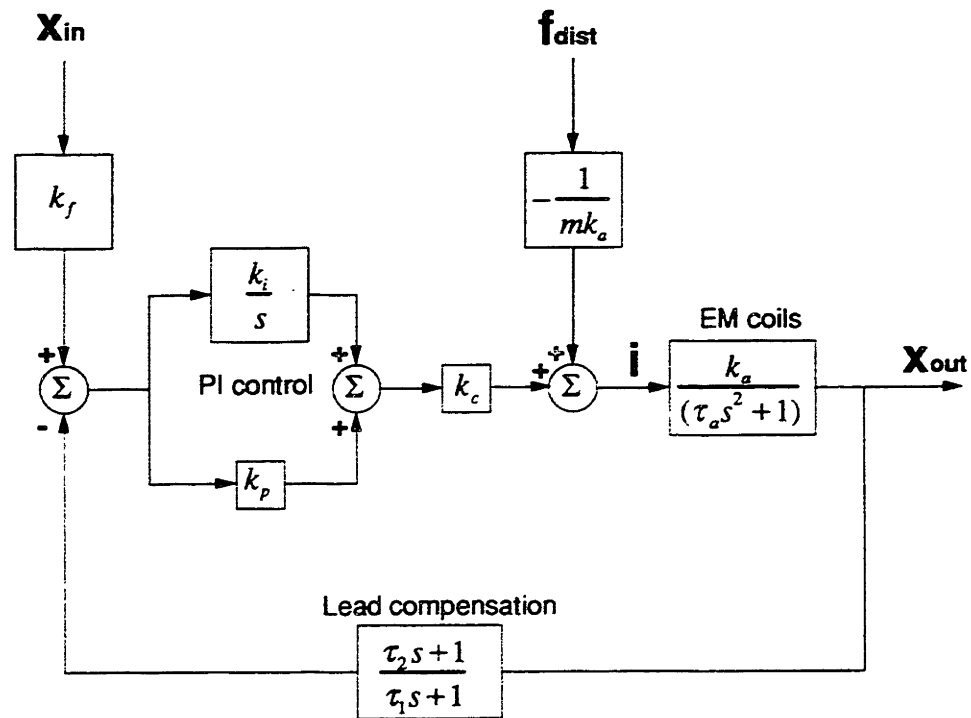


Figure 5.1: EM general block diagram.

Lead compensator

As mentioned at the beginning of the chapter, the addition of a lead compensator to the system is the first step in creating a stabilizing controller. The lead compensator transfer function is,

$$H_l(s) = k_c \frac{(\tau_2 s + 1)}{(\tau_1 s + 1)}. \quad (5.7)$$

The crossover frequency for a lead compensator to give maximum phase increase is given by the geometric mean of the breakpoint frequencies, i.e.,

$$\omega_m = \sqrt{\frac{1}{\tau_1} \frac{1}{\tau_2}}. \quad (5.8)$$

By specifying how much phase margin is desirable to add at crossover, the ratio between the time constants can be stated in terms of

$$\alpha = \frac{\tau_2}{\tau_1}. \quad (5.9)$$

For the electromagnetic coils, the 200 Hz crossover was chosen, and a maximum phase margin was desired of about 60°, which corresponds to an α of 15 [Van de Vegte 1990]. This is all the information needed to specify the time constants of the lead compensator. In order to find the proper lead gain term, the open loop lead compensator plus coil transfer function must be forced to unity at crossover. With $k_i = 0$, the negative of the loop transmission is,

$$-L_o T_o = k_c \frac{(\tau_2 s + 1)}{(\tau_1 s + 1)} \frac{k_p k_a}{(\tau_a s^2 + 1)}. \quad (5.10)$$

Note that the basic transfer function of the uncompensated body (the last term) has been re-written in bode format, in terms of gain k_a and time constant τ_a . The specific values

for the development follow in the table below. The first column is what is predicted by the two-dimensional modeling. The second column is what value was measured from the actual tests, which are described later.

Table 5.2: Electromagnetic lead compensator and system parameters.

| Parameter: | Theoretical value: | Estimated value: |
|-------------------|-------------------------------------|-----------------------------------|
| k_a | $-0.414 \times 10^{-3} \text{ m/A}$ | $-1.7 \times 10^{-3} \text{ m/A}$ |
| τ_a | $5.10 \times 10^{-6} \text{ s}^2$ | $5.1 \times 10^{-6} \text{ s}^2$ |
| k_c | -5.64×10^3 | -1.3×10^3 |
| τ_2 | $3.08 \times 10^{-3} \text{ s}$ | $3.1 \times 10^{-3} \text{ s}$ |
| τ_1 | $205 \times 10^{-6} \text{ s}$ | $210 \times 10^{-6} \text{ s}$ |
| k_p | 1 | 0.8 |
| k_f | 0.572 | 0.45 |

The effects of using just a lead compensator in this scenario are shown in the bode plots of the loop transmission transfer function below.

Several projects using magnetic bearings have argued for placing the lead compensator in the feedback path rather than traditional placement in the forward one [Trumper, 1990], [Olson 1994]. Rather than repeat the full derivation of why this is true, the advantages of this will just be briefly mentioned. In summary, by putting the lead compensator in the feedback path, the closed loop zero is now based on the lead compensator's pole instead of the compensator's zero, as is the case if the compensator is in the forward path. Since the lead's pole is farther out away from the origin than its zero (by α), its effect as a system zero is less prevalent than the lead's zero would have been. In practice, this leads to a system with the same rise time, but reduced control effort and overshoot. This can be seen in the step response of the displacement and current in the figures that follows.

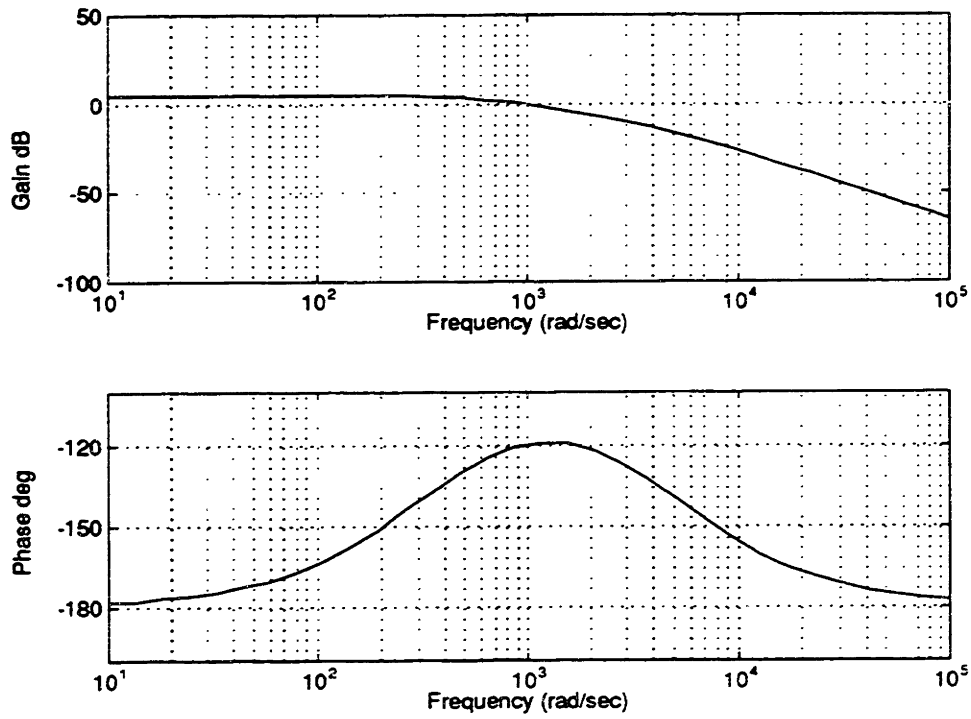


Figure 5.2: Bode of lead compensated electromagnetic coils.

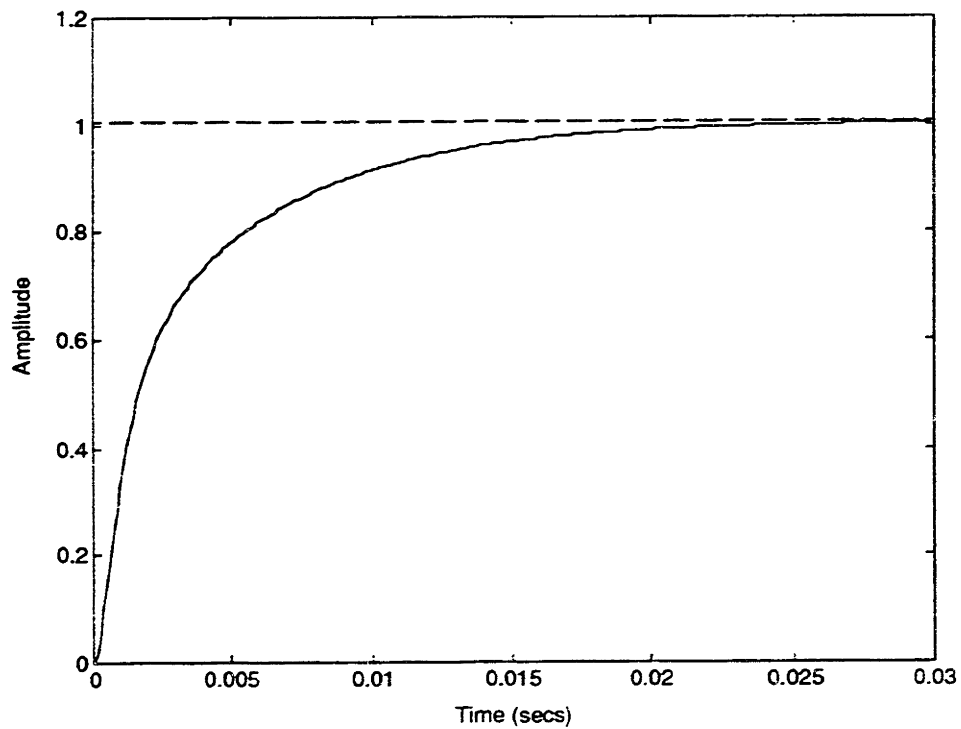


Figure 5.3: Displacement step of lead compensated EM coils.

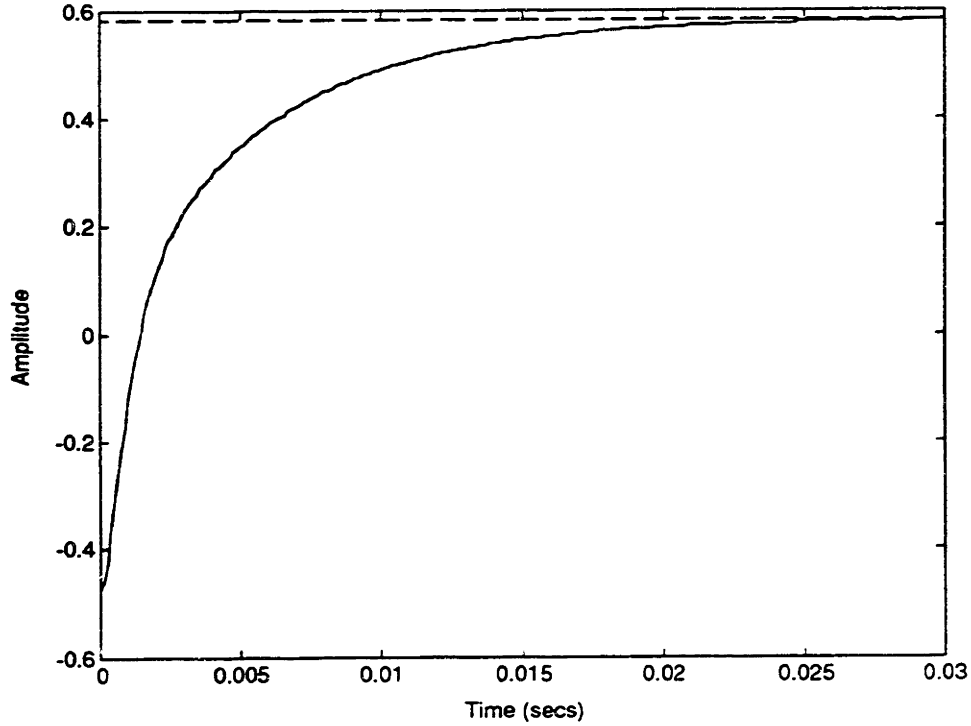


Figure 5.4: Current step of lead compensated EM coils.

PI control

As mentioned at the beginning of the chapter, the addition of a PI controller is desirable to insure zero steady state error and provide better low-frequency disturbance rejection. The additional PI compensator is given by the formula,

$$PI \text{ compensator} = \frac{k_i \left(\frac{k_p}{k_i} s + 1 \right)}{s}. \quad (5.11)$$

The open loop transfer then looks like, including the lead compensator,

$$o.l.t.f. = \frac{k_i k_c k_a \left(\frac{k_p}{k_i} s + 1 \right) (\tau_2 s + 1)}{s (\tau_1 s + 1) (\tau_a s^2 + 1)}. \quad (5.12)$$

The specific values for the PI control follow in the table below. They are chosen to yield a quick settling time without adding too much reduction of phase margin. These parameters are later adjusted on the basis of experimental results.

Table 5.3: Electromagnetic PI compensator parameters.

| Parameter: | Estimated value: |
|------------|------------------|
| k_p | .55 |
| k_i | 130 |
| k_f | 1 |

The effects on the open-loop bode plots can be seen in the figure below. The integrator insures good disturbance rejection.

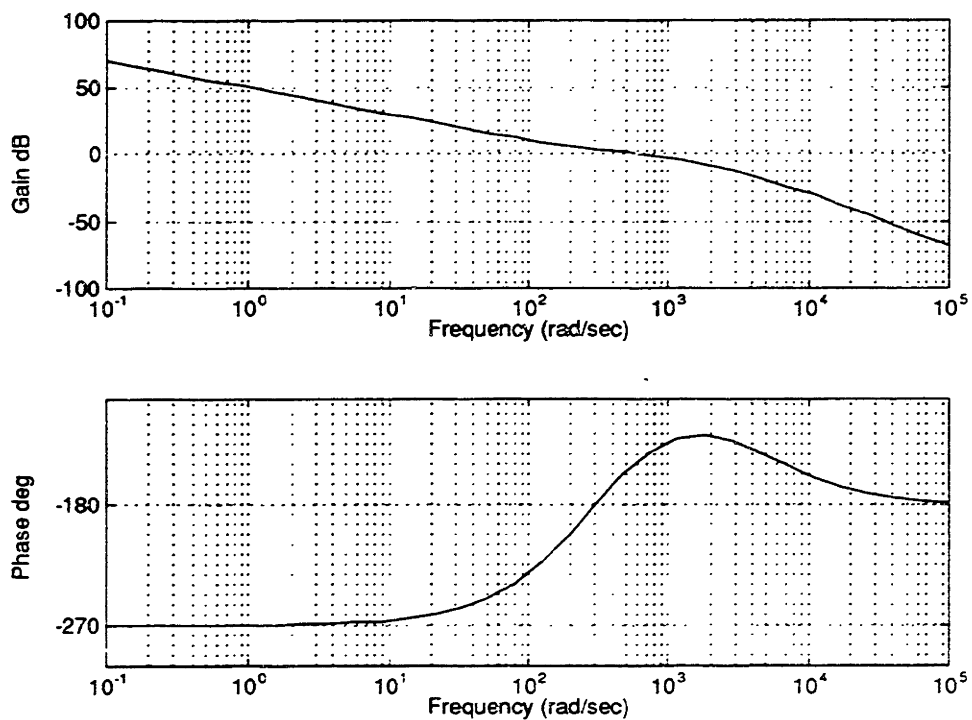


Figure 5.5: Bode of lead and PI compensated electromagnetic coils.

Of course, the addition of this integrator also has an effect on the step response, of both the current and the displacement, as is evident from the figures that follow. In order to fully understand all the implications of the two different types of compensation, one in the forward path, and one in the feedback path, it is instrumental to examine the full closed loop transfer function, which is presently give by Black's formula

$$c.l.t.f. = \frac{k_a k_c (k_p \tau_1 s^2 + (k_p + k_i \tau_1) s + k_i)}{\tau_1 \tau_a s^4 + \tau_a s^3 + (k_a k_c k_p \tau_2 - \tau_1) s^2 + (k_a k_c (k_p + k_i \tau_2) - 1) s + k_i k_a k_c} \quad (5.13)$$

The associated closed loop bode plot can be seen below.

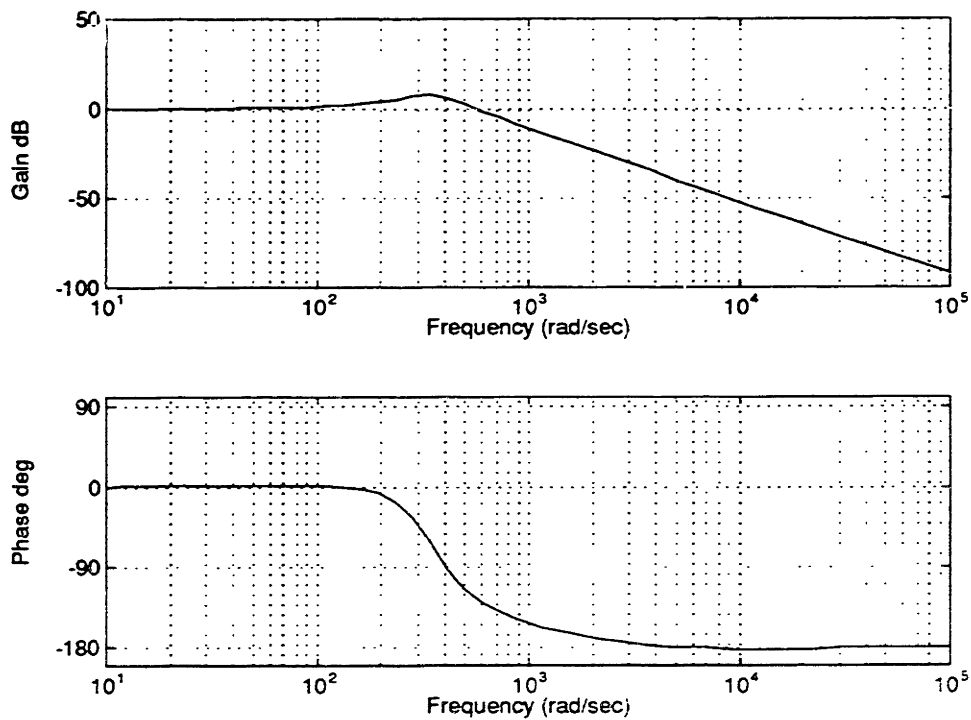


Figure 5.6: Closed loop Bode PI and lead compensated EM coils.

The current response, as was shown with just the lead compensator, is also instrumental to examine. The closed loop transfer function is very similar, and is

obtained via Black's formula by putting the plant in the feedback path. It is given by the formula

$$c.l.t.f.|_{currents} = \frac{k_c(k_p \tau_1 \tau_a s^4 + \tau_a(k_p + k_i \tau_1)s^3 + (k_i \tau_a - k_p \tau_1)s^2 - (k_p + k_i \tau_1)s - k_i)}{\tau_1 \tau_a s^4 + \tau_a s^3 + (k_a k_c k_p \tau_2 - \tau_1)s^2 + (k_a k_c(k_p + k_i \tau_2) - 1)s + k_i k_a k_c}. \quad (5.14)$$

Disturbance rejection

Another important reason for choosing the addition of the integral controller is to insure good disturbance rejection. The closed loop response in terms of just an input disturbance can be found by using the principal of superposition. By setting the input position command to zero and looking at the transfer function between outgoing position and the incoming disturbance force, the effects can be quantified. In doing so, the PI control as well as the plant effectively becomes part of the feedback path around the coil loop. The resulting closed loop control therefore yields the following, again via Black's formula.

$$c.l.t.f.|_{dist} = \frac{-\left(\frac{1}{mk_a}\right)s(\tau_1 s + 1)}{\tau_1 \tau_a s^4 + \tau_a s^3 + (k_a k_c k_p \tau_2 - \tau_1)s^2 + (k_a k_c(k_p + k_i \tau_2) - 1)s + k_i k_a k_c}. \quad (5.15)$$

The main advantage is that in steady state, the disturbance force is forced to zero because of the zero in the numerator at the origin.

5.3 Simulink Model of Electromagnetic Control

Classical continuous-time control schemes give rise to the basic design of the desired compensators. The actual design however deviates a good deal from classical analysis. There are three major reasons for this. First of all, the control is digital, and therefore appropriate digital compensation models are required which are in part

determined by the limited available sample rate. Secondly, there are nonlinearities to contend with. Most notable of these nonlinearities are the various stages of signal quantization as the signal is passed repeatedly through both a/d and d/a boards, all which have 12 bit resolution. Other nonlinear effects include system latency and current amplifier saturation levels. The final deviation from classical controls has to do with the effect that this is all experimental work, where only estimates exist for certain system parameters, as limited by the two dimensional modeling done for the analysis. The first two problems, and even to some extent the third, can be reasonably well studied in the Mathwork's control analysis package entitled Simulink.

Before describing the modeling of the nonlinearities, it is perhaps best to preface the discussion by mentioning the digital implementation of the various controllers. Because the sampling rates were adequate, and for simplicity, the continuous compensators were turned into their digital counterparts via the zero order hold method instead of starting the digital compensation design from scratch in the digital domain. First, and most simple, is the zero order hold equivalent at 2000 Hz of the integrator,

$$\frac{1}{s} \Rightarrow \left(\frac{1}{2000} \right) \frac{1}{z-1}. \quad (5.16)$$

The lead compensator has a little bit less of a direct correlation. At 2000 Hz, its zero order hold equivalent is given by,

$$\frac{-19600(s+324)}{(s+4880)} \Rightarrow \frac{-19600(z-.940)}{z-.0872}. \quad (5.17)$$

These discrete equivalents, along with the modeling of the various other nonlinearities, are shown in the Simulink diagrams which follows.

The two figures are nearly identical except in the gains associated with the PI control, as well as the use of bias versus integrators to counteract any initial offset displacement. These minor difference correspond to the types of tests that were done

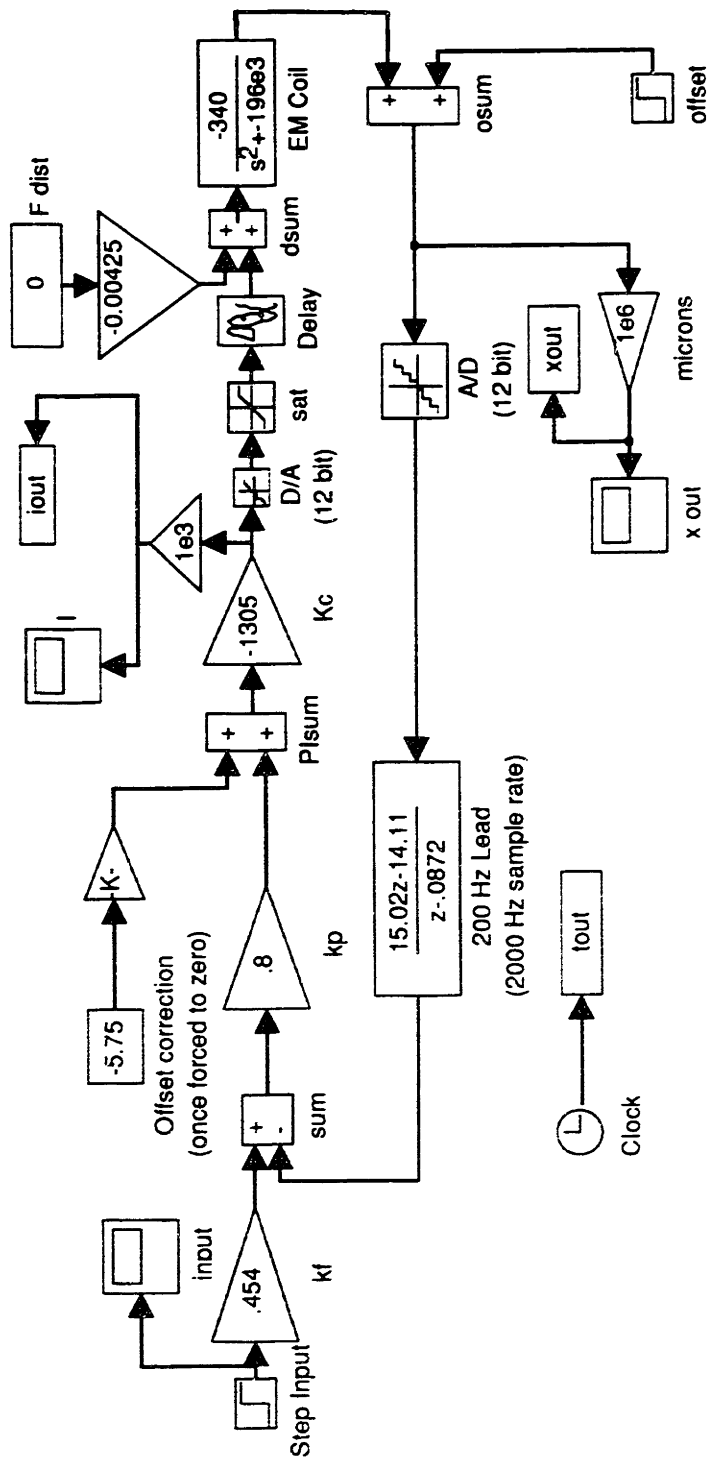


Figure 5.7: Electromagnetic proportional plus lead Simulink model.

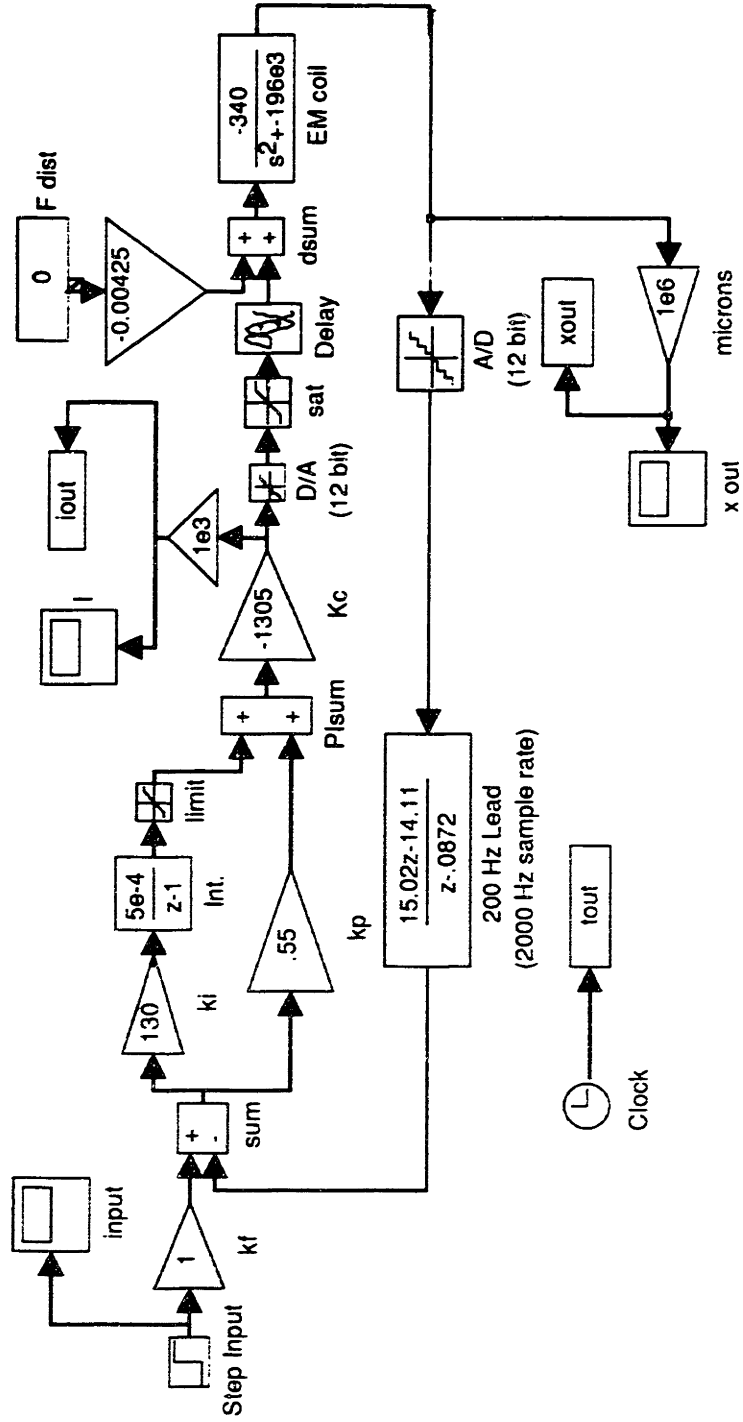


Figure 5.8: Electromagnetic PI plus lead Simulink model.

and is explained more thoroughly in the next chapter. What's important to see from these models now is what exactly is being modeled that cannot be accounted for by classical controls.

Two quantizer blocks can be seen in the model, one labeled D/A and the other A/D. The former is for the output signal from the computer in terms of a voltage which is mapped to a control current as discussed in the last chapter. The boards are 12 bit, yielding a LSB of $1/4096$ over the full range. That means that an output current of 2 amps can have a resolution of about 1 mA. Because the actual value of the LSB is directly related to the full scale range, it is important to choose the smallest LSB value that still yields an acceptable overall desired range. The latter quantizer block, seen in the feedback path, is associated with the capacitive probe measurement device and is 12 bits as well. The values of the LSB depend on the overall range of the probe, which can be set to various value ranging from 500 μm (20 mils) down to 50 μm (2 mils) with LSB values of 250 nm (10 μinches) and 25 nm (1 μinch) respectively.

The other nonlinear control blocks are added. The first is the amplifier saturation. This has a value based on the Crown amplifier, but the actual limit is a parameter that is set in the control program to prevent excessive current input, particularly if the platen should get stuck to either side. Finally, a transport delay block is added, to model how long it takes the control loop to output the voltage signal to the board after the command has been given.

The Simulink model was extremely useful in helping to determine what the actual transfer function of the electromagnetic control block by itself looked like. Recall that the equations which describe the basic transfer function are based on two dimensional estimates. Hence the unknown actual values had to be estimated by fine tuning the various control schemes.

Chapter 6

Results and Conclusions

Given the variety of time delays that were associated with the construction of the hardware, very little time was left at the end of the project to perform actual testing. Whereas the one transverse degree-of-freedom was thoroughly tested and analyzed, at the time of printing of this thesis, tests were still being performed to characterize the voice coil behavior and unfortunately are almost virtually excluded from the body of the thesis. The results of the full setup, with the voice coil, will hopefully be published in an article subsequent to the thesis itself.

Included in the following sections are two types of step response tests that were performed. The first set is by means of the lead and proportional control alone. The second set includes the addition of an integral controller, following the logic that was developed in the last chapter. The last section compares experimental results to the Simulink models, which were also discussed in the last chapter.

6.1 Tested Transverse Step Responses

As was developed in the last chapter, two type of responses, with and without the integral control, were tested. The first test is desirable to best assist in characterizing the actual transfer function of the electromagnetic coils, which was slightly different than two dimensional analysis predicted. The addition of the integrator yields a less well-damped response, but better disturbance rejection.

At this juncture, an important, recurring bias should be mentioned. In the setup, the true magnetic center seemed to be about 10 micrometers off from the physical center of

the actuators and platen combination. This is accounted for with a bias offset current, which is present in all of the tests below. In the case of just the proportional gain, the bias must be slowly injected into the system. For the case of the integrator, it is automatically accounted for. These effects will be discussed in the following subsections.

6.1.1 Straight proportional and lead control

The goal was to use the lead compensator set at the 200 Hz crossover mark and see if the system could be controlled as predicted. The proportional gain as well as the compensator could both be attenuated for a stable system. When initial test were performed, it was shown that the theoretical value for the gain of the electromagnetic transfer function underestimated the actual value. This was most likely due to the three-dimensional effects of the magnets, since more of the permanent magnet flux comes into the e-cores from the permanent magnets on the sides, increasing the resultant MMF and hence, gain. Once a reasonable model of the plant was obtained, then fine adjustments of the control values based on the model could be made.

The testing procedure here is relatively straightforward; adjust the gain to attempt to get the system critically damped. However, before a centered step response can be attempted, the bias must be "removed." This is accomplished by setting the maximum stable gain, and then using a low intensity integrator to slowly create the necessary bias current. Once the bias current is obtained, and the platen is at the center, this bias current can be frozen, and the slow integrator turned off. This zeroing process can be seen in figures 6.1 and 6.2.

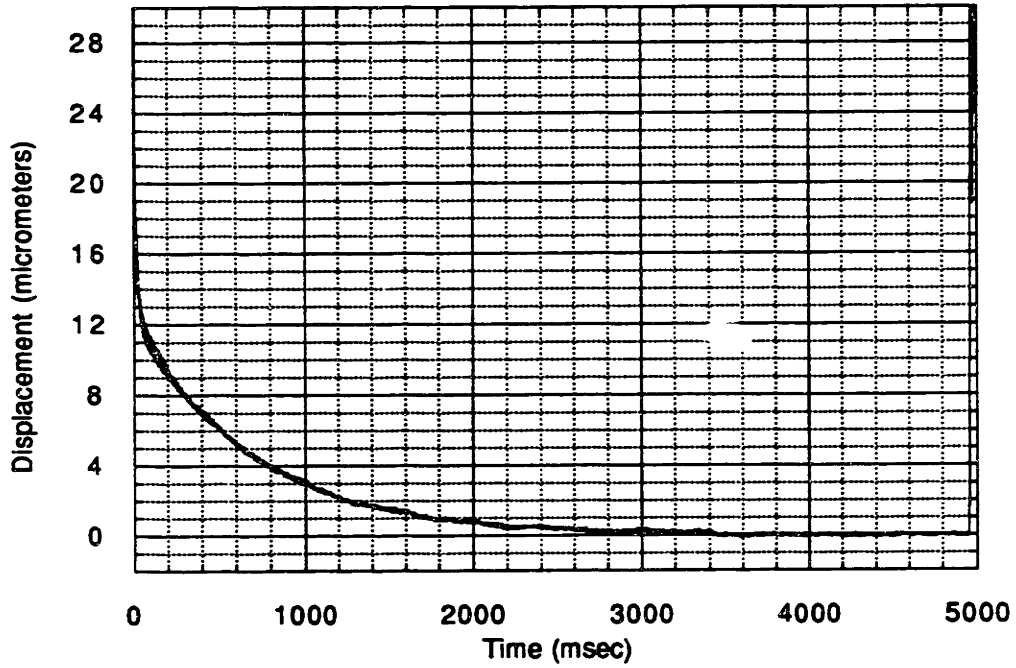


Figure 6.1: Injection of Bias into P controlled system (displacement).

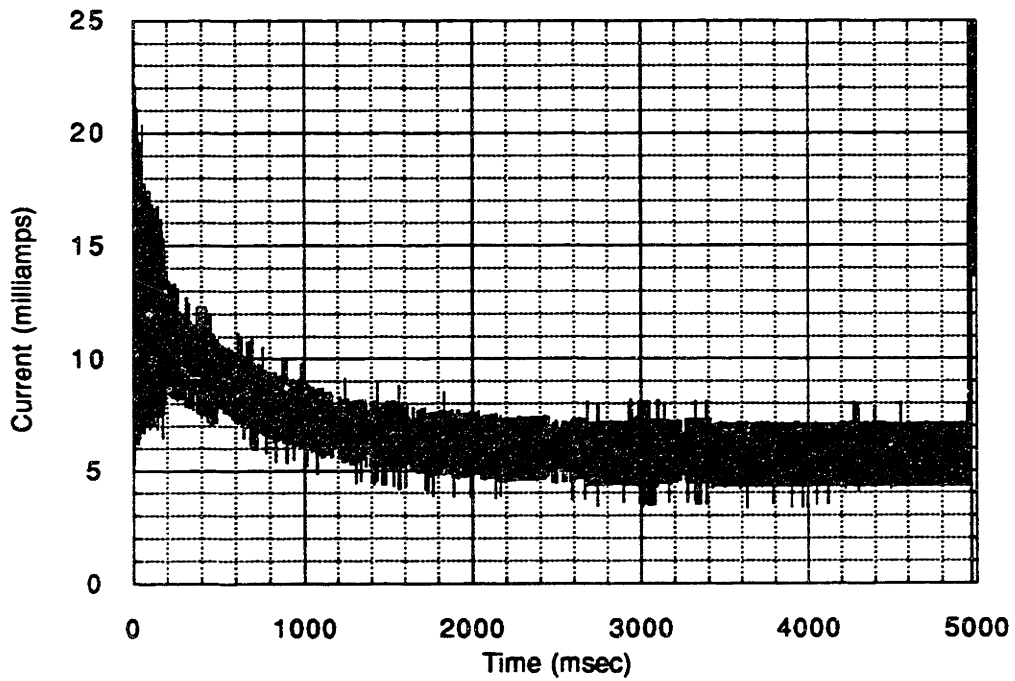


Figure 6.2: Injection of Bias into P controlled system (current).

With the integrator used, this process can be seen to take about 3 seconds. The resulting bias current is then close to 6 mA. It will be demonstrated later that this bias corresponds to about 10 micrometers of offset, which was previously mentioned.

At some time later, the integrator is simultaneously turned off, the bias frozen, and the step is injected. Two different magnitude steps, 4 μm and 10 μm , with both positive and negative values, were injected for this first set of tests. They are presented below in the two graphs, figures 6.3 and 6.4.

From the graphs, a rise time of just over 50 msec can be seen for all the cases. The experimental values also settle to a magnitude slightly higher than the input. Recall that the input must be pre-multiplied by a value to offset the steady-state error typical of this type zero system. In the actual experiment, this pre-multiplied value was estimated during the test slightly on the high side. The resulting currents required for the step responses are also useful to examine. The current commands from the computer are graphed for the two positive value cases in figure 6.5.

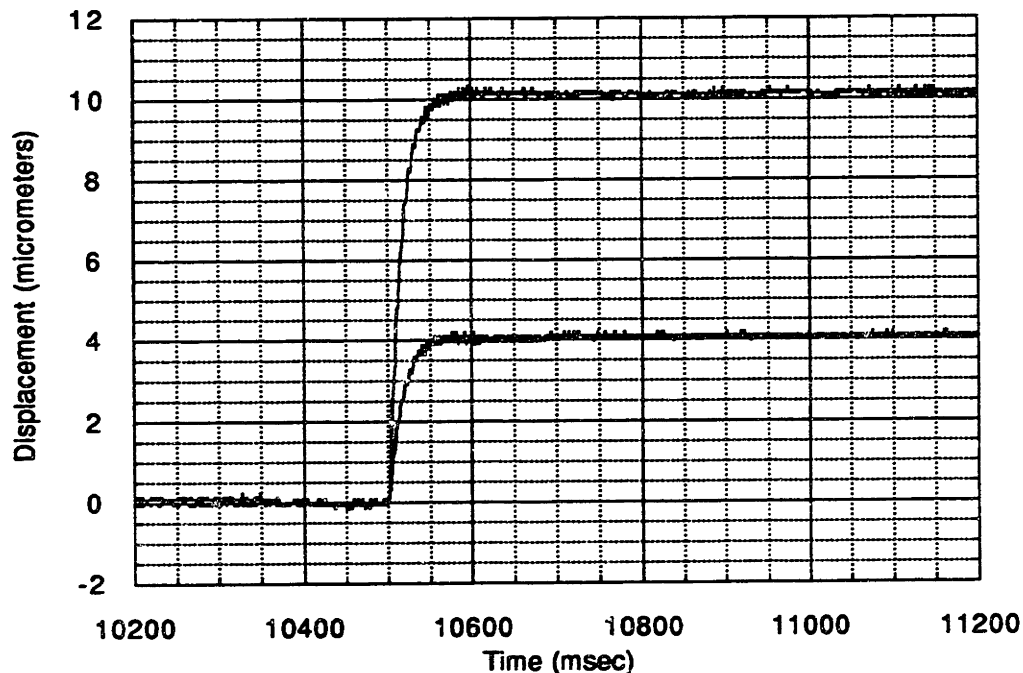


Figure 6.3: Positive step response of P controlled system (displacement).

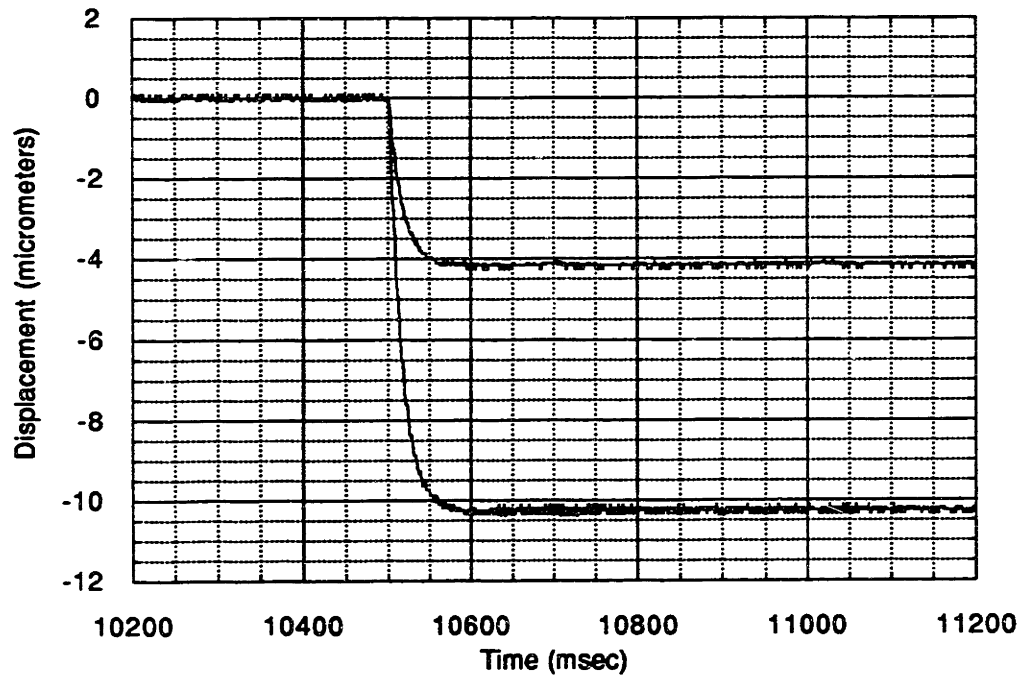


Figure 6.4: Negative step response of P controlled system (displacement).

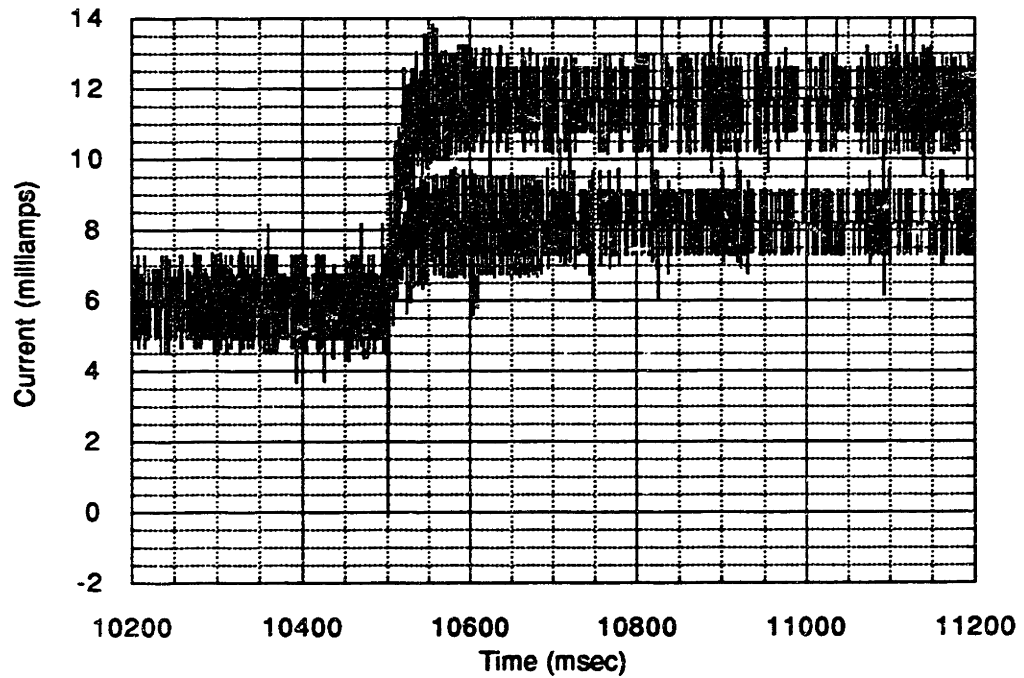


Figure 6.5: Positive step response of P controlled system (current).

From the graph of figure 6.5, the 6 mA offset is observable both before and after the injection of the step. For the 10 micrometer case, note that a 6 mA rise in current corresponds to the said displacement, leading to the conclusion that the offset of the true center of the platen was indeed 10 micrometers.

6.1.2 PI and lead control

Once a reasonably good model of the plant was established in the last section, good simulations of the system behavior could be performed with the modeling program Simulink. The model actually provided an excellent initial reference point in which to set the integrator gain to. Once incorporated, the integrator value could be modified, as well as the gain, for optimal response. Recall that with an integrator, the response will be forced to zero in steady state. The bias current that needed to be slowly injected into the step response tests is taken care of with this added element, and the resulting biases, similar to those of the previous tests, can be observed in the current outputs presented below. In summary, there are two reasons for the addition of the integrator; to increase disturbance rejection, and, in this particular case, to decrease the rise time.

As in the last section, several different magnitudes of step responses were attempted with the controller. The range is from 1 micrometer, which borders the resolution capacity of the probe, to 15 micrometers, which gets close to the plastic shims at 25 micrometers. By comparison of the responses in figures 6.6 and 6.7, many generalizations can be made.

Immediately the drastic change in rise time is apparent, now cut down to about 20 msec, for a sharp response. Notice now that the settled value is exact here. Because it is a type one system, the steady state error, as expected, is forced to zero.

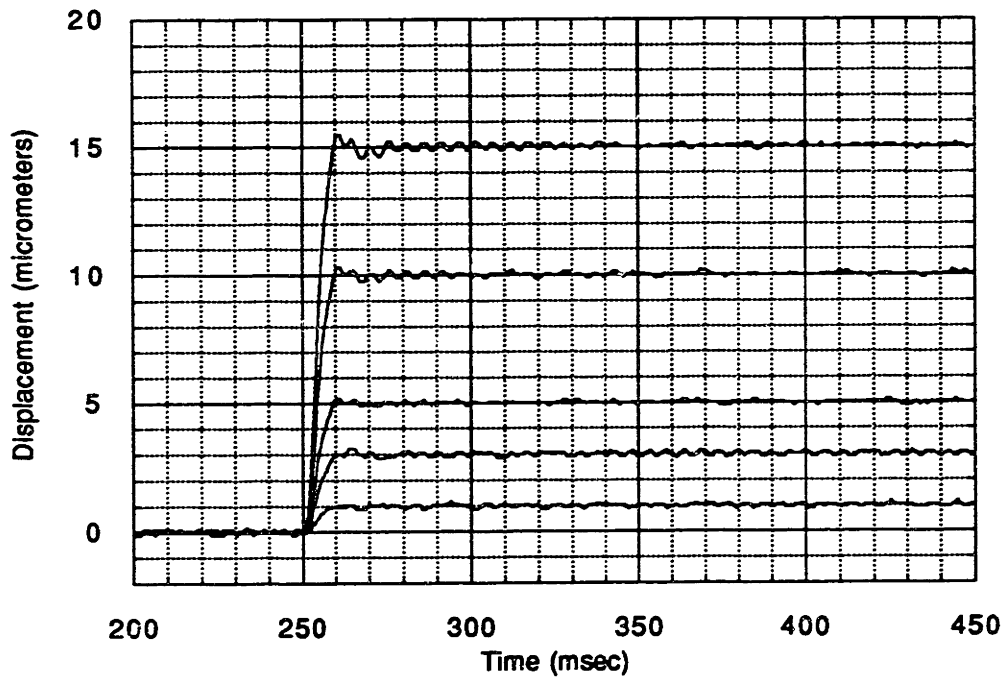


Figure 6.6: Positive step response of PI controlled system (displacement).

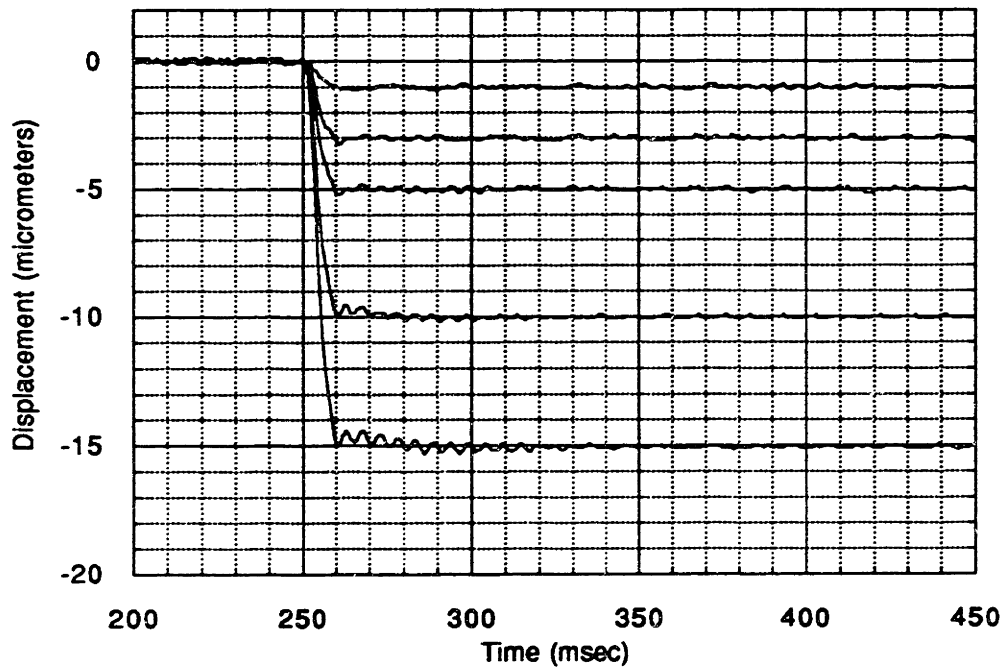


Figure 6.7: Negative step response of PI controlled system (displacement).

Some brief comments on the post-step rippling are warranted here as well. The rippling throughout the entire system occurs at roughly 200 Hz. It is believed that this is due to a structural resonance associated with the pendulum structure. In fact, in the final stage of testing, 1/16" thick 1" x 10" aluminum shims were attached to the pendulum rod with double sided tape to damp this mode and to increase stiffness slightly. Prior to the addition of these strips, the resonance was so lightly damped, that the system was uncontrollable. While the problem was greatly alleviated by this fix, it is clear that it was not entirely eliminated.

The resulting currents required for these step responses are also particularly useful to examine. The current commands from the computer are graphed for the 5 μ m and 15 μ m cases below.

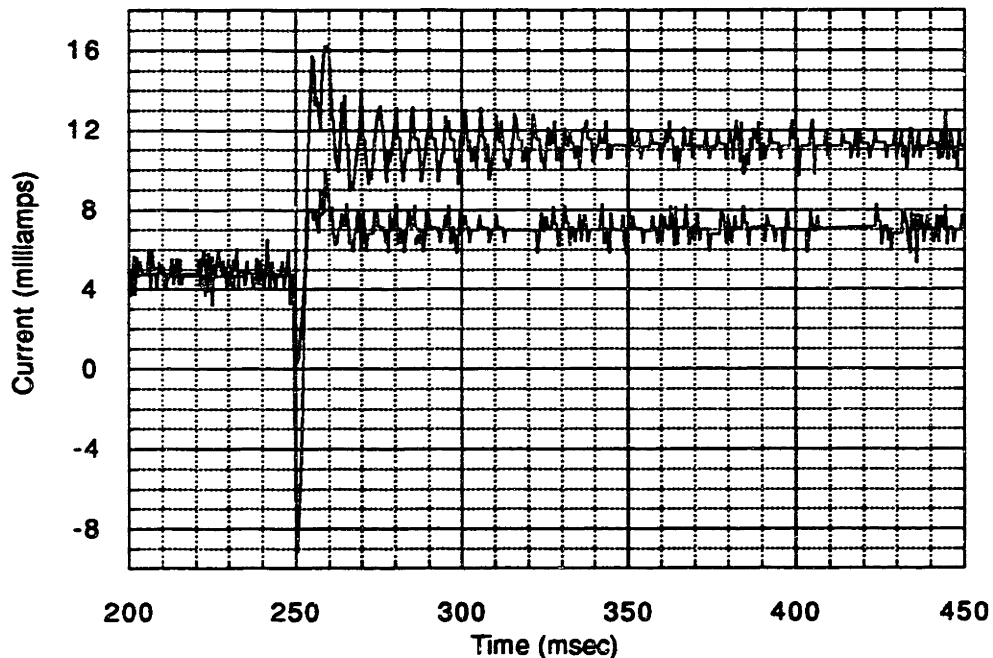


Figure 6.8: Positive step response of PI controlled system (current).

From the graph an offset current of about 5 mA can be noted. This differs slightly from the previous test, as it was done the following day and the probes were realigned.

6.2 Scanning Direction Tests

As mentioned at the onset of the chapter, time limitations precluded obtaining a complete understanding of the voice coil characteristics. However, some significant tests were performed and are presented in this section. First, the mass-and-spring like oscillations in the scanning direction are characterized prior to voice coil insertion. Next, with the voice coil in place and the laser position transducer on line, open loop control of the scan direction is achieved. Finally, several small step responses are made in the scan direction using PI control.

6.2.1 Centering force in the scanning direction

The first observation of the voice coil were made with regards to the free behavior of the transversely centered platen in this scan direction. Particularly, the three dimensional fringe fluxing associated with the magnet is clear from experimental testing, even before the insertion of the voice coils. The fringing flux, some of which returns through the side of the e-core, and which was seen to increase the gain of the plant, also tends to want to keep the platen centered in the scanning direction. This creates an interesting phenomena; in the transverse direction the platen is inherently unstable, while in the scanning direction it is stable, creating a saddle point at the center of both directions of travel.

As the gain (three-dimensional effects) was higher than expected, so was the impact of this restoring force. When suspended, the platen could be tapped in the scanning direction and it would oscillate in this direction with a frequency of about 2 Hz and with

very little damping. This motion could be picked up by the laser position transducer, but the device was not in operation until the voice coils were later inserted. It could also be detected, on a very small scale, by the capacitive probe. Under ideal conditions, the capacitive probe would be exactly parallel to the platen, and would not be able to pick up any scan direction oscillations. A small misalignment of about one micrometer though was all that was needed to see the scanning oscillation with the capacitive probe. This is shown in figure 6.9 below.

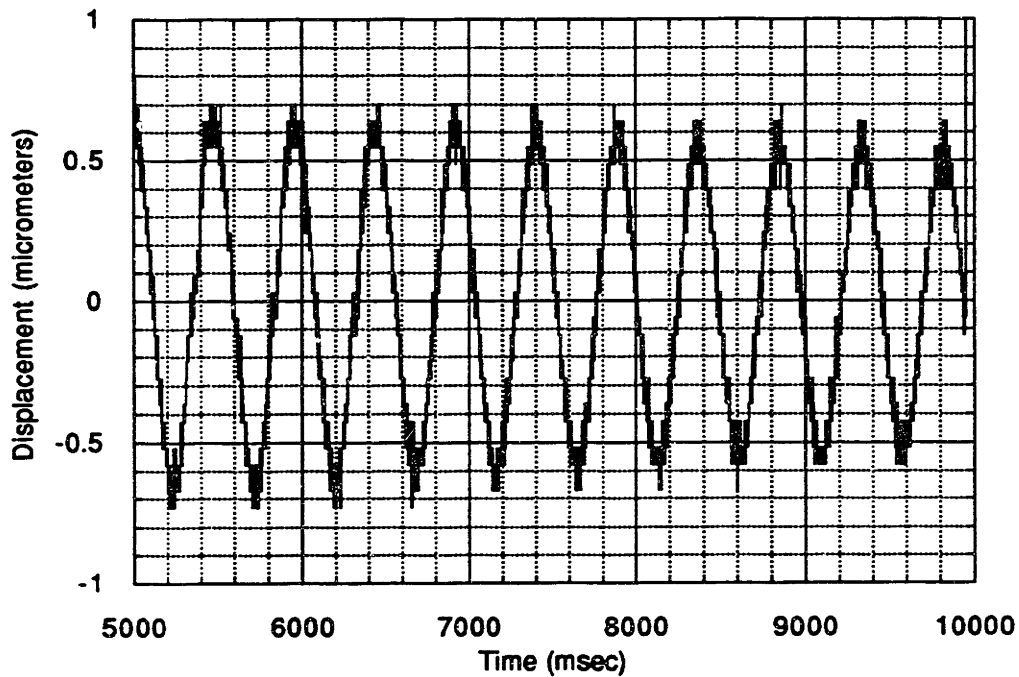


Figure 6.9: Transverse readings of scanning oscillation.

The frequency of these oscillations is about 2 Hz. For a platen, pendulum, and air bearing combination weighing a total of about 1 kg, this corresponds to a spring constant of about 150 N/m. An estimate of the damping can also be obtained by examining the exponential decay from the formula,

$$\|z\| = \|z_0\| e^{-\xi \omega_n t} \quad (6.1)$$

This damping ration is seen to be roughly .001. This is mostly due to air resistance. It is also an indicator of the excellent transverse control which should be achievable when the scan travel axis is in fully controlled.

6.2.2 Open loop control of voice coils

Complete closed loop control via the computer system was the eventual desired result. Once the voice coils are inserted though, they can be immediately tested without the use of the digital control loop by means of a sinusoidal voltage signal generator. Using the mass-and-spring analogy, the scan direction can be driven at its natural frequency of about 2 Hz which happens to close to the scan rate specified in the overall system requirements. In figure 6.10, the resultant scan motion when this loop is driven by a 50 mV sinusoid is shown.

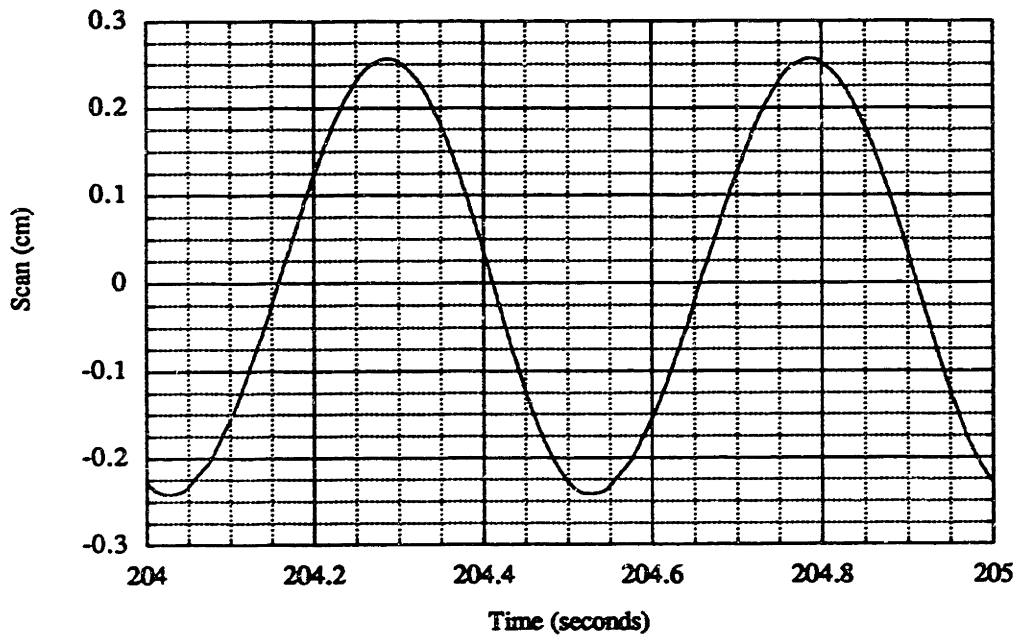


Figure 6.10: Open loop scanning oscillation.

Some amount of coupling between the two axes is inevitable. In all of the previous tests, which were done without the voice coil in place, the system was very well aligned, as is evident from figure 6.9. This type of alignment though was never achieved again with the addition of the voice coils, primarily due to lack of time. Hence for this test and the one presented in the next subsection, coupling between the two axes yielded results that proved the concept, but were limited by this factor. For the scan presented in figure 6.10, the associated motion in the transverse direction is presented in figure 6.11.

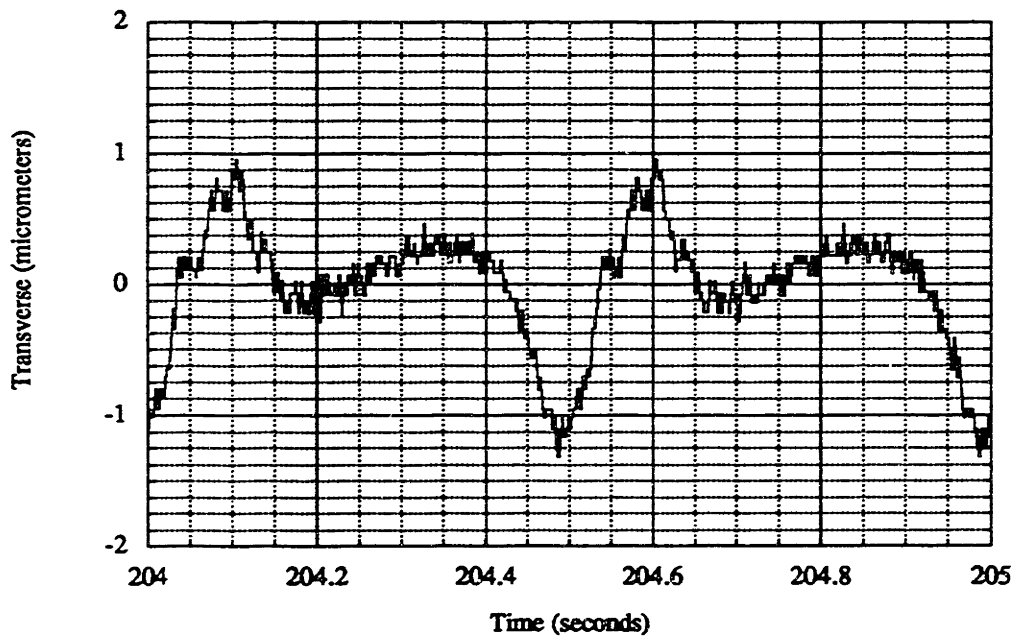


Figure 6.11: Transverse readings of open loop scan.

6.2.3 Scan direction step responses

The transverse reading of the last section is still reasonable, on the order of a micron or less. However, this small misalignment will become critical in the quick

response desired for a step input. With limited amount of time for the project, the scanning direction control could not be fully explored. The misalignment seems to have prevented large scale steps to be attempted in the scan direction. However, small steps, on the order of 10% of the overall scan desired displacement were enough to prove that it could be controlled in the scan direction.

With a limited model of the scan direction dynamics, basic PI control can be applied to yield the desired displacement with no steady state error. Figure 6.12 shows the scan step responses for 3 mil and 6 mil steps.

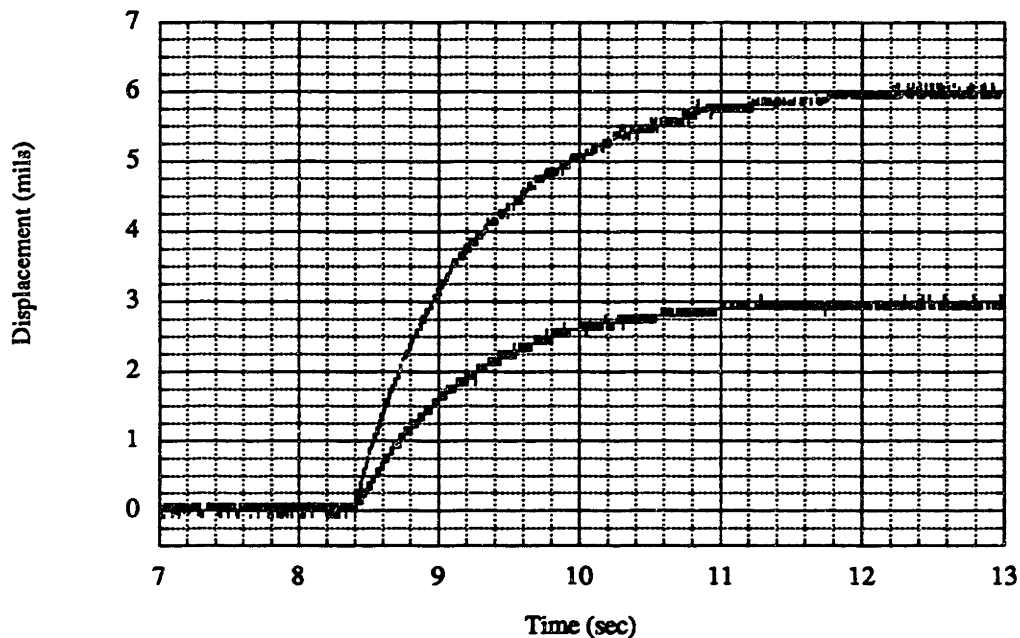


Figure 6.12: Scan direction small step responses for 3 mil and 6 mil steps.

The scan step responses are slow, and intended only to show that, at a minimum, this direction can be controlled. Whereas in the open loop scan presented in the last section demonstrated the transverse controller's ability to keep the platen centered during the slow scan, the scan step input, which happens on a much smaller time scale,

seems to impact the transverse direction a great deal more. The resulting transverse displacements for the two steps of figure 6.12 are shown below in figures 6.13 and 6.14.

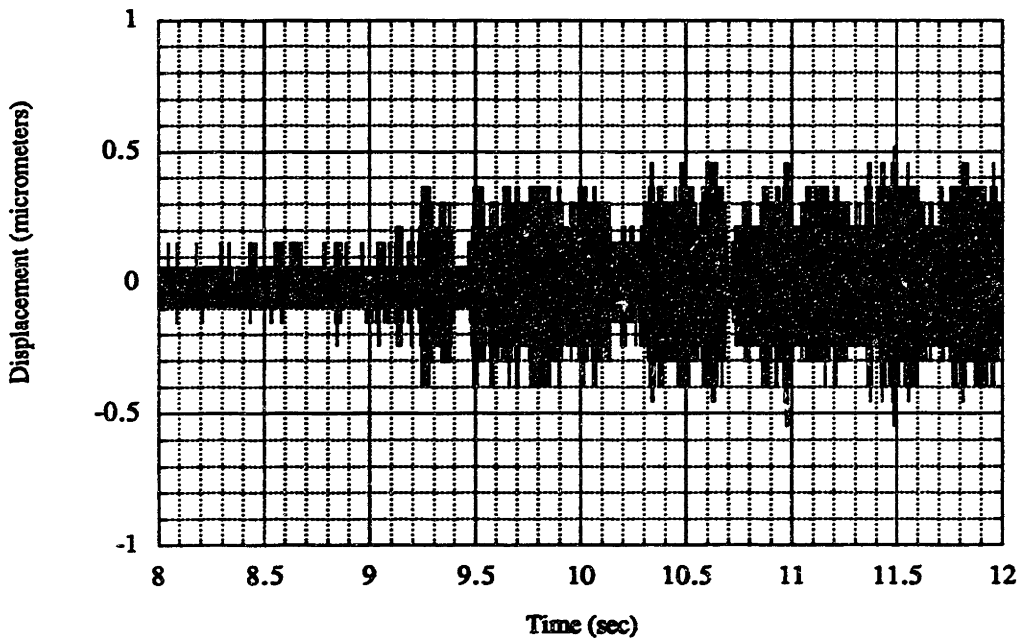


Figure 6.13: Transverse response to a 3 mil scan step.

For these small scan direction steps, the transverse remains stable, but for larger ones it will go unstable. Misalignment between the two axes is probably the largest reason for this. Ideally, transverse motion and scan motion should be exactly perpendicular. When the voice coils were inserted, the transverse reading would see up to ± 1.5 mils as the platen scanned the full range, versus a less than 0.5 mil misalignment prior to insertion. Another factor that affects the compensation of the transverse direction now is that with the addition of a second control loop. Recall that the clock speed of the computer had to be significantly reduce, from 2000 Hz down to

1428 Hz. The digital controller for the transverse, designed with a 200 Hz crossover, is affected by this change.

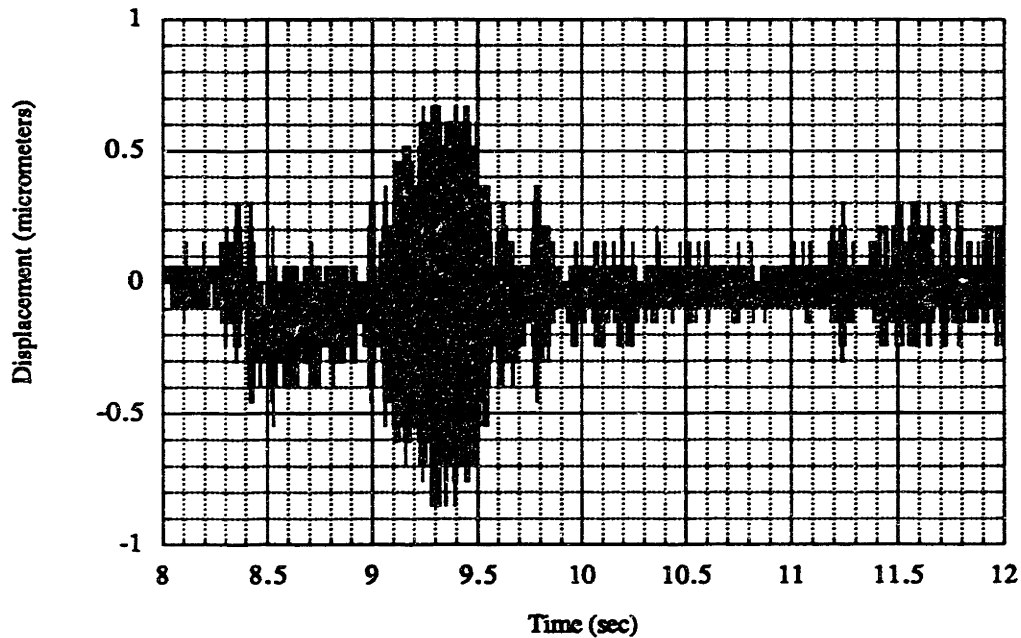


Figure 6.14: Transverse response to a 6 mil scan step.

6.3 Comparison of Actual Results to Simulations

Working models of the control loops were developed, as in the last chapter, first through classical control techniques, and then fine tuned for non-classical effects as much as possible in the program Simulink. The advantages of the program are many, including modeling of discretization, time delays, and saturation levels, as well as the coupling of a mechanical system to a discrete controller. After extensive testing, and reasonable parameter adjustments in the model, the following results are obtained and can be compared. For both cases, the models and comparisons were done for 10 micrometer steps.

6.3.1 Straight proportional and lead control

The ten micrometer step for the proportional control case is re-shown below in figure 6.15.

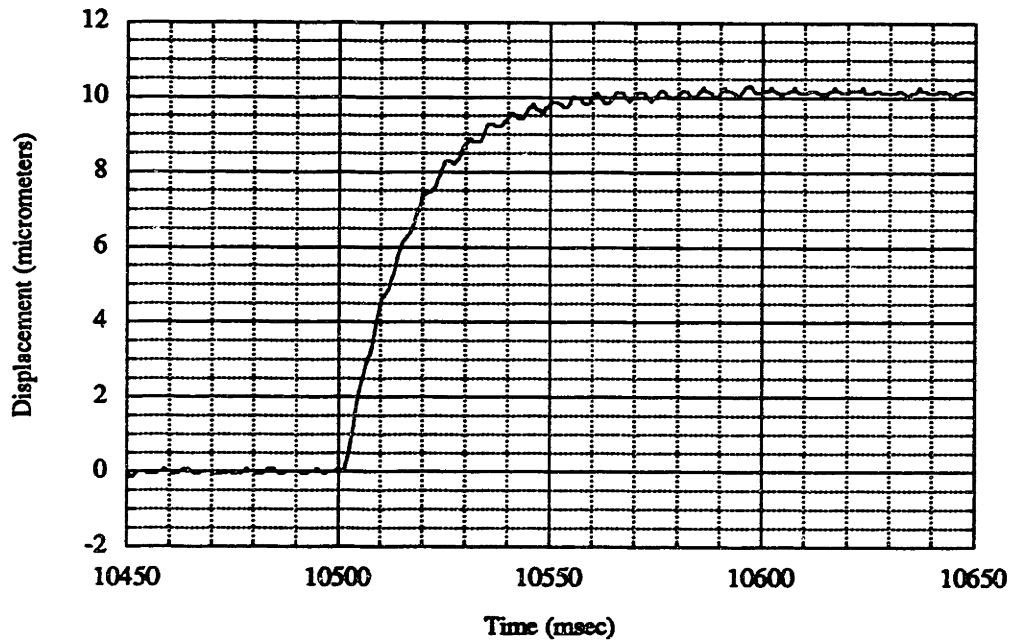


Figure 6.15: P control of 10 micrometer step (actual displacement).

In order to model this on Simulink without having each simulation run for several minutes (as would be required using the slow integrator to get the platen to the center), the required bias is immediately injected into the system, and held throughout at this constant value. The resulting simulation is shown in figure 6.16.

The straight bias injection yields slightly different pre-step behavior as is seen in the second graph. As is evident, the model is a very good match of the actual test, showing a nearly identical behavior approaching the step value. The key difference is the greater

rippling seen in the actual test results. This again is due to the resonance, which never quite died down completely.

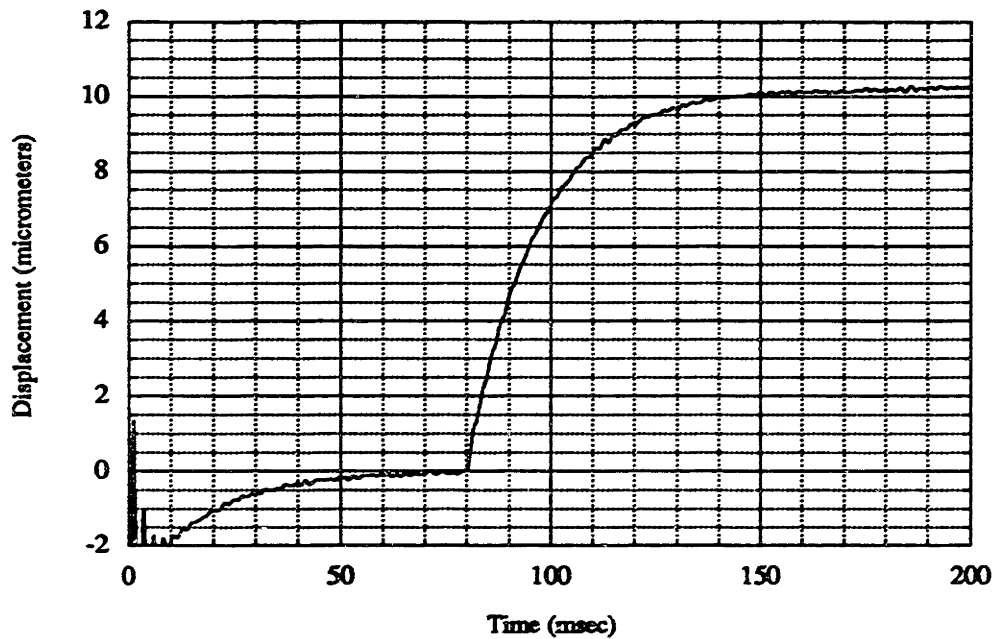


Figure 6.16: P control of 10 micrometer step (simulated displacement).

The current models may also be compared at this step size. First the actual results can be seen in figure 6.17, followed by the simulation in figure 6.18. Whereas the model has slightly different limit cycling in the current, they both show about the same spread of current as well as the same average values.

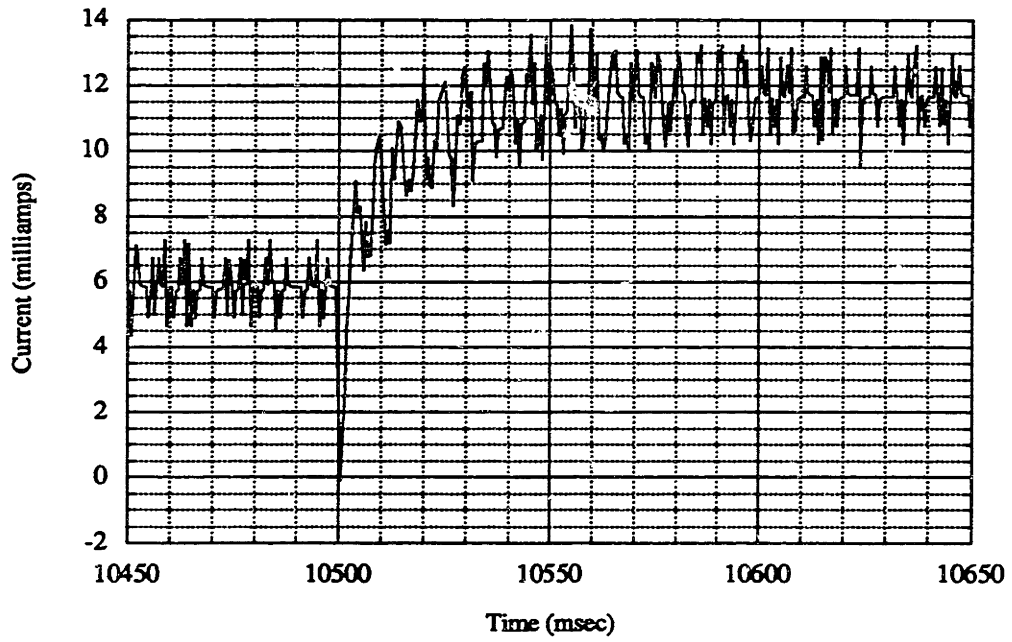


Figure 6.17: P control of 10 micrometer step (actual current).

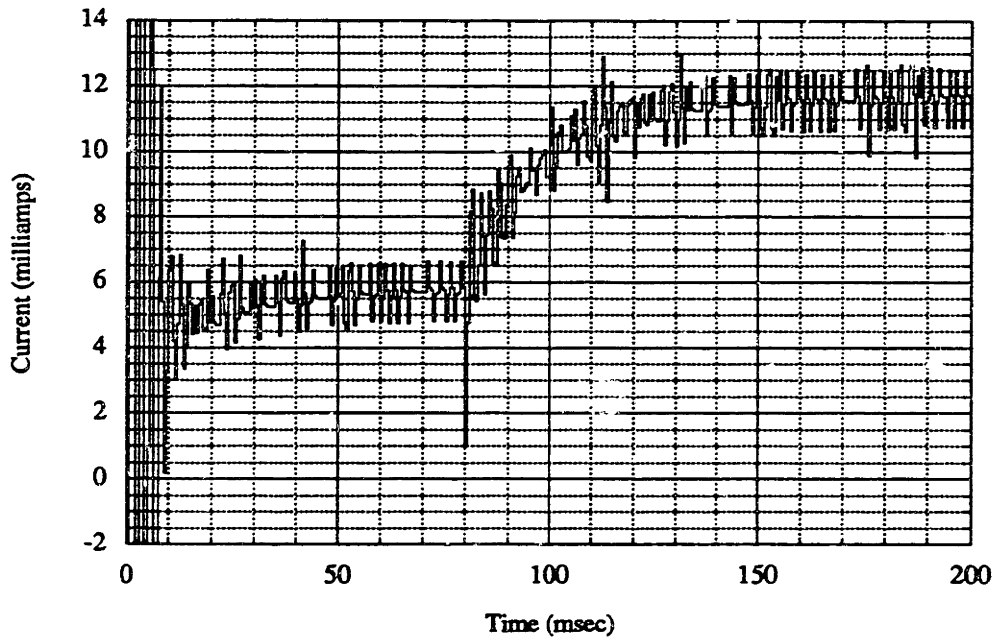


Figure 6.18: P control of 10 micrometer step (simulated current).

6.3.2 PI and lead control

The ten micrometer step for the PI control case is re-shown in figure 6.19.

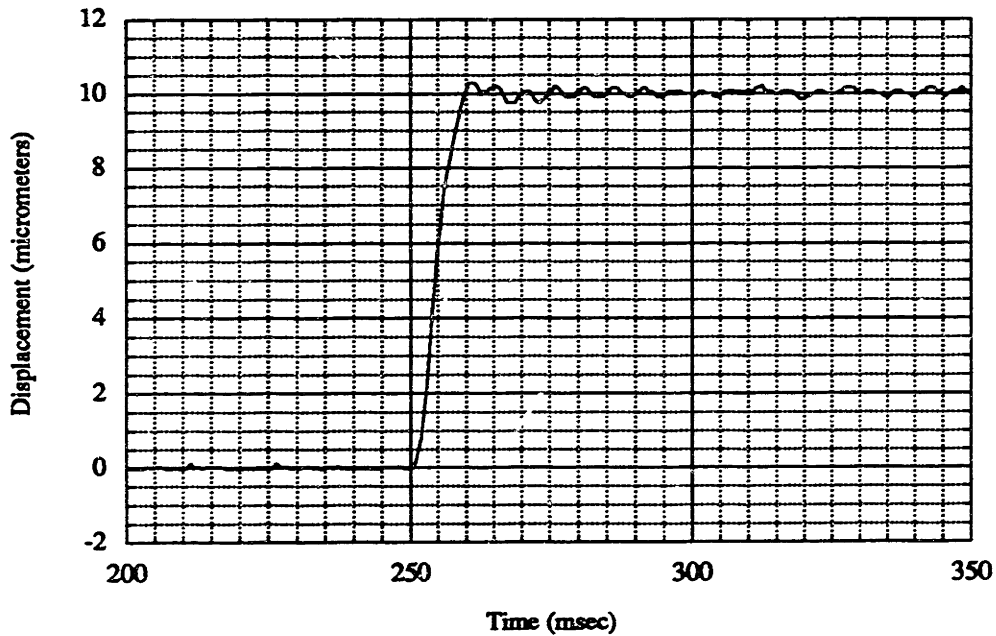


Figure 6.19: PI control of 10 micrometer step (actual displacement).

The model in Simulink yields the step response shown in figure 6.20.

As is evident, the model is a very good match of the actual test, showing a nearly identical behavior approaching the step value. The key difference is the greater rippling seen in the actual test results. This again is due to the resonance.

As before, the current may also be compared, with similar trends, and is shown in figures 6.21 and 6.22.

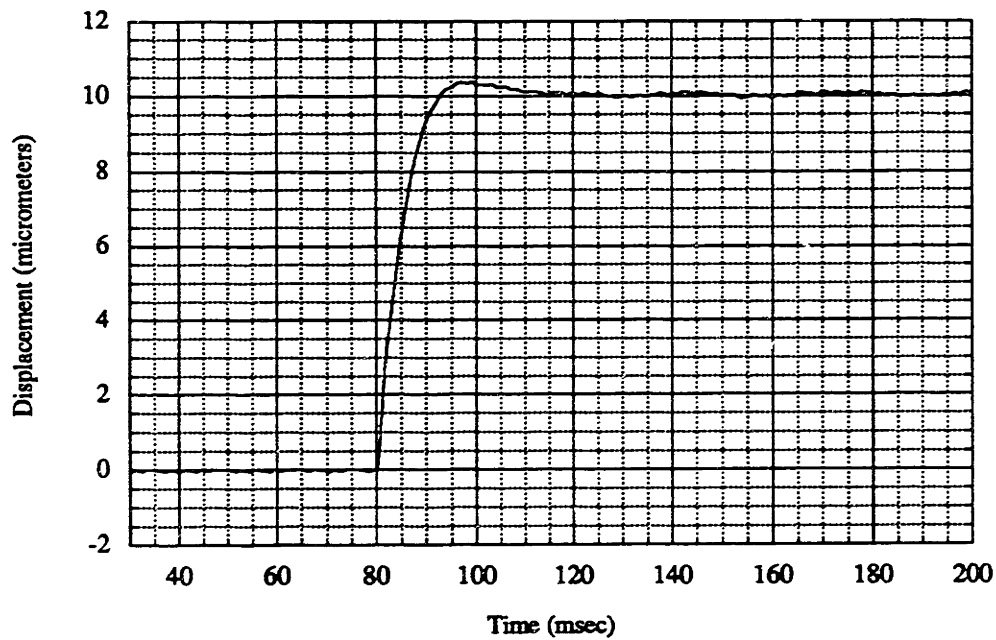


Figure 6.20: PI control of 10 micrometer step (simulated displacement).

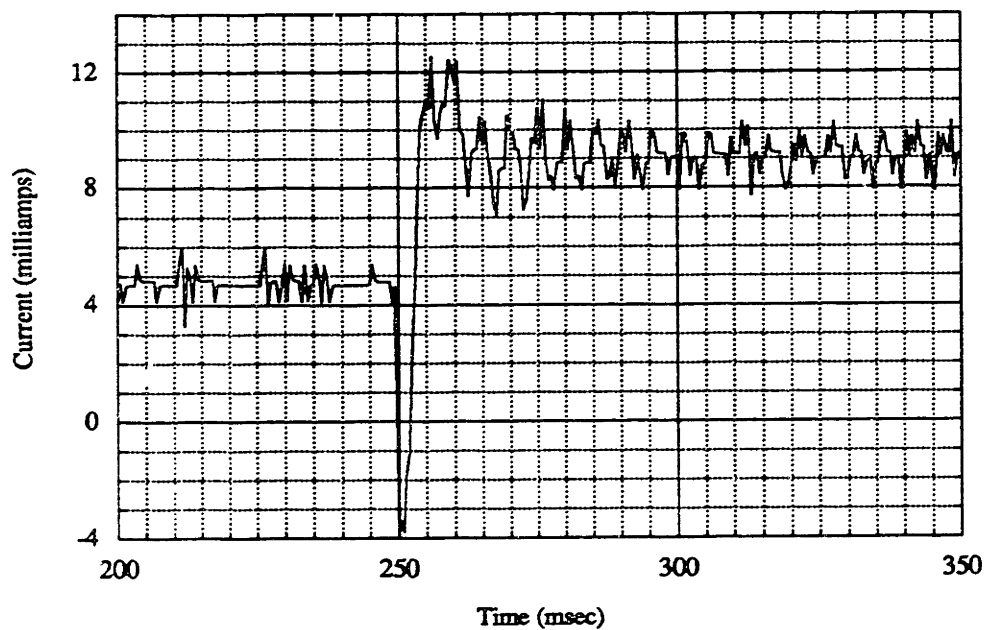


Figure 6.21: PI control of 10 micrometer step (actual current).

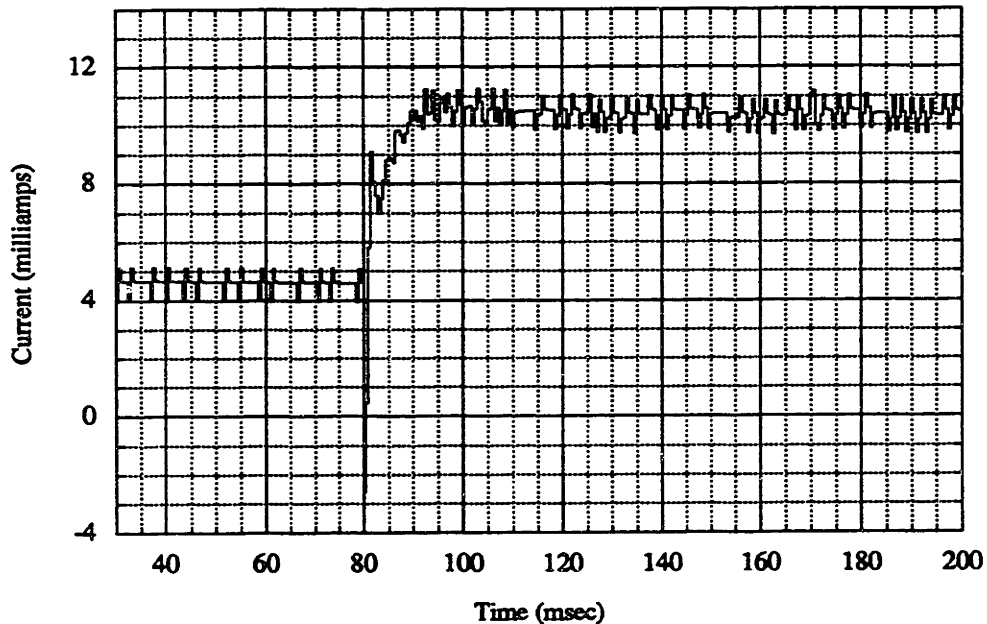


Figure 6.22: PI control of 10 micrometer step (simulated current).

6.3 Conclusions and Suggestions for Further Work

The results of the study and the prototype offer some very promising possibilities for the future of the MOB design. The tests performed proved the hybrid capability of this unique magnetic circuit design. The remaining work on the prototype is to understand the various coupling issues that currently limit the size and speed of the scan step response. The concept may easily be transformed to a much smaller size. The prototype's large size was due to limited experience and resources.

The prototype that has been built can also be re-tested with an analog controller. Analog control of the system could extend the range of possible lead crossover, and enable compensation for smaller and more realistic gaps, which will have higher

frequency unstable poles. Analog implementation also needs to be studied for the fact that it is the method that would most likely be used in a satellite application.

On a detailed level, more could be done to insure a better suppression of the resonance that proved to be a nuisance in the control loop. This would most likely involve redesigning the pendulum bar, most likely into an I-beam configuration of some sort. The actual fixture though could be used to test a variety of scanning bearing lengths, of up to about ten times the current scan length.

In conclusion, the design is successful and opens the door to further exploration of the MOB hybrid magnetic bearing concept. With the technology base in place, the foundation for the full six degree-of-freedom scanning mirror has been established.

During the course of this work, ideas were developed for alternate actuator configurations which decouple the issues of voice-coil and magnetic bearing flux. These alternate designs are presented in the next chapter.

Chapter 7

Alternate Designs

The actuator that was chosen for experimentation was used to demonstrate the basic concepts using reasonable manufacturing methods. As was mentioned in the chapter on the hardware, the project, in terms of making the bearing and particularly the platen, was very time consuming and manufacturing intensive. However, in the theory section, the through surface area of the permanent magnet was shown to be a design parameter that affects the voice coil bias field, the length of travel, and the amount of flux in the small gaps. Several compromises had to be made in the design because of this, sacrificing otherwise desirable design points. For example, in the prototype, increasing the inherent size of the small gaps was chosen as one way to cut down on the excessive amount of flux potentially seen by the electromagnetic actuators. Normally however, this gap is best made as small as possible, in order to reduce power consumption.

During the design phase of the project, the present design was settled upon in part because of time constraints that prohibited exploring more complicated designs, and in part because of the manufacturing limitations of more involved designs. In parallel with this experimental effort, paper studies of alternate configurations that would be able to dump the excess permanent magnetic flux, rather than having it all directed into the small gaps, were undertaken. If the MOB design were to be generalized to larger interferometers, such as the MAMS system, one of the methods to follow would be necessary to implement. This chapter focuses on some of those alternate designs. There are several ways to cut down on the excessive small gap flux. The first is to increase relative areas where the flux travels. The second is to redirect the flux into alternate

paths. The next is to short circuit the flux so that some of it avoids the gaps. Another is to back drive the flux across the gaps. These ideas are introduced and incorporated in the following four designs.

7.1 Bridged Center and Tapered Flux Area

In the previously presented design, all the permanent magnet flux is directed through the center of the platen before returning through the two small gaps (see figure 3.11). The coils must work against this flux to gain control over the small gaps. If some of the permanent magnet flux could be redirected so that it jumps to the E-cores directly, without crossing this small gap, then the center gap flux would be easier to compensate for. One way to do this involves extending the center leg of the E-core, and at the same time, decreasing the width of the center part of the platen. This is shown in figure 7.1.

For the sake of simplicity, assume that the extended E-core center is designed to receive half of the incoming permanent magnet flux through the center gaps, and half directly from across the large gap. This effectively reduces the center small gap fluxes by a factor of two. However, before examining how this directly affects the design equations, two important implications of this new design must be mentioned. First of all, all the flux from the permanent magnet, as seen from the figure, does eventually enter the center leg of the E-core. That means that the E-core will see the same amount of flux as the current design throughout most of its body. This implies that the design is good for reducing the current design's flux at the small middle gap, but not for reducing the flux in the bulk of the E-core, and thus this approach does not alleviate saturation problems. If the flux is followed through its anticipated return path, the next key implication is observed. All of the flux from the large gap face of the permanent magnet must be returned through the opposing face, the one epoxied to the top and

bottom of the center platen. If the standard geometry of the E-core is maintained, the excess flux still must return through the top and bottom small gaps. One way to reduce the flux at this juncture would be to increase the pole face area at the top; for the example this could be done by doubling its two-dimensional length, as is done in the figure. The result is an irregularly shaped E-core, such that the width of all the legs are exactly equal. In a standard E-core design, it is assumed that the middle leg is twice the width of the outer legs so that the flux entering it is evenly split between the outer two. However, in the altered design, the more critical parameter in the new design is the B-field across the gap. The outer leg reduces this by increasing area, and the inner leg only sees half of it by its extension.

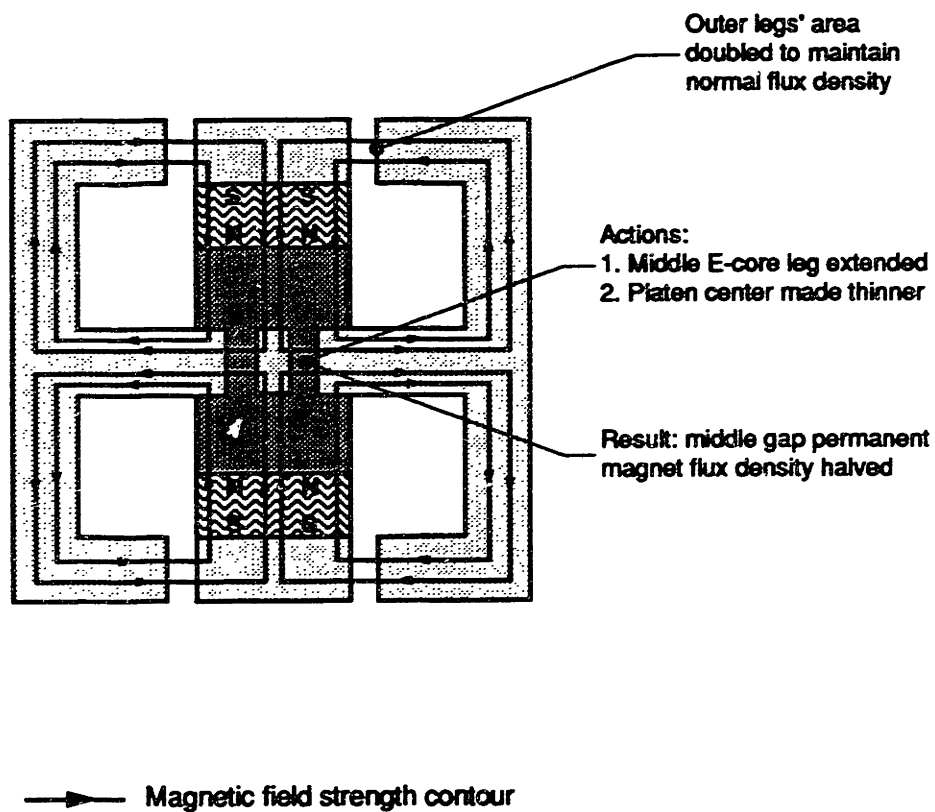


Figure 7.1: Bridged center with tapered flux area.

7.2 Shim Designs

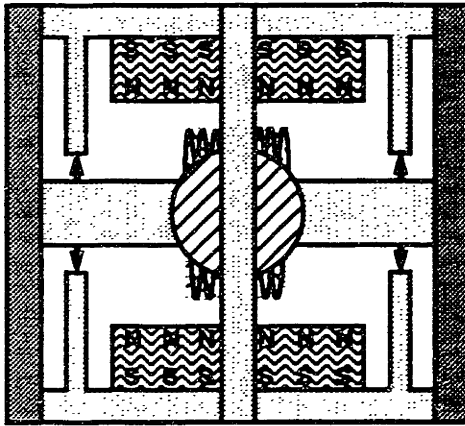
The last example focused on the center of the E-core as a way to avoid getting all of the flux to pass through the small gaps directly. The next three proposed methods will rely on "shims" that could be added to the current prototype design in order to either divert flux paths away from the small gaps, or to use other permanent magnets or saturated shims to back drive the flux at the gaps. In the first two cases, the shim can be thought of as additional E-core material added to the platen. In the last one, the permanent magnets are added in a similar configuration. The shims in reality would be located at the front and back of the platen in the z (scan) direction.

7.2.1 Silicon iron shims

The argument behind this method is that if some of the permanent magnet flux can be redirected back to the magnet through the platen, then the flux buildup in the small gaps could be significantly reduced. The shim added for this purpose can be seen in figure 7.2, which shows the shims in a simplified, 2-D manner. Similar analysis as to what was done in §3.4.2 can be used to rederive the fluxes at the small gaps based on this configuration. Before rederiving these equations though, it should be noted, due to symmetry, that only the upper half of the new design has to be solved for.

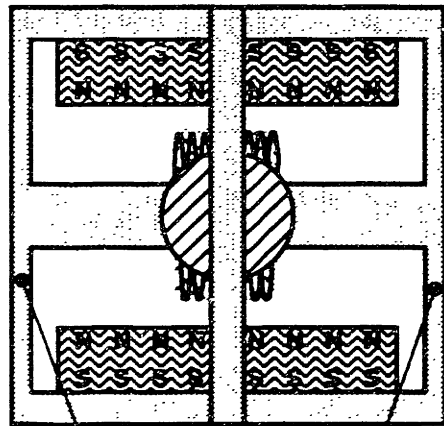
7.2.2 Saturated iron shims

Like the previous case iron shims are added to the fore and aft parts of the center platen. However, a new gap is not created. The shims again create an alternate path for the permanent magnet flux to return by. Here though, the shims are made to intentionally be saturated in operation. When the iron shim saturates, it acts like a



→ New gaps

Figure 7.2: Silicon iron shims.



New shims saturate

Figure 7.3: Saturated iron shims.

magnet and thereby returns a constant flux. Manufacturing of such a new center platen could probably be best achieved used tape wound metals that could create two loops, and be thinned out at the place of the shim. The side view of the concept is seen in the figure 7.3.

7.2.3 Permanent magnet shims

The argument behind this method is that some of the permanent magnet flux can be back-driven through the small gaps, then the net permanent magnet flux through them can be reduced. If another set of permanent magnets are strategically placed in this system, then this goal may be accomplished. Permanent magnet shims, placed much in the same manner that the silicon iron shims were placed, can be seen added in figure 7.4.

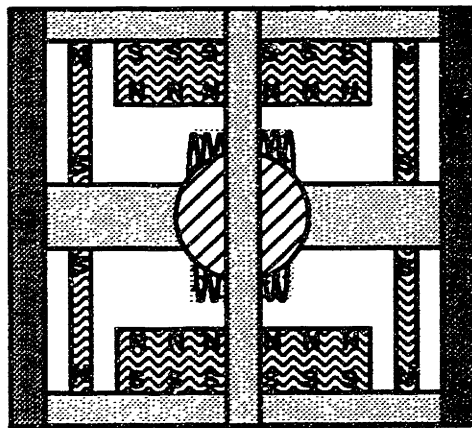


Figure 7.4: Permanent magnetic shims.

Chapter 8

Bibliography

Akiba, T., Shingu, S., Kameda, Y., Akabane, S., and Hirai, S. (1992): "Development of a Magnetically-Suspended Mirror Scanning Mechanism for an Interferometer Monitor for Greenhouse Gasses (IMG)," Third Int'l Symposium on Magnetic Bearings, Alexandria, VA, July 29-31, 1992.

Anschutz-Kaempfe, H. (1926): *Gyroscopic Apparatus*, U.S. Patent #1,589,039, (Appl. Feb. 14, 1923; Pat. Jun. 15, 1926).

Asada, H. and Slotine, J.-J.E. (1986): *Robot Analysis and Control*. John Wiley & Sons Inc., NY, New York, 1986.

Buckley, J., Galburt, D., and Karatzas, C. (1989): "Step-and-Scan Lithography Using Reduction Optics," *Journal of Vacuum Science Technology*, Vol. 7, No. 6, Nov/Dec, 1989, pp. 1607-1612.

deVegete, J.V. (1990): *Feedback Control Systems*. Prentice-Hall, Inc., Englewood Cliffs, NJ, 1990.

Haus, H.A. and Melcher, J.R. (1989): *Electromagnetic Fields and Energy*. Prentice-Hall, Inc., Englewood Cliffs, NJ, 1989.

Johnston, S.F. (1991): *Fourier Transform Infrared: A Constantly Evolving Technology*. Ellis Horwood Limited, Chinchester, England, 1991.

Medbery, J.D., Gupta, A.A. (1991): "Stable Controller Design of a Six Degree-of-Freedom Magnetically Suspended Fine-Steering Mirror (MSFSM)," Active and Adaptive Optical Components, San Diego, CA, Jul. 24-26, 1991.

Melcher, J. (1982): *Continuum Mechanics*. MIT Press, Camb., MA, 1982.

- Olson, S. (1994):** "Nonlinear Compensation of a Single Degree of Freedom Magnetic Suspension System," M.S. Thesis, M.I.T., Camb., Mass., 1994.
- Roberge, J.R. (1975):** *Operational Amplifiers: Theory and Practice*. John Wiley & Sons, Inc., NY, New York, 1975.
- Shimoda, H., Ogawa, T., Hayashi, M., Ono, A., Nishinomiya, A., Hirai, S., Yokota, M. (1991):** "Development of a Spaceborne Fourier Transform Spectrometer for Global Atmospheric Monitoring," International Geoscience and Remote Sensing Symposium, Espoo, Finland, Jun. 3-6, 1991.
- Studer, P. (1977):** "A Practical Magnetic Bearing," *IEEE Transactions on Magnetics*, Vol. MAG-13, No. 5, Sept., 1977, pp. 1155-1157.
- Studer, P. (1977):** *Magnetic Bearing System*, U.S. Patent #4,000,929, (Appl. Jul. 3, 1975; Pat. Jan. 4, 1977).
- Studer, P. (1985):** *Radial and Torsionally Controlled Magnetic bearing*, U.S. Patent #4,634,191, (Appl. Nov. 21, 1985; Pat. Jan. 6, 1987).
- Trumper, D. (1990):** "Magnetic Suspension Techniques for Precision Motion Control," Ph.D. Thesis, M.I.T., Camb., Mass., 1990.

Appendix A: Control Code

```
/******  
*** THESIS.C (4/28/95) ***  
******/  
  
#include <stdio.h>          /* standard library */  
#include "nidaq.h"         /* function definitions */  
#include "nidaqerr.h"      /* error code definitions */  
#include <dos.h>           /* dos library */  
#include <string.h>        /* string library for stringcopy */  
#include <time.h>          /* time conversion */  
#include <ctype.h>         /* special Microsoft character commands */  
#include <math.h>          /* math functions */  
#include <graph.h>         /* graphic functions */  
#include <pgchart.h>       /* presentation graphic functions */  
  
#define DATA 10000        /* Number of data points */  
#define ADE_int 0x78       /* ADE address */  
  
union REGS xregs;          /* ADE structure */  
struct SREGS xregs_s;     /* ADE structure */  
  
typedef enum {FALSE, TRUE} boolean; /* graphics protocol */  
  
char far  
    cmdstr[79],             /* to write ADE string commands */  
    *line_data[1000];      /* used to make a line graph for array */  
  
int far  
    data[50];              /* to translate numbers to and from ADE */  
  
float far  
    small_disp[DATA],      /* final keeps of small displacement */  
    large_disp[DATA],     /* final keeps (disp) for test plot */  
    index[DATA],          /* pseudo time index */  
    cut_small_disp[1000], /* */  
    integrator[DATA];     /* final keeps of integrator results */  
  
int  
    dum,                  /* dummy variable to check boards */  
    board,                /* dummy to check board installation */  
    board_in=1,          /* slot/ID number of input (MIO) board */
```

```

board_out=2,      /* slot/ID number of output (AO) board */
brd_code_in,     /* a number standing for MIO board type */
brd_code_out,    /* a number standing for AO board type */
chan_in,         /* channel for input */
chan_out,        /* channel for output */
chan_out_small, /* channel for small gap output */
err_num_in,      /* error # from MIO library function calls */
err_num_out,     /* error # from AO library function calls */
err_num_out_small, /* error # from small gap library funt call */
gain=1,         /* gain for input; default gain of 1 now*/
board_cl=1,     /* slot/ID number of clocking function */
err_num_cl,     /* error # returned from internal clock */
timebase=4,     /* set clock speed 5=100Hz, 4=1kHz, 3=10kHz */
clock_fact,     /* divides up basic clock speed-see timebase */
ctr=1,          /* counter # for timing signal (1, 2 or 5) */
ade_zero=0;     /* raw zero value for ade */

double
volts_in,       /* yields actul voltage from 12 bit value_in */
loop=0,         /* size of recordable loop */
loop_long=0,   /* size of main loop */
stst,          /* when in loop step starts */
ref = 0,       /* step displacement */
x_mils,        /* x transverse, in mils */
z_mils,        /* z transverse, in mils */
Gin = 1,       /* input conditioner */
K = 1,         /* forward loop gain */
Ki = 0,        /* integrator gain */
Kc = -1305,    /* lead gain */
Kl = 1;        /* lead pre - gain */

float
fact,           /* amplitude out/in when following input */
fact_short,    /* follow amplitude for transverse */
duration=0,    /* duration time for run */
MIO_zero=0,    /* raw zero value for MIO */
MIO_calib=20.5, /* MIO measurement calibration */
ade_calib=-.001*1.197; /* ade measurement calibration */

char
freeze,        /* option to freeze integrator */
cr,           /* consumes the carriage return from scanf */
po,          /* print orede - a 'n' means no printing */
reply,       /* locally used for yes/no answers */
use_output='y';

void board_setups(void); /* sets up boards */
void calibration(void); /* calibrates measurement */
void user_inputs(void); /* user defines inputs */
void clock_setup(void); /* sets up clock */
void controller(void); /* including all i/o */
void graphit_em(void); /* to graph e-m data */
void graphit_ed(void); /* to graph e -d data */

```

```

void disksave(void);           /* to save data */
void reinitialize(void);      /* reinitializes boards */
void adecall( char far *cmd, int far *xarray); /* talks to ADE board */
void zero(void);             /* zeroes output board */

main()
{
    board_setups();
    zero();
    calibration();
    user_inputs();
    clock_setup();
    controller();
    graphit_em();
    graphit_ed();
    disksave();
    reinitialize();

    printf("\nG'day!\n");
}

void board_setups(void)
{
    extern int
        getBoardToUse();           /* procedure to get the slot/ID */

    /*** Prep ADE board for action ***/

    strcpy( cmdstr, "SP3A");       /* choose channel 3A */
    adecall( cmdstr, data);

    data[0]=(int) 1;              /* # data points in each block */
    strcpy( cmdstr, "SL");
    adecall(cmdstr, data);

    data[0]=(int) 2;              /* Sets 2nd small distance range */
    strcpy( cmdstr, "SR3A");
    adecall( cmdstr, data);

    /*** Makes sure boards are there and operational ***/

    printf("\nChecking to see if boards are there:\n");
    board = getBoardToUse ();

    err_num_in = Get_DA_Brds_Info (board_in, &brd_code_in, &dum, &dum,
                                   &dum, &dum, &dum, &dum);
    ErrPrint ("Get_DA_Brds_Info", err_num_in);

    err_num_out = Get_DA_Brds_Info (board_out, &brd_code_out, &dum, &dum,
                                    &dum, &dum, &dum, &dum);
    ErrPrint ("Get_DA_Brds_Info", err_num_out);
}

void calibration(void)

```



```

{
int
    ade_first=0,          /* first calibration position */
    ade_second=0,        /* second calibration position */
    zero_count,          /* how long to run zeroing loop */
    z_c_total=5000;      /* duration for zero_count */

float
    MIO_first=0,         /* first calibration position */
    MIO_second=0,        /* second calibration position */
    MIO_change=0,        /* change in MIO position */
    ade_offset=0,        /* calibrated off - zero x */
    off_wall=0,          /* additional offset factor */
    MIO_offset=0;        /* calibrated off - zero z */

double
    ade_change=0;        /* change in ade position */

/** Calibration options */

printf("\n\nKill output? (find zero) - default is no ");
use_output=getchar();
cr=getchar();

printf("\n%c\n",use_output);

printf("\n\nDo you want to calibrate? (default is no): ");
/**!!!reply=getchar();
cr=getchar();!!!***/

reply='y';

if (reply != 'y') return;

printf("\n\nDo you want to check inputs? (d=n)?\n");
reply=getchar();
cr= getchar();

if (reply == 'y')
{
    for(zero_count=0;zero_count<z_c_total;zero_count++)
    {
        AI_Clear( board_in );
        err_num_in = AI_VRead( board_in, chan_in, gain, &volts_in);
        ErrPrint ("AI_VRead", err_num_in);

        strcpy( cmdstr, "AB");
        adecall( cmdstr, data);

        if (data[0] == 32766) data[0] = 5000;
        if (data[0] == 32767) data[0] = -5000;

        printf("count %d of %d MIO/chan %d: %.3f  ADE/chan %d: %d\n",
            zero_count,z_c_total,chan_in,volts_in,3,data[0]);
    }
}

```

```

    }

    /*** Save the zeroe values ***/

    ade_zero=data[0];
    MIO_zero=volts_in;
    }

    /*** Calibrate the transverse direction ***/

    printf("\n\nCalibrate TRANSVERSE displacements? (default is yes) ");
    reply=getchar();
    cr=getchar();

    if (reply != 'n')
    {
        printf("\n\nSwing? (default is yes)");
        reply=getchar();
        cr=getchar();

        if (reply != 'n')
        {
            printf("Move to red actuator and hit 'enter': ");
            cr=getchar();

            strcpy( cmdstr, "AB");
            adecall( cmdstr, data);
            ade_first=data[0];
            printf("red = %d\n", ade_first);

            printf("Move to green actuator and hit 'enter': ");
            cr=getchar();

            strcpy( cmdstr, "AB");
            adecall( cmdstr, data);
            ade_second=data[0];
            printf("green = %d\n", ade_second);

            ade_change=ade_second-ade_first;

            printf("\nChange in ADE is %.0lf, (approx %.5lf mils by 1.2)",
                ade_change,(ade_change*1.197/1000));
            printf("\nHow many ABSOLUTE mils is that?\n");
            scanf("%f%c",&ade_calib,&cr);

            ade_calib=ade_calib/ade_change;
            ade_zero=(int)((ade_first+ade_second)/2);
        }

        ade_offset=ade_calib*ade_zero;

        printf("\nCalibration yields %f mils/ade_click w/ offset %f mils",
            ade_calib,ade_offset);
    }

```

```

printf("\nWhat offset do you desire? \n");
scanf("%f%c",&off_wall,&cr);

ade_offset=off_wall;
ade_zero=(int)(ade_offset/ade_calib);
ade_offset=ade_zero*ade_calib;

printf("\nCalibration yields %f mils/ade_click w/ offset %f mils",
      ade_calib,ade_offset);
}

/**/ Calibrate the scanning direction ***/

/**/!!!printf("\n\nCalibrate SCANNING displacements? (default is no) ");
reply=getchar();
cr=getchar();

if (reply == 'n')
{
printf("Move to your first scan position and hit 'enter':\n");
cr=getchar();

AI_Clear( board_in );
err_num_in = AI_VRead( board_in, chan_in, gain, &volts_in);
ErrPrint ("AI_VRead", err_num_in);
MIO_first=volts_in;

printf("Move to your second scan position and hit 'enter': ");
cr=getchar();

AI_Clear( board_in );
err_num_in = AI_VRead( board_in, chan_in, gain, &volts_in);
ErrPrint ("AI_VRead", err_num_in);
MIO_second=volts_in;

MIO_change=MIO_second-MIO_first;

printf("\nYour change in MIO volts is %.3f, how many mils is this? ",
      MIO_change);
scanf("%f%c",&MIO_calib,&cr);

MIO_calib=MIO_calib/MIO_change;
MIO_offset=MIO_calib*MIO_zero;

printf("\nCalibration yields %f mils/volt with offset %f mils",
      MIO_calib,MIO_offset);
}!!!***/

/**/ Sample calibrated measurement loop ***/

printf("\nDo you want to try a calibrated measurement loop (d=n)?\n");
cr = getchar();
reply=getchar();
cr= getchar();

```

```

printf("\nreply = %c\n",reply);

if (reply == 'y')
{
    for(zero_count=0;zero_count<z_c_total;zero_count++)
    {
        AI_Clear( board_in );
        err_num_in = AI_VRead( board_in, chan_in, gain, &volts_in);
        ErrPrint ("AI_VRead", err_num_in);

        strcpy( cmdstr, "AB");
        adecall( cmdstr, data);

        if (data[0] == 32766) data[0] = 5000;
        if (data[0] == 32767) data[0] = -5000;

        x_mils = (data[0]-ade_zero)*ade_calib;
        z_mils = (volts_in-MIO_zero)*MIO_calib;

        printf("count %d of %d z_mils %d: %.3f  x_mils %d: %.3f\n",
            zero_count,z_c_total,chan_in,z_mils,3,x_mils);
    }
}

void user_inputs(void)
{
    int
        clock_user,      /* user picks clock rate from menu */
        clock_rate;     /* numerical value of clock rate */

    /*** User interface ***/

    printf("\nEnter the input channel (0-2): ");
    /***!!!scanf("%d%c",&chan_in,&cr);!!!***/

    chan_in=0;

    printf("\nEnter an output channel for scan control (0-3): ");
    /***!!!scanf("%d%c",&chan_out,&cr);!!!***/

    chan_out=0;

    printf("\nEnter an output channel for transverse control (0-3): ");
    /***!!!scanf("%d%c",&chan_out_small,&cr);!!!***/

    chan_out_small=1;

    printf("\nHere are your clock speed options*** hacked!***:\n");
    printf("(1)  2 KHz\n");
    printf("(2)  1 KHz\n");
    printf("(3) 100 Hz\n");
    printf("(4)  10 Hz\n");
}

```

```

printf("\nEnter desired clock speed: ");
/**/scanf("%d%c",&clock_user,&cr);/**/

clock_user=5;

switch(clock_user)
{
    case 1 : clock_rate = 2000; timebase = 3; clock_fact = 5; break;
    case 2 : clock_rate = 1000; timebase = 4; clock_fact = 1; break;
    case 3 : clock_rate = 100; timebase = 5; clock_fact = 1; break;
    case 4 : clock_rate = 10; timebase = 5; clock_fact = 10; break;
}

/**/Added for clock rate intervals 1000 - 10000/**/

clock_fact=clock_user;
clock_rate=(int)(10000/clock_fact);
timebase=3;

printf("\nSpeed is %dHz\n",clock_rate);

/** */

printf("\nEnter the loop size (<%f): ",(float)DATA);
scanf("%lf%c",&loop_long,&cr);

printf("\nEnter step start (in final 10,000): ");
scanf("%lf%c",&stst,&cr);

duration = loop_long/clock_rate;
printf("\nEstimated duration (w/o printing) is %.3f seconds\n\n",
    duration);

printf("\nEstimated step start is %.3f seconds\n\n",
    stst/clock_rate);

loop=loop_long;
if (loop_long > 10000) loop=10000;

printf("\nDo you want to print? ('n' for no):");
/**/cr=getchar();
po=getchar();/**/

po='n';

printf("\nFreeze integrator at step start? ('n' for no):");
cr=getchar();
freeze=getchar();

printf("\nEnter step size, ref, in micrometers: ");
scanf("%lf%c",&ref,&cr);

ref=ref*1e-6;

```

```

printf("\nEnter pre-conditioner gain, Gin: ");
scanf("%lf%c",&Gin,&cr);

printf("\nEnter proportional gain K: ");
scanf("%lf%c",&K,&cr);

printf("\nEnter pre-lead gain Kl: ");
scanf("%lf%c",&Kl,&cr);

printf("\nEnter integrator gain Ki: ");
scanf("%lf%c",&Ki,&cr);

/*printf("\nEnter TRANSV conversion factor (.05 V/mil typical 1V rg): ");
scanf("%f%c",&fact_short,&cr);
if (fact_short > .5 || fact_short <-.5) fact_short=.5;
printf(" %f",fact_short);

printf("\nEnter SCAN conversion factor (.005 V/mil typical 1 V rg): ");
scanf("%f%c",&fact,&cr);

fact=10;

if (fact > .005 || fact < -.005) fact=.005;
printf(" %f",fact);*/

printf("\nEnter Ready to go? ***BREAK NOW IF YOU MUST***");
scanf("\n%c",&cr);

printf("\nEnter Center & it will go!.....\n\n");
}

void clock_setup(void)
{
    /*** Configure the counter ***/

    err_num_cl = CTR_Config(board_cl,ctr,0,0,0,0);
    ErrPrint ("Get_DA_Brds_Info", err_num_cl);

    err_num_cl = CTR_EvCount(board_cl,ctr,timebase,1);
    ErrPrint ("Get_DA_Brds_Info", err_num_cl);
}

void controller(void)
{
    int
        chan_clock,      /* channel number for clock input (if used) */
        value_out,      /* 12 bit command to write to the D/A output */
        value_in,       /* 12 bit reading of A/D conversion of input */
        lo_count=0,     /* local, integer count */
        outState=1,     /* logic level of counter */
        overflow,       /* checks for counter overflow */
        ctrcount=0,     /* counts for the clock delay */
        dumctrcount=0;  /* dummy for ctrcount */
}

```

```

double
    volts_out=0,      /* from desired voltage, to 12 bit value_out */
    cap_out=0,       /* small displacement output voltage */
    count=0,        /* used to count main loop */
    remain=0,       /* helps check for even # in main loop */
    skip=0,         /* determines how many time clock skips*/
    reg_delay,      /* used for holdover delay (vs. getch()) */
    new_negsum,     /* used in lead */
    old_negsum=0,   /* used in lead */
    amps,          /* amps going out */
    new_x,         /* new x for control loop */
    old_x,         /* old x for control loop */
    Gref,         /* Conditioned input */
    Ppi,         /* proportional value */
    sum=0;        /* integrator sum */

/**/ Get an initial old_x value /**/

strcpy( cmdstr, "AB");
adecall( cmdstr, data);

if (data[0] == 32766) data[0] = 5000;
if (data[0] == 32767) data[0] = -5000;

old_x=(data[0]-ade_zero)*ade_calib*25.4e-6;

/**/ Hold until centered /**/

/*while (!((old_x < (double)(.000005)) && (old_x > (double)(-.000005))))
{
    strcpy( cmdstr, "AB");
    adecall( cmdstr, data);

    if (data[0] == 32766) data[0] = 5000;
    if (data[0] == 32767) data[0] = -5000;

    old_x=(data[0]-ade_zero)*ade_calib*25.4e-6;
}*/

/**/ Removed from control loop /**/

AI_Clear( board_in );

/**/ /**/

/**/***** DO THE LOOP *****/

while (count < loop_long)
{

/**/ Clock Hold /**/

outState=1;
    while (outState == 1)

```

```

    {
        err_num_cl = CTR_EvRead(board_cl,ctr,&overflow,&ctrcount);
        /*printf("%d %d %.0f\n",ctrcount,dumctrcount,count);*/
        if (ctrcount == 0 || ctrcount == dumctrcount+clock_fact ||
            ctrcount == -dumctrcount) outState=0;
        if (ctrcount > dumctrcount+clock_fact)
            {skip=skip+1; outState=0;}
    }

/*printf("%d %d %.0f\n",ctrcount,dumctrcount,count);*/

/** Inputs from MIO and ADE boards & ADE limit check ***/

/*err_num_in = AI_VRead( board_in, chan_in, gain, &volts_in);*/
/*ErrPrint ("AI_VRead", err_num_in);*/

strcpy( cmdstr, "AB");
adecall( cmdstr, data);

if (data[0] == 32766) data[0] = 5000;
if (data[0] == 32767) data[0] = -5000;

/** Small displacement control loop ***/

Gref=Gin*ref;

if (count<stst) Gref=0;          /* Determines start of step */

new_x=(data[0]-ade_zero)*ade_calib*25.4e-6;

/** Lead compensator ***/

x_mils=new_x;                   /* Laying around for printout*/

new_negsum=(15.02*new_x-14.11*old_x)+.0872*old_negsum;

/** Proportional ***/

Ppi = K * (Gref - new_negsum);

/** Integrator ***/

if (count < stst)
    sum = sum + Ki * 5e-4 * (Gref - new_negsum);

if (count >= stst && freeze != 'y')
    sum = sum + Ki * 5e-4 * (Gref - new_negsum);

/** Ant-windup ***/

if (sum >= .020) sum = .020;

if (sum <= -.020) sum = -.020;

```



```

/** Forward path */
amps=Kl*Kc*(Ppi + sum);

/** Caution on output */

if (amps > .5)
    amps = .5;
if (amps < -.5)
    amps = -.5;
if ((new_x > 500e-6) || (new_x < -500e-6))
    amps=0;

cap_out = amps*20;

/*cap_out = x_mils*fact_short;*/ /* follower option */

/** Large displacement control loop */

/*z_mils = (volts_in-MIO_zero)*MIO_calib;

volts_out = z_mils*fact;*/ /* follower option */

/*-> Note: PI control was added here - see thesim18.c for that information <-*/

/*remain=count/2 - (long int)(count/2); .. square wave option ..
volts_out=1;
if (remain > 0) volts_out=-1;*/

/** Outputs to AO board */

/*if (!err_num_out && !err_num_in)
{*/
    /*err_num_out = AO_VWrite( board_out, chan_out, volts_out);*/
    if (use_output == 'y') cap_out=0;
    if (count>(loop_long-100)) cap_out=0;
    err_num_out = AO_VWrite( board_out, chan_out_small, cap_out);
/*}*/

/** Array storing of the output */

small_disp[lo_count]=new_x;
large_disp[lo_count]=amps; /*** altered to monitor integrator current */
integrator[lo_count]=sum*Kl*Kc;
index[lo_count]=count;

/** Other main loop events such as incrementing, setting, printing */

if(po != 'n') /* decide whether to print results */
printf("IN: %.3f mics **LEAD: %.3f **AMPS %.3f \n",
    new_x*1e6,new_negsum,amps);

count = count+1;
lo_count=lo_count+1;

```

```

if(count < (loop_long-loop)) lo_count=lo_count-1;
if(lo_count > ((int)DATA-1)) /* maximum storage capacity */
    lo_count=lo_count-1;
dumctrcount=ctrcount;
old_x = new_x;
old_negsum=new_negsum;
}

/***** DONE - Zero Output *****/

zero();

/**** Skip Ratio ****/

printf("\n Skip ratio is %.0f out of %.0f for %.2f percent\n"
    ,skip,count,skip/count*100);
printf("\nlo_count = %d\n",lo_count);
}

void graphit_em(void)
{
    _chartenv env; /* graphics protocol */

    int
        mode = _VRES16COLOR, /* stuff for graphics */
        _getch( void); /* used to wait for user input */

    double
        graph_delay=0; /* holds graph like _getch() */

    float
        portion=0; /* what % of data to show */

    int
        showpoints=0, /* how many points to show */
        scat_to_line=0, /* transfer data to char */
        cut_index=0,
        intportion;

    /**** Graph options ****/

    printf("\n\nDo you want to see e-m graph? (default='y'): ");
    cr=getchar();
    reply=getchar();

    /**** If given the go-ahead, graph with respective parameters ****/

    if (reply != 'n')
    {
        printf("\n\nWhat %% of the time %.3f secs for graph (%.0f points): "
            ,duration,loop);
        printf("\n(Literal max: 1000 points - pick 1000 intervals)\n");
        scanf("%f%c",&portion,&cr);
    }
}

```

```

printf("\npre-portion: %f\n",portion);

portion=portion/100;
portion=(portion*loop/1000);

printf("\nportion: %f\n",portion);

intportion=(int)portion;

showpoints=999;

printf("\nintportion: %d\n",intportion);

for (graph_delay=1;graph_delay < 7000000; graph_delay++);

for(scat_to_line=0;scat_to_line < 1000; scat_to_line++)
{
    cut_index=cut_index+intportion;
    if (cut_index > (loop-1)) cut_index=0;
    cut_small_disp[scat_to_line]=small_disp[cut_index];
    /*printf("cut_index=%d  cut_small =%f  small = %f\n",
        cut_index,cut_small_disp[scat_to_line],small_disp[cut_index]);*/
    *line_data[scat_to_line]=(char)index[scat_to_line];
}

/** Set highest video mode available ***/

if( _setvideomode( _MAXRESMODE ) == 0)
    exit( 0 );

/** Initialize chart library and default scatter diagram ***/

_pg_initchart();
_pg_defaultchart( &env, _PG_LINECHART, _PG_POINTANDLINE);

strcpy (env.xaxis.axistitle.title, "Time");
strcpy (env.yaxis.axistitle.title, "Displacement");

/** Add titles and some chart options for 1st chart ***/

strcpy( env.maintitle.title, "Your Data");
env.maintitle.titlecolor = 6;
env.maintitle.justify = _PG_RIGHT;

strcpy( env.subtitle.title, "For The Small Displacements");
env.subtitle.titlecolor = 6;
env.subtitle.justify = _PG_RIGHT;

env.chartwindow.border=FALSE;

/** If all ok, scatter graph variables (1st set) interested in ***/

if( _pg_chart( &env, line_data, cut_small_disp, showpoints) )
{

```

```

        _setvideomode( _DEFAULTMODE );
        _outtext( "Error: can't draw chart" );
    }
    else
    {
        for (graph_delay=1;graph_delay < 50000000; graph_delay++);
        /* _getch(); */
        _setvideomode( _DEFAULTMODE);
    }
}

void graphit_ed(void)
{
    _chartenv env;                /* graphics protocol */

    int
        mode = _VRES16COLOR,      /* stuff for graphics */
        _getch( void);           /* used to wait for user input */

    double
        graph_delay=0;           /* holds graph like _getch() */

    float
        portion=0;               /* what % of data to show */

    int
        showpoints=0,            /* how many points to show */
        scat_to_line=0;         /* transfer data to char */

    /*** Graph options ***/

    printf("\n\nDo you want to see e-d graph? (default='y'): ");
    cr=getchar();
    reply=getchar();

    /*** If given the go-ahead, graph with respective parameters ***/

    if (reply != 'n')
    {
        printf("\n\nWhat %% of the time %.3f secs for graph (%.0f points): "
            ,duration,loop);
        printf("\n(Literal max: 1000)\n");
        scanf("%f%c",&portion,&cr);

        showpoints = (int)(portion * loop/100);
        if (showpoints > 999) showpoints=999;

        printf("\nshowpoints: %d\n",showpoints);

        for(scat_to_line=0;scat_to_line < 1000; scat_to_line++)
            *line_data[scat_to_line]=(char)index[scat_to_line];

        /*** Set highest video mode available ***/

```

```

if( _setvideomode( _MAXRESMODE ) == 0)
    exit( 0 );

/**/ Initialize chart library and default scatter diagram ***/

_pg_initchart();
_pg_defaultchart( &env, _PG_LINECHART, _PG_POINTANDLINE);

strcpy (env.xaxis.axistitle.title, "Time");
strcpy (env.yaxis.axistitle.title, "Displacement");

/**/ Add titles and some chart options for 1st chart ***/

strcpy( env.maintitle.title, "Your Data");
env.maintitle.titlecolor = 6;
env.maintitle.justify = _PG_RIGHT;

strcpy( env.subtitle.title, "For The Large Displacements");
env.subtitle.titlecolor = 6;
env.subtitle.justify = _PG_RIGHT;

env.chartwindow.border=FALSE;

/**/ If all ok, scatter graph variables (2st set) interested in ***/

if( _pg_chart( &env, line_data, large_disp, showpoints) )
{
    _setvideomode( _DEFAULTMODE );
    _outtext( "Error: can't draw chart" );
}
else
{
    for (graph_delay=1;graph_delay < 50000000; graph_delay++);
    /* _getch(); */
    _setvideomode( _DEFAULTMODE);
}
}
}

void disksave(void)
{
    FILE *outfile, *fopen();

    long int
        j=0;

    int
        last_up=0;

    char
        fname [30];

    double

```

```

    inc=(double)1,
    count=(long int)loop;

printf("\nLet's save it...\n");
printf ("\nInput file name to save to: ");
scanf("%s",fname);

if (outfile = fopen(fname,"w"))
{
    printf("\nOpening the file (%lf pieces of data)...", count);

    fprintf(outfile,"K= %lf and offset =%f\n",K,ade_calib*ade_zero);

    for (j=0;j < (count-1);j++)
    {
        /*printf("\n j= %d, rest is %.2f %.3f %.3f"
                ,j,(index[j]/2),small_disp[j], large_disp[j]);*/
        fprintf(outfile,"%.2f %.3f %.2f %.2f\n",(index[j]/2),
                small_disp[j]*1e6, large_disp[j]*1000, integrator[j]*1000);
    }

    fclose(outfile);
    printf ("%d... Done.\n\n",j);

    /**Print last few before power is cut***/

    for (last_up=(j-110); last_up < (j-100); last_up++)
    {
        printf("Last -%d...disp = %.3f mics, amps = %.2f mA, int= %.2f\n",
                last_up,small_disp[last_up]*1e6,large_disp[last_up]*1000,
                integrator[last_up]*1000);
    }

    /**Print last value when it has slammed back to a side***/

    printf("\nFinal %d disp = %.3f mics, amps = %.2f mA, int = %.2f\n",
            0,small_disp[j]*1e6,large_disp[j]*1000,integrator[last_up]*1000);
}
else
{
    fclose(outfile);
    printf("Error saving data!!!");
}
}

void reinitialize(void)
{
    printf("\nReady to re-init? ");
    scanf("\n%c",&cr);

    printf("\nReinitializing the boards...");

    err_num_in = Init_DA_Brds( board_in, &brd_code_in );
    ErrPrint ("Init_DA_Brds", err_num_in);
}

```

```

err_num_out = Init_DA_Brds( board_out, &brd_code_out );
ErrPrint ("Init_DA_Brds", err_num_out);

err_num_cl = CTR_Stop(board_cl,ctr);
ErrPrint ("Get_DA_Brds_Info", err_num_cl);

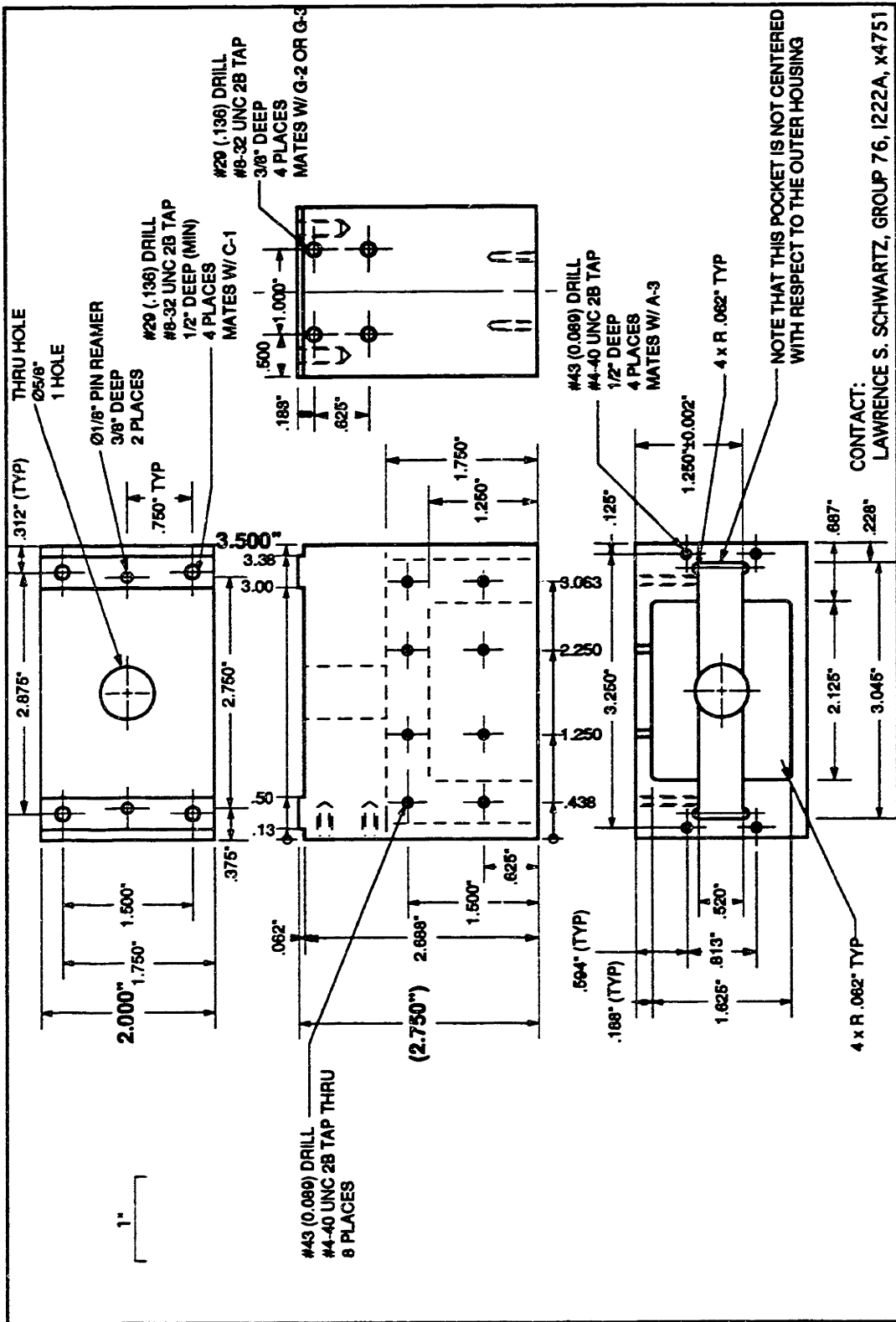
printf(" Boards & timer reinitialized\n");
}

void adecall( char far *cmd, int far *xarg)
{
    xregs.x.si = (unsigned) FP_OFF(cmd);
    xregs.x.di = (unsigned) FP_OFF(xarg);
    xregs_s.ds = (unsigned) FP_SEG(cmd);
    xregs_s.es = (unsigned) FP_SEG(xarg);
    int86x(ADE_int, &xregs, &xregs, &xregs_s);
    cmd[xregs.x.cx] = '\0';
}

void zero()
{
    err_num_out = Init_DA_Brds( board_out, &brd_code_out );
    ErrPrint ("Init_DA_Brds", err_num_out);
}

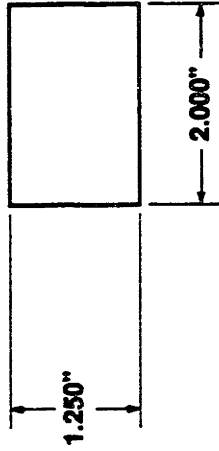
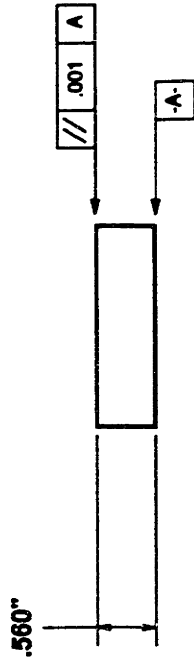
```

Appendix B: Drawings



| | | | |
|------------|--|-------------|--|
| PART: (A1) | DATE DRAWN: 23 OCT 94 REVISED: 5 DEC 94 | QUANTITY: 2 | <p>ACTUATOR HOUSING</p> <p>MATERIAL: ALUMINUM 6061-T6</p> |
| | | | <p>NOTES FINISH: ETCH AND CLEAN</p> |

1"



CONTACT:
LAWRENCE S. SCHWARTZ, GROUP 76, 1222A, x4751

PART: (A2)

ACTUATOR ASSEMBLY BLOCK

MATERIAL:
ALUMINUM 6061-T6

DATE DRAWN:
23 OCT 94

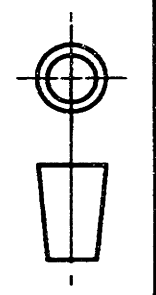
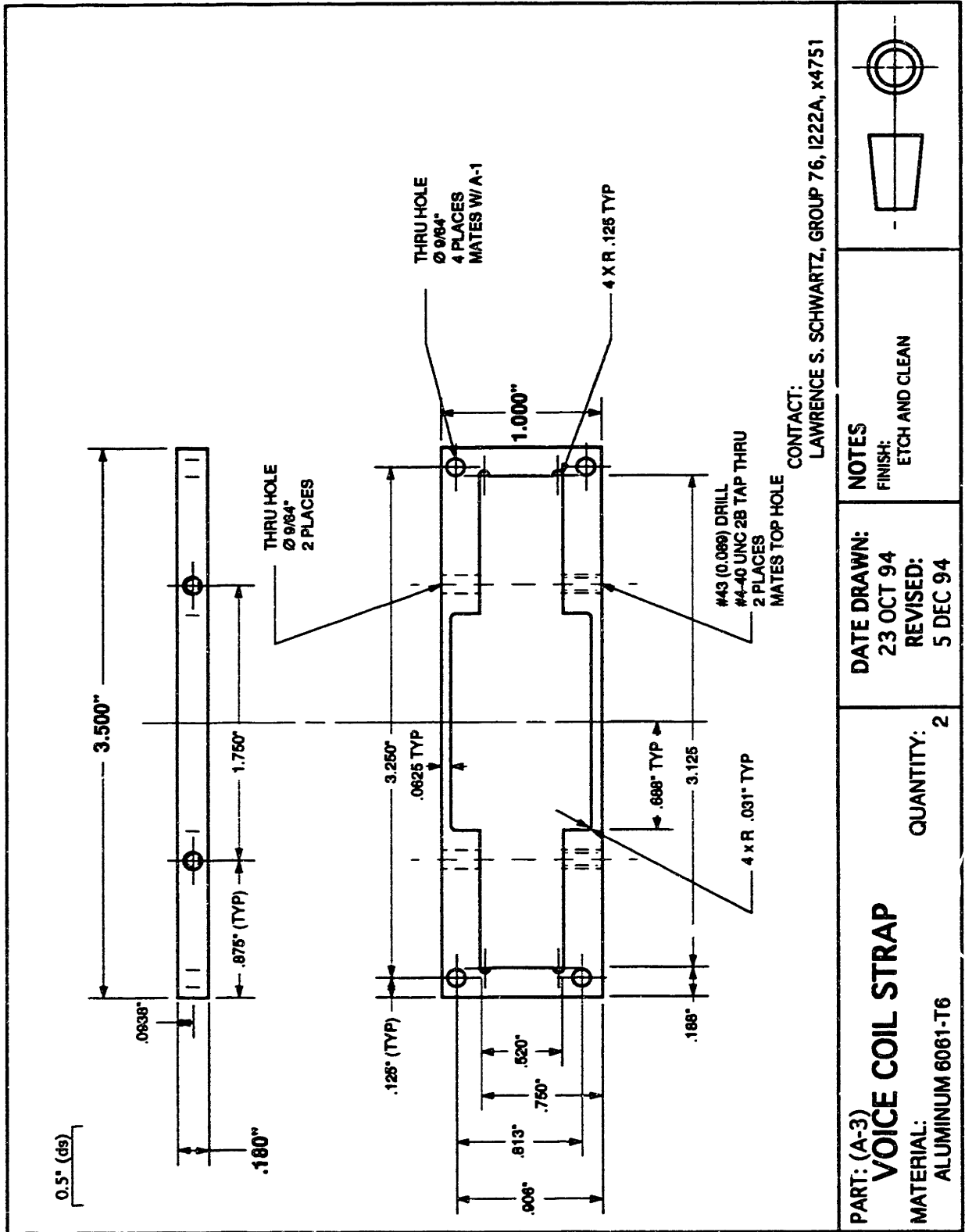
REVISD:
6 DEC 94

NOTES

FINISH:
ETCH AND CLEAN

QUANTITY: 4



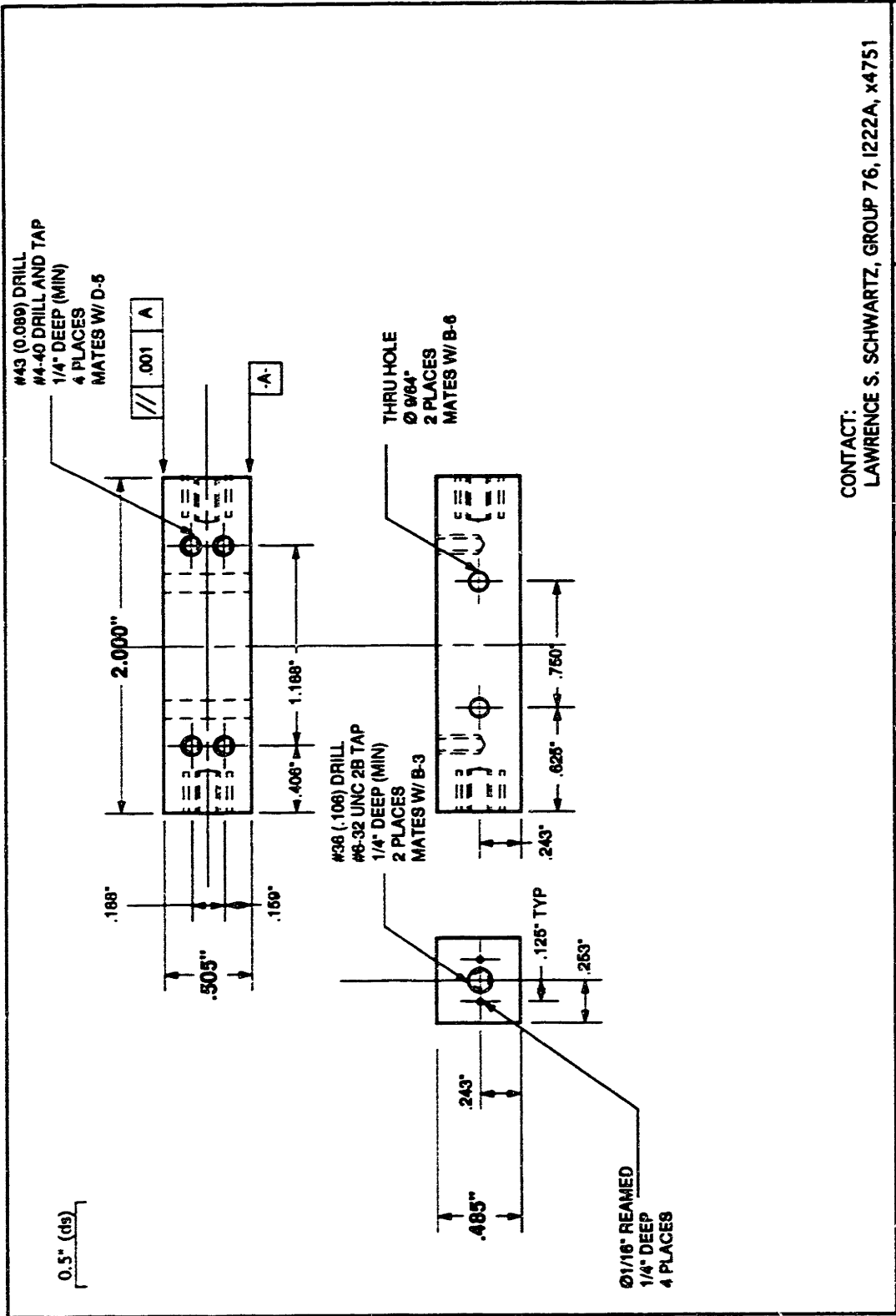


NOTES
FINISH:
ETCH AND CLEAN

DATE DRAWN:
23 OCT 94
REVISED:
5 DEC 94

QUANTITY: 2

PART: (A-3)
VOICE COIL STRAP
MATERIAL:
ALUMINUM 6061-T6

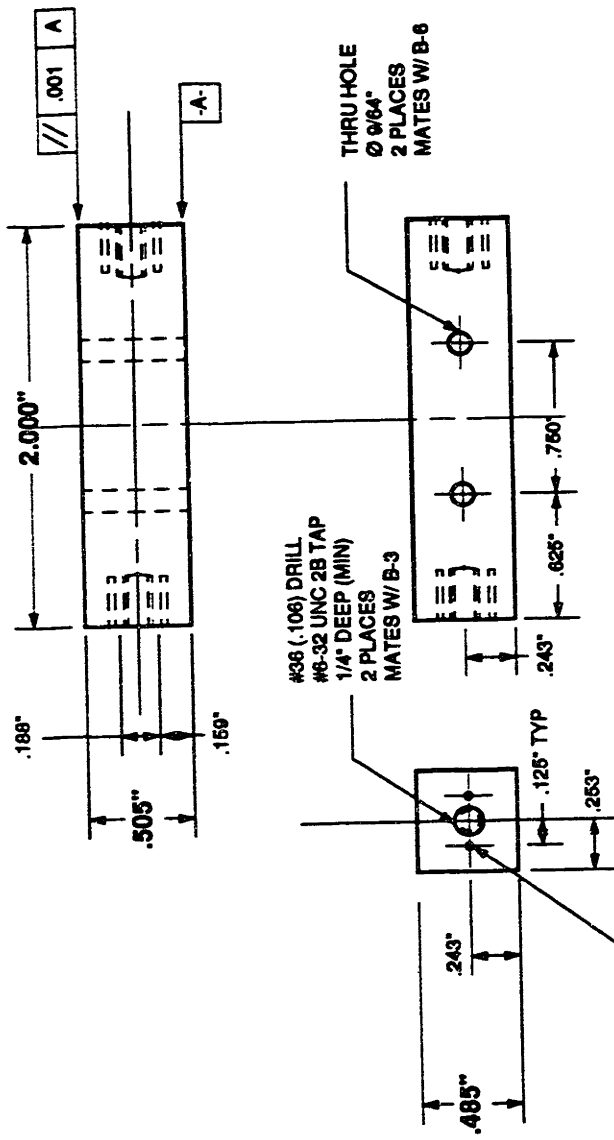


CONTACT:
LAWRENCE S. SCHWARTZ, GROUP 76, 1222A, X4751

| | | | |
|---|--------------------|--|---|
| <p>PART: (B-1) PLATEN TOP MATERIAL: ALUMINUM 6081-T6</p> | <p>QUANTITY: 1</p> | <p>DATE DRAWN: 23 OCT 94 REVISED: 5 DEC 94</p> | <p>NOTES FINISH: ETCH AND CLEAN</p> |
|---|--------------------|--|---|



0.5" (dis)




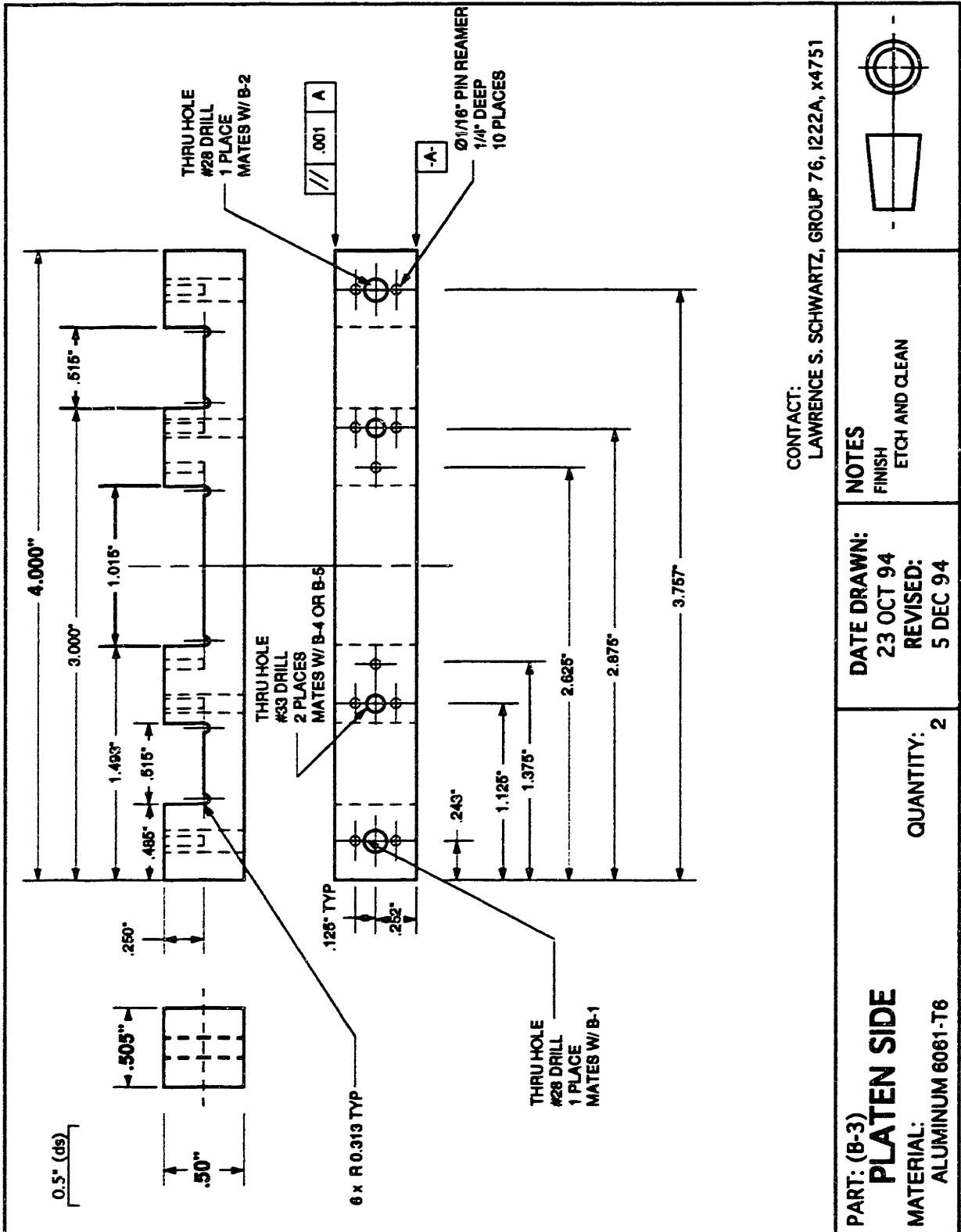
Ø1/16" REAMED
1/4" DEEP
4 PLACES

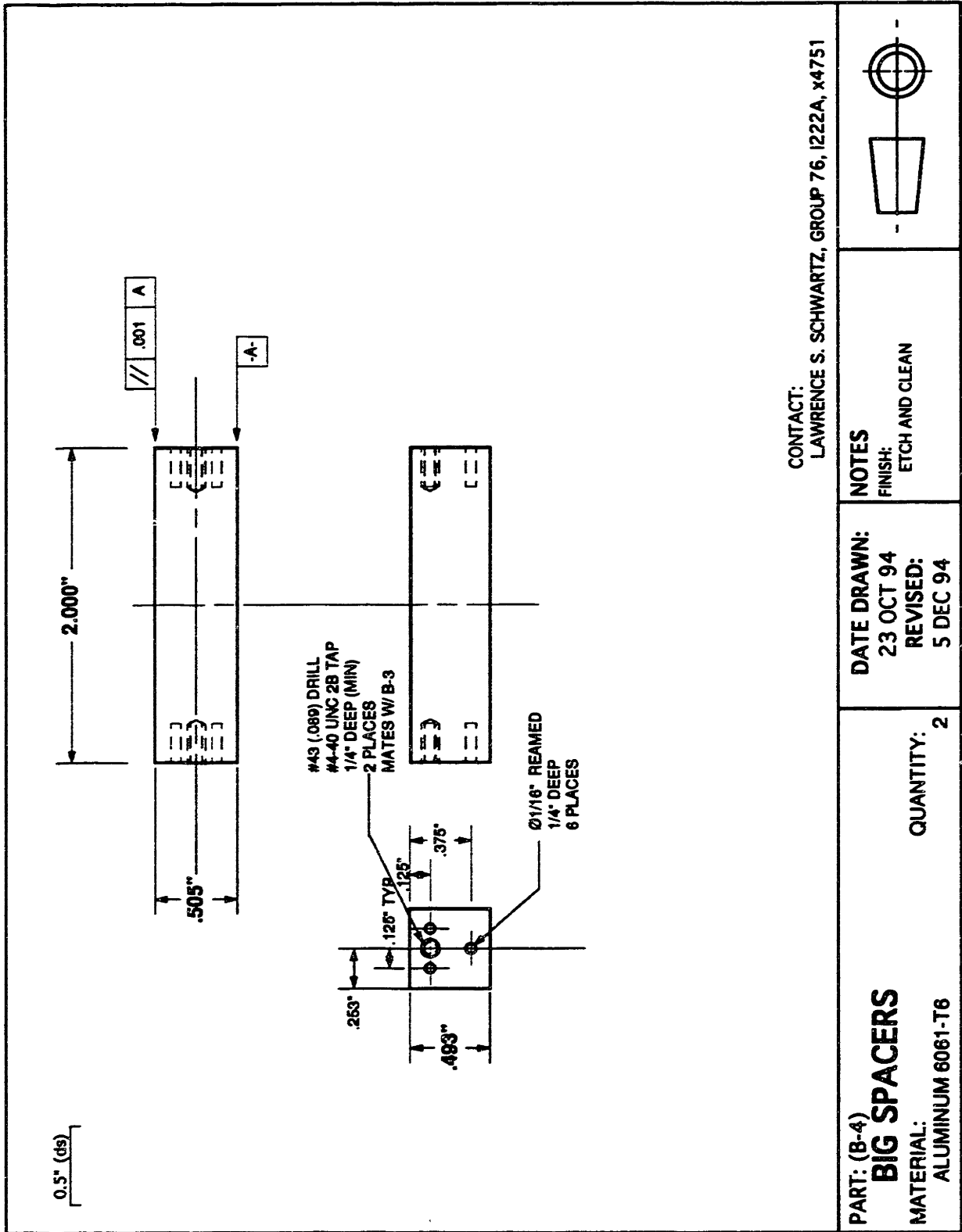
#38 (.106) DRILL
#6-32 UNC 2B TAP
1/4" DEEP (MIN)
2 PLACES
MATES W/ B-3

THRU HOLE
Ø 9/64"
2 PLACES
MATES W/ B-6

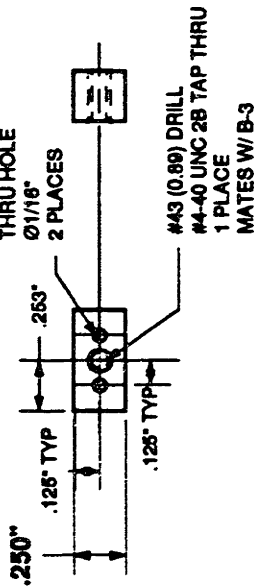
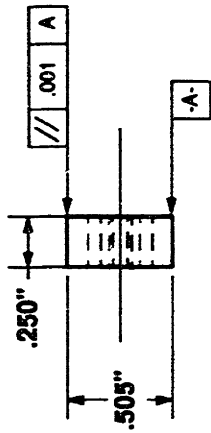
CONTACT:
LAWRENCE S. SCHWARTZ, GROUP 76, 1222A, X4751

| | |
|---|--|
|  | <p>NOTES FINISH: ETCH AND CLEAN</p> |
| <p>DATE DRAWN: 23 OCT 94 REVISED: 5 DEC 94</p> | <p>PART: (B-2) PLATEN BOTTOM MATERIAL: ALUMINUM 6061-T6</p> <p>QUANTITY: 1</p> |





0.5" (ds)



CONTACT:
LAWRENCE S. SCHWARTZ, GROUP 76, 1222A, X4751

PART: (B-5)

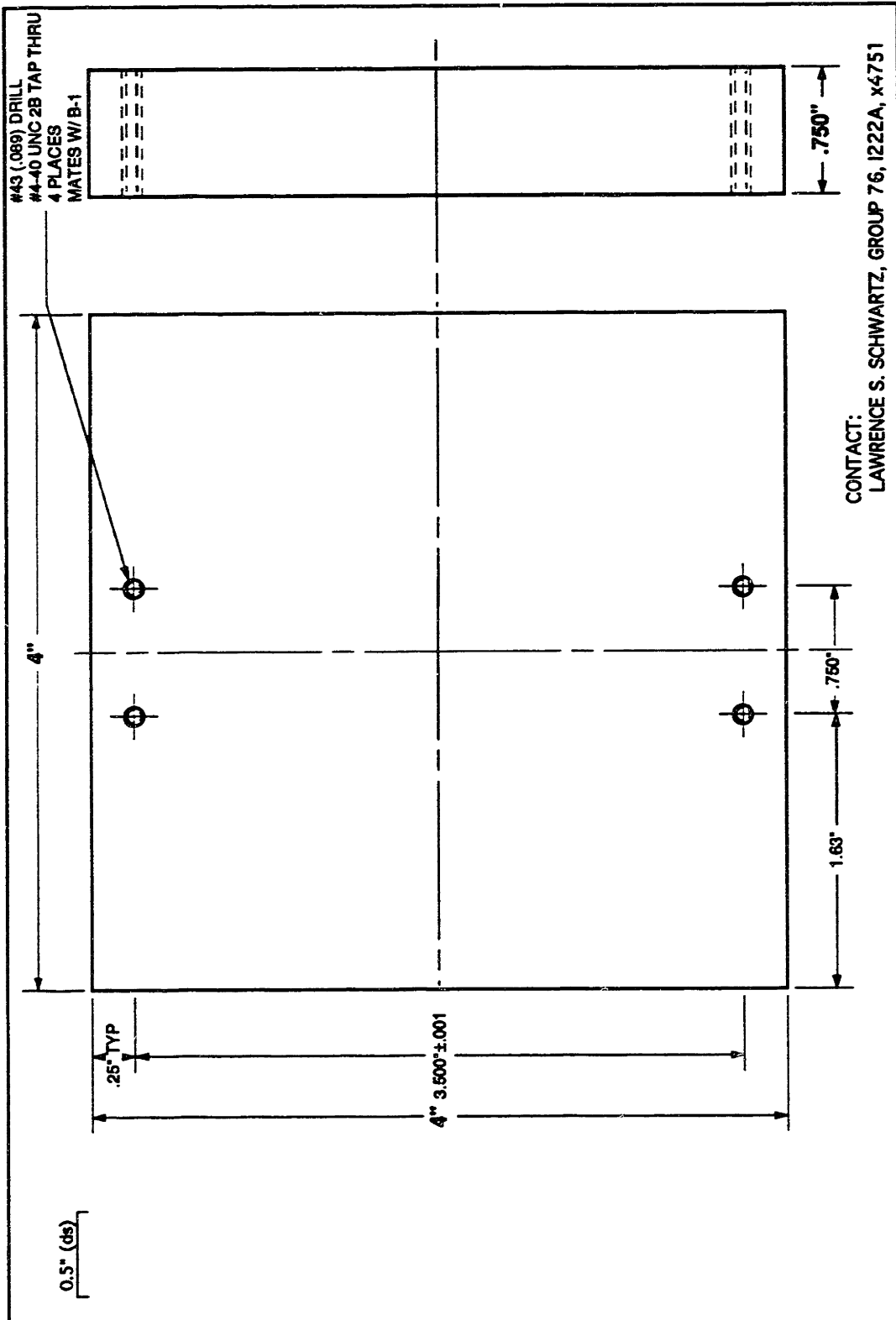
MAGNET BOOKENDS


MATERIAL:
ALUMINUM 6061-T6

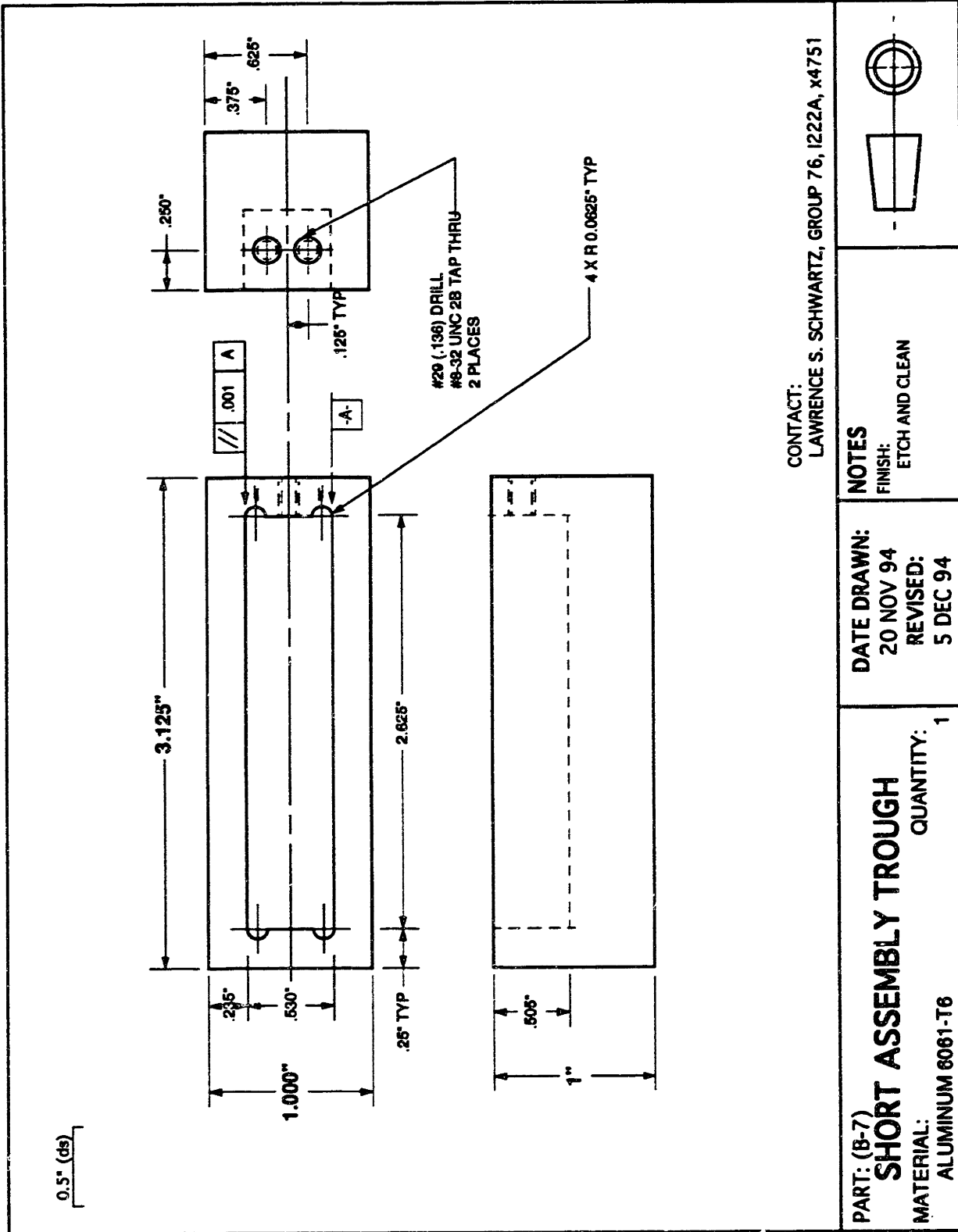
DATE DRAWN:
23 OCT 94
REVISED:
5 DEC 94

NOTES
FINISH:
ETCH AND CLEAN

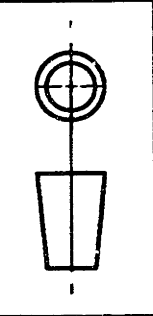




| | | | |
|--|--------------------|--|---|
| <p>PART: (B-6) PLATEN BACK MATERIAL: ALUMINUM 6061-T6</p> | <p>QUANTITY: 1</p> | <p>DATE DRAWN: 23 OCT 94 REVISED: 5 DEC 94</p> | <p>NOTES FINISH: ETCH AND CLEAN</p>  |
|--|--------------------|--|---|



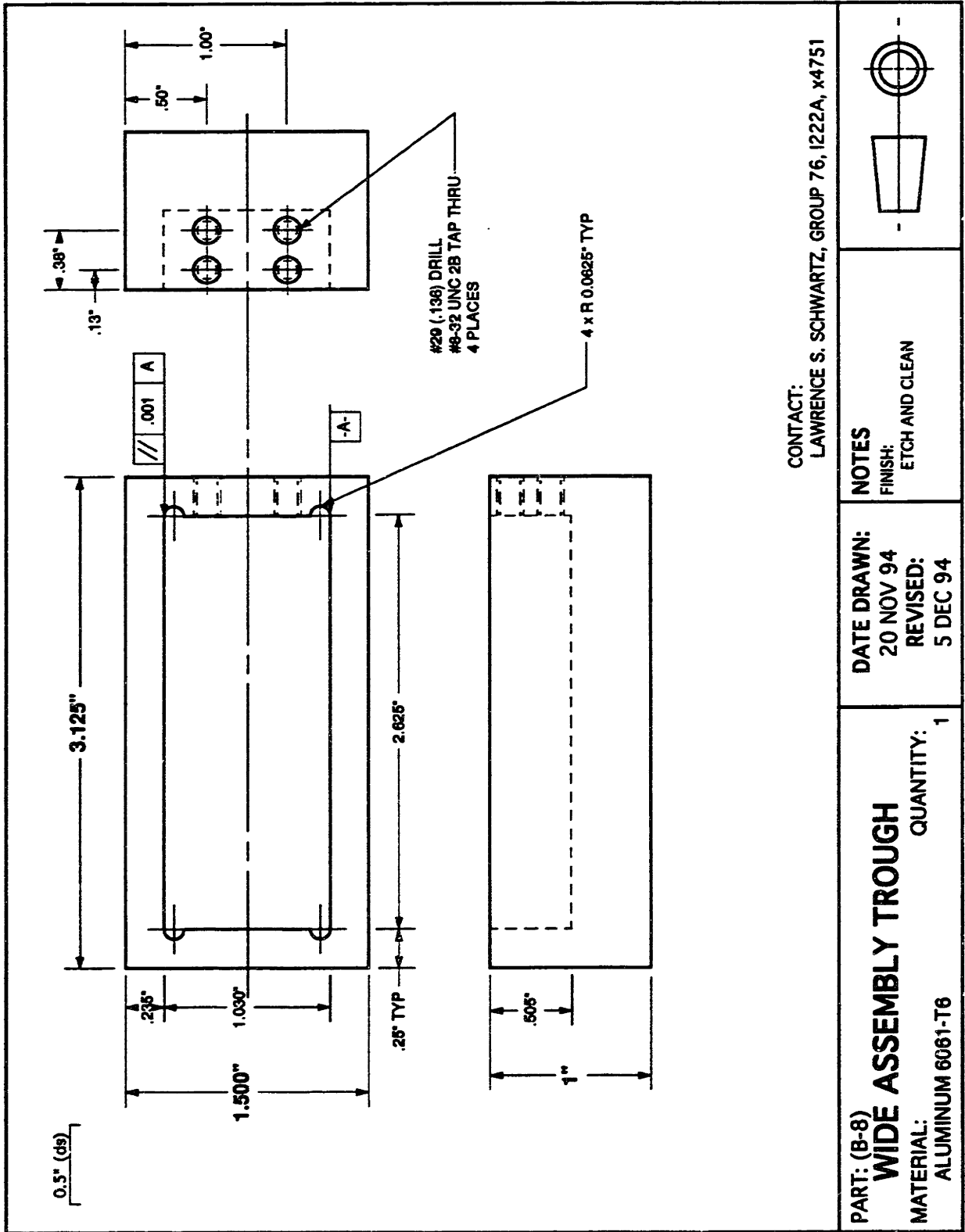
CONTACT:
LAWRENCE S. SCHWARTZ, GROUP 76, 1222A, x4751

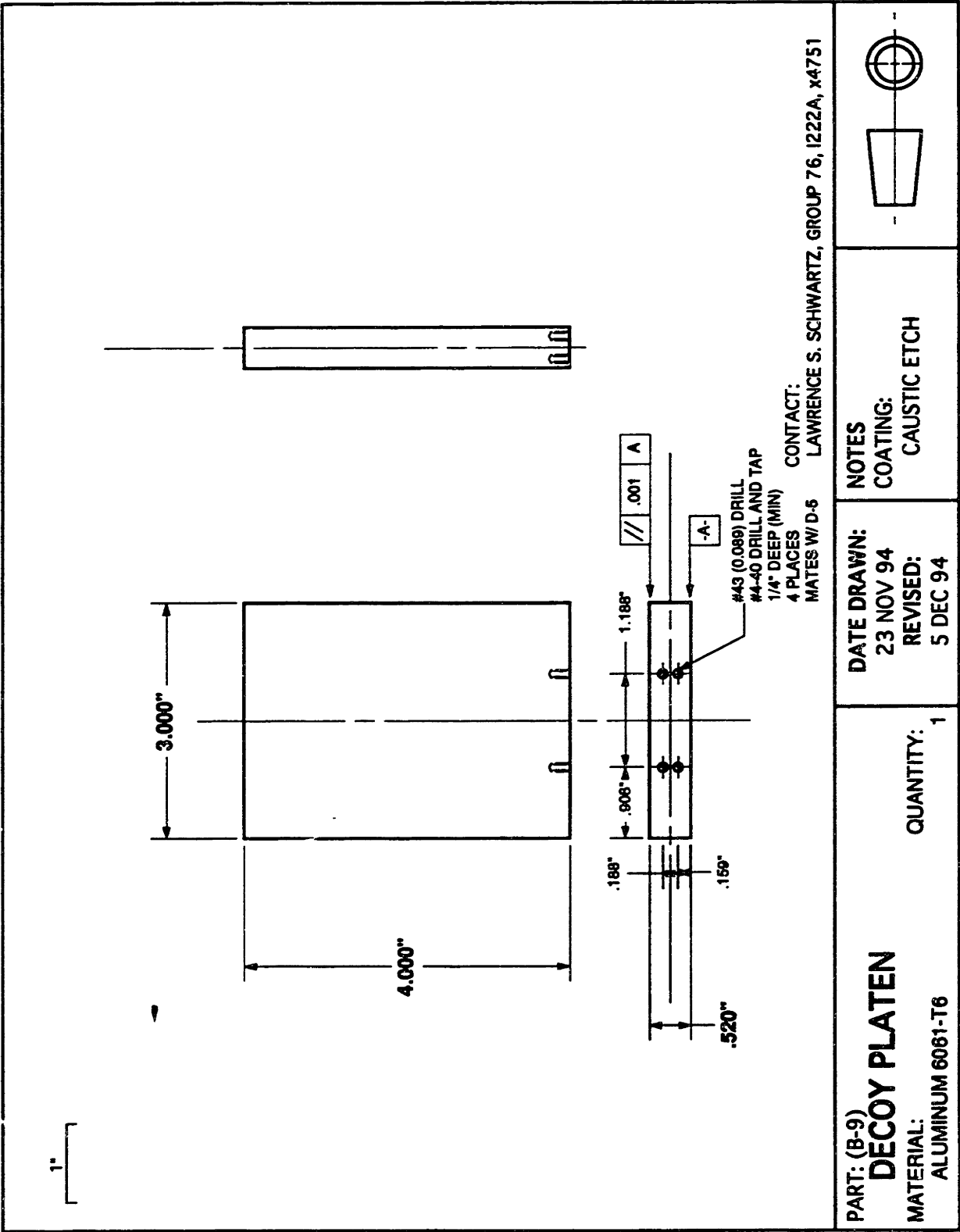


NOTES
FINISH:
ETCH AND CLEAN

DATE DRAWN:
20 NOV 94
REVISED:
5 DEC 94

PART: (B-7)
SHORT ASSEMBLY TROUGH
MATERIAL:
ALUMINUM 6061-T6
QUANTITY: 1

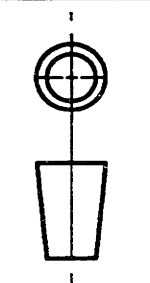


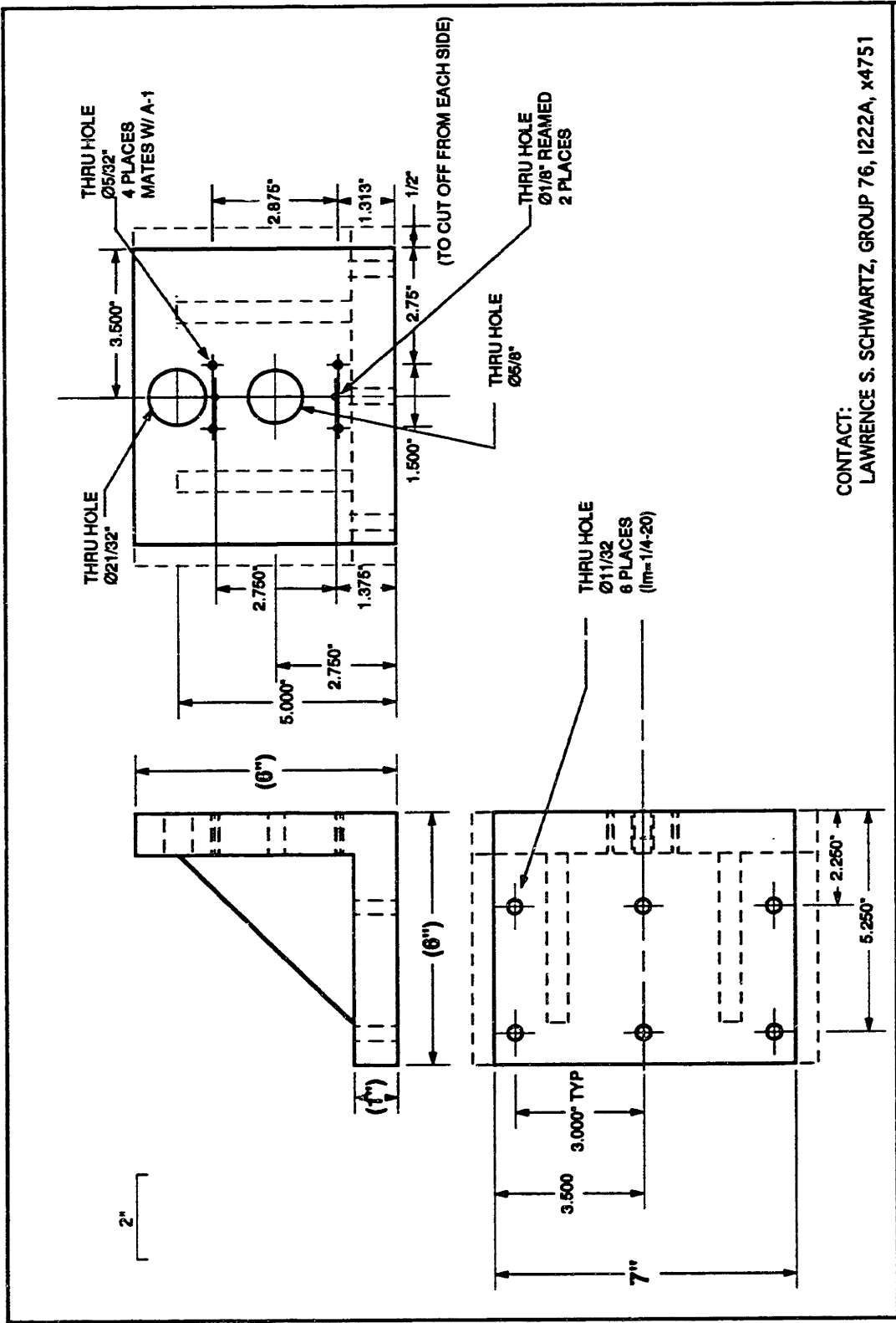


PART: (B-9)
DECOY PLATEN
 MATERIAL:
 ALUMINUM 6061-T6

DATE DRAWN:
 23 NOV 94
 REVISIONS:
 5 DEC 94

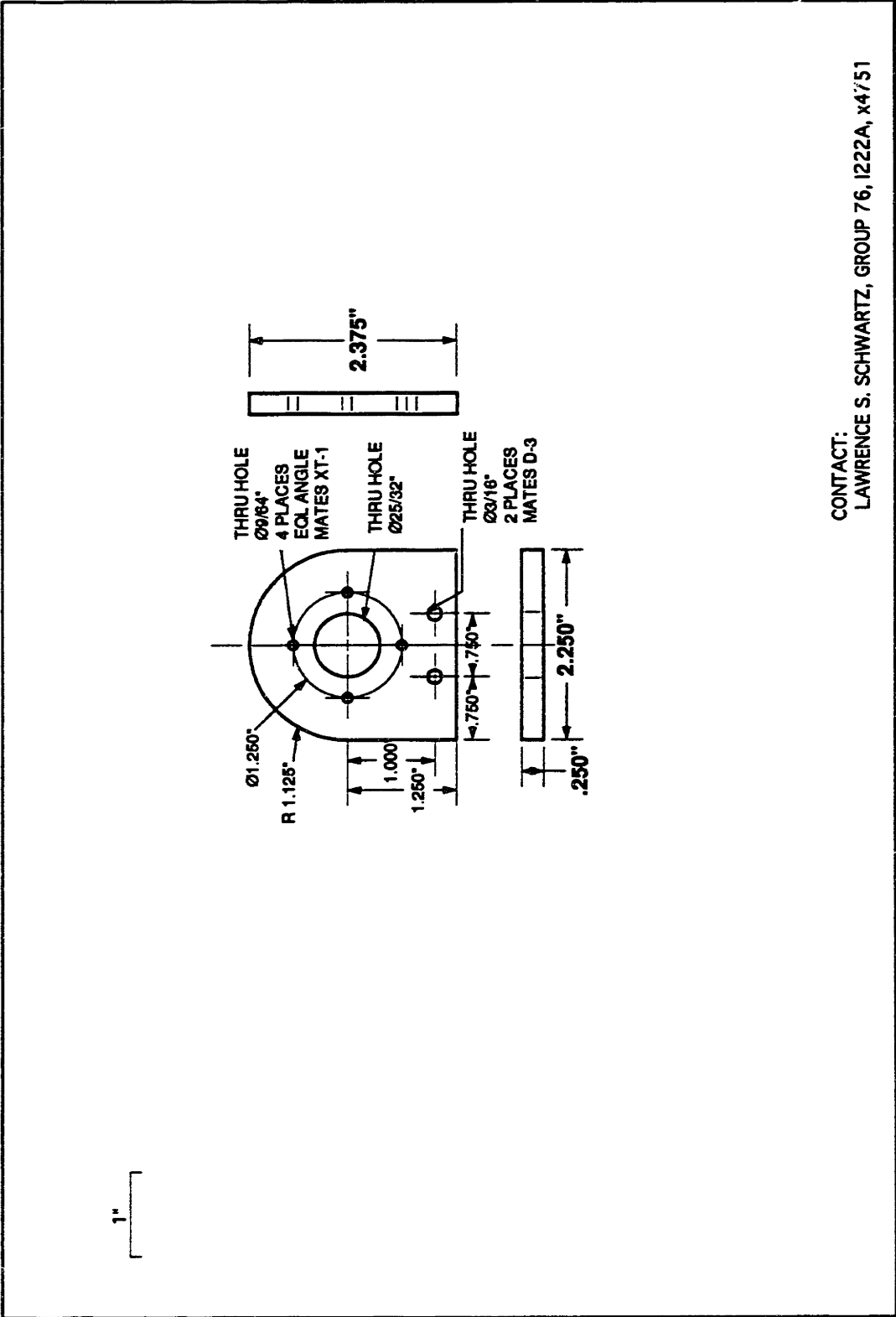
NOTES
 COATING:
 CAUSTIC ETCH







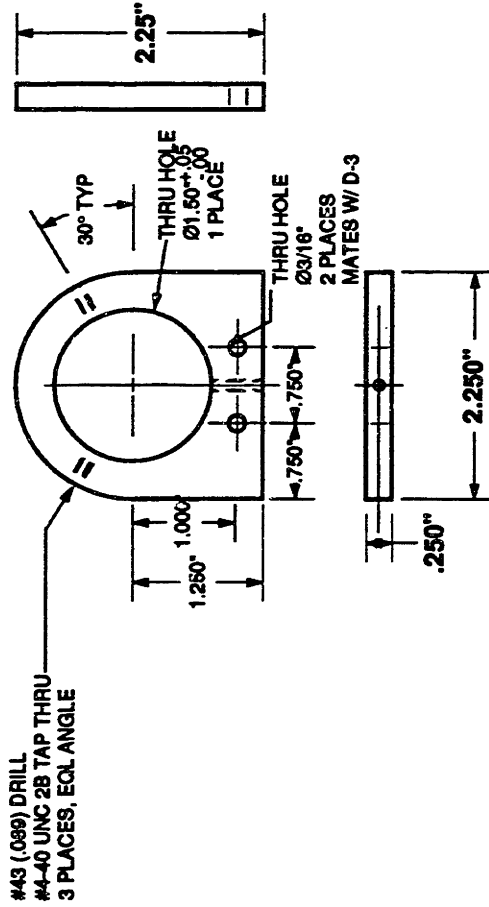
| | | | | |
|---|--------------------|--|--|--|
| <p>PART: (C-1) ANGLE MATERIAL: Pre-Cut Precision Angle Steel</p> | <p>QUANTITY: 2</p> | <p>DATE DRAWN: 30 OCT 94 REVISED: 5 DEC 94</p> | <p>NOTES CUT BRACKET WIDTH FIRST LEAVE OUTER FACES EXACTLY PERPENDICULAR</p> | |
|---|--------------------|--|--|--|

CONTACT:
LAWRENCE S. SCHWARTZ, GROUP 76, 1222A, x4751



| | | | | | | |
|--|------------------------------------|---|---|---|-------------|---|
| CONTACT: LAWRENCE S. SCHWARTZ, GROUP 76, 1222A, x4751 | NOTES FINISH: ETCH AND CLEAN | DATE DRAWN: 7 NOV 94 REVISED: 5 DEC 94 | PART: (D-1) AB MOVING CLAMP MATERIAL: ALUMINIUM 6061-T6 |  | QUANTITY: 1 |  |
|--|------------------------------------|---|---|---|-------------|---|

1"



CONTACT:
LAWRENCE S. SCHWARTZ, GROUP 76, 1222A, X4751

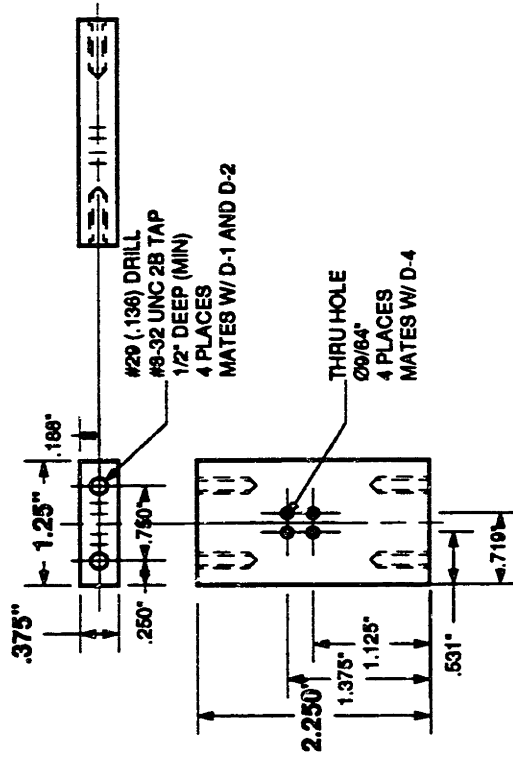
PART: (D-2)
AB 2ND MOVING CLAMP
MATERIAL:
ALUMINUM 6061-T6

DATE DRAWN:
7 NOV 94
REVISD:
5 DEC 94

NOTES
FINISH:
ETCH AND CLEAN



1"



CONTACT:
 LAWRENCE S. SCHWARTZ, GROUP 76, I222A, X4751

PART: (D-3)

AB MOVING PLATFORM

MATERIAL:
 ALUMINIUM 6061-T6

QUANTITY: 1

DATE DRAWN:

7 NOV 94

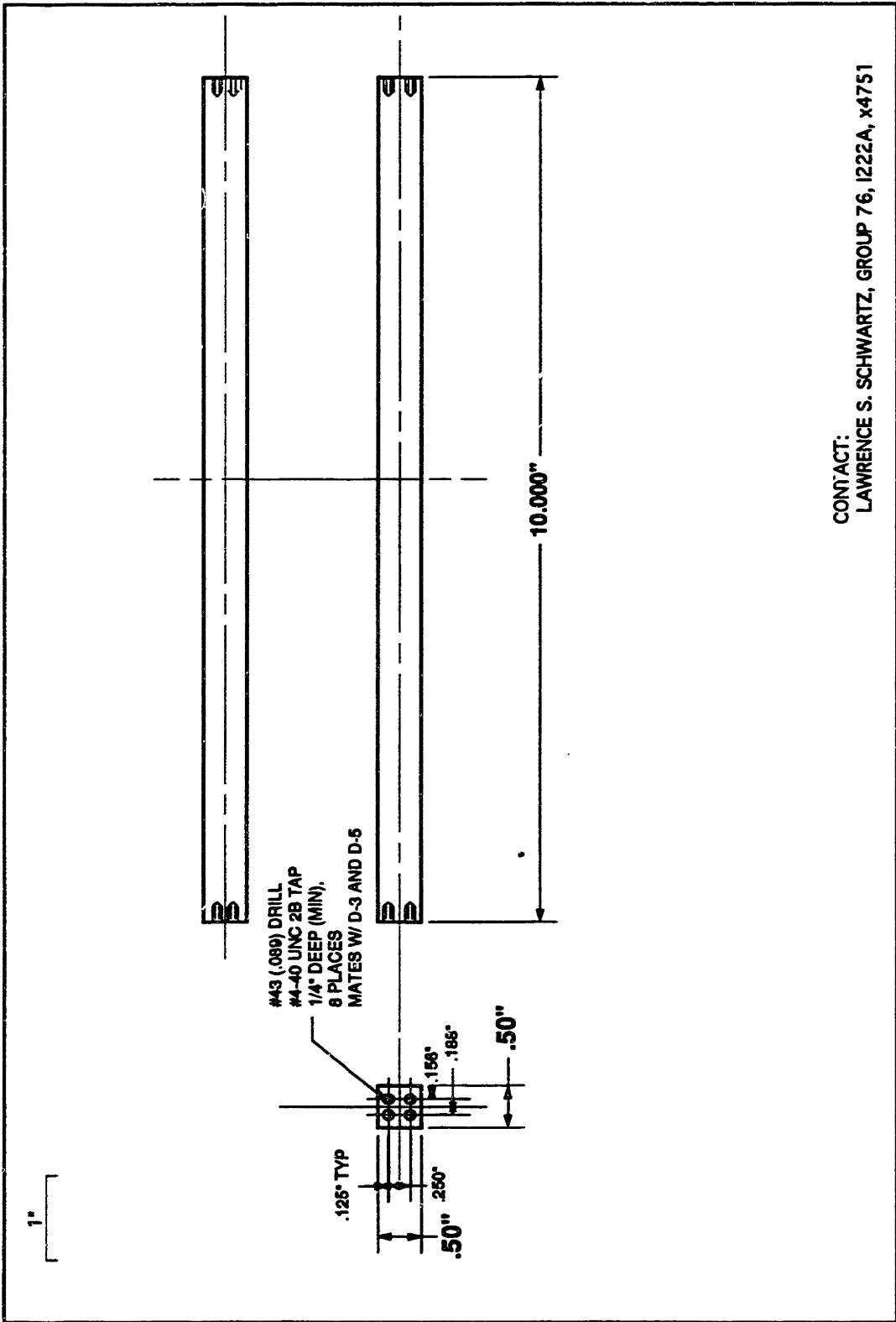
REVISED:

5 DEC 94

NOTES

FINISH:
 ETCH AND CLEAN



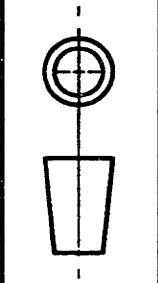


CONTACT:
LAWRENCE S. SCHWARTZ, GROUP 76, 1222A, x4751

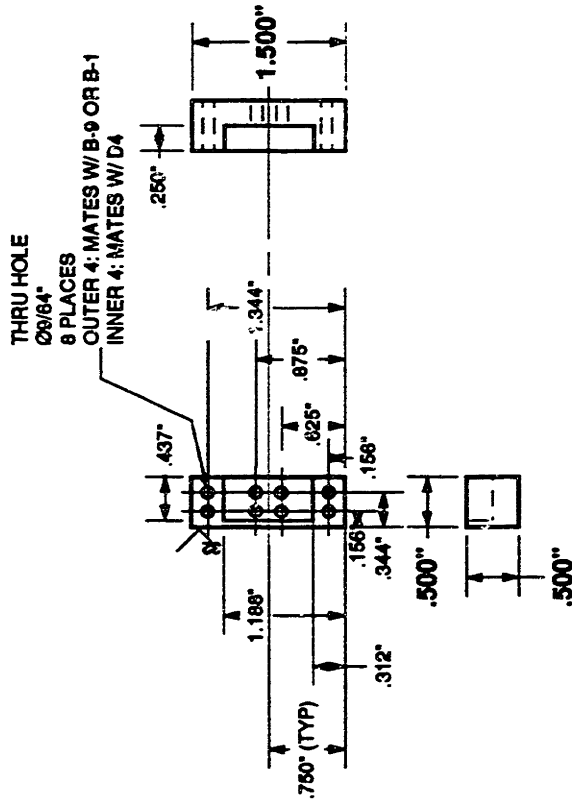
PART: (D-4)
AB MOVING PENDULUM
MATERIAL: ALUMINUM 6061-T6

DATE DRAWN:
7 NOV 94
REVISED:
5 DEC 94

NOTES
FINISH:
ETCH AND CLEAN



1"



CONTACT:
LAWRENCE S. SCHWARTZ, GROUP 76, I222A, x4751

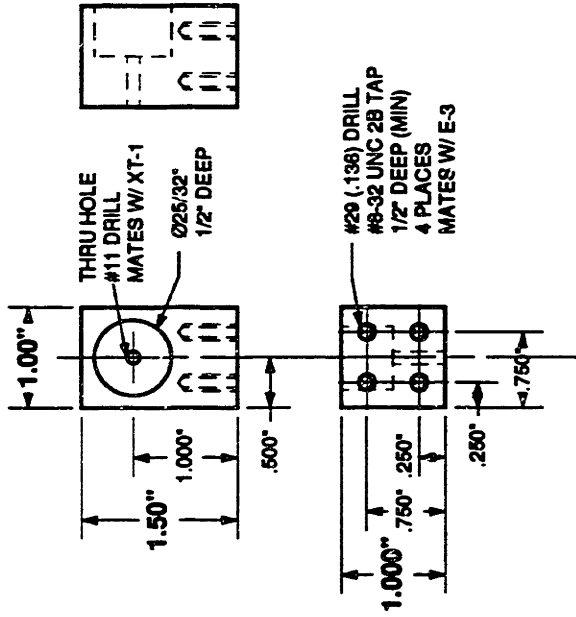
PART: (D-5)
AB MOVING PENDULUM BLOCK
 MATERIAL:
 ALUMINUM 6061-T6
 QUANTITY: 1

DATE DRAWN:
7 NOV 94
 REVISED:
5 DEC 94

NOTES
 FINISH:
 ETCH AND CLEAN
 1 POLISHED SURFACE



1"



CONTACT:
LAWRENCE S. SCHWARTZ, GROUP 76, I222A, X4751

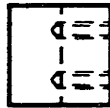
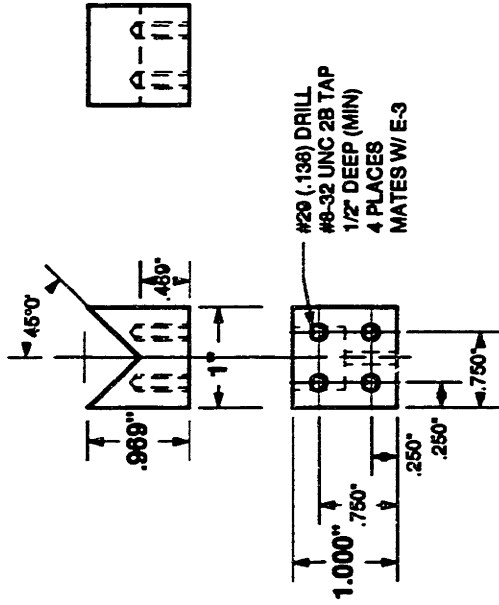
PART: (E-1)
AB STATIONARY BRACKET-L
MATERIAL:
ALUMINUM 6061-T6

DATE DRAWN:
7 NOV 94
REVISED:
5 DEC 94

NOTES
FINISH:
ETCH AND CLEAN



1"



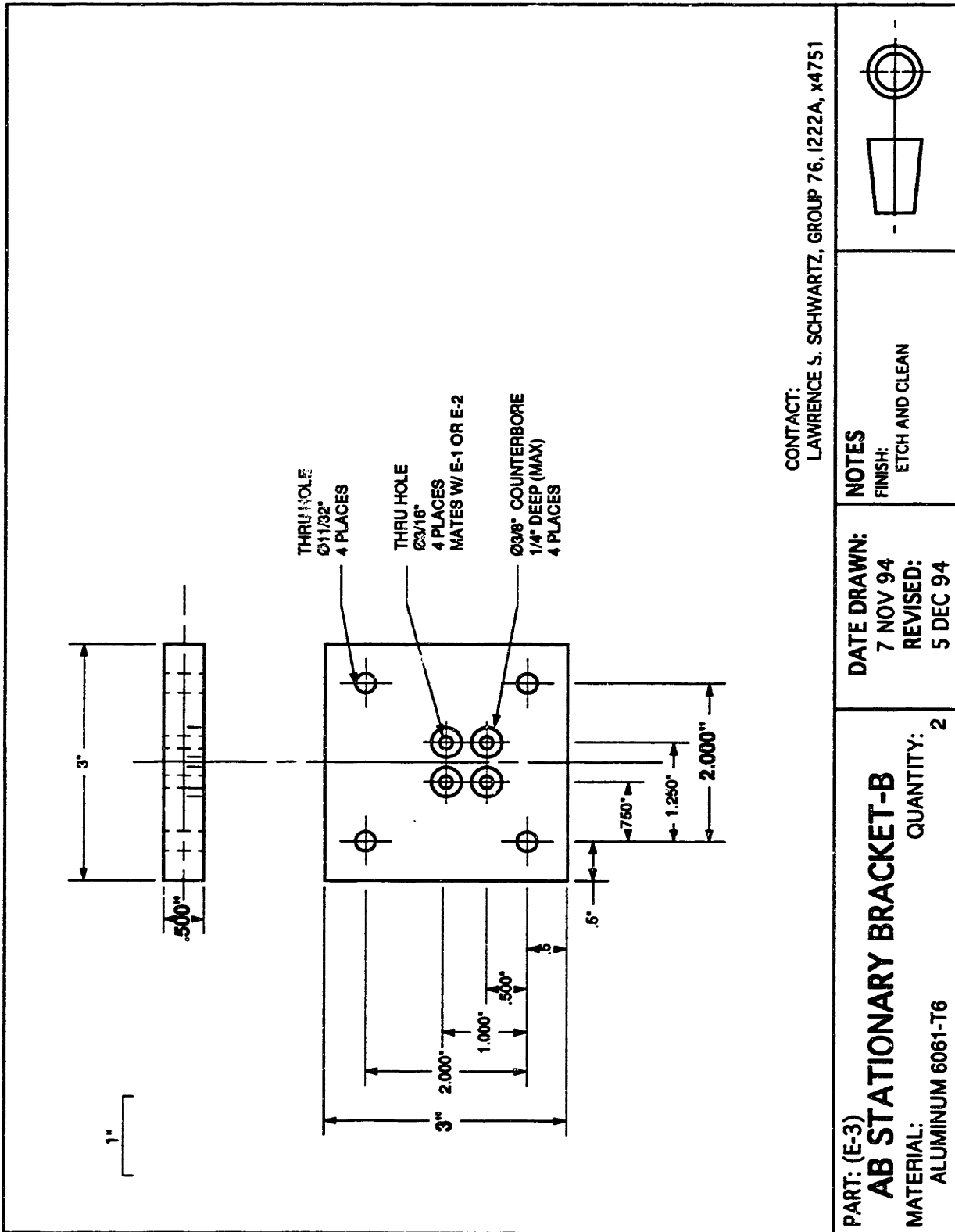
CONTACT:
LAWRENCE S. SCHWARTZ, GROUP 76, 1222A, x4751

PART: (E-2)
AB STATIONARY BRACKET-R
MATERIAL:
ALUMINUM 6061-T6

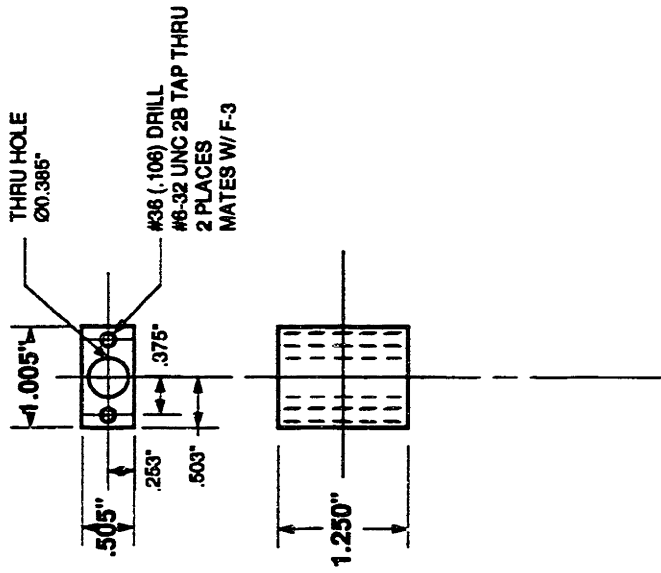
DATE DRAWN:
7 NOV 94
REVISED:
5 DEC 94

NOTES
FINISH:
ETCH AND CLEAN





1"



CONTACT:
LAWRENCE S. SCHWARTZ, GROUP 76, 1222A, x4751

PART: (F-1)

THE E.M. WINDING ROD

MATERIAL:
ALUMINUM 6061-T6

QUANTITY: 1

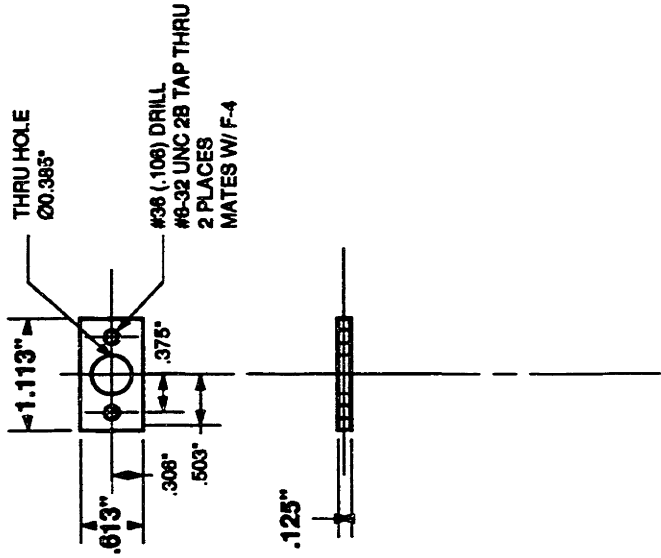
DATE DRAWN:
8 NOV 94

REVISD:
6 DEC 94

NOTES
FINISH:
ETCH AND CLEAN



1"



CONTACT:
LAWRENCE S. SCHWARTZ, GROUP 76, 1222A, X4751

NOTES
FINISH:
ETCH AND CLEAN

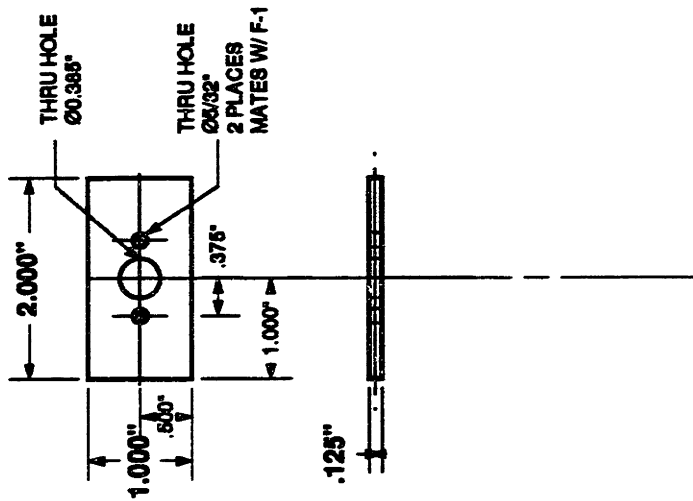
DATE DRAWN:
8 NOV 94
REVISED:
6 DEC 94

PART: (F-2)
THE V.C. WINDING ROD
MATERIAL:
ALUMINUM 6061-T6

QUANTITY: 1



1"



CONTACT:
LAWRENCE S. SCHWARTZ, GROUP 76, I222A, X4751

PART: (F-3)
THE E.M. BOBBIN PLATE
MATERIAL:
ALUMINIUM 6061-T6

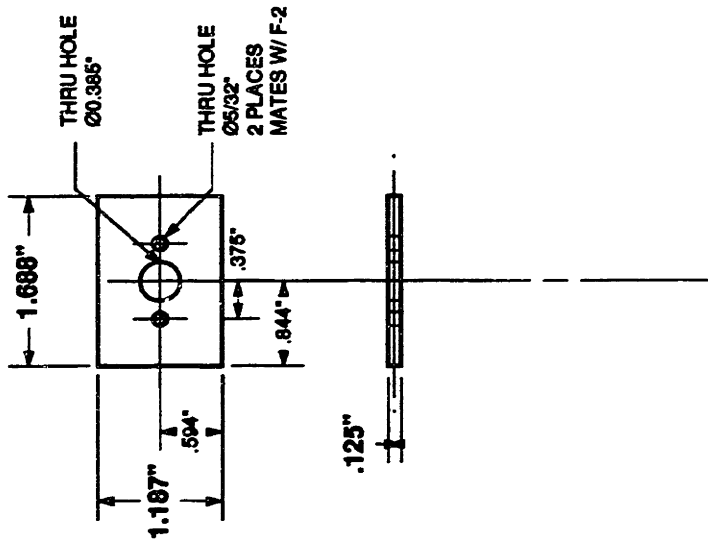
QUANTITY: 2

DATE DRAWN:
8 NOV 94
REVISED:
6 DEC 94

NOTES
FINISH:
ETCH AND CLEAN



1"



CONTACT:
LAWRENCE S. SCHWARTZ, GROUP 76, 1222A, x4751

PART: (F-4)

THE V.C. BOBBIN PLATE

MATERIAL:
ALUMINUM 6061-T6

QUANTITY: 2

DATE DRAWN:

8 NOV 94

REVISED:

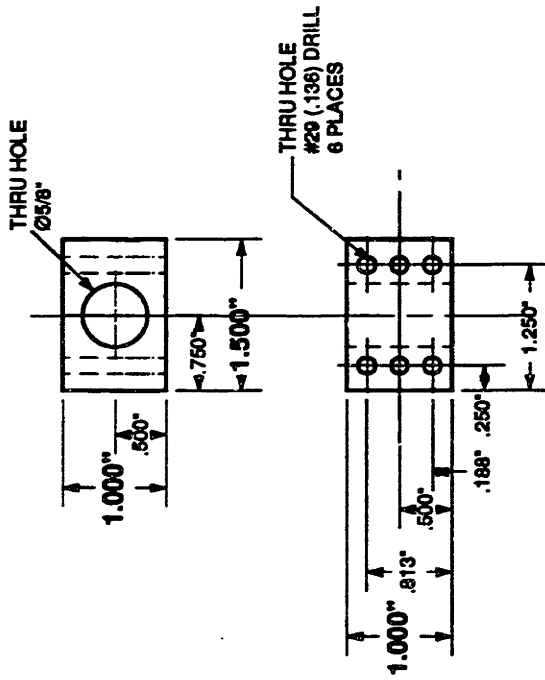
6 DEC 94

NOTES

FINISH:
ETCH AND CLEAN



1"



CONTACT:
LAWRENCE S. SCHWARTZ, GROUP 76, 1222A, x4751

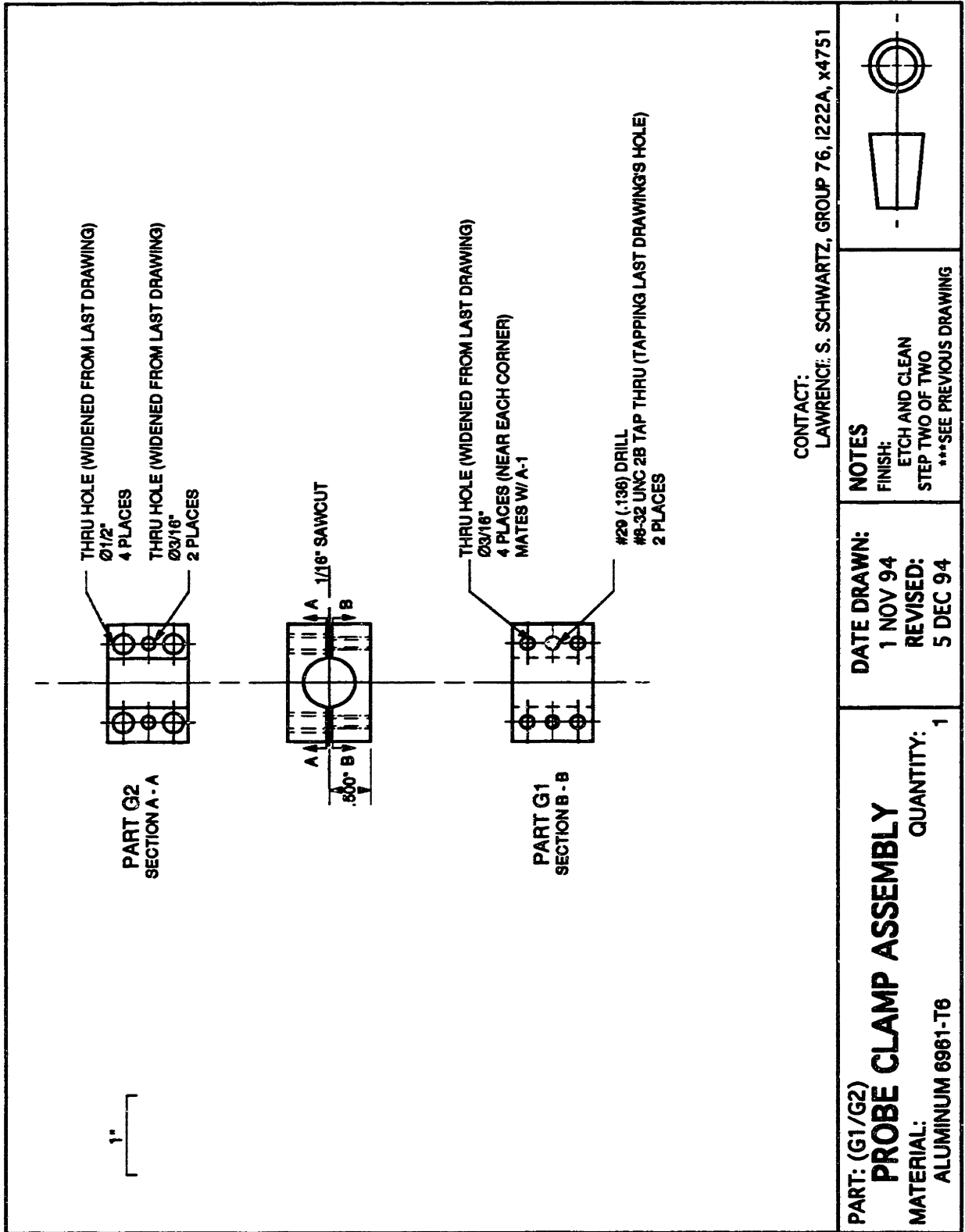
NOTES
FINISH:
ETCH AND CLEAN
STEP ONE OF TWO
***SEE NEXT DRAWING

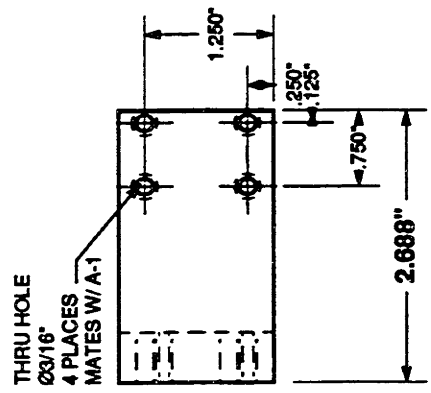
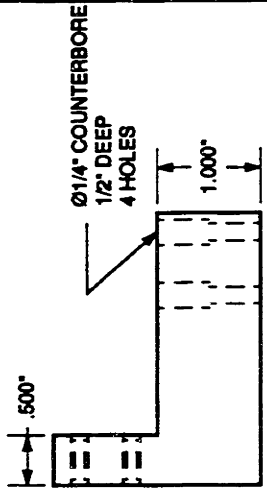
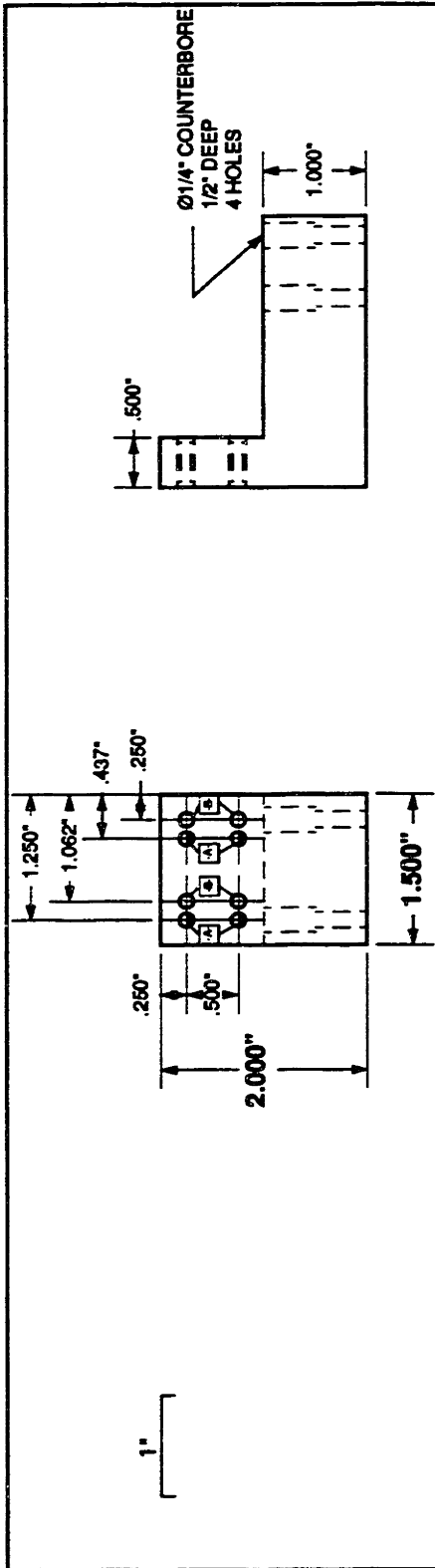


DATE DRAWN:
1 NOV 94
REVISID:
5 DEC 94

QUANTITY: 1


PART: (G1/G2)
PROBE CLAMP ASSEMBLY
MATERIAL:
ALUMINUM 6961-T6



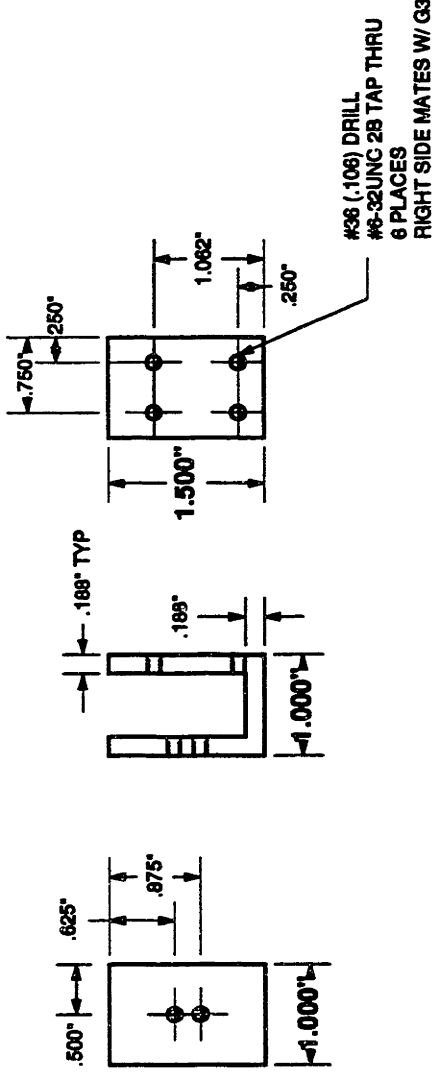


- A** #36 (.106) DRILL
#6-32 UNC 2B TAP THRU
4 PLACES
- B** THRU HOLE
Ø5/32"
4 PLACES
MATES W/ G-4

CONTACT:
LAWRENCE S. SCHWARTZ, GROUP 76, 1222A, x4751

| | | | |
|---|--------------------|---|---|
| <p>PART: (G3) STATIONARY STOP MATERIAL: ALUMINUM 6961-T6</p> | <p>QUANTITY: 1</p> | <p>DATE DRAWN: 1 NOV 94 REVISED: 5 DEC 94</p> | <p>NOTES FINISH: ETCH AND CLEAN</p>  |
|---|--------------------|---|---|

1"



CONTACT:
LAWRENCE S. SCHWARTZ, GROUP 76, 1222A, x4751

| | | | | |
|---|--------------------|--|---|--|
| <p>PART: (G4) STOPPER CLAW MATERIAL: ALUMINIUM 6981-T6</p> | <p>QUANTITY: 1</p> | <p>DATE DRAWN: 20 NOV 94 REVISED: 5 DEC 94</p> | <p>NOTES FINISH: ETCH AND CLEAN</p> | |
|---|--------------------|--|---|--|

THESIS PROCESSING SLIP

FIXED FIELD ill _____ name _____

index _____ biblio _____

▶ COPIES Archives Aero Dewey Eng Hum
Lindgren Music Rotch Science

TITLE VARIES ▶ _____

NAME VARIES ▶ _____

IMPRINT (COPYRIGHT) _____

▶ COLLATION 213 l

▶ ADD DEGREE: _____ ▶ DEPT.: _____

SUPERVISORS _____

NOTES:

cat'r:

date:

▶ DEPT M. E.

| |
|-----------------------|
| page: ▶ <u>J99</u> |
|-----------------------|

▶ YEAR: 1995 ▶ DEGREE: M.S.

▶ NAME: SCHWARTZ, Lawrence
Scott